Behavior of iron, and other ions capable for electron exchange in subduction settings

Margarita Merkulova

To cite this version:

Margarita Merkulova. Behavior of iron, and other ions capable for electron exchange in subduction settings. Earth Sciences. Université Grenoble Alpes, 2016. English. NNT : 2016GREAU030 . tel-01561762

HAL Id: tel-01561762
https://theses.hal.science/tel-01561762

Submitted on 13 Jul 2017

Communauté
UNIVERSITÉ Grenoble Alpes

THÈSE

Pour obtenir le grade de

DOCTEUR DE LA COMMUNAUTÉ UNIVERSITÉ GRENOBLE ALPES

Spécialité : **Terre Solide**

Arrêté ministériel : 7 août 2006

Présentée par

Margarita Merkulova

Thèse dirigée par **Manuel Muñoz** et **Olivier Vidal**

préparée au sein du **Laboratoire ISTerre**
dans **l'École Doctorale Terre, Univers Environnement**

Comportement du fer et autres ions échangeurs d'électrons en contexte de subduction

Thèse soutenue publiquement le **10 octobre 2016**,
devant le jury composé de :

M. Alexander SOBOLEV
Professeur à l'Université Grenoble-Alpes, ISTerre; Président du jury
M. Joerg HERMANN
Professeur à l'Université de Bern, Institute de Géologie, Rapporteur
M. Gleb POKROVSKI
Directeur de Recherche CNRS à Géosciences Environnement Toulouse, Rapporteur
M. José Alberto PADRÓN-NAVARTA
Chargé de Recherche CNRS à Géosciences Montpellier
M. Manuel MUÑOZ
Maître de Conférence à l'Université Grenoble Alpes, ISTerre, Directeur de thèse
M. Olivier VIDAL
Directeur de Recherche CNRS à l'Université Grenoble Alpes, ISTerre, Directeur de thèse

THÈSE

Pour obtenir le grade de

DOCTEUR DE LA COMMUNAUTÉ UNIVERSITÉ GRENOBLE ALPES

Spécialité : **Terre Solide**

Arrêté ministériel : 7 août 2006

Présentée par

Margarita Merkulova

Thèse dirigée par **Manuel Muñoz** et **Olivier Vidal**

préparée au sein du **Laboratoire ISTerre**
dans **l'École Doctorale Terre, Univers Environnement**

Behavior of iron and other ions capable for electron-exchange in subduction settings

Thèse soutenue publiquement le **10 octobre 2016**,
devant le jury composé de :

M. Alexander SOBOLEV
Professeur à l'Université Grenoble-Alpes, ISTerre; Président du jury
M. Joerg HERMANN
Professeur à l'Université de Bern, Institute de Géologie, Rapporteur
M. Gleb POKROVSKI
Directeur de Recherche CNRS à Géosciences Environnement Toulouse, Rapporteur
M. José Alberto PADRÓN-NAVARTA
Chargé de Recherche CNRS à Géosciences Montpellier
M. Manuel MUÑOZ
Maître de Conférence à l'Université Grenoble Alpes, ISTerre, Directeur de thèse
M. Olivier VIDAL
Directeur de Recherche CNRS à l'Université Grenoble Alpes, ISTerre, Directeur de thèse

Acknowledgments

First I would like to thank my PhD supervisors, Prof. Dr. Manuel Muñoz and Dr. Olivier Vidal, who introduced me to the world of experimental petrology and mineralogy, thermodynamics and X-ray spectroscopy. Manuel and Olivier continuously guided me, helped and shared enthusiasm during my PhD. Also, I would like to express my deepest thanks to Dr. Fabrice Brunet, the head of Mineralogy team of ISTerre, who helped to carry out all my piston-cylinder experiments and shared with me his scientific and technical expertise. We had many fruitful scientific discussions with Manuel, Olivier and Fabrice throughout three years of my PhD and I learned a lot from them. I appreciate a lot the possibility to have my PhD under supervision of these wonderful people.

I would like to thank all technicians of ISTerre, especially Nathaniel Findling, Valentina Batanova, and Martine Lanson, and also beamline scientists, in particular Thomas Huthwelker (SLS), Delphine Vantelon (SOLEIL), Olivier Mathon (ESRF) and Angelika Rosa (ESRF). No results would be produced without help and assistance of these people. I appreciate very much discussions with Stephane Guillot, Bernard Evans, François Renard and Keiko Hattori, who supported my results and helped me to generate new ideas.

One more time I would like to send my gratitude to Manuel and Angelika for a fun time which we spend during many experiments and measurements at different synchrotrons.

I am very grateful to my family, especially to my parents, who developed my curiosity which now I find the most important quality for a scientist. I would like to thank my mom for her support, love and belief in me. Люблю вас, мама и папа! Very warm thanks goes to Sjaak for his care, support, insistence and positive thoughts!

I am extremely grateful to all my friends in Grenoble, Moscow and in other parts of the planet. Thank you Frans, Maor, Katya, Igor, Natalie, Ellie, Paul, Claudia, Ana, Catalina, Ayumi, Vika, Eric, Gosia, Elliot, Clara, Owen, Afifa, Ismael, Johanes, Simon for nice and fun moments, which we had together during work and outside the institute, for help in scientific and daily life. I wish to thank Alena, Natasha, Arina and Masha for our infinite friendship and their support. Special thanks go to Audrey, my ideal office mate. Also, I would like to acknowledge Prof. Dr. Pavel Plechov, who inspired me to study petrology and introduced me to the world of science.

Abstract

Subduction zones are the largest recycling systems of our planet. Subduction zones involve recycling of water from hydrated oceanic crust and lithosphere to the upper mantle. Water plays a key role in subduction zone processes, including plate tectonics, magma generation, elemental transport and earthquake generation. The chemical composition, H_2O content of oceanic lithosphere sinking to the mantle, age and geometry of subducting oceanic slab are the main factors controlling subduction zone processes including dehydration.

The principle aim of this dissertation is to investigate the behavior of iron and other ions capable for electron-exchange and to describe the regime of water release from the oceanic plate in subduction settings. The experimental approach of my work allows one to compare chemical and mineral changes occurring during dehydration of serpentinites with different composition. A number of analytical techniques were applied to study the influence of bulk rock composition on the mineral chemistry of produced assemblages. The experimentally investigated pressure-temperature ranges, i.e. 2 GPa and 450-900°C, are representative for hot subduction zones. The extrapolation to other common geothermal gradients was done through thermodynamic modeling. The investigated serpentinite compositions correspond to natural serpentinized peridotites described for oceanic lithosphere.

Bulk Fe content was demonstrated to decrease thermal stability of Fe-Mg-antigorite by 25°C on average compared to stability of Mg-antigorite. Dehydration of Fe-bearing serpentinites, consequently, occurs at lower temperatures compared to Fe-free assemblages. Dehydration reactions observed in Fe-free systems are univariant reactions, while in Fe-bearing systems, serpentinites dehydration appears over a range of temperature through divariant reactions. Moreover, the presence of Al in serpentinite stabilized clinochlore, which retains 15% of water initially contained in serpentinite down to ~120 km (820°C/2 GPa) within hot subduction. Such a dependence of serpentinite dehydration on bulk Fe and Al brings importance of considering not only geometry and the age of the slab, but also a composition of slab lithologies while modeling and interpreting processes in subduction zone. A comparison of the depths of serpentinite dehydration and seismicity revealed a strong correlation and, therefore, a potential contribution of water release to seismicity in the case of hot subduction zones (i.e., Chili type subduction).

X-ray absorption spectroscopy measurements revealed a progressive reduction of Fe and S in with increasing PT conditions investigated serpentinites. The initially high bulk

Fe^{3+}/Fe_{total} ratio in serpentinite is shown to decrease in anhydrous and high temperature assemblages due to magnetite and Fe^{3+}-bearing antigorite breakdown at <550°C and 700°C, respectively. The presence of pyrite in serpentinite, which transforms to pyrrhotite below 450°C, imposes a release of ¼ of initial sulfur, in the H_2S form. The presence of magnetite and pyrite in serpentinite, is crucial and responsible for the production of highly oxidized fluids and volatile sulfur species, which can be transported from the subducting slab into the mantle wedge. Application of the results, obtained in the present study, to natural systems demonstrates that fluids rising from subducting slab are responsible for oxidation of overlying mantle, and in addition, magnetite and antigorite breakdown which occurs with at least 150°C difference may cause a release of chemically different fluids at shallow (low-T) and deep (high-T) parts of subduction.

Keywords: serpentinite, dehydration, subduction, iron reduction, sulfur mobility, seismicity, X-ray absorption, experimental petrology, thermodynamic calculations

Abstract

Les zones de subduction sont les plus grands systèmes de recyclage de notre planète. Elles permettent le recyclage de l'eau contenue dans la croûte océanique hydratée et de la lithosphère du manteau supérieur. L'eau joue un rôle clé dans de nombreux processus associés aux zones de subduction, comme la tectonique des plaques, la production de magma, le transport élémentaire et la génération de tremblement de terre. La composition chimique, le contenu H_2O de la lithosphère océanique, l'âge et la géométrie de la plaque océanique sont les principaux facteurs contrôlant les processus de subduction, y compris la déshydratation.

L'objectif principal de cette thèse est d'étudier le régime de la libération de l'eau depuis la plaque océanique subductante et le comportement du Fe et du S en contenus dans les serpentinites, qui représentent la principale lithologie de roche hydratées océaniques. L'approche expérimentale de ce travail permet d’étudier les changements chimiques et minéralogiques associés lors la déshydratation des serpentinites de différentes compositions. Un certain nombre de techniques d'analyse ont été utilisées pour étudier l’influence de la composition de la roche totale sur la composition des assemblages produits. Les intervalles de pression de température expérimentalement étudiés, à savoir 2 GPa et 450-900°C, représentent des zones de subduction chaudes. L'extrapolation à d'autres gradients géothermiques communs a été faite par thermodynamique. Les compositions de serpentinite étudiées correspondent aux péridotites serpentinisées naturelles décrites pour la lithosphère océanique.

Mon travail indique que la teneur en Fer contrôle a stabilité thermique d’antigorite. Déshydratation de serpentinites avec Fe, par conséquent, pasee à des températures plus basses par rapport aux assemblages Fe-libres. La déshydratation observée dans les systèmes sans Fer se fait le long d'une réaction univariante, alors que dans les systèmes contenant du Fer, la déshydratation se fait sur un domaine de température (réactions de déshydratation divariantes). De plus, la présence de Al dans serpentinite stabilise clinochlore, qui conserve 15% de l'eau initiale jusqu'à ~ 120 km (820°C/2 GPa) dans subduction chaud. Cette dépendance sur Fe et Al apporte importance de considérer non seulement la géométrie et l'âge de la plaque océanique, mais aussi une composition de lithologies lors de la modélisation et d’interprétation de subduction. Une comparaison entre la profondeur des séismes et la profondeur de déshydratation des serpentinites indique une possible contribution de la libération de l'eau à la sismicité dans les zones de subduction chaudes et à pente faible.

La spectroscopie d'absorption des rayons X montre une réduction progressive de Fe et de S dans des serpentinites. Le rapport $Fe^{3+}/Fe_{total,}$ de la roche totale, élevé dans la serpentinite, diminue dans les assemblages anhydres de haute température par décomposition de la magnétite (< 550°C) et de l'antigorite (700°C). La pyrite des serpentinites se transforme en pyrrhotite en-dessous de 450°C et induit une libération de ¼ de soufre initial, probablement sous forme de H_2S. La magnétite et la pyrite présentes dans des serpentinites, sont des phases cruciales pour la production de fluides très oxydés et d'espèces volatiles soufrées qui peuvent être transportés depuis la plaque subductée vers le coin mantellique. Application des résultats montre que les fluides s'élevant de la plaque océanique sont responsables de l'oxydation du manteau; et décomposition de la magnétite et l'antigorite avec au moins 150°C différence peut provoquer une libération de fluides chimiquement différents à peu profond (basse-T) et profondes (T-élevé) parties de subduction.

Mots-clés: serpentinite, déshydratation, subduction, réduction du fer, mobilité de soufre, sismicité, pétrologie expérimentale, calculs thermodynamiques

Table of Contents

I Introduction

Subduction zones are convergent margins which stretch over 55000 km around the Earth. Descend of oceanic or continental plate into the mantle in subduction zones control plate tectonics, birth of volcanic arcs and seismicity. The geological processes, which are generated in subduction zones, have a great impact on human life, mainly because the most destructive natural hazards occur within convergent plate boundaries. On the other hand, most of mineral deposits are associated with subduction settings and, thus, subduction plays also a significant role in human society as a source of economically important ore deposits.

Sedimentary, volcanic and metamorphic rocks of the subducting oceanic or continental plate, undergo metamorphism at elevated pressure and temperature conditions, dehydrate and release large amounts of aqueous fluid which rise to the overlying mantle wedge and interact with the mantle. Fluids formed in subduction zones are responsible for the transport of economically important fluid-mobile elements (FME) which become mobile under certain environment conditions, at high pressure and temperature. Thus, subduction zones are large recycling systems, which deliver material from the surface to the deep mantle and back to the subsurface and surface. The fluids released from the slab are the main transporting agents in the elemental recycling. Aqueous fluids released at deep levels of subduction decrease melting temperature of mantle rocks and, consequently, cause partial melting and generate magmas below the front of arc volcanism. Seismicity in subduction zones has been also proposed to be a consequence of slab dehydration and release of fluids (e.g., Okazaki and Hirth, 2016; Faccenda et al., 2012). Hence, slab dehydration and consequent release of the aqueous fluid are the main driving forces for (1) global elemental cycling within the Earth’s lithosphere; (2) partial melting and generation of arc volcanism; (3) seismicity; (4) mobilization and transfer of economically important elements and their deposition in subsurface conditions. The term “subduction factory” (Eiler, 2003), which is often used among petrologists, perfectly describes the complex systems which process and recycle “raw” crustal and lithospheric material and “manufactures” magmas and continental crust as products.

Understanding dehydration mechanisms, composition of the released fluids and dependence of dehydration on the slab composition, age and subduction geometry will bring light on fundamental questions about functioning of the subduction “factory”.

I.1 Composition of subducting slab

H_2O content

Three main rock lithologies composing modern subducting oceanic lithosphere: sediments, volcanic layers that mainly consist of basalts and gabbro, and peridotites (Fig. I.1-1). The alteration of the oceanic crust taking place on the oceanic floor and in fault zones results in hydration of the mentioned lithologies. Sediments which compose the upper layer of the oceanic crust contain 5 wt.% H_2O on average (Kerrick and Connolly, 2001a). Metabasalts and metagabbro compose a thicker layer of the crust compared to sediments, ~6 km thick, and the amount of H_2O in altered volcanic lithologies does not exceed 3 wt.% (Kerrick and Connolly, 2001b). Main hydrous phases presented in oceanic sediments and metabasalts are clay minerals, chlorite, lawsonite and glaucophane. Clay minerals dehydrate at temperatures below 400°C at 1 GPa and below 300°C at higher pressures (Vidal and Dibacq, 2009), which corresponds to depths of 40-60 km depending on the slab geotherm. Chlorite is stable up to ~400°C and 2 GPa within sediment and metabasalt mineral assemblages (Schmidt and Poli, 1998; Kerrick and Connolly, 2001a), glaucophane and lawsonite breakdown at about 400-500°C below 1.5 GPa, glaucophane breaks down at 300-400°C at about 3 GPa (Kerrick and Connolly, 2001a), whereas, lawsonite can be stable up to 6-7 GPa (Ravna et al., 2010; Kerrick and Connolly, 2001a). According to the pressure and temperature stability limits of the mentioned hydrous phases, depths of sediments and metavolcanic rocks dehydration are from 60 km up to 160 km for hot and cold geothermal gradients, respectively. Lawsonite, whose amount can reach ~20-25 wt.% (Kerrick and Connolly, 2001b), is the only stable H_2O-bearing phase in dehydrated metasediments and volcanic lithologies at pressures over 3 GPa. Lawsonite breaks down to phengite at 7-8 GPa (Schmidt and Poli, 1998; Auzanneau et al., 2010) and thus about 2-3 wt.% of H_2O can be transported within the upper layer of the slab to depths of ~200 km typical of cold subduction.

The process of serpentinization, which results in hydration of mantle peridotites, takes place in mid-ocean ridges and continues in normal faults of the oceanic plate when it bends before sinking into subduction (Kerrick, 2002; Ranero et al., 2003). Olivine-pyroxene assemblages of peridotite transform into serpentine and magnetite and hydrogen since serpentinization is a redox reaction (Andreani et al., 2013). Due to the presence of Al in natural peridotites, chlorite is also present in serpentinized lithologies. Serpentine and chlorite contain ~12 wt.% and 16 wt.% of H_2O respectively. The average degree of peridotite serpentinization is about 60-70 vol.% (Christensen, 1972; Hacker, 2003), which corresponds to ~8 wt.% H_2O in the ultramafic lithologies of the slab. Stability of serpentine and chlorite during subduction will be discussed later. However, we can claim that the amount of H_2O, which is carried by serpentinites into subduction, is much higher compared to the H_2O content of metasediments, metabasalts and metagabbro. Taking into account that slab serpentinites are ~6 km thick (e.g. Guillot et al., 2015; Boudier and Nicolas, 1985), H_2O amount in serpentinites is about 3 times higher than in overlying altered volcanic lithologies and sediments.

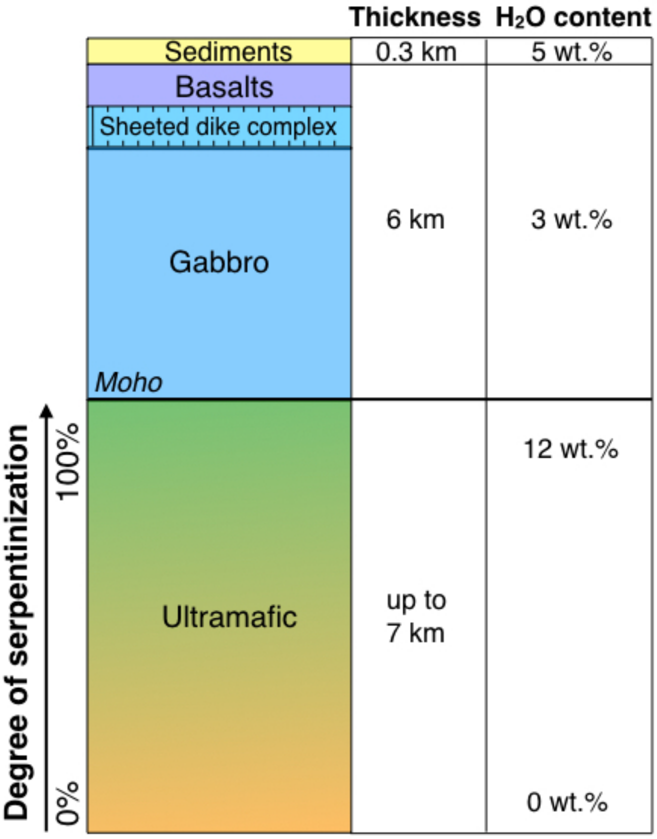

Fig. I.1-1. Lithology, thickness and water content of an average oceanic lithosphere after Boudier and Nicolas, 1985. The Moho border indicated by a thick line between the gabbro complex and the ultramafic mantle.

Composition of slab serpentinites

The principal mineral composition of oceanic serpentinites comprises lizardite, magnetite, brucite and chlorite. Primary mantle minerals, olivine and pyroxene, can be present in lithologies (e.g., Debret et al., 2014) with low degree of serpentinization at deep parts of the lithosphere. Serpentinites can vary in composition depending on the chemical composition of the initial peridotites. Table I.1-1 reports major oxides of several abyssal serpentinized peridotites from different localities. The comparison reveals that major element content is consistent in different serpentinites. Significant variations can be noticed in FeO (Fe_2O_3), MgO, CaO and H_2O contents, however, differences do not exceed 2 wt.%.

Table I.1-1. Bulk rock major oxide (wt.%) compositions of serpentinized peridotites from various localities.

	Lz-serpentinite	Atg-serpentinite	Lz-serpentinite	Lz-serpentinite	Atg-serpentinite	Opx-Ol-serpentinite	Lz-Atg-serpentinite
	Debret et al., 2014		Krishnakanta Singh, 2013	Zeng et al., 2012	Padron-Navarta et al., 2011		Li et al., 2004
	Western Alpes		Northeast India	Southwest Indian Ridge	Nevado-Filábride Complex, Southern Spain		Zermatt-Saas ophiolite
SiO_2	38.80	39.00	41.04	40.42	40.34	45.07	39.43
Al_2O_3	2.00	2.40	2.18	2.72	2.81	2.19	2.72
Fe_2O_3	8.10	8.40	8.97	7.47	4.26	3.08	-
FeO	-	-	-	-	2.87	3.78	6.80
MgO	37.80	38.10	37.48	35.64	37.48	36.98	38.28
CaO	1.00	0.00	1.03	1.38	0.07	0.16	0.59
Na_2O	0.00	0.30	0.04	0.10	0.04	0.05	0.00
K_2O	0.00	0.30	0.07	0.03	0.00	0.01	0.00
TiO_2	0.10	0.10	0.06	0.06	0.10	0.08	0.05
MnO	0.10	0.00	0.20	0.09	0.09	0.09	0.11
P_2O_5	0.00	0.00	0.02	0.01	0.00	0.00	0.00
LOI	12.10	11.30	9.16	11.84	11.47	7.71	10.37
Total	100.10	100.10	99.50	99.75	99.50	99.20	99.10

A range of Fe^{3+}/Fe$_{total}$ ratios in serpentinites is found to be about 0.7-0.8 (Evans, 2008; Debret et al. 2014; 2015). Sulfur is present in serpentinites as a minor element and mainly in form of Fe-Ni sulfides (Evans et al., 2014; Alt et al., 2013). Total sulfur content in serpentinites changes from ~0.03 to ~1 wt.% (Alt et al., 2013). Ni and Cr, as minor elements, are contained mainly in sulfides and oxides, and their content in bulk rock reaches 0.2 wt.% (Deschamps et al., 2013) and 0.6 wt.% (Zeng et al., 2012), respectively.

Trace element composition of abyssal oceanic serpentinites is variable (e.g., Deschamps et al., 2013; De Hoog et al., 2014; Hattori and Guillot, 2007) from one locality to another. Such elements as Sr, Zn and Li were shown to have higher concentrations, 200 ppm, 50 ppm and 30 ppm respectively, compared to other trace elements (Rb, As, Sb, B), which in turn do not exceed 10 ppm in average (Deschamps et al., 2013; Krishnakanta Singh, 2013; Zeng et al., 2012; De Hoog et al., 2014; Hattori and Guillot, 2007).

Variable compositions of oceanic serpentinites may provide different types of fluids while dehydrating in subduction zones. Some trace and minor elements can become mobile in a fluid at elevated P-T conditions, and thus their presence is crucial regarding chemical composition of the fluids released from serpentinites. High Fe^{3+}/Fe$_{total}$ ratios of serpentinites, total Fe content and the presence S$^-$ incorporated in pyrite are significant for the oxidizing potential of the released fluids.

I.2 Serpentinite dehydration in subduction zones and the stability of hydrous phases

Dehydration of serpentinites starts with destabilization of main hydrous phases, serpentine minerals and chlorite. Lizardite, the low temperature variety of serpentine, is the dominant hydrous mineral of the seafloor serpentinites (Mével et al., 2003), chrysotile can be also found in minor amounts. As the oceanic plate subducts and P-T conditions increase, lizardite and chrysotile transform to antigorite (e.g., Schwartz et al., 2013) which is the only serpentine mineral stable at elevated pressure and temperature, typically above 400°C (e.g., Evans, 2004; Fig. I.2-1). The common reaction that is assumed to be responsible for the lizardite-antigorite transition is described as following:

$$\text{17 Lizardite} = \text{Antigorite} + \text{3 Brucite} \qquad \text{(I.2-1)}$$

Other reactions, involving production of olivine and H_2O were also suggested by Evans (2004):

$$\text{16 Lizardite} + 2\,SiO_2 = \text{Antigorite} + H_2O \qquad \text{(I.2-2)}$$

$$\text{Lizardite} + \text{Brucite} = \text{2 Forsterite} + 3\,H_2O \qquad \text{(I.2-3)}$$

$$\text{20 Lizardite} = \text{Antigorite} + \text{6 Forsterite} + 9\,H_2O \qquad \text{(I.2-4)}$$

Consequently, lizardite-antigorite transition may already initiate dehydration at low P-T conditions. No experimental work has been done on the lizardite-to-antigorite reaction and thus, this process is poorly understood. It has been shown that lizardite is more enriched in Fe^{3+} and Al compared to antigorite (e.g., Wicks and O'Hanley, 1988), also differences in crystal structures of antigorite and lizardite results in the loss of an octahedral site in antigorite (Mével et al., 2003). Comparative look at mineral chemistry and crystallography of these two serpentine varieties suggests that lizardite-antigorite transition is not a polymorphic transition. Moreover, systematically higher Fe^{3+}/Fe_{total} values of lizardite relative to antigorite may apply the occurrence of redox reaction during lizardite-antigorite transition.

At temperature above ~400°C, antigorite is the only stable serpentine variety, it can coexist with minor amounts of chlorite if the Al content of the rock is higher than ~2 wt.%. Thus antigorite is the main mineral that controls serpentinite dehydration.

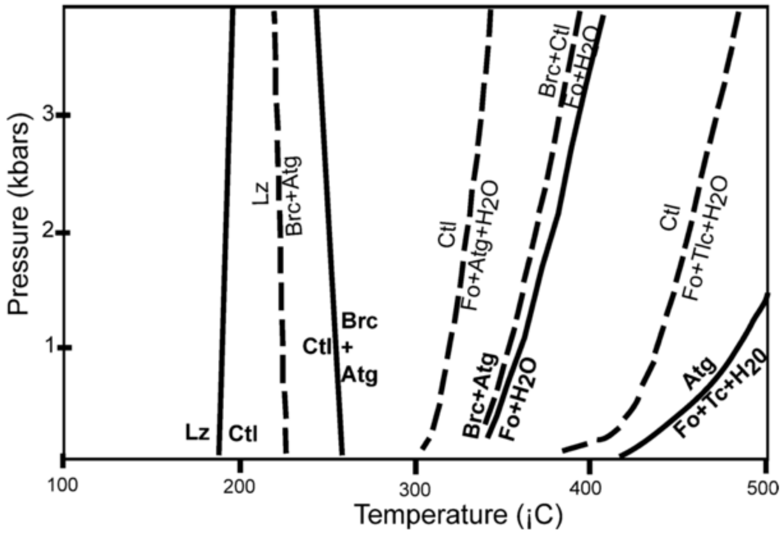

Fig. I.2-1. Phase relationships of serpentine species and related minerals in a T-P diagram. Continuous lines represent stable reaction curves, dashed lines- metastable reaction curves. Atg - antigorite; Brc - brucite; Ctl - chrysotile; Fo - forsterite; Lz - lizardite; Tc - talc. (after Mével et al., 2003).

Based on experimental studies of antigorite breakdown (Ulmer and Trommsdorff, 1995; Bose and Ganguly, 1995; Wunder and Schreyer, 1997; Bromiley and Pawley, 2003; Perrillat et al., 2005; Padron-Navarta et al., 2010) upper thermal stability limit of antigorite was defined as 700°C at 2GPa. The field of antigorite stability narrows at pressures below and above 2 GPa, as it is shown in Figure I.2-2. Figure I.2-2 summarizes selected experimental results on antigorite breakdown reaction and shows that geothermal gradients of two common types of subduction slabs widely overlap with a field of antigorite. And thus, dehydration of serpentinites which follow subduction along the geotherms occurs at 600-650°C at 2.5-3 GPa (100 km) for hot subduction and 550-600 °C at ~5 GPa (200 km) for cold subduction.

Most of the mentioned studies performed dehydration experiments within MgO-SiO$_2$-H$_2$O systems. Bromiley and Pawley (2003) and Padron-Navarta et al. (2010) showed that even small amounts of Al can increase the antigorite stability field to higher temperatures. The effect of Fe on antigorite stability was not studied experimentally. However, incorporation of Fe^{3+} in antigorite is likely to have the same effect on its stability as Al (Evans, 2012; Diener and Powell, 2010). On the contrary, ferrous Fe (Fe^{2+}) usually decreases mineral stability (Ganguly, 2008) and thus, expected to decrease temperature of antigorite breakdown.

Discrepancies in antigorite stability fields between experimental studies on serpentinite dehydration result from the use of different starting materials, such as synthetic gels (Wunder and Schreyer, 1997), mixtures of antigorite with forsterite and enstatite (Ulmer and Trommsdorff, 1995; Bromiley and Pawley, 2003; Perrillat et al., 2005) and different mineral compositions in terms of Fe and Al contents.

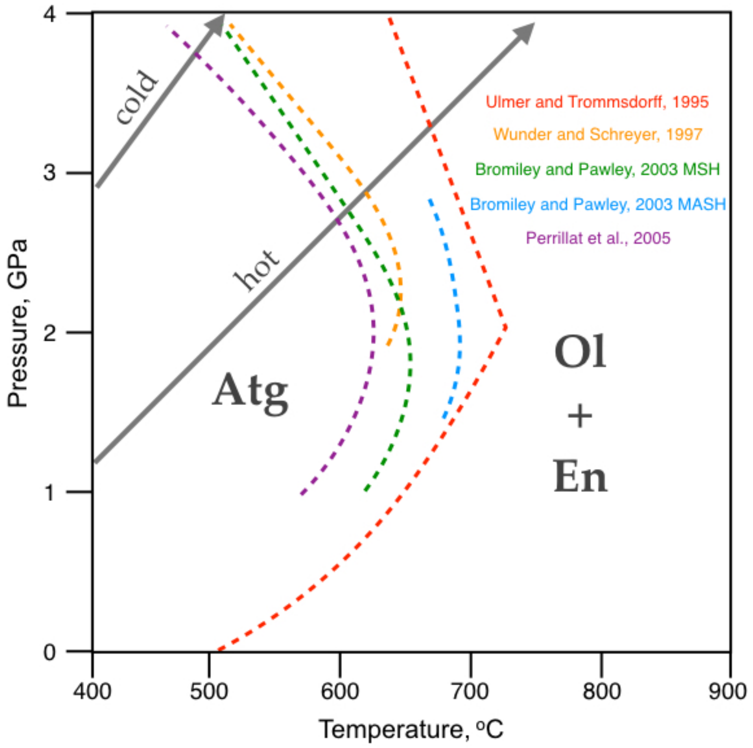

Fig. I.2-2. Selected experimental limits of antigorite stability. Arrows indicate P-T paths of geotherms relevant for Moho boundary below the crust for hot and cold subduction (from Syracuse et al., 2010). Atg – antigorite, Ol – olivine, En – enstatite.

Chlorite, hydrous Al-bearing phyllosilicate, often accompanies antigorite in natural serpentinites (e.g., Debret et al., 2015; Padron-Navarta et al., 2010). In addition, because natural antigorite may contain significant amount of Al, chlorite is a product of antigorite dehydration reaction (Bromiley and Pawley, 2003; Trommsdorff et al., 1998), and this way chlorite appears to be stable at higher temperatures than antigorite. The maximum temperature of chlorite stability is 900°C at pressures between 1.5 GPa and 3 GPa (Staudigel and Schreyer, 1977; Bromiley and Pawley, 2003), at higher temperatures chlorite reacts with orthopyroxene and produces garnet and olivine. High thermal stability of chlorite may indicate that this mineral is the main water-carrier in the mantle and deep parts of subduction zone after antigorite is no longer stable.

I.3 Composition of subduction fluid

Subduction of oceanic lithosphere leads to the release of fluids from sediments, meta-volcanic rocks and serpentinites at depths from 50 to 200 km. Each lithology contains significant amounts of trace elements (e.g., Ba, Rb, Sr, B, U, As, S; Tenthorey and Hermann; 2004; Ribeiro et al., 2013), which become mobile in a fluid. Aqueous fluids released from the breakdown of hydrous minerals may uptake fluid mobile elements and transport them to the mantle wedge. Although, the composition of the slab-originated fluid is still poorly understood, the concentration of REE (rare-earth elements), LILE (large-ion lithophile elements), As, S and other minor and trace element in subduction fluid is derived based on experimental work and natural observations, such as composition of fluid inclusions from mantle wedge and composition of arc magmas (e.g., Bali et al., 2011; Ribeiro et al., 2013).

Sediments are considered to contain a significant amount of carbonate, and consequently they should be a major source of CO_2, which can be volatilized and dissolved in aqueous fluid. But Kerrick and Connoly (2001a) demonstrated that in order to devolatilize CO_2 infiltration of H_2O-rich fluid through sediments is required. If H_2O infiltration is absent, then carbonates may be subducted to the deep mantle. In addition, fluid released from sediment dehydration at depths ~50-80 km, were shown to contain significant amount of trace elements such as LILE, Th and U (Plank and Langmuir, 1998; Tenthorey and Hermann, 2004). The presence of these trace elements in sediment-derived fluids was also highlighted by correlations between compositions of sediments and arc magmas. This suggests that aqueous fluids can potentially carry the mentioned elements into the mantle wedge (Elliott, 2003).

Dehydration of metabasalts may also produce fluids enriched in CO_2, since metabasalts contain up to 3 wt.% of CO_2 (Kerrick and Connoly, 2001b). The presence of minor sulfides and phosphates in metabasalts (Kerrick and Connoly, 2001b; King et al., 2004) suggests that sulfur and phosphorous can be volatilized during dehydration. Metabasalts are characterized by much lower REE and LILE content and, thus, fluids released from meta-volcanic rock dehydration are assumed to be poor in FME (fluid-mobile elements).

Serpentinites, main hydrous lithology in the oceanic slab, have a capacity to carry significant amount of FME such as B, Cs, Li, As, Sb, U, Rb, Ba, Sr, S (Tatsumi and Nakamura, 1986; Hattori and Guillot, 2003; Tenthorey and Herman, 2004; Ribeiro et al., 2013; Evans and Powell, 2015). The dehydration of serpentinites below the fore-arc suggests the release of aqueous fluids rich in FME (e.g., Ribeiro et al., 2015; Hattori and Guillot, 2003; 2007), since these elements are incompatible in olivine and pyroxene, which are products of serpentine decomposition.

The composition of fluid directly depends on a rock lithology from which it is released and consequently fluid composition may vary along the slab from ~50 km down to 200 km. Mobility and compatibility of FME carried by subducting slab into the fluid may be dependent on redox conditions in subduction zones (Parkinson and Arculus, 1999; Bali et al., 2011).

I.4 Redox state of subduction zones

The oxygen fugacity (fO_2) in subduction zones is an important parameter that controls phase stabilities, mobility of volatile species in slab lithologies, released fluid and overlying mantle (Arculus 1985; Parkinson and Arculus, 1999). Oxygen fugacity of mantle rocks can vary from QFM (quartz-fayalite-magnetite oxygen buffer) -3 to QFM +2 (Frost and McCammon, 2008); the value of fO_2 depending mostly on temperature, pressure and rock composition of a rock. The redox conditions in subduction zones are still a poorly investigated question; however, some attempts to interpret the redox conditions that occur in such complex environments have been made by various authors (e.g., Evans and Powell, 2015; Evans, 2012; Debret et al., 2016).

Thanks to its ability to accommodate different valence states for iron, serpentinite is the lithology that represents the principal redox buffer, i.e. fO_2, in subduction zones. When olivine and pyroxene, which are primary minerals in oceanic peridotite, react with sea water at hydrothermal temperatures (<300°C; Marcaillou et al., 2011; Andreani et al., 2013) in mid-ocean ridge settings, serpentine and magnetite are produced (Andreani et al., 2013). Subsequently, Fe^{3+}-rich serpentinite enters subduction zones. Some other oxidized components, such as sulfates, can be present in serpentinite (Alt et al., 2012) and increase its oxidizing potential. The presence of Fe^{3+}-bearing serpentine and magnetite and sulfates in serpentinites suggest that they were formed under high fO_2 conditions. However, no fO_2 calculations state have been done in such mineral systems. Based on the study of natural chlorite-harzburgite assemblages produced by serpentinite dehydration, Debret et al. (2015) estimated the fO_2 value at about QFM+2. Moreover, Debret et al. (2014; 2015) demonstrated a decrease of bulk Fe^{3+}/Fe_{total} from serpentinites to chlorite-harzburgites, which suggests that fO_2 of initial serpentinites was even higher than QFM+2. The dehydration of serpentinites and associated decrease of Fe^{3+}/Fe_{total} (Debret et al., 2014; 2015) may lead to a transfer of oxidized components to the overlying mantle through release of fluids (Frost and McCammon, 2008). And this way, fO_2 of the subducting slab can be decreased. However, exact mechanisms of the redox change in subduction zones are still debated.

Evidence for oxidized fluids released from the slab has also been demonstrated by high Fe^{3+}/Fe_{total} ratios and, respectively, high oxygen fugacity (QFM+2) of arc basalts, which inherited these high parameters from slab-derived fluids (e.g., Kelley and Cottrell, 2009). The fact that arc volcanic rocks are more oxidized than MORB (mid-ocean ridge basalts) and OIB (ocean island basalts) (Kelemen et al, 2003; Parkinson and Arculus, 1999; Brandon et al, 1996; Wang et al., 2007; Kelley and Cottrell, 2009; Evans et al., 2012) indicates that subducting slab provides oxidizing conditions for arc magma generation.

Some ultramafic massives from ophiolites and subduction zones record fO_2 conditions from FMQ-3 to +2 (Frost and McCammon, 2008). Peridotites from these ultramafic massifs could be originated by dehydration of slab serpentinites. Such a diversity of peridotite redox state may indicate that the reduction of the slab can occur in a different extent: oxidized components may be retained in the slab after dehydration and thus subducting slab records high fO_2, or oxidized species may be released and recycled to the lower mantle leaving the slab residue with a low fO_2.

II Open questions and strategy

The complexity of subduction zones and their inaccessibility for direct observations and measurements raise a number of unsolved problems regarding subduction zone functioning. Despite many experimental, natural and thermodynamic studies dedicated to serpentinite dehydration and redox state in subduction, there is still a large number of uncertainties in these topics. Discrepancies between experimental studies pose questions: what is the main factor affecting antigorite destabilization? Which serpentinite compositions used in experiments better correspond to natural systems? Simplified experimental and thermodynamic models require their extrapolation to complex natural settings. Natural serpentinites are very diverse in terms of chemical and mineral compositions, and, thus, there cannot be one unique solution for interpreting serpentinite dehydration. Progress in thermodynamic modelling allows to establish serpentinite dehydration models for various compositions and, what is equally important, for different geothermal gradients. Advanced thermodynamic modelling which can describe processes in natural settings demands robust thermodynamic databases. However, data sets present within computational packages and available for thermodynamic modelling do not include all mineral end-members, in particular Fe-antigorite. At this stage, experimental work can help to constrain the stability of mineral phases to allow their introduction to the thermodynamic databases. Few experimental and thermodynamic studies have made successful attempts to model dehydration of serpentinites including Fe- and Al-bearing antigorite. But, redox changes have not been quantified yet due to the absence of knowledge about Fe^{3+} and S behavior in serpentinites during dehydration. Experimental setups used by petrologists may intrinsically differ in oxygen fugacity that potentially affects experimental conditions and thus causes discrepancies in the interpretation of results.

In this context, several open questions dedicated to dehydration and compositional evolution of serpentinites are raised in the present thesis:

1. How much water is released from the slab, and serpentinites in particular, at different depths of subduction zones? What is the correlation with intermediate and deep earthquakes?
2. How does serpentinite composition affect the stability of antigorite and dehydration process?

3. What is the behavior of major elements capable for electron exchange such as iron and sulfur during serpentinite dehydration?
4. What are consequences regarding the properties of the fluids released and their transport to the mantle wedge?

The main objective of this thesis is to experimentally investigate the dehydration of serpentinite with different compositions, in terms of Fe and S content, in order to compare the effect of serpentinite composition on dehydration regime and on a chemistry of released fluid. The experimental results were compared with thermodynamic modelling and models were corrected by the introduction of Fe-bearing antigorite end-member.

To study the effect of bulk composition on the temperature of antigorite stability and on the redox potential of serpentinites *ex-situ* and *in-situ* experiments were performed at P-T conditions relevant for subduction zone settings. Detailed characterization of experimental products provided information about changes in mineral chemistry and mineral modes as a function of temperature. Thermodynamic calculations were performed to extrapolate experimental results to different geothermal gradients relevant to “hot” and “cold” subduction zones. One of the goals of the study was to develop theoretical antigorite solid solution, including Fe^{2+} and Fe^{3+}-end-members, to model processes with rock and mineral compositions close to natural and apply the developed model to natural rock study. X-ray absorption spectroscopy measurements were applied to investigate bulk Fe and S speciation changes during serpentinite dehydration. Analysis of spectroscopic measurements allowed to quantify the oxidizing potential of different compositions of serpentinites. The Fe and S redox information was used to derive fluid properties and composition. The comparison of experimental results with natural rock observations provides new insights into subduction zone processes and opens new perspectives for further investigations.

III Outline of the thesis

The manuscript contains 4 chapters, accompanied with a general introduction and conclusions.

Chapter 1 is dedicated to presentation of the experimental and analytical methods used in this study to investigate serpentinite dehydration. Detailed descriptions of *ex-situ* experiments, performed with the use of piston-cylinder apparatus, and *in-situ* experiments, carried out at the synchrotron radiation facility with the use of several types of diamond-anvil cells, are provided. Analytical techniques applied in this study are also described, including basic principles of X-ray absorption spectroscopy.

Chapter 2 is based on the article, which is published in Lithos journal, and devoted to the effect of Fe on antigorite stability and serpentinite dehydration. Nine HP-HT experiments are described, which were performed with the starting material contained mixture of antigorite and magnetite. Electron probe microanalysis, X-ray diffraction characterization and mass balance calculations of the experimental products provide information on mineral chemistry, as well as the amount of released fluids. Thermodynamic modelling performed with introduced Fe-bearing antigorite was compared with experimental results. Good agreement between thermodynamic and experimental data allowed to model serpentinite dehydration along two typical P-T paths of the slab Moho. A comparison of earthquake hypocenters depths and water-release events along the geotherms demonstrated a potential link between dehydration and seismicity in hot subduction zones.

Chapter 3 presents results regarding the behavior of Fe and S during serpentinite dehydration. This chapter includes the manuscript of article, which is prepared for submission to Earth and Planetary Science Letters journal and describes the evolution of serpentinite redox state during dehydration and the effect of Fe and S reduction on the composition of the released aqueous fluids. The second part of the Chapter is devoted to results on Fe reduction evidenced during *in-situ* diamond-anvil cell experiments. Redox reactions were also investigated during the partial breakdown of two serpentine varieties, antigorite and lizardite. The third part of the Chapter describes the results on sulfur mobility that occurred in *ex-situ* experiments and incudes a discussion about S oxidation states in the released fluid.

Chapter 4 summarizes the main approach of thermodynamic calculations, development of the antigorite solid solution, and application of the modelling to subduction zone processes.

This chapter also includes an article, published in Doklady Academii Nauk journal on the topic of mantle wedge hydration.

Chapter 1 Experimental techniques and analytical methods

1.1. Experimental techniques

1.1.1. High pressure experimental techniques.

With a progress in high-pressure high-temperature experimental techniques, geologists, in particular petrologists, have an opportunity to investigate the behavior of rocks and minerals under conditions relevant to deep Earth's mantle. Two principal experimental apparatuses were used in the present work – press piston-cylinder and diamond-anvil cell (DAC).

Piston-cylinder apparatus is aimed to perform experiments at relatively high pressure (up to 6 GPa) and temperature (up to 900-1200°C depending on pressure medium and the cell assembly materials; Shilling and Wunder, 2004; Moore et al., 2008). The first advantage of the piston-cylinder experiments is the use of a large sample volume (~0.5 cm^3) and therefore a possibility of using different analytical techniques on the same quenched sample. Another advantage is a possibility to perform long runs, from few hours up to few weeks, because of the precisely controlled pressure and temperature and stability of these two parameters. A limitation of the piston-cylinder experiments is an inability of performing *in-situ* experiments, which allows to follow phase transitions and mineral chemistry during pressure and temperature increase and with time at stable experimental PT conditions.

Recent analytical and experimental advances have allowed to perform *in-situ* experiments in diamond-anvil cells. Diamond-anvil cell can reach much higher pressures than piston-cylinder apparatus (up to 300 GPa; Loubeyre et al., 2002) and temperatures (900 – 5000°C depending on heating system; Bassett et al., 1993; Jeanloz and Heinz, 1984). Another, and the most important for us, advantage is that DAC allows the direct observation of the sample changes under pressure and temperature thanks to transparency of the diamond anvils in the visible domain. The observation of the sample in the DAC can be performed by using optical microscopes, diffraction and spectroscopic techniques. There are two main methods of reaching high temperature in DAC, which are electrical resistive heating and laser heating. In the present study, we carried out experiments in a few types of DACs using electrical resistive heating. The typical temperature range that was targeted in the present work is between 350°C and 900°C. Due to this reason electrical heating in DACs is more efficient to use for temperatures below 1000°C compared to laser heating. Electrical heating allows to increase temperature from 0 to ~1000°C with a rate from few degrees per hour to 100°C per minutes. Moreover, the electrically heated DAC provides homogenous heating inside the sample chamber. Another advantage of the electrically heated DAC is a compact size which can be installed on different X-ray beamlines without dismantling the beamline setup.

1.1.2. Piston-cylinder experiments

In order to study phase relations, mineral chemistry and bulk rock Fe and S speciation changes of serpentinites, their anhydrous analogues and transitional assemblages three series of piston-cylinder experiments were performed at ISTerre (Grenoble). The results of piston-cylinder experiments were also used for thermodynamic modelling. In particular, the results were employed for developing new parameters in thermodynamic dataset and for calculating phase diagrams in model chemical systems related to experimental ones.

Experimental setup

Experiments were carried out in an end-loaded piston-cylinder apparatus. Figure 1.1.-1a. demonstrates the piston-cylinder apparatus and indicates main parts of the press. The main part of the apparatus is the pressure vessel, which is composed of a steel bridge and so-called "bomb". The bridge contains a piston that advances into the "bomb" when the pressure applied. The "bomb" consists of a steel frame, tungsten carbide (WC) core and a pressure assembly.

The piston cylinder assembly used in this study is shown schematically in Figure 1.1.-1b. Capsules for all experiments were made of gold, two types of capsule dimensions were used: 1. 15 mm length and 3 mm inner diameter; 2. 12 mm length and 2 mm inner diameter. After starting material was placed in a capsule, capsule was welded shut. The capsule was then fitted into a pyrophyllite sleeve and loaded in a NaCl-based pressure cell with a graphite furnace. Temperature was measured with a Pt-Rh thermocouple (S-type), the junction of which was placed at *ca.* 1mm from the sample top (see Brunet et al., 2003). Uncertainties on temperature are within ± 9.3°C. Pressure was controlled by oil pump and calibrated according to the ratio: Pressure on the sample [bars] = Oil pump pressure [bars]*74.88 [bars].

The pressure could change due to cell assembly relaxation and room temperature oscillations during an experiment. Uncertainties on pressure are within ± 0.07 GPa.

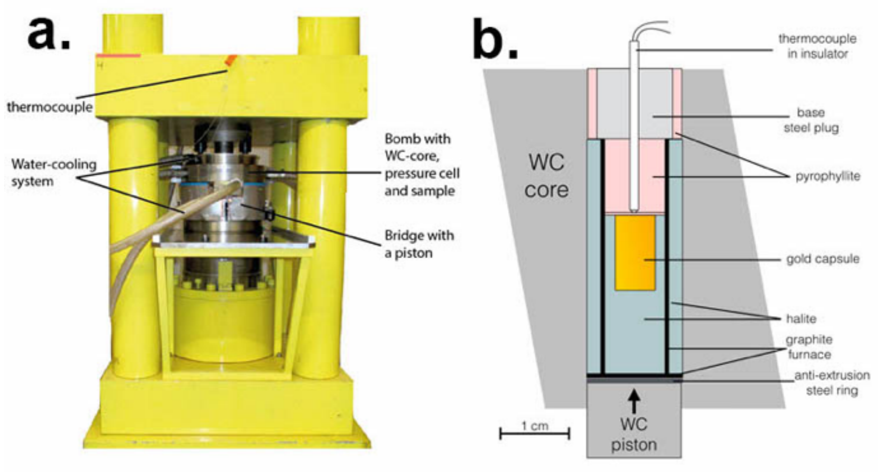

Fig. 1.1.-1. a. Piston-cylinder apparatus. b. press assembly.

Each experimental run was isobarically quenched, the recovered capsule was weighed and pierced to check that the water produced during mineral reactions, if any, had not escaped in the course of the experiment. The experimental products were divided in three parts for (1) X-ray powder diffraction characterization; (2) electron microprobe analyses and scanning electron microscope observations; (3) X-ray absorption spectroscopy measurements.

Experimental conditions, starting materials and experimental products of performed piston-cylinder run are given in Table 1.1.-1.

Table 1.1.-1. Experimental conditions, composition of starting material and experimental products. No water was added to starting materials.

Run #	T, C	P, Gpa	Starting material	Duration	Solid run products
Set#1					
Atg_15	600	2	Atg 100%	7 days	Atg, Ol, Clc, Cpx
Atg_16	700	2	Atg 100%	5 days	Ol, Clc, Opx, Cpx
Atg_17	800	2	Atg 100%	6 days	Ol, Opx, Clc, Cpx
Atg_18	550	2	Atg 100%	7 days	Atg, Ol, Clc
Atg_19	650	2	Atg 100%	5 days	Atg, Ol, Clc, Cpx, Tr
Atg_20	850	2	Atg 100%	6 days	Ol, Cpx, Opx, Clc
Atg_22	875	2	Atg 100%	7 days	Ol, Cpx, Opx, Clc
Set#2					
Ant_Mgt5_01	600	2	Atg 95%, Mag 5%	9 days	Atg, Clc, Ol, Cpx
Ant_Mgt5_02	700	2	Atg 95%, Mag 5%	5 days	Ol, Opx, Tr, Clc
Ant_Mgt5_03	650	2	Atg 95%, Mag 5%	6 days	Atg, Ol, Cpx, Clc, Adr
Ant_Mgt5_06	750	2	Atg 95%, Mag 5%	4 days	Ol, Opx, Clc, Cpx
Ant_Mgt5_07	800	2	Atg 95%, Mag 5%	4 days	Ol, Opx, Clc, CPx
Ant_Mgt5_08	675	2	Atg 95%, Mag 5%	4 days	Atg, Ol, Clc, Tr, Cpx
Ant_Mgt5_09	725	2	Atg 95%, Mag 5%	4 days	Ol, Opx, Clc, Cpx
Ant_Mgt5_11	850	2	Atg 95%, Mag 5%	4 days	Ol, Opx, Prp
Ant_Mgt5_12	550	2	Atg 95%, Mag 5%	5 days	Atg, Clc, Ol
Set#3					
Atg_Py_15	550	2	Atg 98.5%, Py 1.5%	4 days	Atg, Clc, Py, Po
Atg_Py_16	700	2	Atg 98.5%, Py 1.5%	5 days	Atg, Tr, Clc, Ol, Cpx Po
Atg_Py_17	850	2	Atg 98.5%, Py 1.5%	6 days	Ol, Opx, Cpx, Clc, Po
Atg_Py_18	450	1.5	Atg 98.5%, Py 1.5%	8 days	Atg, Ol, Cpx, Clc, Py
Atg_Py_19	600	2	Atg 98.5%, Py 1.5%	6 days	Atg, Ol, Cpx, Clc, Po
Atg_Pyt_20	900	2	Atg 98.5%, Py 1.5%	6 days	Fo, Opx, Cpx, Po, Prp
Additional experiments					
Py-Po	700	2	Py, 10 ml H_2O	5 days	Py
Hem-Mgt	700	2	Hem 93%, Mgt 7%	6 days	Hem 25%, Mag 75%
T calibration	100-900	2	Qz 100%	1 day	-

Temperature gradient

The temperature gradient across the capsule was determined from double-thermocouple experiment which was carried out at temperatures from 100 to 900°C at 2 GPa. During this experiment the temperature was measured above and inside the gold capsule every 100°C. The results show that the maximum temperature difference within the capsule is less than 10°C.

The double-thermocouple experiment was conducted using the same cell assembly as for the serpentinite dehydration experiments. A schematic drawing of the cell assembly for the temperature calibration experiment is shown in Figure 1.1.-2a. The only difference from the usual experiments was the use of open capsule filled with crushable quartz which was filled up to the middle of the capsule. The upper part of the capsule was filled with a pyrophyllite piece which had an axial hole for the thermocouple. Two Pt-Rh (S-type) thermocouples were used for temperature measurements. The thermocouples were placed in a four-bore tube insulator. One side of the insulator was grinded away to expose two of the holes at 8 mm from the end (Fig. 1.1.-2b), then two sets of thermocouple wires were placed in the insulator and welded. This way the junctions of the thermocouples were positioned at 8 mm from each other; one being placed in the center of the capsule, and the second 8 mm above the capsule (Fig. 1.1.-2b).

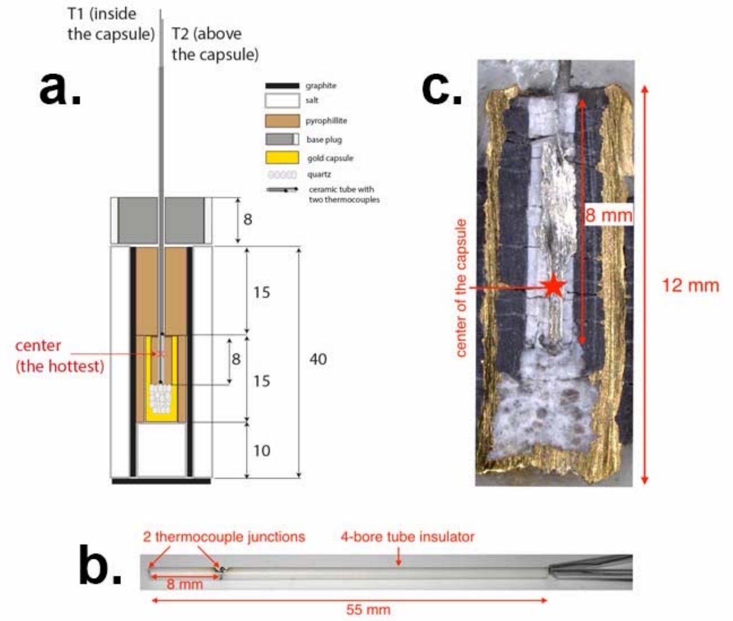

Fig. 1.1.-2. a. Schematic drawing of the cell assembly used for temperature-calibration experiment; b. photograph of the 4-bore ceramic tube with two thermocouples; c. photograph of the cut capsule after performed temperature-calibration experiment.

The experiment was carried out at 2 GPa, maximum temperature was 900°C. The thermocouples were connected to a Eurotherm temperature controller one after another at each temperature step and the temperature of both thermocouples was measured every 100°C. After the experiment was cooled down, the capsule was recovered and cut along in order to check positioning of the thermocouple junctions. Photographs of the cut capsule (Fig. 1.1.-2c) reveal that the bottom junction of the thermocouple was displaced and located 2 mm lower the capsule center. The displacement occurred due to the capsule squeezing during the experiment.

The results of the experiment are shown in Table 1.1.-2. Figure 1.1.-3 displays temperature values inside the capsule *versus* temperature above the capsule. The results demonstrate that the temperature is 2-13°C lower in the center of the capsule compared to the temperature measured above the capsule. The thermal gradient along the length of the capsule is getting smaller with temperature increase. Deviation of temperature value in the middle and above the capsule at 100-600°C is 2.5%, whereas at 700-900°C the deviation is only 1.4%. The average difference on temperature is ± 9.3°C, this value was taken as the temperature uncertainty for all experiments presented in the study.

Table. 1.1.-2. Temperature difference and relative % deviation between two T measurements during temperature-calibration experiment.

T	T difference	rel. %
100	2	2.00
200	6	3.00
200	5	2.51
300	8	2.67
400	10	2.50
500	11	2.19
600	12	2.00
700	7	1.00
700	12	1.72
800	12	1.50
800	12	1.50
900	10	1.11
800	12	1.49
700	11	1.58
600	12	2.00
500	11	2.17
500	13	2.55
400	10	2.53
300	9	2.98
200	7	3.45
100	3	3.00
average T	9.2	2.16

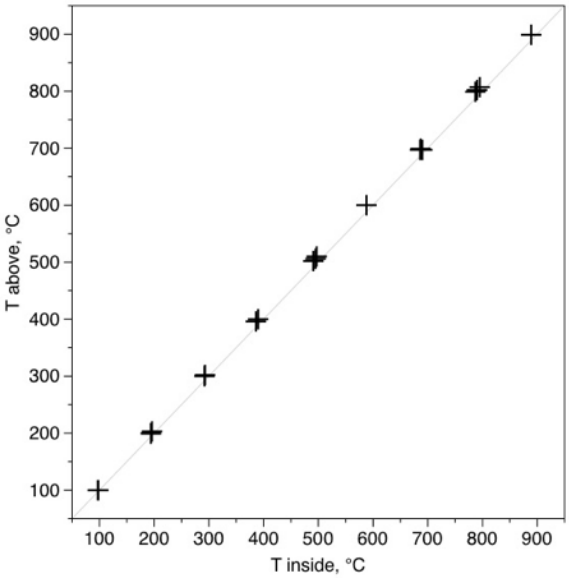

Fig. 1.1.-3. Plot showing correlation between two simultaneous temperature measurements (inside and above the capsule) during temperature-calibration experiment.

Starting materials

The antigorite sample that was chosen as a major component for all starting material mixtures in the experiments is a natural antigorite collected in at the Mont-Cenis massif, French Alps (Muñoz et al., 2013; Debelmas et al., 1980). Mont-Cenis massive includes an exhumed ophiolite partly consisted of serpentinites from which the antigorite used in this study is originated. Therefore, the antigorite sample represents a principal mineral of serpentinized oceanic lithosphere. This sample was chosen in part because of its homogeneity, and in part because it is well crystallized and available in sufficient quantity for experimental petrology.

The antigorite was analyzed by XRD and EPMA. The diffraction pattern of the antigorite is shown in Fig. 1.1.-4 and reveals main peaks of antigorite (2 theta = 12.13, 24.64). In addition, minor phases are observed, such as clinochlore and andradite in amounts of 6 wt.% and 6.4 wt.% respectively in according to Rietveld refinement of the XRD pattern. The presence of clinochlore and andradite can be explained by the natural origin of the chosen antigorite. The observed together with antigorite minor phases are known to be present in natural serpentinites (Debret et al., 2014, Plumper et al., 2014).

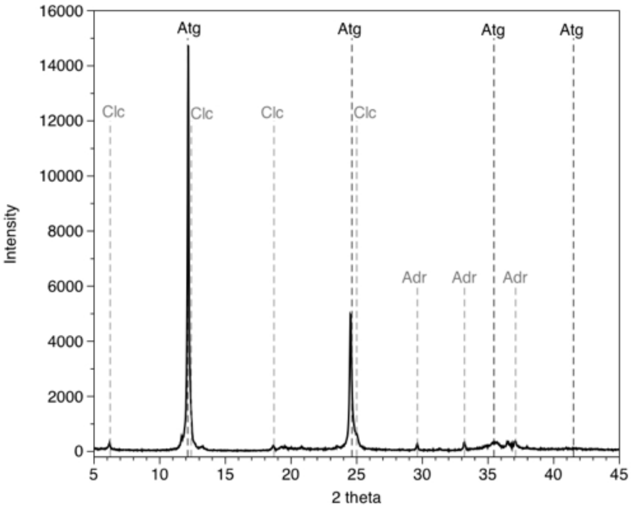

Fig. 1.1.-4. XRD pattern of antigorite used in starting material for piston-cylinder experiments. Atg – antigorite, Clc – clinochlore, Adr – andradite.

The electron microprobe analyses reveal that the antigorite is atypically depleted in iron and contains 1.37 wt.% of FeO (Table 1.1.-3). The comparison of the antigorite from Mont Cenis massive with antigorite from other ophiolite complexes (Table 1.1.-3) demonstrates that Fe content in the antigorite used in this study is 2.5-6 times lower than in antigorite from other localities. Moreover, Muñoz et al. (2013) showed that iron is mainly incorporated as ferric iron in this antigorite, which will be also shown later in the manuscript (see Chapter 3.2).

Table 1.1.-3. Major-oxide chemical composition of starting material for piston-cylinder experiments and

	Atg Mt Cenis	Debret et al., 2014	Debret et al., 2015	Schwartz et al., 2013	**Atg+Mgt**	**Atg+Py**
Oxide	wt. %					
SiO_2	44.12	40.10	42.46	43.98	39.02	35.99
TiO_2	0.02	0.70	0.00	0.01	0.45	0.00
Al_2O_3	0.72	1.80	2.65	0.40	1.92	1.96
FeO	1.37	8.00	3.61	4.52	6.07	3.24
MgO	41.49	37.80	37.87	37.82	38.52	42.50
CaO	0.01	0.70	0.00	0.00	2.43	1.99
Cr_2O_3	0.00	0.00	0.25	0.01	0.16	0.16
NiO	0.00	0.00	0.20	0.24	0.04	0.00
H_2O	12.14	11.60	11.99	12.95	11.50	12.00
SO3	0.00	0.00	0.00	0.00	0.00	1.94
Total	100.00	100.70	99.03	99.93	100.12	100.00
Fe^{3+}/Fe_{tot}	0.96				0.96	0.82

Three starting material mixtures were prepared for the experiments: (1) 100 wt.% natural antigorite; (2) 95 wt.% natural antigorite + 5 wt.% magnetite; (3) 98.5 wt.% natural antigorite + 1.5 wt.% natural pyrite. For reasons of simplicity experiments with 100 % of antigorite in the starting material will further be called “set#1”, with magnetite - “set#2”, and with pyrite - “set#3”. The same natural antigorite was used in all three starting mixtures.

The starting material for experimental set#2 is represented by a mixture of the finely crushed antigorite with 5 wt.% of synthetic magnetite (Magnox powder, 99% purity). The prepared mixture was ground in an agate mortar for 10 minutes. The bulk composition of the starting material displays 6.07 wt.% of FeO, and matches typical oceanic serpentinites (e.g., Li et al., 2004).

For the experimental set#3 a starting material consisted of the Mont Cenis antigorite and natural pyrite in the amount of 1.5 wt.% was. The bulk FeO content of the third starting material is 3.24 wt.% according to XRF measurements (Table 1.1.-3).

Open-like system conditions and intrinsic oxygen fugacity in the cell assembly

The experimental setup of the present work and NaCl-pyrophyllite cell assembly including graphite heater imposes intrinsic oxygen fugacity (fO_2) related to C-CO-CO_2 (CCO) buffer. The values of fO_2 in such conditions was reported to be between QFM and QFM-2 (e.g., Truckenbrodt et al., 1997).

Gold capsules were chosen for piston-cylinder experiments of this study. Gold as a material for capsules has an advantage over other materials (e.g., Pt, AgPd alloys), such as low permeability for hydrogen. The study of Chou (1986) shows a comparison of hydrogen permeability through different capsule materials, gold capsules occurred to be less permeable for H_2 (at up to 812°C). Nevertheless, gold is usually taken as the best shielding material against H_2 leakage, hydrogen still can transfer through walls of gold capsules, especially at elevated temperatures (Chou, 1986). Thus, we performed an experiment on H_2 permeability in our experimental setup in order to quantify the amount of H_2 passing through the capsule walls.

The experiment consisted of hematite-magnetite transformation in the presence of hydrogen. Starting material for the experiment was prepared as a homogeneous mixture of synthetic hematite (93 wt.%) and natural magnetite (7 wt.%) with a drop of water. The experiment duration was 6 days, temperature and pressure were 700°C and 2 GPa, respectively. The run was quenched and the capsule was weighed, the weighing indicated that no mass loss occurred during the experiment. Experimental products were characterized by XRD. XRD patterns of the starting material and experimental product together with the results of the Rietveld refinement are shown in Figure 1.1.-5. The results demonstrate that part of the hematite was reduced into magnetite. Such a reduction evidences a presence of hydrogen in the capsule. The following reaction describes the Hematite-Magnetite reduction:

$$3Fe_2O_3 + H_2 = 2Fe_3O_4 + H_2O \quad (1.1.-1)$$

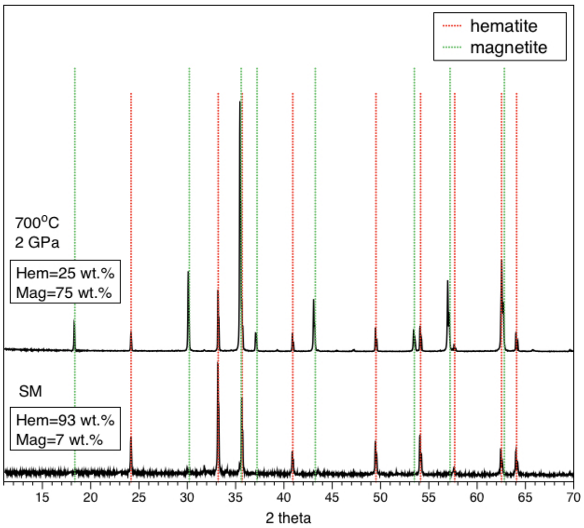

Fig. 1.1.-5. XRD patterns of starting material (SM) and experimental product at 700°C, 2GPa. Wt.% obtained from Rietveld refinement. Green dotted lines indicate peaks of magnetite, red dotted lines indicate peaks of hematite.

The Hem/Mag wt% ratios of starting material and experimental product allow to calculate mole amount of H_2 that is required for the Hem-Mag transition based on Reaction (1.1.-1). Results of the calculation are shown in Table 1.1.-4. Thus, $7x10^{-5}$ moles of H_2 were present in the capsule. Further calculations of O_2 moles, released in the experiments of this work, will show that the maximum amount of released O_2 from the experimental starting material is $8x10^{-5}$ moles per sample, which is enough to be coupled with H_2 coming from the outside of the capsule. The following reaction is responsible for the mentioned O_2 consumption:

$$1/2O_2 + H_2 = H_2O \qquad (1.1.-2)$$

Therefore, piston-cylinder experiments of the present work were performed under an "open-like" condition, since H_2 was shown to be able to pass through the Au capsule and react with O_2 formed due to phase transitions and mineral chemistry changes of the starting material.

Table. 1.1.-4. Mineral composition (wt.%, grams and moles) of starting material and experimental product at 700°C of magnetite-hematite experiment. SM – starting material.

	wt%		**g weight**		**g/mole**	**moles**	
	SM	**700°C**	**SM**	**700°C**	**molar mass**	**SM**	**700°C**
Mag	7	75	0.00351	0.03750	232	0.00002	0.00016
Hem	93	25	0.04669	0.01250	160	0.00029	0.00008
H_2 needed	-	-	-	0.00015	-	-	0.00007

Py-Po transition experiment

An additional experiment was carried out in order to check the permeability of the gold capsule for H_2 and therefore to check the influence of the cell assembly on pyrite reduction, which will be described in Chapter 3.2. The starting material consisted of 100 wt.% natural pyrite, and 8 mg of H_2O were added. The starting material mixture was left in the oven overnight (12 hours) to check that capsule is hermetic and no water leakage occurred. The pressure and temperature of the experiment were 1.5 GPa and 700°C, respectively. After 5 days, the experiment was quenched and capsule was recovered. The experimental product was crushed in agate mortar for XRD characterization. Figure 1.1.-6 presents two XRD patterns, one of the starting pyrite, and the second – of the experimental product. As it is shown, both XRD patterns are identical and no pyrrhotite or other sulfur-bearing phases were detected.

Such an observation can be explained by insufficient amount of H_2O in the capsule and consequently saturation of sulfur in H_2O. Several reactions of pyrite-pyrrhotite transition may occur in the capsule:

$FeS_2 + H_2O = FeS + H_2S + 1/2O_2$ (1.1.-3)

$3FeS_2 + 2H_2O = 3FeS + SO_2 + 2H_2S$ (1.1.-4)

$FeS_2 + H_2 = FeS + H_2S$ (1.1.-5)

All mentioned reactions result in a release of fluid sulfur-bearing phase, which systematically requires either H_2O or H_2. The amount of H_2O present in the capsule turned out to be insufficient for the reaction with visible and detectable products.

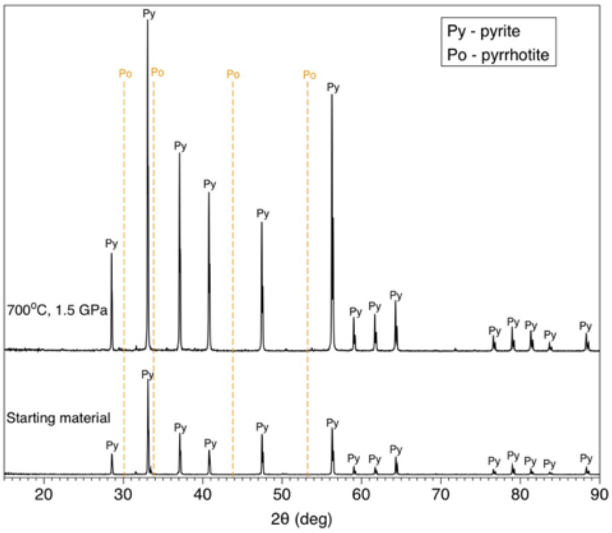

Fig. 1.1.-6. XRD pattern of starting material and experimental product of Py-Po transition experiment.

Alternatively, the absence of pyrrhotite formation in the experiment also can be explained by the absence of Fe source for pyrrhotite growth at such conditions. This process of pyrrhotite formation will be discussed later.

1.1.3. Diamond anvil cell experiments

Diamond anvil cell experiments were performed to investigate *in-situ* continuous phase transformations and Fe speciation using X-ray absorption near edge structure (XANES) spectroscopy and X-ray diffraction (XRD) at the European Synchrotron Radiation Facility (ESRF) in Grenoble. Three types of DAC were used: hydrothermal internally heated DAC, internally resistively heated DAC (RH-DAC) and externally RH-DAC.

Diamonds which are usually used in DAC experiments have thickness about 1-2 mm, such thick diamonds significantly absorb X-rays. At the Fe *K*-edge (7112 eV), the absorption of X-rays by diamonds is close to 100 %. In order to minimize the absorption, fully perforated diamonds were used for the experiments of this work.

Hydrothermal diamond anvil cell

Hydrothermal diamond anvil cell (HDAC) used in the present study is a Bassett-type diamond anvil cell (Bassett et al., 1993) which is able to exceed temperature up to 1000°C with slow heating rate and pressures up to 4.5 GPa. A schematic cross section of the HDAC is shown in Figure 1.1.-7. The diamond anvil cell is designed in the following way. The HDAC consists of two metal anvil holders, which have similar set up. The upper metal holder equipped with a pressurizing nut. Both anvil holders have adjustable seats different in shape. The upper seat has a square shape, whereas the bottom seat has a round shape. Such a design allows one to align the anvils in x and y axis position and adjust the tilt using upper and bottom adjustable seats respectively. Lower and upper WC (tungsten carbide) anvil holders are mounted on the adjustable seats. WC anvil holders are covered with ceramic plates which have 8 holes for WC electrodes. Electrical current provided by a power supply goes through wires, which are connected to the screws in the cell body, then through wires and springs (in the spring holder) that touch the electrodes. To provide heating of the diamond anvils, a new coating technique was developed and performed in Institute Néel in Grenoble. The technique included: (1) covering diamond anvil with tape and leaving uncovered area only about 2 mm on the side of the diamond; (2) itching diamond anvils in oxygen plasma for 1 hour; (2) spattering of 200 nm of WTi alloy on the anvils. Figure 1.1.-8 demonstrates the resulting coating on the diamond.

Rhenium gaskets well-polished on both sides were drilled in the center to make a hole 1-2 mm in diameter which is used as a sample chamber. To isolate the sample from the rhenium gasket, which may provide reduced conditions, a gold foil was inserted inside the sample chamber.

One full diamond and one fully perforated diamond were used during the experiments in HDAC. A diamond plate was placed and stick on the top of the drilled diamond.

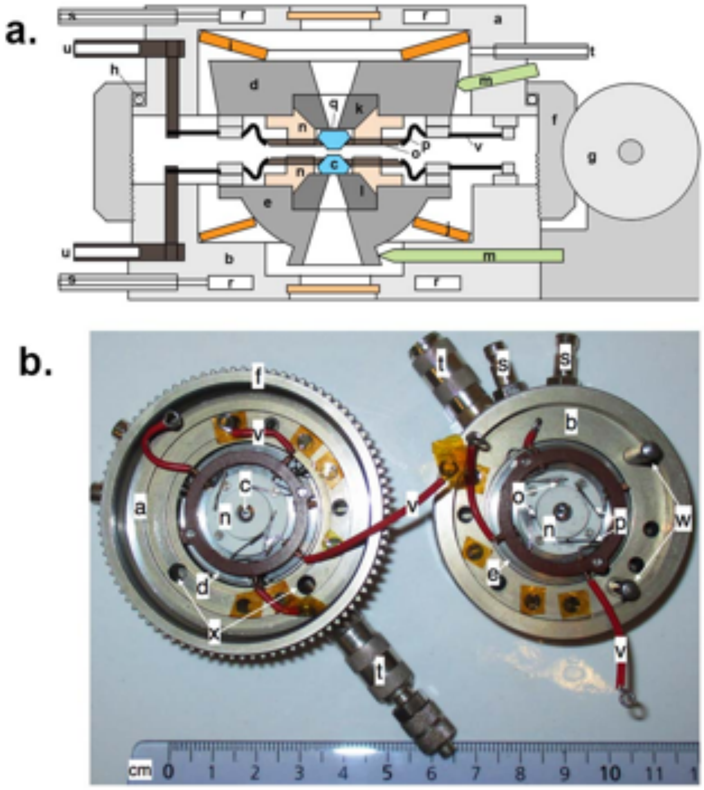

Fig. 1.1.-7 a. schematic cross-section of the HDAC. b. Photograph of HDAC. a. Upper plate. b. Lower plat, c. Diamond anvils, d. Upper adjustable seat, e. Lower adjustable seat, f. Pressurizing nut with sprocket, g. Worm drive, h. Ball bearing, i. Upper Bellville springs, j. Lower Bellville springs, k. Upper anvil holder, l. Lower anvil holder, m. Adjusting screws, n. Ceramic plate guiding the electrode, o. Tungsten carbide electrodes, p. Steel wire springs, q. Thermal isolation plate, r. Cooling conduit, s. Inlets of the cooling system, t. Protective gas inlet, u. Electrical connectors, v. Electric wire, w. Guiding posts, x. Holes for the guiding posts.

Fig. 1.1.-8. Diamond coated with WTi alloy and gold.

After alignment of the diamonds a sample was loaded. A drop of water was put in some experimental runs together with the sample to assure pressure homogenization in the sample chamber.

The HDAC used in this study is equipped with water-cooling and gas-flowing systems. Ar gas flow was used in the experiments in order to protect cell pieces from oxidation during heating.

The procedure of temperature determination was based on temperature calibration. Temperature was measured by a chromel-alumel thermocouple (K-type), junction of which was placed in the sample chamber. Voltage controlled on the power supply was slowly increased, while current was changed automatically with voltage. Voltage values were calibrated with associated temperature. Figure 1.1.-9 demonstrates a typical calibration curve, which is used to determine temperature during further sample heating.

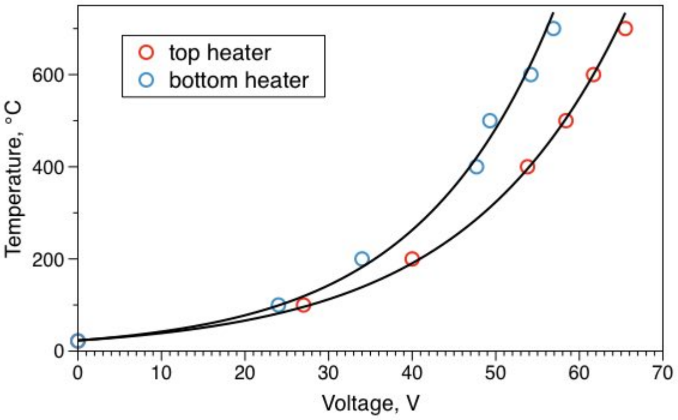

Fig. 1.1.-9. Temperature calibration curves for bottom and top heater. Circles – measured values, black curves – fits.

Once temperature calibration is done, the thermocouple can be removed and sample and water are loaded, the pressurizing can be started. The pressurizing nut is used to increase pressure (Fig. 1.1.-7) by screwing the nut with a worm drive. The heating may be started after the pressurizing nut is screwed tight. Air bubble that appears in the sample chamber should be monitored in optical microscope while heating in order to trace the temperature of its disappearance (homogenization temperature). Water equation of state (Bassett et al., 1996) is used to determine the pressure from the measured temperature of homogenization (Fig. 1.1.-10). The accuracy of a pressure determination depends on the accuracies of the temperature measurements and the equation of state of H_2O. Further, pressure can be traced using P-T diagram of the equation of state of H_2O.

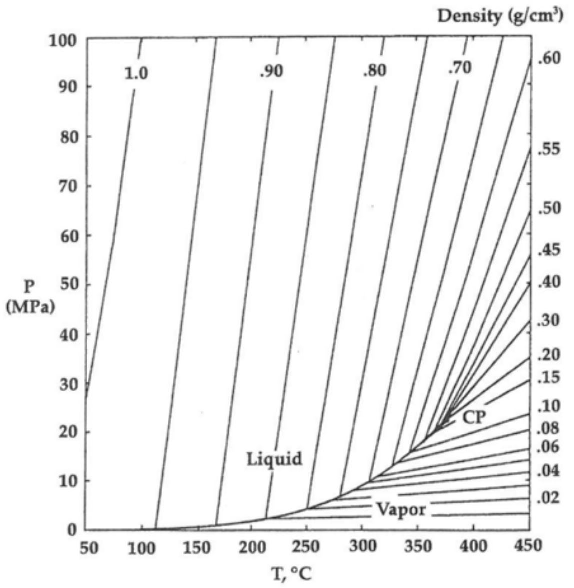

Fig. 1.1.-10. P-T diagram of equation of state for H_2O (Bassett et al., 1996).

Resistively heated DAC

Resistively heated diamond anvil cells (RH-DAC) used for experiments was provided by high pressure lab of ESRF (collaboration with A. Rosa). The RH-DAC was developed at ID27 beamline of ESRF (Rosa et al., 2015; Petitgirard et al., 2015). Figure 1.1.-11 shows the design of the RH-DAC. The RH-DAC is a membrane driven DAC based on the LeToulec design (LeToulec et al., 1988). The use of this design of DAC allows for the pressure and temperature to be changed independently and remotely. The insert made of Zirconia (ZrO_2 from Sceram, France) is mounted in the WC seats to ensure a better thermal insulation of the diamonds and the sample.

Two different resistive heater designs are used for two RH-DAC. Internally RH-DAC is equipped with two heaters consisted of graphite rings adapted from Du et al. (2013) (Graphite grade 2020 from Mersen). The graphite heaters are mounted around each diamond anvil. Two holes of 0.5 mm diametrically opposite are drilled in the graphite rings and are used to connect the 0.5 mm molybdenum wires for the current supply. This design of the internally RH-DAC allows to heat each graphite heater, which permits to reach temperature up to 1200°C. Type K thermocouples used to measure the temperature are placed in contact with each of the graphite heaters. An electrically conductive graphite glue was used to fill the void between the diamond anvil and the graphite heater to ensure better thermal conduction.

Externally RH-DAC is equipped with a heater ring which is placed around the cell body.

Using such a design, the maximum temperature that can be reached is about 600°C. Two K-type thermocouples are used to measure the temperature, one thermocouple is mounted on top of the heater ring and the second is placed close to the sample inside the cell.

Temperature during the experiments was remotely regulated by a digital power supply and Eurotherm temperature controller which provides a remote temperature control and temperature stability.

The RH-DAC, whatever the heater design, is placed in a vacuum chamber that permits a secondary vacuum of 10^{-6} mbar. The use of a vacuum limits the oxidation of the different parts of the DAC and specifically prevent the graphitization of the diamond anvils. The vacuum chamber is connected to a vacuum pump. Mylar windows with low absorption of the X-rays compared to other window materials, e.g. sapphire, are mounted on both sides of the vacuum chamber. To maintain mylar windows at room temperature, an air cooling system is mounted.

Gaskets used for RH-DACs are made of rhenium. The initial thickness of the gasket is 200 μm. To isolate a sample from the gasket two different isolation materials were used: amorphous boron epoxy and gold powder.

For the experiments in internally RH-DAC, gasket was pre-indented to 80 μm thickness and a hole 320 μm in diameter was drilled. The hole in the gasket was filled with amorphous boron epoxy (aBE) and the gasket was pre-indented to 90 μm. Then a hole 150 μm in diameter was drilled and used as a sample chamber. The use of amorphous boron epoxy in DAC experiments was shown in previous studies (e.g., Wang et al., 2011; Funamori and Sato, 2008; Merkel et al., 2002; Rosa et al., 2013; Morard et al., 2007) to reinforce the gasket strength, which allows to maximize the sample thickness and to reach higher pressures.

Gasket used for externally RH-DAC was pre-indented to 80 μm and a hole ~350 μm was drilled. The hole was filled with powdered gold, then the gasket was pre-indented again and a hole of 150 μm in diameter was drilled and used as a sample chamber.

Pressure in RH-DACs was increased using a membrane system connected to a portable gas (He) pressure controller. Gold (Au) and NaCl were used as pressure markers in experiments in both, internally and externally RH-DAC. A piece of Au and a pellet of NaCl were loaded together with a sample and *P/T* conditions were obtained using the thermal equation of state of gold from Shim et al. (2002) and for NaCl from Masanori et al. (2012). The use of both, Au and NaCl, gives cross-calibration and more reliable pressure values.

In both cases, i.e., using internally and externally RH-DAC, fully perforated diamonds were used for the X-ray absorption measurements. A diamond plate was placed on each diamond cullet and stick with a graphite glue.

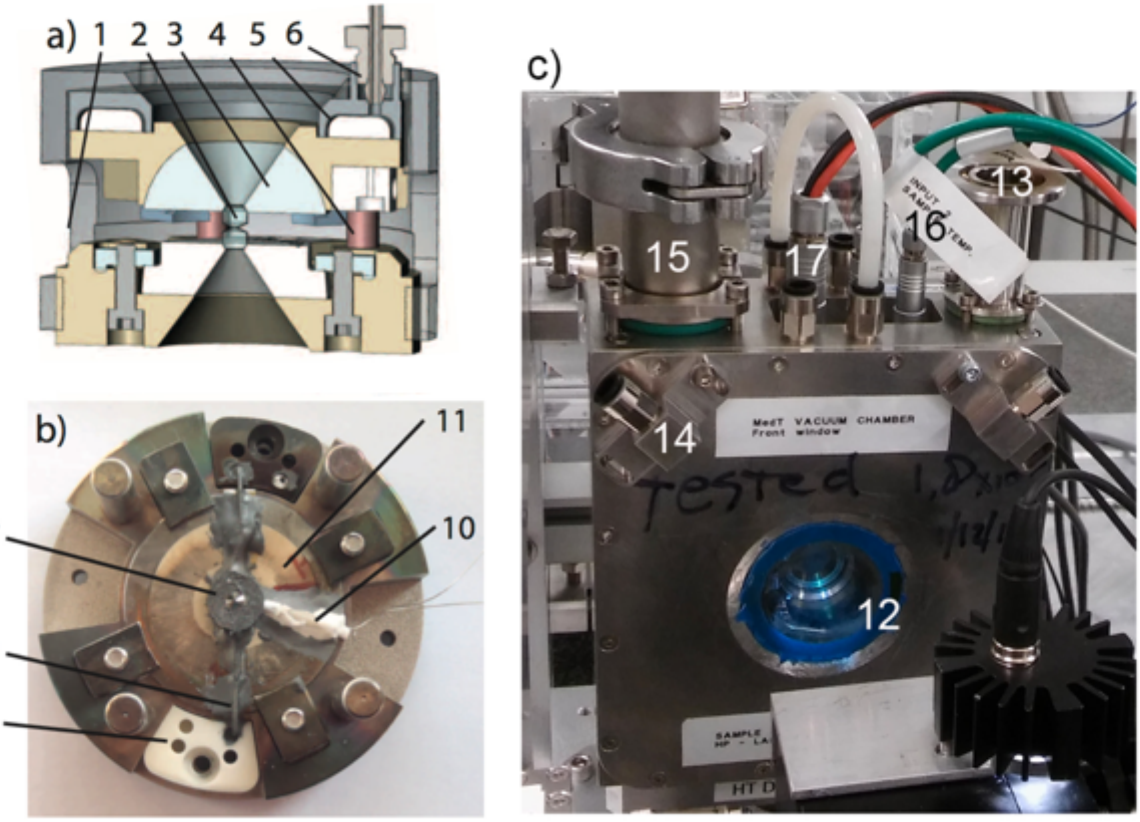

Fig. 1.1.-11. 3D model and photographs of the RH-DAC and its vacuum chamber. a) A cross section view of the CAD 3D model of the HT DAC. 1. opening for electrical connections; 2. conical diamonds; 3. conical seat; 4. guiding post; 5. gas membrane; 6. welding-free connector for inlet gas to the membrane (after Petitgirard et al., 2015); b) Picture of the DAC with final assembly of furnace and thermocouple. 7. graphite ring furnace; 8. Mo connector; 9. ceramic holder for electrical connections; 10. thermocouple in contact with the diamond; 11. ZrO_2 seat (after Petitgirard et al., 2015); c) Picture on the beamline with the RH-DAC inside its vacuum chamber. 12. window (Mylar or saphire); 13. membrane connector; 14. air cooler for the windows; 15. vacuum or gas connector; 16. Thermocouple feedthrough; 17. electrical feedthrough.

1.2. Analytical methods

Results shown in this study are obtained thanks to a variety of analytical techniques available at ISTerre (Grenoble, France), synchrotron facilities (ESRF, SLS, SOLEIL) and at the University of Ottawa (Canada). Mineral phases formed in experimental products resulting from piston-cylinder experiments were identified by X-ray powder diffraction. Back-scattered electron images of experimental products were performed by scanning electron microprobe. Major-element compositions of minerals were analyzed by electron microprobe using wavelength-dispersive spectrometer. X-ray fluorescence spectrometer was used to analyze major-element bulk composition of starting materials and reference minerals. The speciation of Fe and S was measured by X-ray absorption near edge structure spectroscopy using synchrotron X-ray radiation. In addition, concentration of S and sulfur isotopic ratio ($\delta^{34}S$) in sample contained sulfides were determined by isotope ratio mass spectrometer.

In case of DAC experiments, the analytical techniques were applied *in-situ* at ESRF (Grenoble). XANES spectroscopy was used to determine Fe oxidation state, while synchrotron XRD was used simultaneously to characterize mineral phases.

1.2.1 X-ray Powder Diffraction (XRPD)

X-ray powder diffraction is one of the most common and direct techniques to identify crystalline phases. In this work X-ray powder diffraction was performed using a Bruker D8 diffractometer available in ISTerre (Grenoble). Samples of piston-cylinder experiments were finely crashed in an agate mortar in order to obtain an average bulk phase composition. Cu-$K\alpha1$ radiation was used running at 40 kV and 40 mA. Intensities were measured from 5 to 90° 2θ-angle, with a step angle of 0.03° and a dwell time of 6 to 8 s per step. The Eva software (Bruker) was used to identify peaks on XRPD patterns.

1.2.2 Scanning electron microscope

The back-scattered electron (BSE) imaging can provide a qualitative phase composition by displaying different phase contrast on BSE images. BSE images are useful to assess homogeneity of mineral phases and for textural description of samples. Electron probe JEOL JXA-8230 EPMA available at ISTerre (Grenoble) can provide high resolution scanning BSE imaging by the use of BSE detector. Samples for scanning electron microscope (SEM) observations and for further electron probe micro-analysis were mounted in epoxy and polished.

Back-scattered electron images of the piston-cylinder experimental products are shown in Annex (Fig. 1.-S1).

1.2.3 Electron probe microanalysis

Electron probe microanalysis (EPMA) is an analytical technique that allows to analyze chemical composition of a single mineral. The use of focused electron beam permits to analyze mineral grains 5-10 μm size, which is useful in case of experimental petrology since the average size of minerals in experimental products is ~10 μm. Wavelength dispersive spectrometer used for EPMA provides quantitative and high precision analyses. In order to quantify chemical compositions, the intensities of characteristic X-rays fluorescence lines emitted from samples must be compared with intensities from known standards, which are listed further.

The analyses shown in this study were performed on a JEOL JXA-8230 EPMA at ISTerre (Grenoble, France). Operating conditions for analyses were 15 kV accelerating voltage, 12 nA beam current with a focused beam. The standardization was made using certified natural minerals and synthetic oxides: wollastonite (Si, Ca), olivine (Si, Fe, Mg), corundum (Al), orthoclase (K), rhodonite (Mn), albite (Na), rutile (Ti), sphalerite (S). The San-Carlos olivine USNM111312-44 was used for olivine and serpentine calibration of Mg, Fe, Si (Jarosewich et al., 2002). The on-peak counting time was 30 s for each element and 30 s for two background measurements on each side of the peak. ZAF correction procedure was applied using the JEOL software for quantitative analysis. The San-Carlos olivine and an in-house Cr-Augite standards were run as unknowns (3 points) after each 30 analyses of samples to monitor instrumental drift and estimate accuracy of analyses. A drift correction was made when necessary, using a regression equation.

1.2.4 Elemental and isotope ratio analysis of sulfur

The determination of sulfur concentration and sulfur isotope ratios in piston-cylinder experimental products were performed at G.G. Hatch Lab (Ottawa, Canada).

The procedure of elemental analysis consisted of mixing a sample with tungsten oxide (1:2) and placing the mixture in a tin capsule, which is loaded to Vario Micro Cube (Elementar) for S % analysis using a calibration with internal standards.

For isotope ratio analyses, the tin capsule with a sample is flash combusted at 1800°C with the addition of oxygen. The SO_2 is separated for analysis by the chemical adsorption "trap and purge" method (Vario Micro Cube). The SO_2 gas carried then introduced into a Thermo Finnigan DeltaPlusXP IRMS spectrometer for the analysis. The isotopic delta measurements are made relative to Vienna Cañon Diablo troilite (VCDT) and expressed as:

$\delta^{34}S$ (in ‰) = $((^{34}S/^{32}S_{sample})/(^{34}S/^{32}S_{vcdt})-1)$ *1000

Standard reference materials used for the analysis are sulfides IAEA-S1, IAEA-S2 and AG-2. The analytical precision is +/- 0.2 ‰. The analytical method is explained in details in Grassineau et al. (2001).

Using the described methods the relative abundance of two stable isotopes of sulfur, i.e. isotope ratios ($\delta^{34}S$) and precise concentration of total S are provided for 4 experimental products containing sulfides.

1.2.5 X-ray absorption spectroscopy (XAS)

A large part of the results presented in this work are based on X-ray absorption spectroscopy, which therefore deserves a more detailed technical description compared to the other analytical methods outlined above.

XAS is one of the most powerful atomic probes. The physical quantity that is measured by XAS is X-ray absorption coefficient $\mu(E)$. The coefficient $\mu(E)$ describes how X-ray is absorbed by an atom as a function of X-ray energy (E) (Bunker, 2010). XAS is performed by scanning the energy range corresponding to the K or L-absorption edge of the selected element using a synchrotron X-ray beam. An absorption edge characterizes a sharp rise in absorption (Fig. 1.2.-1) when the incident X-ray has an energy equal to that of the binding energy of a core-level electron. Analysis of the fine structure of the absorption coefficient $\mu(E)$ provide information about the chemical properties of the absorbing atom and its structural environment. A typical X-ray absorption spectrum is divided into two regions: 1). X-ray absorption near-edge structure (XANES) spectrum within 30 eV of the main absorption edge, and 2). Extended X-ray absorption fine-structure (EXAFS) spectrum, which has energies above the edge (typically hundreds of eV; Fig. 1.2.-1). XANES part is sensitive to oxidation (e.g., Fe^{2+} vs. Fe^{3+}) state and coordination (e.g., octahedral, tetrahedral coordination) of the absorbing atom, whereas the EXAFS part of the spectrum is used to quantify the distances, coordination numbers, and to determine species of the neighbors around the absorbing atom.

XAS experiments are performed at synchrotron radiation sources. XAS measurements can be carried out in two modes: transmission and fluorescence. Transmission includes measurements of the X-rays before and after the sample, when X-ray beam passes through the sample. Whereas fluorescence mode involves measurement of the initial incident X-ray flux and the fluorescence X-ray which is emitted by the sample. In order to minimize contribution of scattered radiation fluorescence detector is usually placed at ~90° to the incident beam in the horizontal plane.

Ex-situ XANES measurements were performed in this study to determine the speciation of Fe and S in piston-cylinder experimental products. *In-situ* XANES measurements were carried out at Fe *K*-edge to obtain Fe speciation during phase transitions using a diamond anvil cell.

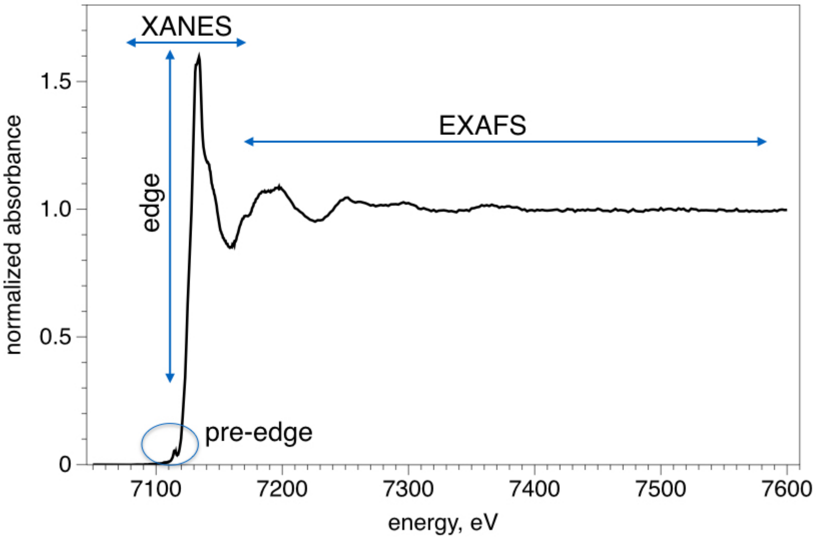

Fig. 1.2.-1. XAS spectrum at Fe K-edge. Blue arrows indicate the two different regions of the spectrum.

Ex-situ XAS measurements

Each run product produced in piston-cylinder experiments was homogenized by fine crushing in an agate mortar during 10 minutes. A finely ground sample was then prepared as a 5 mm diameter pellet for XANES spectroscopy. Samples containing sulfides were crushed in a glove bag filled with He/Ar gas to prevent oxidation of sulfides.

XANES analyses of piston-cylinder experimental products and starting materials were performed at the Phoenix beamline of the SLS (Swiss Light Source) and at the LUCIA beamline of SOLEIL synchrotron (France). Experimental products from set#2 (Table 1.1.-1) were analyzed at the Fe *K*-edge at the Phoenix beamline. Incident energy was selected from 7050 eV to 7290 eV using a Si(111) double-crystal monochromator. The spot size on the sample was 1.4 x 1.4 mm. In order to prevent beam damage and possible changes in valence for iron (i.e., photo-oxidation/reduction) during measurements, XANES spectra were collected in a vacuum chamber cooled using a liquid nitrogen cryostat. XANES spectra were collected in fluorescence mode using a 1-element silicon-drifted diode (SDD) located at 90° from the incident X-ray beam direction.

XANES spectra of experimental products from set#1 and set#3 (Table 1.1.-1) were collected at LUCIA beamline. Fe *K*-edge XANES spectra were acquired between 7050 and 7600 eV, using a Si(311) fixed-exit double-crystal monochromator, and the S *K*-edge XANES spectra were acquired between 2400 and 2600 eV using the same monochromator equipped with KTP ($KTiOPO_4$) (011) crystals. The beam size on the sample was ~1 mm in diameter. For the same reasons of possible beam damage and photo-oxidation/reduction as at Phoenix beamline (SLS), XANES spectra were collected in a primary vacuum chamber cooled at -70°C using a liquid nitrogen cryostat. Spectra were collected in fluorescence mode using 4-element silicon drift diode (SDD) detector located at 86° from the incident beam.

To perform linear combination fits as a post-treatment data analysis, XANES spectra of 9 standard minerals (antigorite, olivine, orthopyroxene, clinopyroxene, clinochlore, andradite, magnetite, pyrite, pyrrhotite) were collected at SLS (Phoenix beamline) and SOLEIL (LUCIA beamline) at the Fe *K*-edge and S *K*-edge (pyrite, pyrrhotite). Standard minerals were prepared as powdered pellets of 5 mm in diameter. Silicate and oxide standards (antigorite, olivine, orthopyroxene, clinopyroxene, clinochlore, andradite and magnetite) come from a personal collection of M. Muñoz. The pyrrhotite spectrum, used as a reference, was provided by B. Lassalle (LUCIA beamline scientist).

XANES spectra were normalized using the Athena software (Ravel and Newville, 2005). Quantitative bulk rock Fe^{3+}/Fe_{tot} was obtained from Fe-*K* pre-edge analysis, which includes baseline substraction and fitting the pre-peak region (energies between 7110 and 7118 eV for Fe K-edge) of the spectra using a Matlab routine from the XasMap package (Muñoz at al., 2006; 2008). The Fe^{3+}/Fe_{tot} quantification was based on the pre-edge centroid energy calibration (see Wilke et al., 2001) using the following model phases: olivine, staurolite, andradite and sanidine (Muñoz et al., 2013).

In-situ XAS and XRD measurements

In-situ XANES measurements at Fe *K*-edge were performed at X-ray absorption spectroscopy beamline BM23 at the European Synchrotron Radiation Facility (ESRF, Grenoble, France). Experiments of two beamtime sessions were carried out at the BM23 beamline: 1) experiments in HDAC and 2) experiments in RH-DAC. The analytical technique and beamline optic scheme are the same for both experiments.

The XANES spectra at Fe *K*-edge were collected together with with XRD patterns and *in-situ* optical observations of the experiemnts. The experimental setup is shown in Fig. 1.2-2 XANES spectra were collected at Fe *K*-edge from 7000 eV to 7250 eV and from 7050 eV to 7350 eV for HDAC and RH-DAC experiments, respectively. A monochromator equipped with two Si(111) crystals was used to tune energy to the Fe *K*-edge. Beam was focused to 6x6 μm^2. XAS measurements were performed in transmission mode, the incoming and transmitted monochromatic intensities were measured using ionization chambers filled with appropriate gas mixtures of Ar and He to achieve absorption of 30 % in the first, and 70 % in the second chamber at 7500 eV. The fixed exit monochromator-crystal angles were calibrated to the iron edge energy 7112 eV using a standard iron foil of 3 μm thickness. The Bragg diffraction peaks arising from the diamond anvils were removed from the energy range of interest by changing the orientation of the diamond anvil cell. Obtained XANES spectra were normalized using the Athena software (Ravel and Newville, 2005).

X-ray diffraction images were obtained using a MarCCD detector placed at a distance of 190 mm from the sample at a wavelength of 0.9537 Å (energy of 13 keV) for the experiment in HDAC and 0.6199 Å (energy of 20 keV) for the experiment in RH-DAC. The sample-to-detector distance, beam center position, detector tilt angles and pixel size ratios were determined precisely using a CeO_2 standard and the program DIOPTAS (Prescher and Prakapenka, 2015). Background substraction and diffraction peak identification were performed using the program DIOPTAS (Prescher and Prakapenka, 2015).

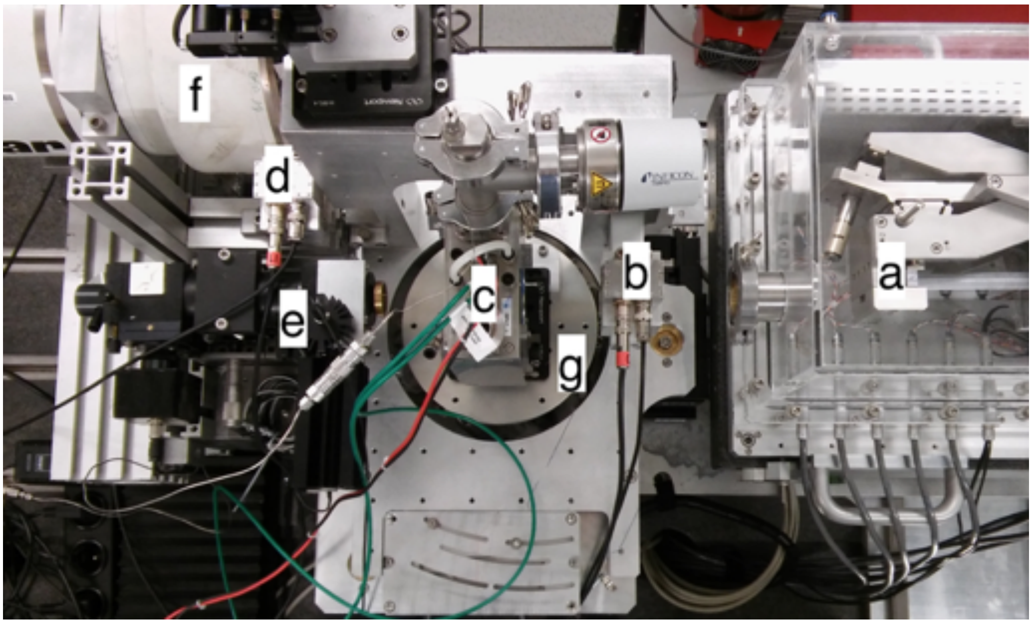

Fig. 1.2.-2. Experimental setup at BM23 beamline (ESRF) during *in-situ* XAS measurements. a. KB mirrors system, b. first ionization chamber, c. vacuum chamber with DAC, d. second ionization chamber, e. microscope, f. MarCCD detector, g. µXAS station for precise positioning of the DAC (Mathon et al., 2015).

Chapter 2 Role of iron content on serpentinite dehydration depth in subduction zones: Experiments and thermodynamic modeling

Margarita Merkulova[1,*], Manuel Muñoz[1], Olivier Vidal[1,2], Fabrice Brunet[1,2]

[1] *Univ. Grenoble Alpes, ISTerre, F-38041 Grenoble, France*

[2] *CNRS, ISTerre, F-38041 Grenoble, France*

Published article

Lithos (2016) 264, 441-452

http://dx.doi.org/10.1016/j.lithos.2016.09.007

Lithos 264 (2016) 441–452

Contents lists available at ScienceDirect

Lithos

journal homepage: www.elsevier.com/locate/lithos

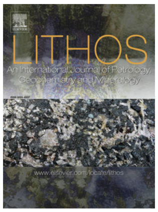

Role of iron content on serpentinite dehydration depth in subduction zones: Experiments and thermodynamic modeling

Margarita Merkulova [a,*], Manuel Muñoz [a], Olivier Vidal [a,b], Fabrice Brunet [a,b]

[a] Univ. Grenoble Alpes, ISTerre, F-38041 Grenoble, France
[b] CNRS, ISTerre, F-38041 Grenoble, France

ARTICLE INFO

Article history:
Received 6 April 2016
Accepted 7 September 2016
Available online 17 September 2016

Keywords:
Serpentinite
Dehydration
Antigorite
Iron
Subduction zone
Earthquakes

ABSTRACT

A series of dehydration experiments in the piston-cylinder apparatus was carried out at 2 GPa and 550–850 °C on a natural antigorite sample mixed with 5 wt.% of magnetite. Chemical analyses of experimental products show a progressive decrease of the Mg# in antigorite and clinopyroxene between 550 and 675 °C, whereas the Mg# of olivine increases. The observed behavior of Mg# signifies Fe–Mg exchange between coexisting minerals. At higher temperatures, between 700 and 850 °C, compositions remain stable for all minerals in experimental assemblages.

Thermodynamic parameters of the ferrous antigorite end-member were refined with the use of Holland and Powell (1998) data set and added to the antigorite solid solution. Good agreement between theoretical calculations performed for the studied bulk composition and experimental results confirms extrapolated thermodynamic data for Fe-antigorite. Constrained parameters allowed to calculate phase relationships for various serpentinite compositions. First, we assessed the effect of bulk iron content, from 0 to 10 wt.% FeO, on the stability field of antigorite. The results show significant decrease of the antigorite thermal stability with increasing bulk Fe content. Second, we demonstrated the influence of bulk iron content on dehydration reactions in subduction zones along typical thermal gradients. Dehydration observed in pure MSH ($MgO–SiO_2–H_2O$) systems comprised of antigorite appears as a univariant reaction, which happens at 710 °C/3.7 GPa and 640 °C/6 GPa in "hot" and "cold" subduction, respectively. In contrast, more complex in composition Fe-bearing serpentinites show spread dehydration profiles through divariant reactions from ~300 °C/0.8 GPa to 700 °C/3.6 GPa and from 450 °C/4 GPa to 650 °C/7.4 GPa for "hot" and "cold" thermal gradients respectively.

A comparison between depths of "water-release events" and "earthquake occurrence" in the South Chile slab ("hot" subduction) highlights a clear correlation between each other, suggesting a possible contribution of the dehydration of Fe-bearing serpentinites to the occurrence of seismic events. In contrast, and based on the same comparison applied to the Kermadec slab, our results demonstrate that there is no correlation in depth between serpentinite dehydration and seismicity in "cold" subduction zones.

1. Introduction

Antigorite is the dominant hydrous phase in subducting ocean slabs and the major water carrier to the deep mantle (Rüpke et al., 2004; Ulmer and Trommsdorff, 1995). Along with metasediments and metabasalts, serpentinized lithospheric mantle can potentially deliver large volumes of water into subduction zone and mantle wedge (Rüpke et al., 2004; van Keken et al., 2011). The lizardite variety, formed during peridotite serpentinization in oceanic lithosphere, contains up to 13 wt.% H_2O and transforms into antigorite at elevated pressure and temperature, typically above 300 °C, in subduction zone setting (Evans, 2004, Schwartz et al., 2013). Antigorite is known to breakdown at around 700 °C, in the 150–200 km depth range, to form secondary olivine and pyroxene, thus releasing aqueous fluids in large amounts (Peacock, 2001; Rüpke et al., 2004; Syracuse et al., 2010; Trommsdorff et al., 1998; Ulmer and Trommsdorff, 1995). The "dehydration" of antigorite may have an important geophysical implication regarding initiation of intermediate-depth earthquakes in subduction zones, triggering the so-called process of "dehydration embrittlement" (e.g., Hacker et al., 2003). Moreover, Peacock (2001) suggested that the formation of the lower plane of double seismic zone in subducting plates may be explained by antigorite dehydration in the deeper parts of the oceanic mantle.

Another important issue linked to serpentinite dehydration is a decrease of melting temperatures in the mantle wedge due to the release of hydrous fluids from the slab, which in turn generates arc magmas (Ulmer and Trommsdorff, 1995). These magmas that originated from melts above the dehydration front are typically enriched in slab-derived fluid-mobile elements (FME) (e.g. Stern et al., 2006), which can be provided by antigorite devolatilization, as antigorite is known

---

* Corresponding author.
E-mail address: margarit.merkulova@gmail.com (M. Merkulova).

http://dx.doi.org/10.1016/j.lithos.2016.09.007

to be a carrier of FME, e.g., Li, B, Cl (Deschamps et al., 2012; Scambelluri et al., 2004), As, Sb, S (Hattori and Guillot, 2007; Spandler and Pirard, 2013), Rb, Sr (Hattori and Guillot, 2007; Marchesi et al., 2013), Pb, Cs, and U (Marchesi et al., 2013; Scambelluri et al., 2004).

Subduction zone magmas are essential in ore genesis processes. Magmas enriched in FME are associated with gold and transition metal deposits found in arc (e.g., Chile, Alpes, Indonesia) and back-arc settings (e.g., Alaska, Nevada, Patagonia) (Cooke and Simmons, 2000; Sillitoe, 2008). Therefore, the contribution of antigorite devolatilization to enrichment of magmas in FME is potentially linked to economically important ore depositions.

Antigorite breakdown and phase relationships at high pressure and temperature in subduction zones have stimulated numbers of experimental investigations. Most previous experimental studies aimed at defining P–T conditions of antigorite breakdown reactions in the MgO–SiO_2–H_2O (MSH) ± Al_2O_3 system (Bose and Ganguly, 1995; Bromiley and Pawley, 2003; Padrón-Navarta et al., 2010; Perrillat et al., 2005; Ulmer and Trommsdorff, 1995; Wunder and Schreyer, 1997; Wunder et al., 2001). Antigorite breakdown was systematically shown as a univariant reaction at a temperature of 630 °C (e.g., Bromiley and Pawley, 2003), or 710 °C (e.g., Ulmer and Trommsdorff, 1995) at 2 GPa. Ulmer and Trommsdorff (1995) and Bose and Ganguly (1995) proposed similar stability limits for antigorite in the presence of other hydrous phases such as talc and “phase A”. Wunder and Schreyer (1997) reported lower temperatures for the antigorite breakdown than those proposed by Ulmer and Trommsdorff. Moreover, Bromiley and Pawley (2003) showed that the alumina content expands the stability field of antigorite to higher P and T. Additionally, the presence of Al was shown to stabilize clinochlore, another hydrous mineral that is stable at higher P–T conditions than antigorite. To account for this discrepancy, starting materials used in Ulmer and Trommsdorff (1995), Bromiley and Pawley (2003) and Perrillat et al. (2005) consisted of natural antigorite mixed with synthetic forsterite and enstatite, whereas other studies were performed using synthetic oxide gels seeded with natural antigorite (Wunder and Schreyer, 1997), synthetic mixtures of orthopyroxene, quartz and talc (Bose and Ganguly, 1995) and synthetic mixtures of brucite and talc (Wunder et al., 2001). In addition, starting materials differed in Al, Fe and water contents due to the use of natural antigorite in some experiments. Padrón-Navarta et al. (2010) reported that Al expands antigorite thermal stability in silica enriched serpentinites by 60–70 °C compared to Al-free assemblages. Moreover, Padrón-Navarta et al. (2010) emphasized the effect of Fe on antigorite dehydration temperature and demonstrated thermodynamically the decrease of serpentinite dehydration temperature with an increase of bulk ferrous Fe. The work of Padrón-Navarta et al. (2010) shows that Fe in serpentinite transforms univariant mineral reactions in Fe-free systems (e.g., Bromiley and Pawley, 2003) into divariant fields in more realistic Fe-bearing serpentinite systems. In addition, Trommsdorff and Evans (1974) thermodynamically estimated that the Fe content typical for ultramafic metamorphic rocks decreases the temperature of mineral reactions by around 10 °C compared to pure MSH systems.

Petrological studies of natural samples demonstrated that antigorite breakdown occurs over a range of temperatures, from 650 to 725 °C (e.g., Debret et al., 2014, 2015; Padrón-Navarta et al., 2011; Trommsdorff et al., 1998). Moreover, antigorite dehydration was shown to occur through a series of continuous reactions forming intermediate olivine (Ol) and pyroxene-bearing serpentinites to finally produce an anhydrous assemblage composed of garnet–orthopyroxene–olivine (Debret et al., 2014; Padrón-Navarta et al., 2011, 2013; Trommsdorff and Evans, 1972). Pioneer works of Trommsdorff and Evans (1972, 1974) demonstrated compositional relations between coexisting antigorite, olivine, clinopyroxene, orthopyroxene and chlorite in serpentinites and their prograde lithologies. As was reported in Trommsdorff and Evans (1972, 1974) and in later studies by Li et al. (2004), Rebay et al. (2012), Scambelluri et al. (1991), Trommsdorff et al. (1998), Padrón-Navarta et al. (2011), and Debret et al. (2015) Mg# in antigorite is always higher than in olivine in prograde metamorphic assemblages. However, only a few studies addressed the compositional evolution of natural antigorite (Atg) along a subduction geotherm (e.g., Debret et al., 2014; De Hoog et al., 2014; Li et al., 2004; Padrón-Navarta et al., 2011, 2013; Rebay et al., 2012; Scambelluri et al., 1991; Schwartz et al., 2013; Trommsdorff and Evans, 1974). The Mg# in antigorite is shown to decrease with temperature in natural samples as the metamorphic facies changed from low- to high-grade (e.g., Padrón-Navarta et al., 2011; Schwartz et al., 2013), while olivine Mg# increases (Li et al., 2004; Padrón-Navarta et al., 2011). Clinopyroxene was found to be almost pure diopside, with no significant change in Mg# (e.g., Trommsdorff and Evans, 1972, 1974). Mentioned works demonstrated the coexistence of minor magnetite with silicate phases, whereas, Li et al. (2004) revealed the disappearance of magnetite in Atg–Ol assemblages produced during subduction related metamorphism. Additionally, Debret et al. (2014, 2015) observed a decrease of bulk rock Fe^{3+}/Fe_{tot} ratio in serpentinites, together with a progressive disappearance of magnetite with increasing metamorphic grade. Finally, as the grade of metamorphic facies increases antigorite disappears from the assemblages (e.g., Evans, 1977; Trommsdorff and Evans, 1974).

The P–T conditions of antigorite breakdown and the amount of fluid subsequently released are determined by antigorite phase relationships in the FMSH (FeO + MgO + SiO_2 + H_2O) ± Al_2O_3 system in the present study. In order to clarify the relation between serpentinite composition and the amount and depth of fluids released in subduction zones, we conducted a series of antigorite dehydration experiments at temperatures ranging between 550 and 850 °C and at a fixed pressure of 2 GPa. As a starting material, we used natural antigorite including minor amounts of andradite and clinochlore, mixed with 5 wt.% of magnetite in order to approximate the average bulk composition of serpentinized oceanic lithosphere (Deschamps et al., 2013; Hattori and Guillot, 2007; Li et al., 2004; Schwartz et al., 2013). We investigated the mineralogy, phase abundance and mineral chemistry of experimental products, which allowed us to constrain thermodynamic parameters of a hypothetical Fe-antigorite end-member. A thermodynamic-based model of serpentinite dehydration is provided, and then used to further investigate the role of the iron content on the dehydration processes in both, “hot” and “cold”-type subduction geotherms.

2. Methods

The starting material for the experiments performed in this study is composed of antigorite (#AU1) collected from the serpentine outcrop La Vachère located at the northwestern tip of Mont-Cenis–Vanoise massif in French Alpes (Muñoz et al., 2013; Etienne Jaillard, personal communication, 2016). The outcrop represents tectonically sliced remnants of ophiolite, which underwent metamorphism in blueschist and greenschist facies (Fudral et al., 1993). This sample was chosen in part because of its homogeneity, and in part because it is well crystallized and available in sufficient quantity for experimental petrology. An average natural serpentinite contains FeO distributed among antigorite and iron oxide phase (magnetite) (e.g., Debret et al., 2014). Thus, natural serpentinite comprises both FeO and Fe_2O_3 (e.g., Debret et al., 2015; O'Hanley and Wicks, 1995). The antigorite used in our study contains 1.37 wt.% of FeO_{total}, however most of iron is ferric (Table 1; Muñoz et al., 2013). The present antigorite sample differs from the average subducted serpentine in terms of Fe_2O_3 and SiO_2 contents (Evans et al., 2012). High SiO_2 content and high Fe^{3+}/Fe_{total} ratio of the chosen antigorite (Table 1; Muñoz et al., 2013) may be explained by the close location of ophiolite blocks to sediments (Fudral et al., 1993). However, typical lizardite entering subduction zones within oceanic serpentinites was shown to have also high Fe^{3+}/Fe_{total} ratios (Evans et al., 2012).

To better match the typical composition of an oceanic serpentinite, we mixed the finely crushed antigorite with 5 wt.% of synthetic

Table 1
Bulk rock and antigorite major element composition (wt.%) of starting material measured by XRF and EPMA respectively; μ-XRF analysis of the identical antigorite sample AU1 is taken from Muñoz et al. (2013); Fe^{3+}/Fe_{total} of antigorite measured by XANES spectroscopy (from Muñoz et al., 2013); mineral abundances of starting material obtained by Rietveld refinement of XRD pattern (Fig. 2). *m* — number of SiO_4 tetrahedra in one wavelength of the antigorite polysome.

Oxide	Bulk rock	Antigorite AU1 EPMA	Antigorite AU1 (Muñoz et al., 2013) μ-XRF	Mineralogy	wt.%
SiO_2	39.02 ± 1.42	44.12 ± 0.15	41.53 ± 1.25	Antigorite ($m = 17$)	83.23
TiO_2	0.45 ± 0.10	0.02 ± 0.01	0.05 ± 0.00	Clinochlore	5.64
Al_2O_3	1.92 ± 0.96	0.72 ± 0.04	1.12 ± 0.03	Magnetite	5.04
FeO_{total}	6.07 ± 0.27	1.37 ± 0.06	–	Andradite	6.09
Fe_2O_3	–	–	1.16 ± 0.03		
MgO	38.52 ± 1.38	41.49 ± 0.11	42.91 ± 1.29		
CaO	2.43 ± 1.02	0.01 ± 0.01	0.00 ± 0.00		
Cr_2O_3	0.16 ± 0.02	0.00 ± 0.00	0.13 ± 0.00		
NiO	0.04 ± 0.01	0.00 ± 0.00	0.05 ± 0.00		
H_2O	11.5 ± 0.02	12.14 ± 0.11	12.81 ± 0.00		
Total	100.11	99.87	99.76		
Fe^{3+}/Fe_{total}			0.81		

magnetite (Magnox powder, 99% purity). The prepared mixture was ground in an agate mortar for 10 min. The bulk composition of the starting material displays 6.07 wt.% of FeO_{total}, part of which is Fe_2O_3, and matches typical oceanic serpentinites (e.g., Deschamps et al., 2013; Li et al., 2004; Fig. 1). The bulk major-element composition of the starting material was measured by X-ray fluorescence using (XRF) EDAX Eagle III XRF spectrometer and relative mineral abundance was determined using X-ray powder diffraction (XRD; Table 1). The XRD patterns (Fig. 2) revealed the presence of minor amounts of andradite and clinochlore, which accounted for the presence of CaO and Al_2O_3 (2.43 wt.% and 1.92 wt.% respectively) in the starting mixture (Table 1).

Experiments were carried out in an end-loaded piston-cylinder apparatus at 2 GPa and temperatures from 550 to 850 °C, with experimental durations ranging from 5 to 9 days (Table 2). Twenty milligrams of the starting material was placed in a gold capsule (15 mm length and 3 mm inner diameter) that was welded shut. No water was added to the capsule. The capsule was then fitted into a pyrophyllite sleeve and loaded in a NaCl-based pressure cell with a graphite furnace. Temperature was measured with a Pt–Rh thermocouple (S-type), the junction of which was placed at ca. 1 mm from the sample top (see Brunet et al., 2003). Uncertainties on pressure and temperature are within ±0.05 GPa and ±10 °C, respectively. The temperature gradient across the capsule was determined from double-thermocouple experiment which was carried out at temperatures from 100 to 900 °C at 2 GPa. The experiment comprised temperature measurements above and inside the capsule every 100 °C. The results show that the maximum temperature difference within the capsule is 10 °C.

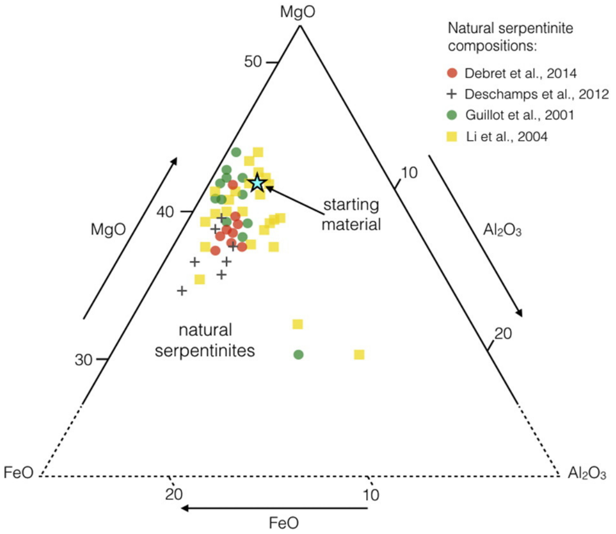

Fig. 1. Ternary diagram presenting the compositions of natural serpentinites from Debret et al., 2014 (red circles); Deschamps et al., 2012 (crosses); Guillot et al., 2001 (green circles); Li et al., 2004 (yellow squares). Blue star indicates the composition of the starting material used in this work. FeO stands for total Fe content. (For interpretation of the references to color in this figure legend, the reader is referred to the web version of this article.)

The serpentinite dehydration experiments were buffered by a cell assembly due to the permeability of gold capsule to hydrogen, produced by the graphite furnace oxidation (Chou, 1986). The oxygen fugacity (fO_2) in such graphite–NaCl–pyrophyllite cell assemblies was reported to be between QFM and QFM-2 (e.g., Truckenbrodt et al., 1997).

After each run, the recovered capsule was pierced to check that the water produced during mineral reactions had not escaped in the course of the experiment. Water was present as a fluid phase in the capsule of all experimental runs. A large portion of the recovered powder sample was crushed in an agate mortar for further XRD characterization. The remaining sample was mounted in epoxy and polished for electron probe micro-analysis (EPMA) and scanning electron microscope (SEM) observations.

X-ray diffraction was performed on a Bruker D8 diffractometer using Cu–Kα1 radiation running at 40 kV and 40 mA. Intensities were measured from 5 to 90° 2θ, with a step size of 0.03° and a dwell time of 6 to 8 s per step. X-ray diffraction patterns were analyzed by Rietveld refinement using BGMN software (Bergmann et al., 1998).

The quantitative point analyses were performed on a JEOL JXA-8230 EPMA at ISTerre (Grenoble, France). Operating conditions for analyses were 15 kV accelerating voltage and 12 nA beam current with a focused beam. The standardization was made using certified natural minerals and synthetic oxides: wollastonite (Si, Ca), olivine (Si, Fe, Mg), corundum (Al), orthoclase (K), rhodonite (Mn), albite (Na), and rutile (Ti). The San-Carlos olivine USNM111312-44 was used for olivine and serpentine calibration of Mg, Fe, Si (Jarosewich, 2002). The on-peak counting time was 30 s for each element and 30 s for two background measurements on each side of the peak. ZAF correction procedure was applied using the JEOL software for quantitative analysis. The San-Carlos olivine and an in-house Cr-Augite standards were run as unknowns (3 points) after each 30 analyses of samples to monitor instrumental drift and estimate accuracy of analyses. A drift correction was made when necessary, using a regression equation.

Additional experiments were carried out to check kinetics of antigorite dehydration (Table 2). Four experiments were performed at 700 °C/2 GPa and quenched after 2.5, 4, 5 and 10 days. Run products were analyzed by X-ray diffraction and electron microprobe (EPMA). Assemblages produced after 4, 5 and 10 days consist of olivine, clinopyroxene, orthopyroxene, clinochlore and tremolite. Corresponding mineral phases of mentioned 3 experiments have identical composition. 2.5 days run product contains antigorite, olivine, clinopyroxene and clinochlore. Consequently, equilibrium was not reached after 2.5 days of the experiment, since antigorite is present in the run product. All presented in this work dehydration experiments were performed during 5–9 days (Table 2).

Thermodynamic calculations were performed with Theriak–Domino software (de Capitani and Petrakakis, 2010) using the database of Holland and Powell (Holland and Powell, 1998). Theriak program calculates equilibrium phase assemblages, phase compositions and phase abundances for a given bulk rock composition at any P and T. Domino computes equilibrium assemblage diagrams based on Gibbs free energy minimization for a given bulk rock composition. Thermodynamic properties of ferrous antigorite end-member were calculated by the method similar to that in Rüpke et al. (2004). Enthalpy effect of octahedral iron substitution in antigorite is similar to that in talc, since both minerals are hydrous Mg–Fe sheet silicates, both solid solutions are set as ideal and

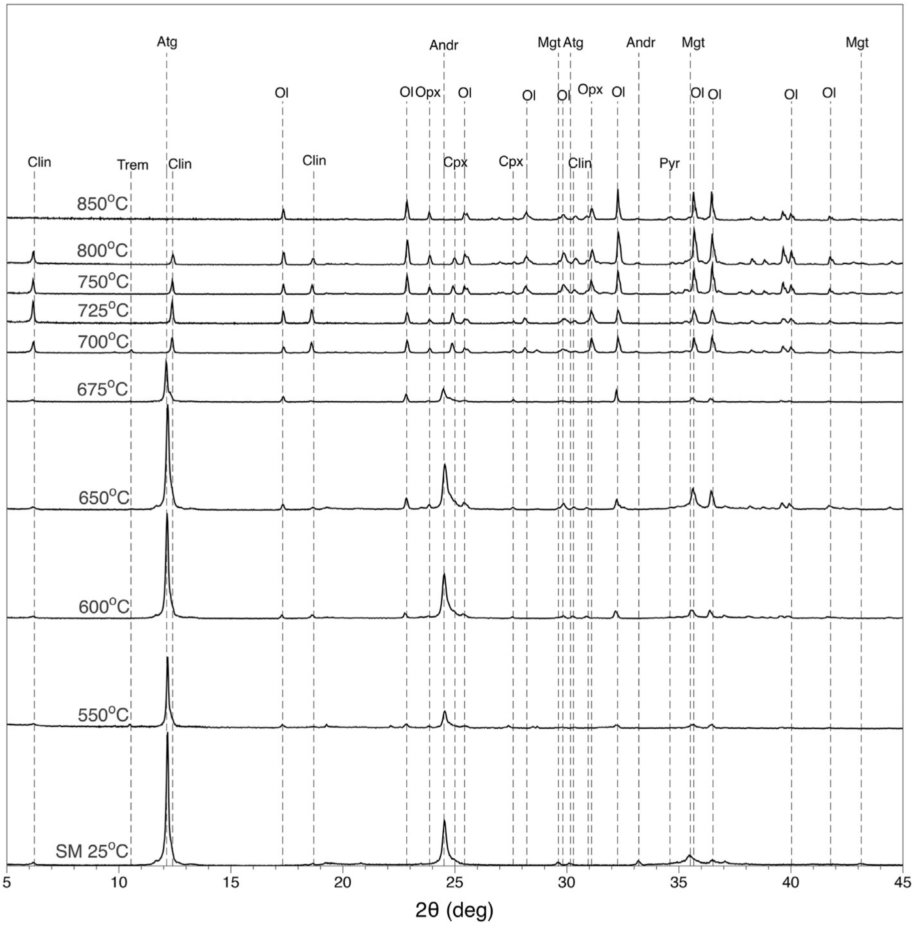

Fig. 2. XRD patterns of starting material (SM) and experimental products as a function of temperature. Dashed lines indicate peaks corresponding to different mineral phases. Atg — antigorite, Clin — clinochlore, Mgt — magnetite, Andr — andradite, Trem — tremolite, Ol — olivine, Opx — orthopyroxene, Cpx — clinopyroxene, Pyr — pyrope.

PT conditions for talc and antigorite solutions are nearly the same. Thermodynamic properties of antigorite, obtained in this work, were compared with those recently determined using a calorimetric method by Ogorodova et al. (2009). Thermodynamic calculations were performed in the presence of a QFM (quartz–fayalite–magnetite) oxygen fugacity (fO_2) buffer.

Table 2
P–T conditions, durations, starting materials and mineral assemblage in run products of performed piston-cylinder experiments. Atg — antigorite, Mag — magnetite, Clin — clinochlore, Ol — olivine, Cpx — clinopyroxene, Opx — orthopyroxene, Trem — tremolite, Pyr — pyrope.

Run #	T, °C	P, GPa	Starting material	Duration, days	Solid run products
Ant_Mgt5_01	600	2	Atg 95%, Mag 5%	9	Atg, Clin, Ol, Cpx
Ant_Mgt5_02	700	2	Atg 95%, Mag 5%	5	Ol, Opx, Trem, Clin
Ant_Mgt5_03	650	2	Atg 95%, Mag 5%	6	Atg, Ol, Cpx, Clin
Ant_Mgt5_06	750	2	Atg 95%, Mag 5%	5	Ol, Opx, Clin, Cpx
Ant_Mgt5_07	800	2	Atg 95%, Mag 5%	5	Ol, Opx, Clin, Cpx
Ant_Mgt5_08	675	2	Atg 95%, Mag 5%	5	Atg, Ol, Clin, Tr, Cpx
Ant_Mgt5_09	725	2	Atg 95%, Mag 5%	5	Ol, Opx, Clin, Cpx
Ant_Mgt5_11	850	2	Atg 95%, Mag 5%	5	Ol, Opx, Pyr
Ant_Mgt5_12	550	2	Atg 95%, Mag 5%	6	Atg, Clin, Ol, Cpx
Additional experiments performed to check reaction kinetics					
Ant_Mgt5_04	700	2	Atg 95%, Mag 5%	2.5	Ol, Atg, Cpx, Clin
Ant_Mgt5_05	700	2	Atg 95%, Mag 5%	4	Ol, Opx, Trem, Clin
Ant_Mgt5_10	700	2	Atg 95%, Mag 5%	10	Ol, Opx, Trem, Clin

3. Results

3.1. Mineral assemblage

3.1.1. X-ray diffraction

Mineralogical changes from the starting material (SM) to the run products obtained in the 550–850 °C temperature range can be first described on the basis of the XRD data (Fig. 2) collected on the quench products. The diffraction pattern of the starting material mainly shows the presence of antigorite (Atg) and magnetite (Mgt), in agreement with the mechanical mixture initially prepared, however the peaks of the other phases such as clinochlore (Clin) and andradite (And) are also detected. The phase abundances of the starting material mixture obtained by Rietveld refinement are shown in Table 1. At 550 °C, diffraction peaks of olivine (Ol) and clinopyroxene (Cpx) are detected; the intensities of Atg diffraction peaks slightly decrease, and magnetite and andradite are no longer detected. From 550 to 675 °C, diffraction peaks of antigorite gradually decrease in intensity, while those for olivine slightly increase. At 700 °C and above, peaks attributed to olivine significantly increase in intensity, together with those of clinochlore, clinopyroxene and orthopyroxene. Atg is no longer observed. Tremolite (Trem) is observed at 700 °C with a concentration that can be estimated at about 4 wt.% according to Rietveld refinement (Table 3). With increasing temperature diffraction peaks of clinochlore grow significantly and reach a maximum in intensity at 725 °C. At higher temperatures peak intensities decrease until complete disappearance of clinochlore at 850 °C. The diffraction peaks of olivine and orthopyroxene both increase in intensity from 700 to 800 °C. For the 850 °C sample, the

Table 3
Rietveld refinement results of three experimental products. The numbers in parenthesis are 2σ. Unit-cell parameters of phases used to fit XRD patterns (Fig. 2) are provided in Table 4.

T (°C)	Atg	Ol	Clin	Cpx	Opx	Trem	Fe in Ol (apfu)
600	69(1.1)	16.47(0.63)	8.58(0.41)	6(0.27)	–	–	0.49
700	–	58.63(0.63)	14.27(0.48)	11.23(0.61)	12.12(0.42)	3.75(0.37)	0.27
800	–	61.56(0.38)	7.93(0.3)	9.53(0.31)	20.0(0.34)	–	0.23

diffraction pattern records the presence of olivine, enstatite, diopside and pyrope (Pyr).

XRD patterns of the 600, 700 and 800 °C experiments were analyzed by Rietveld refinement to estimate modal abundances (Table 3). The Rietveld data are consistent with those obtained by mass balance (see Section 3.3). In addition, Rietveld refinement suggests that the fayalite content of olivine decreases, suggesting that olivine becomes less Fe-rich with increasing temperature: the Fe-content in olivine decreases from 0.49 to 0.27 apfu between 600 and 800 °C.

3.1.2. Scanning electron microprobe

The most representative back-scattered electron images of the experimental products are displayed in Fig. 3. SEM characterization of the run products obtained at 550, 650, 675, 700, 800 and 850 °C confirms that magnetite has fully reacted in every sample. Antigorite occurs as elongated grains of 10–20 μm in length in samples run at 550, 650 and 675 °C. At higher temperatures, antigorite is no longer observed. Grains of olivine of 1–5 μm in size are observed in minor amounts at 550 °C. The proportion of olivine increases in the assemblages, together with the grain size. Clinopyroxene is clearly observed in all experimental products except at 850 °C. It forms prismatic grains of ~10 μm length, occupying about 5–7% of the surface on BSE images. Orthopyroxene is observed from 675 to 850 °C. It crystallizes as lath crystals of up to 12 μm length and 1–2 μm width. Clinochlore is observed in the 700 and 800 °C experiments where it forms crystals of 5–7 μm in size, and is no longer observed at 850 °C. At 850 °C, the mineral assemblage is only composed of anhydrous minerals such as garnet, olivine, clinopyroxene and orthopyroxene. Garnet forms euhedral grains homogenous in composition, with a size of about 10 μm in diameter. Olivine is clearly the dominant mineral phase which occupies more than 50% of the polished sample surface area. No indication for the former presence of a melt phase has been encountered even in the higher temperature samples.

3.2. Mineral compositions

Mineral compositions derived from electron microprobe analyses are listed in Supplementary Table S1. The structural formulae of antigorite were calculated based on the ideal antigorite mineral formula $M_{3m\text{-}3}T_{2m}O_{5m}(OH)_{4m\text{-}6}$ for the most commonly observed $m = 17$ polysome (i.e., number of SiO_4 tetrahedra in a single chain defined by the antigorite wavelength; Mellini et al., 1987) and were normalized to 6.825 oxygen atoms. Water contents (wt.%) in hydrous minerals were calculated from the difference from 100 wt.% after ZAF correction assuming total iron as FeO. Mineral formulae of antigorite and clinochlore were calculated assuming total iron as Fe^{2+}, since calculation of Fe^{3+} in antigorite formula based on microprobe analysis is not well consistent. As it was shown by Evans et al. (2012) values of Fe_2O_3 wt.% from Mössbauer spectroscopy do not correlate well with those calculated from microprobe analyses. Mineral formula of garnet was first calculated with Fe^{2+} as total Fe, then Fe^{3+} was calculated using deficiencies in the sum of cations, taking into account that Fe^{3+} occurs in Y (Al, Cr, Fe^{3+}) site. The structural formulae of chlorite were calculated on the basis of 14 anhydrous oxygen atoms.

The evolution of Mg# ($MgO/[MgO + FeO_{total}]$) defines two distinct trends with increasing temperature depending on the presence (below 675 °C) or the absence (above 700 °C) of antigorite in the run products (Fig. 4). At 550 °C, following magnetite disappearance, the iron initially present in magnetite was likely redistributed among the newly formed minerals. Note that magnetite disappearance with increasing temperature is consistent with natural observations reported in Debret et al. (2014, 2015). The first olivine crystals that formed at 550 °C show, i) an enrichment in Fe compared to olivine crystallizing at higher temperatures, but ii) a lower Mg# compared to the other coexisting Fe–Mg minerals. Mg# of olivine at 550 °C ranges from 0.73 to 0.81 and gradually increases to ~0.85 at 675 °C. In parallel, the Mg# of antigorite and clinopyroxene (diopside) also changes significantly

Table 4
Unit-cell parameters of phases used for Rietveld refinement fitting. *m* — number of SiO_4 tetrahedra in one wavelength of the antigorite polysome.

	Space group no.	a (Å)	b (Å)	c (Å)	α (°)	β (°)
SM						
Antigorite ($m = 17$)	6	43.8^a	9.217(13)	7.27624(96)		89.04(11)
Clinochlore	12	5.3870(34)	9.2332(56)	14.3^a		96.197(50)
Magnetite	227	8.3832(10)			90	
Andradite	230	12.06518(95)			90	
600						
Antigorite ($m = 17$)	6	43.2^a	9.298(27)	7.27625(67)		90.858(89)
Olivine	62	10.26270(58)	6.00972(24)	4.77045(12)		
Clinochlore	12	5.3323(17)	9.3^a	14.3008(47)		93.465(34)
Clinopyroxene	15	9.7581(19)	8.9359(21)	5.2452(13)		105.94(16)
700						
Olivine	62	10.23306(29)	5.99720(12)	4.764040(62)		
Clinochlore	12	5.3328(22)	9.2364(19)	14.4310(13)		96.920(34)
Clinopyroxene	15	9.6055(73)	8.8952(64)	5.2919(37)		106.868(60)
Orthopyroxene	61	18.25135(100)	8.8355(11)	5.172(18)		
Amphibole	12	9.8137(21)	18.0672(63)	5.2980(40)		104.659(38)
800						
Olivine	62	10.22714(19)	5.994705(78)	4.762761(40)		
Clinochlore	12	5.3316(32)	9.2274(18)	14.3799(10)		97.061(24)
Clinopyroxene	15	9.7^a	8.9^a	5.3^a		105.772(29)
Orthopyroxene	61	18.2435(13)	8.81394(98)	5.18771(81)		

[a] Fixed parameter.

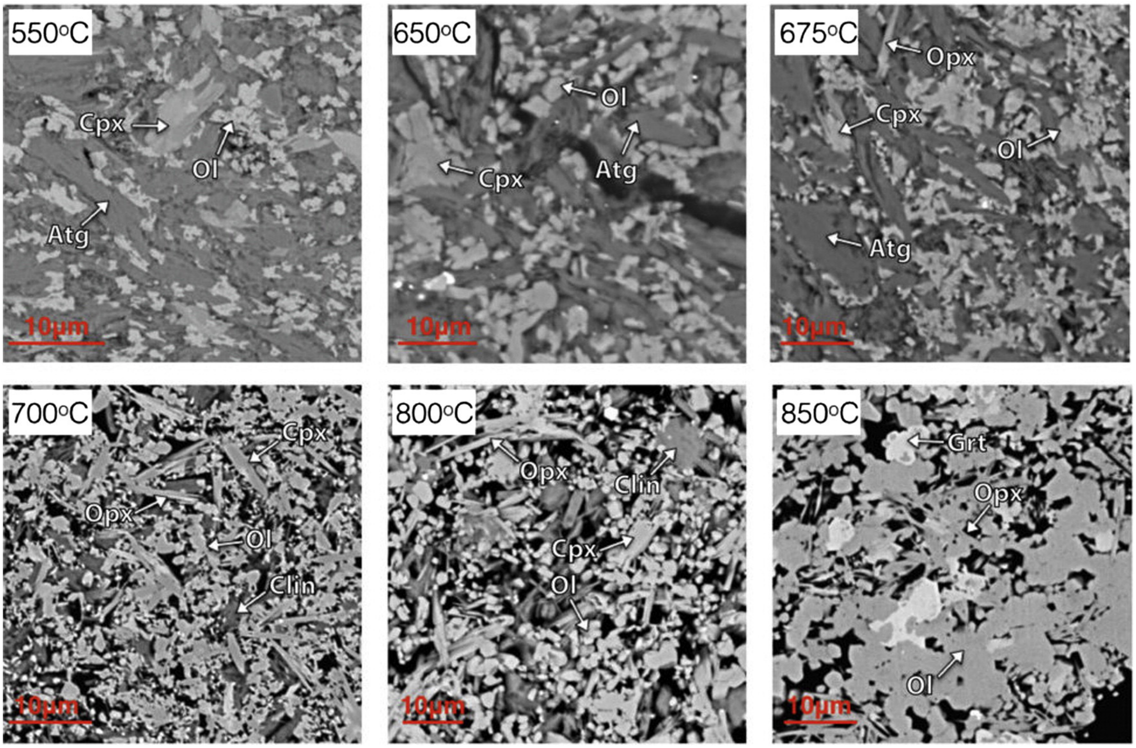

Fig. 3. Back-scattered electron images showing mineral phases (white arrows) and textures of representative experimental assemblages. Atg — antigorite, Ol — olivine, Cpx — clinopyroxene, Opx — orthopyroxene, Clin — clinochlore, Grt — garnet.

with temperature. From 550 to 675 °C, the Mg# of antigorite decreases from ~0.98 to 0.94, while one of the diopside decreases from ~0.93 to 0.88. This change of Mg# values for the coexisting phases with temperature points to Fe–Mg exchange between Ol, Cpx and Atg.

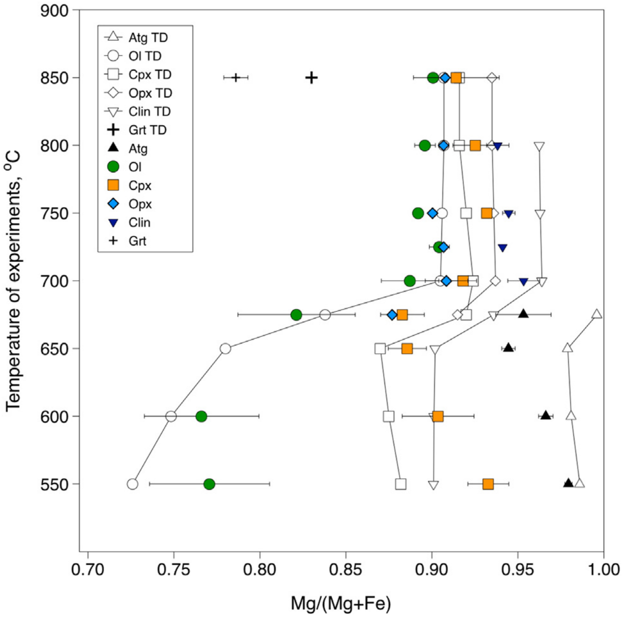

Fig. 4. Mg# of observed minerals in experimental products as a function of temperature. Mg# (MgO/[MgO + FeO_{total}] was calculated assuming total iron as FeO. Solid symbols show the average of individual point analyses; error bars are 2 standard deviations. Green circles indicate Mg# of olivine, black triangles — Mg# of antigorite, orange squares — Mg# of clinopyroxene, light blue diamonds — Mg# of orthopyroxene, blue triangles — Mg# of clinochlore, crosses — Mg# of garnet. Open symbols with lines indicate thermodynamically calculated (TD) values. (For interpretation of the references to color in this figure legend, the reader is referred to the web version of this article.)

Above 700 °C, antigorite is no longer observed in mineral assemblages due to its breakdown between 675 and 700 °C. Mg# values of olivine and diopside increase drastically to about 0.90 and 0.92, respectively, and both remain relatively stable to 850 °C. Orthopyroxene (enstatite) is formed at 675 °C and displays a Mg# of ~0.86, which then increases up to 0.87–0.93 at 700 °C (light blue diamonds in Fig. 4), and finally reaches ~0.91 at 850 °C. In parallel, clinochlore grains (only observed at 700, 725, 750 and 800 °C) show Mg# values that slightly decrease from ~0.95 to 0.94 with increasing temperature (blue triangles in Fig. 4). Garnet, which forms only at 850 °C, is represented by a mixture of almandine, grossular and pyrope end-members, and has an average Mg# of 0.78 (crosses in Fig. 4).

A comparison of mineral assemblages and mineral chemistry between the experimental products and natural serpentinites may help to understand mineral relations in prograde metamorphic rocks. Olivine and antigorite Mg# are described to be 0.9 and 0.94 on average respectively in most natural prograde serpentinites (e.g., Debret et al., 2015; Padrón-Navarta et al., 2011; Trommsdorff and Evans, 1972; Trommsdorff et al., 1998). The Mg# values are in a good agreement with those experimentally obtained. However, Mg# values in clinopyroxene reported in natural rock studies (e.g., Scambelluri et al., 1991; Trommsdorff and Evans, 1972) are higher (~0.97) compared to the experiment (0.9 on average, Fig. 4). High Mg# in clinopyroxene may be explained by the presence of magnetite in natural antigorite-bearing serpentinites and their prograde lithologies. In addition, Fe^{3+} component in antigorite may influence Fe–Mg exchange between antigorite and coexisting olivine and clinopyroxene, and moreover affect antigorite thermal stability (e.g., Evans et al., 2012).

3.3. Mass balance

The phase abundances in each experimental product were estimated from mass balance calculations using the average individual mineral compositions measured by EPMA (Table S1) and the bulk composition of the starting material (Table 1). Mass balance equations were written in the form of three matrices for each experiment: weight percent of oxides in each mineral phase, weight percent of oxides in bulk composition and weight fraction of minerals, the latter being determined. Modal abundances were derived following the method described by Lamberg et al. (1997) assuming that $Fe^{2+} = Fe_{total}$. Estimated deviations from average values are ± 1–20%. Uncertainties of the calculated phase abundances (Fig. 5) are obtained from variations in the analytical data of mineral compositions. The mineral fractions estimated by mass balance calculations are consistent with those estimated by Rietveld refinement of XRD patterns (Table 3, Fig. 5b).

From the mass balance calculations (Fig. 5b), the amount of antigorite is found to decrease continuously from 550 to 650 °C and further vanishes at 700 °C. The amounts of olivine and orthopyroxene both increase with temperature, and a strong increase of their relative proportions is observed between 675 and 700 °C, which coincides with the antigorite breakdown in this temperature range. The maximum amounts of clinopyroxene and clinochlore are reached at 700 °C.

Water was considered as an individual phase in the mass balance calculations, so that the amount of released H_2O was also calculated (Fig. 5a). The water content in the bulk rock composition equaled to 11.5 wt.% (Table 1). Two hydrous phases, antigorite and clinochlore, were assumed to be present in the low-temperature assemblages (550, 600, 650 and 675 °C). Above 700 °C, clinochlore is the only water-bearing phase present in the experimental products. The H_2O wt.% values of antigorite and clinochlore at each temperature were calculated from the difference from 100 wt.% of oxides measured by electron microprobe. The results show a progressive release of about 30% of the total water at 675 °C, followed by a sudden release of about 55% of the total water between 675 and 700 °C. The last 15% of water are then released between 800 and 850 °C following the breakdown of clinochlore.

3.4. Thermodynamic modeling

The molar proportions of Mg and Fe in all phases, including antigorite, change from 550 to 700 °C suggesting solid solution of Fe–Mg in antigorite. Support for this assumption comes from reports of iron-bearing antigorite in natural samples (e.g., Debret et al., 2014, 2015; Evans et al., 2012; Padrón-Navarta et al., 2011). Therefore, any thermodynamic modeling of our experimental results requires incorporation of a Fe-antigorite end-member, which is absent in the thermodynamic database of Holland and Powell (1998). Since microprobe analyses do not allow accurate determination of Fe^{3+}/Fe_{tot}, only a simplified Fe^{2+}-antigorite end member was used for the thermodynamic modeling.

The standard state enthalpy of formation ($\Delta H_f°$), third law entropy (S°), volume (V°) and heat capacity (Cp) of Fe-antigorite $(Fe)_{48}Si_{34}O_{85}(OH)_{62}$ were estimated using the standard-state properties of Mg-antigorite and the difference between those of Fe- and Mg-talc: ($\Delta H_f°$, S°, V°, Cp)Fe-antigorite = ($\Delta H_f°$, S°, V°, Cp)Mg-antigorite + ($\Delta H_f°$, S°, V°, Cp)(Fe-Talc–Mg-Talc), where ($\Delta H_f°$, S°, V°, Cp)Mg-antigorite are the original properties reported by Holland and Powell (1998) for the $Mg_{48}Si_{34}O_{85}(OH)_{62}$ structural formula. The estimated standard state properties of Fe-antigorite are listed in Table 5. The antigorite solid solution was assumed to be ideal. Solid solution models of phases used in the calculations are present in Table 6. The results of thermodynamic modeling with the internally consistent database of Holland and Powell (1998) complemented with the Fe-antigorite end-member properties calculated above and assuming an ideal Fe–Mg antigorite solid solution are shown in Figs. 4–7.

To validate our thermodynamic model, we calculated the abundances of each mineral phase and compared these with experimental data. Fig. 5 demonstrates consistency between observed and calculated phase amounts along the studied temperature gradient.

As discussed above, the Mg# of olivine was found experimentally to increase with temperature, whereas that of clinopyroxene and antigorite decrease (Fig. 4). In agreement with the experimental results, the same behavior is reproduced by the thermodynamic modeling Mg# in coexisting olivine, clinopyroxene, antigorite and additionally clinochlore. The sharp change of Fe content in Cpx, Atg and Clin, observed in the computed Mg# versus T curves of these phases at about 650 °C, can be explained by the appearance of orthopyroxene in the assemblage (Fig. 4).

Fig. 6 shows a P–T pseudosection calculated by Gibbs free energy minimization using Theriak–Domino (de Capitani and Petrakakis, 2010) for the starting composition, and the known P–T conditions of our experiments. In agreement with our experimental results, the calculated pseudosection shows continuous dehydration of Clin–Ol–Atg serpentinites (the dark-gray field on P–T pseudosection) to produce assemblages with only clinochlore as the main hydrous phase and then to the anhydrous Ol–Opx–Cpx–Grt assemblage at 800 °C.

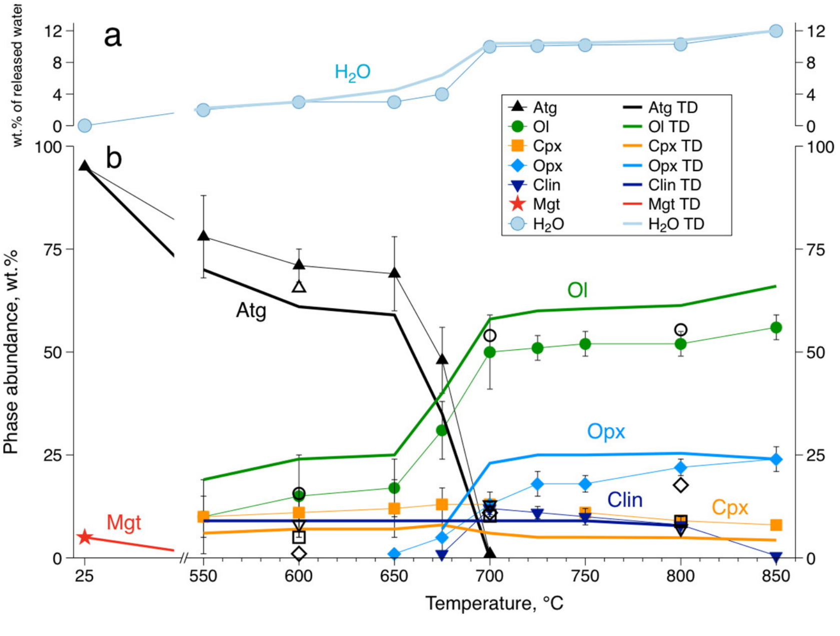

Fig. 5. Phase abundance of experimental products as a function of temperature at 2 GPa. a) Integrated amount of released water; b) abundance of mineral phases estimated by mass balance calculation (filled symbols) or Rietveld refinement (open symbols). Bold lines without symbols indicate phase abundance estimations obtained from thermodynamic modeling.

Table 5
Enthalpy, entropy, volume and heat capacity function coefficients for (1) Mg-antigorite taken from Holland and Powell (1998) database and for (2) Fe-antigorite calculated using the standard-state properties of Mg-antigorite and the difference between those of Fe- and Mg-talc taken from Holland and Powell (1998).

	Formula	$\Delta_f H°$ (J)	S° (J/K)	V° (J/Bar)	a ($J \cdot K^{-1}$)	b ($J \cdot K^{-2}$)	c ($J \cdot K$)	d ($J \cdot K^{-1/2}$)
Mg-atg	$Mg_{48}Si_{34}O_{85}(OH)_{62}$	−71,417,980	3591	175.48	9621	−0.0962	−35,941,600	−83,034
Fe-atg	$Fe_{48}Si_{34}O_{85}(OH)_{62}$	−53,905,950	5396	180.00	8558	0.55803	−35,773,992	−66,315

In order to compare phase relationships at different bulk iron contents, we computed phase diagrams (Fig. 6) for Fe-free bulk composition ($MgO–SiO_2–H_2O$), for the composition corresponding to our starting material (6.07 wt.% FeO_{total}), and a composition containing 10 wt.% FeO_{total}, which is the average upper limit for iron in natural serpentinites (e.g., Debret et al., 2014; Deschamps et al., 2012; Guillot et al., 2001; Li et al., 2004). The mineral reactions calculated for these three compositions shift to lower temperatures as FeO increases from 0 to 10 wt.%. The breakdown temperature of antigorite is 25 °C lower in the system with 10 wt.% of FeO than in a Fe-free system, and about 10 °C lower than in the system with 6 wt.% FeO. Likewise, the temperature of clinochlore-out reactions for the Fe-rich (10 wt.% FeO) composition is 5 to 20 °C lower than for the composition with 6 wt.% FeO, and, consistently, clinochlore is absent in the Fe- and Al-free systems. The shift in temperature of reactions with increasing bulk iron is accompanied by decreasing Mg# in coexisting minerals.

Theriak–Domino calculations show the disappearance of magnetite between 380 and 550 °C along the pressure range of 5 GPa (Fig. 6). The magnetite-out redox reaction leads to the release of free oxygen, which is buffered by QFM oxygen buffer defined in our calculations. Such a fO_2 buffer was chosen following studies of natural rock observations (e.g., Debret et al., 2016; Frost, 1985), which demonstrated that subducted serpentinites typically record oxygen fugacity varying between QFM +4 and QFM −4.

4. Discussion

4.1. Mineral reactions during dehydration

Our experimental results provide detailed information on Fe–Mg exchange between coexisting minerals, as well as on the mineral reactions that occur during prograde serpentinite metamorphism. The starting material was a mixture of antigorite (~95 wt.%) and magnetite (~5 wt.%) in order to match bulk average oceanic mantle lithosphere composition (e.g., Debret et al., 2014, 2015; Deschamps et al., 2012; Li et al., 2004; Marcaillou et al., 2011). Characterization of piston-cylinder experimental products shows that magnetite is entirely consumed in the presence of antigorite at relatively low temperature (<550 °C) to form iron-rich secondary olivine, as in the following reaction:

$$\underset{antigorite}{6Mg_3Si_2O_5(OH)_4} + \underset{magnetite}{2Fe_3O_4} \rightarrow \underset{olivine}{12(Mg_{1.5}Fe_{0.5})SiO_4} + \underset{oxygen}{O_2} + \underset{water}{12H_2O}\,. \quad (1)$$

Table 6
Solid solution models used in the present study consistent with Holland and Powell (1998) thermodynamic data set.

Phase	Formula	Solid solution model
Antigorite (Atg)	$(Mg, Fe)_{48}Si_{34}O_{85}(OH)_{62}$	Ideal
Olivine (Ol)	$(Mg, Fe)_2SiO_4$	Ideal
Chlorite (Chl)	$(Mg, Fe)_4(Mg, Fe, Al)_2(Al, Si)Si_3O_{10}(OH)_4$	Regular
Clinopyroxene (Cpx)	$Ca(Mg, Fe)Si_2O_6$	Regular
Orthopyroxene (Opx)	$(Mg, Fe, Al)SiO_3$	Regular
Garnet (Grt)	$(Ca, Mg, Fe)_3Al_2Si_3O_{12}$	Regular
Talc (Ta)	$(Mg, Fe, Al)_3(Si, Al)_4O_{10}(OH)_2$	Ideal

In Eq. (1), the structural formula of olivine is determined in agreement with its chemical composition observed in the run product at 550 °C.

Fe–Mg exchange between olivine and antigorite was observed between 550 and 675 °C. Fayalite end-member of olivine reacts with Mg-antigorite according to the following reaction, and along with Reaction (1):

$$\underset{Mg\text{-}antigorite}{Mg_3Si_2O_5(OH)_4} + \underset{Fe\text{-}olivine}{Fe_2SiO_4} \rightarrow \underset{Fe\text{-}antigorite}{Fe_3Si_2O_5(OH)_4} + \underset{Mg\text{-}olivine}{Mg_2SiO_4}\,. \quad (2)$$

According to our model, Reaction (1) is complete below 550 °C and 2 GPa (Fig. 6), which is consistent with experimental results. In addition to the formation of Fe-rich olivine, Reaction (1) leads to the production of water and oxygen in the redox conditions of our experiments. The total amount of oxygen directly depends on the presence of Fe^{3+} in serpentinites, which is mainly related to the amount of magnetite in the starting material, although antigorite might also contain ferric iron (e.g., Debret et al., 2014; Muñoz et al., 2013). However, ferric iron in antigorite was here considered as negligible compared to the total amount of ferric iron hosted by magnetite in the starting material. Note that a complete description of redox reactions that occur in such chemical system will be detailed in a forthcoming article (Merkulova et al., in prep).

Another reaction coincident with magnetite destabilization and responsible for olivine formation is a brucite-out reaction. However, brucite was not present in the experimental starting material, it appeared on the P–T pseudosection (Fig. 6) due to non-stoichiometric bulk rock composition used as an in-put parameter in Theriak–Domino software. Thus, we don't discuss the brucite-out reaction, since the amount of brucite didn't exceed 1 wt.% and considered as negligible.

After the complete disappearance of magnetite, antigorite reacts to form secondary olivine and pyroxene with a large release of water, according to the following reaction:

$$\underset{antigorite}{2(Mg, Fe)_3Si_2O_5(OH)_4} \rightarrow \underset{olivine}{2(Mg, Fe)_2SiO_4} + \underset{orthopyroxene}{(Mg, Fe)_2Si_2O_6} + \underset{water}{4H_2O}\,. \quad (3)$$

Reaction (3) begins at 650 °C and is completed at around 680 °C at 2 GPa (see Fig. 6). In contrast to pure magnesium end-member system (Fig. 6) in which antigorite breakdown reaction is univariant, our experimental data and thermodynamic calculations show that Fe-bearing antigorite breaks down by Reaction (3) over about 30 °C (between 650 and 680 °C). Consequently, complete antigorite breakdown in subduction zones is expected to occur over a range of temperatures, depending on the bulk iron content of the subducting serpentinite (Fig. 6).

Since the starting material also contains calcium and aluminum (Table 1), mineral phase relations are actually more complex than the combination of Reactions (1) and (3), because the extra components lead to the formation of tremolite, diopside, and clinochlore. Clinochlore is the most significant phase in the context of dehydration due to its stability at relatively high temperatures and its potential to retain water after antigorite breakdown.

The increase of clinochlore content at 700 °C, beyond antigorite breakdown, can be interpreted by the partial breakdown of Al-bearing antigorite, which contains in average 1.09 ± 0.22 wt.% Al_2O_3. Therefore, the presence of aluminum in the starting antigorite leads to the

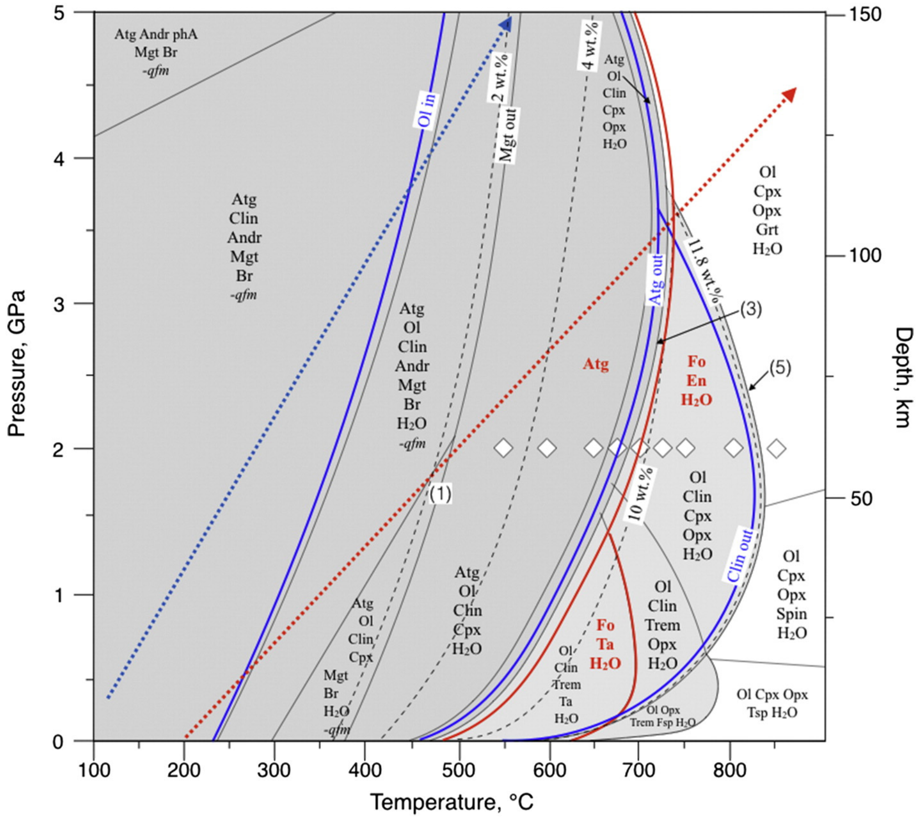

Fig. 6. P–T equilibrium pseudosection for the bulk composition of the experimental starting material (6 wt.% FeO; gray lines). White diamonds indicate experimental P–T. Dark-gray field indicates a stability field of both, antigorite and clinochlore together. Light-gray field indicates stability field of clinochlore. White field indicates stability of anhydrous assemblages. Dashed black isolines indicate wt.% H_2O released from the solid rock. Numbers in parenthesis correspond to numbers of mineral reactions mentioned in the text. Blue lines correspond to reactions for the serpentinite bulk composition with 10 wt.% of FeO. Red lines indicate reactions in the Fe-free system. *–qfm* "phase" signifies higher oxygen fugacity of the Mgt-bearing assemblages compared to Mgt-free assemblages. Red and blue dashed arrows indicate approximate thermal gradients typical for the slab Moho for hot and cold subduction zones, respectively (Syracuse et al., 2010). (For interpretation of the references to color in this figure legend, the reader is referred to the web version of this article.)

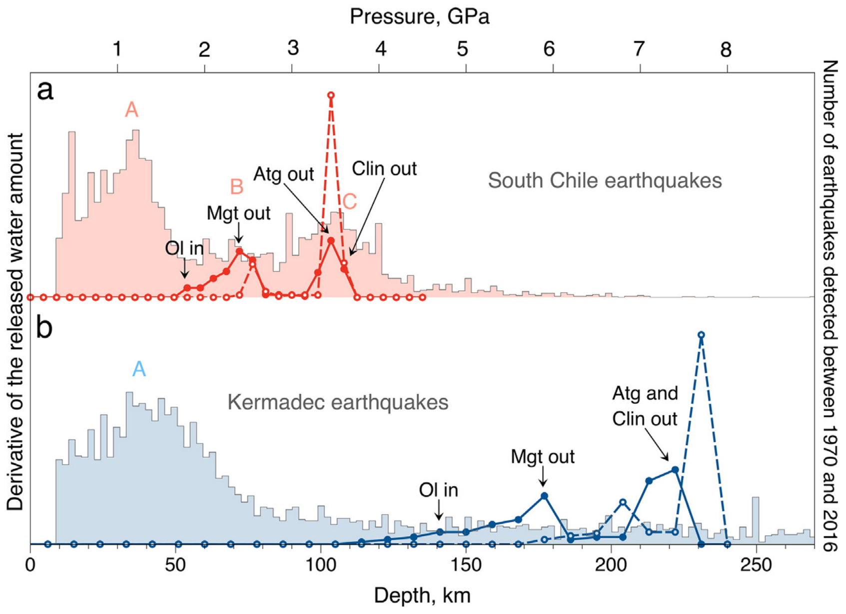

Fig. 7. a) Pressure-derivative of the amount of released water along the PT path of the slab Moho in hot subduction (red lines). Light red bars represent the distribution histogram of earthquake hypocenters in South Chilean subduction. b) Pressure-derivative of the amount of released water along PT path of slab Moho in cold subduction (blue lines). Light blue bars represent the distribution histogram of earthquake hypocenters in Kermadec subduction. Dashed lines indicate water release in serpentinites with 1 wt.% of FeO, solid lines indicate water release in serpentinites with 10 wt.% of FeO. PT paths of the slab Moho are taken from Syracuse et al. (2010). (For interpretation of the references to color in this figure legend, the reader is referred to the web version of this article.)
Data of earthquake hypocenters taken from USGS ANSS Comprehensive Catalog.

formation of secondary clinochlore above 700 °C (up to ~12 wt.%), according to the reaction:

$$\underset{\text{Al-antigorite}}{(Mg_2Al)(SiAl)O_5(OH)_4} + \underset{\text{antigorite}}{Mg_3Si_2O_5(OH)_4} \rightarrow \underset{\text{clinochlore}}{Mg_5Al_2Si_3O_{10}(OH)_8}. \quad (4)$$

We were not able to present this reaction in Fig. 6 because our antigorite solid solution has no Al-antigorite end-member. However, it is expected that aluminum plays a major role in natural settings (Padrón-Navarta et al., 2013) since it allows the formation of clinochlore – a phase containing about 14 wt.% water – after the antigorite breakdown, potentially carrying water to greater depths.

In the last step, clinochlore breaks down into garnet at T > 800 °C through the reaction:

$$\underset{\text{clinochlore}}{Mg_5Al_2Si_3O_{10}(OH)_8} + \underset{\text{orthopyroxene}}{Mg_2Si_2O_6} \rightarrow \underset{\text{olivine}}{2Mg_2SiO_4} + \underset{\text{garnet}}{Mg_3Al_2Si_3O_{12}} + \underset{\text{water}}{4H_2O}. \quad (5)$$

Reaction (5) occurs at 820 °C and 2 GPa (Fig. 6); it corresponds to the last prograde dehydration and releases around 20 wt.% of the total water (Fig. 5a).

Described mineral reactions in Fe- and Al-bearing system are present as divariant fields on P–T pseudosection (Fig. 6) with maximum temperature width between 1 and 2 GPa.

4.2. Antigorite upper thermal stability limit

According to the previous experimental studies (Bromiley and Pawley, 2003; Eggler and Ehmann, 2010; Padrón-Navarta et al., 2010; Ulmer and Trommsdorff, 1995; Wunder and Schreyer, 1997), the temperature of antigorite breakdown ranges from 630 to 710 °C at pressures from 1.5 to 3 GPa. This large temperature range probably results from the use of starting materials of variable bulk compositions. In particular, differences among the experimentally derived antigorite stabilities can be accounted for by different total iron and ferric iron contents as well as the presence of other trivalent cations such as Al(III) and Cr(III), which extend the antigorite stability field (Bromiley and Pawley, 2003; Evans et al., 2012). Our experimental dataset shows that the upper thermal stability limit of antigorite is between 675 and 700 °C for a starting composition including 6 wt.% of FeO_{total} (Fig. 5), while our thermodynamic modeling gives the value of the upper limit of antigorite stability of 680 °C at 2 GPa (Fig. 6). The thermodynamic modeling also shows complete antigorite breakdown in Fe-rich (10 wt.% FeO_{total}) systems at 25 °C less than in Fe-free systems (Fig. 6). The presence of iron also affects the upper thermal stability of chlorite, which is reduced by up to 20 °C for the composition with 10 wt.% FeO compared to the system with 6 wt.% FeO. A 25 °C temperature difference corresponds to depth differences of 3 to 10 km depending on the inclination of the subduction plane (Syracuse et al., 2010).

4.3. Continuous water release

Based on our experimental results and thermodynamic modeling, we show that 30% of the water initially contained in the starting material is released below 550 °C by Reaction (1). About 50% of the water is liberated in a narrow temperature range between 675 and 700 °C due to antigorite breakdown (Reaction (3)). The remaining 20% is released between 700 and 820 °C due to the breakdown of clinochlore (Reaction (5)). Consequently, the ultimate dehydration of subducted serpentinized peridotite occurs with the clinochlore breakdown at around 820 °C. Such a three-step dehydration is likely to occur in natural systems, as clinochlore is observed in many antigorite-bearing peridotites (Debret et al., 2014, 2015).

Models of the continuous dehydration of subducted oceanic lithosphere have been proposed previously (e.g., van Keken et al., 2011). Extrapolation of our results to realistic geothermal gradients demonstrates that dehydration of serpentinites starts at low pressure and temperature (Fig. 6), at depths below 50 km, and is accomplished at 100 km or more depending on angle of subduction. Thus, taking into account the greater volume of serpentinites than sediments and altered basalts in subducted lithosphere, serpentinites are the most significant water carriers in subduction zones down to ~200 km.

Variations in serpentinite composition, especially in terms of Fe and Al, as it was discussed above, affect upper thermal stability limits of antigorite and clinochlore and consequently P–T conditions of serpentinite dehydration. The FeO contents of serpentinites from different localities range from 4.91 to 10 wt.% (Debret et al., 2014; Deschamps et al., 2012; Li et al., 2004) and Al_2O_3 contents from 0.3 to 7.68 wt.% (Guillot et al., 2001; Hattori and Guillot, 2007) (Fig. 1). As a consequence, Al-rich systems carry abundant water through chlorite into deeper parts of subduction zones, while systems with high Fe contents dehydrate at shallower depths due to the instability of Fe-antigorite at lower P and T.

4.4. Implications for subduction zone seismicity

We computed pressure-derivatives of the amount of released water along the slab Moho (typically 7 km beneath the slab surface) in the case of South Chile subduction (Fig. 7a) and for Kermadec subduction (Fig. 7b) using the P–T distribution data of Syracuse et al. (2010). Water release profiles were calculated for two serpentinite compositions with different FeO_{total} contents. Two water releasing events are clearly distinguished in both profiles corresponding respectively to, 1) magnetite destabilization, consumption of antigorite and formation of olivine (Reaction (1)), and 2) breakdown of antigorite (Reaction (3)) and clinochlore (Reaction (5)). The water release for serpentinites with 10 wt.% FeO is shifted towards lower pressures compared to profiles for serpentines with 1 wt.% FeO (Fig. 7). Dehydration within Fe-rich serpentinites happens in a wider depth-range, between 50 and 110 km, for hot subduction, and between 120 and 230 km for cold subduction. In contrast, dehydration in serpentinites with lower FeO is observed in a narrower range, between 70 and 110 km for hot subduction and between 190 and 230 km for cold subduction (Fig. 7).

To investigate possible link between dehydration reactions and seismicity in subduction zones, we compare, according to depth, the pressure-derivatives of the released water amount to the number of earthquakes detected between 1970 year and 2016 year (Fig. 7a, b). Earthquake hypocenters for South Chile and Kermadec subduction zones are taken from the USGS ANSS comprehensive catalog. The histogram of earthquake depth distribution within South Chilean subduction (Fig. 7a) shows three maxima of seismic events. The first maximum (peak A; Fig. 7a) indicates earthquake hypocenters located around 40 km in depth. According to, e.g., Stern (2002), such shallow-depth seismic events are likely caused by slab faulting and dehydration of sediments and metabasalts. A low peak of seismic events is observed around 70 km depth (peak B), which appears in agreement with a peak of water release caused by olivine-in and magnetite-out reaction (solid curve in Fig. 7). More significant maximum of seismic events is located around 110 km depth (peak C) and correlates perfectly with the highest peak of dehydration depth-profile for the Fe-rich serpentine. This maximum corresponds to a water release due to antigorite and clinochlore breakdown. Such a correlation potentially suggests, as already proposed by some authors (e.g., Peacock, 2001; Ulmer and Trommsdorff, 1995), that dehydration of serpentinites could contribute to intermediate-depth seismic events in hot-type subduction settings.

In contrast, the dehydration reactions in cold subduction zone do not coincide with the maximum of earthquake hypocenters (Fig. 7b). The only significant peak (peak A; Fig. 7b) of seismic events on the histogram for Kermadec subduction zone is located around 40 km, these seismic events, as in the case of hot subduction, correspond to dehydration of sediments and metabasalts. The dehydration of Fe-bearing serpentinites in such geological settings occurs at greater depths, >150 km (Fig. 7).

Such a discrepancy between depths of seismicity and serpentinite dehydration suggests that earthquakes in steep-angle cold-type subduction zones, such as Kermadec, are not triggered by serpentinite dehydration.

The contrasted rheological effect of serpentinite dehydration in hot and cold subduction settings is puzzling and the effective role of serpentinite dehydration in promoting intermediate-depth earthquakes is still to be answered (e.g., Gasc et al., 2011; Okazaki and Hirth, 2016). It is known that Kermadec-type subduction zones are characterized by reduced intermediate seismicity and a lack of deep earthquakes (Stern et al., 2003). The maximum of seismic events at shallow and intermediate depths (20–80 km) may be caused by slab faulting mechanisms (Stern et al., 2003) and dehydration in the oceanic crust of minerals such as lawsonite (Okazaki and Hirth, 2016).

5. Conclusions

Using experimental results and thermodynamic modeling, we have constrained the stability of mineral phases in serpentinites with different Fe contents and demonstrated the effect of Fe on reducing the upper thermal stability limit of main hydrous phases, antigorite and clinochlore (Fig. 6), compared to pure Mg-systems. The presence of Al in our starting material stabilized clinochlore at temperatures up to 820 °C. Dehydration of subducting slabs depends on 1) the thermal structure of subduction zone, which is regulated by the age and speed of the slab (Syracuse et al., 2010; van Keken et al., 2011), and 2) the chemistry of the slab, particularly the Fe and Al contents, which influence the stability fields of hydrous minerals and consequently, the P–T conditions of water release from the slab. Our work shows that, the composition of serpentinites and the pressure–temperature gradient must be considered when modeling and interpreting processes in subduction zone, especially the process of dehydration. Future work and modeling included ferric iron substitution in antigorite will help to constrain P–T conditions of natural serpentinite dehydration and oxidation state of the released fluid.

The comparison between focal depths and water-release depth profiles in two different subduction zones demonstrates that, depending on the angle of subduction and the PT conditions in the slab, the contribution of serpentinite dehydration to seismicity, if any, could be highly contrasted. A clear correlation between depths of dehydration and of peak seismic activity in hot subduction zones strongly contrasts with the absence of such a correlation in cold subduction zones.

Acknowledgments

We thank B. Evans and F. Renard for useful discussions and V. Batanova and N. Findling for analytical assistance. We also thank the EPMA team of ISTerre. The EPMA facility in ISTerre was established and maintained by funds from the Agence Nationale de la Recherche, France Chair of Excellence grant ANR-09-CEXC-003-01 and Labex OSUG@2020 (Investissements d'avenir-ANR10 LABX56). We acknowledge support of ANR HYDEEP grant. We thank Stefano Poli and one anonymous reviewer for helpful comments. We are also very grateful to N. Arndt and O. Neill for their helpful English language reviews.

Appendix A. Supplementary data

Supplementary data to this article can be found online at http://dx.doi.org/10.1016/j.lithos.2016.09.007.

References

Bergmann, J., Friedel, P., Kleeberg, R., 1998. BGMN — a new fundamental parameters based Rietveld program for laboratory X-ray sources, it's use in quantitative analysis and structure investigations. Commission on Powder Diffraction Newsletter 20, 5–8.

Bose, K., Ganguly, J., 1995. Antigorite and phase a at high pressures with applications to subduction processes. Earth and Planetary Science Letters 136, 109–121.

Bromiley, G.D., Pawley, A.R., 2003. The stability of antigorite in the systems MgO–SiO_2–H_2O (MSH) and MgO–Al_2O_3–SiO_2–H_2O (MASH): the effects of Al^{3+} substitution on high-pressure stability. American Mineralogist 88, 99–108.

Brunet, F., Bagdassarov, N., Miletich, R., 2003. $Na_3Al_2(PO_4)_3$, a fast sodium conductor at high pressure: in-situ impedance spectroscopy characterization and phase diagram up to 8 GPa. Solid State Ionics 159, 35–47.

Chou, I.-M., 1986. Permeability of precious metals to hydrogen at 2 kb total pressure and elevated temperatures. American Journal of Science 286, 638–658.

Cooke, D., Simmons, S.F., 2000. Characteristics and genesis of epithermal gold deposits. Reviews in Economic Geology 13, 221–244.

de Capitani, C., Petrakakis, K., 2010. The computation of equilibrium assemblage diagrams with Theriak/Domino software. American Mineralogist 95, 1006–1016.

De Hoog, J.C.M., Hattori, K., Jung, H., 2014. Titanium- and water-rich metamorphic olivine in high-pressure serpentinites from the Voltri Massif (Ligurian Alps, Italy): evidence for deep subduction of high-field strength and fluid-mobile elements. Contributions to Mineralogy and Petrology 167, 990.

Debret, B., Andreani, M., Muñoz, M., Bolfan-Casanova, N., Carlut, J., Nicollet, C., Schwartz, S., Trcera, N., 2014. Evolution of Fe redox state in serpentine during subduction. Earth and Planetary Science Letters 400, 206–218.

Debret, B., Bolfan-Casanova, N., Padrón-Navarta, J.A., Martin-Hernandez, F., Andreani, M., Garrido, C.J., López Sánchez-Vizcaíno, V., Gómez-Pugnaire, M.T., Muñoz, M., Trcera, N., 2015. Redox state of iron during high-pressure serpentinite dehydration. Contributions to Mineralogy and Petrology 169, 36.

Debret, B., Millet, M.-A., Pons, M.-L., Bouilhol, P., Inglis, E., Williams, H., 2016. Isotopic evidence for iron mobility during subduction. Geology 44, 215–218.

Deschamps, F., Godard, M., Guillot, S., Chauvel, C., Andreani, M., Hattori, K., Wunder, B., France, L., 2012. Behavior of fluid-mobile elements in serpentines from abyssal to subduction environments: examples from Cuba and Dominican Republic. Chemical Geology 312–313, 93–117.

Deschamps, F., Godard, M., Guillot, S., Hattori, K., 2013. Geochemistry of subduction zone serpentinites: a review. Lithos 178, 96–127.

Eggler, D.H., Ehmann, A.N., 2010. Rate of antigorite dehydration at 2 GPa applied to subduction zones. American Mineralogist 95, 761–769.

Evans, B.W., 1977. Metamorphism of alpine peridotite and serpentinite. Annual Review of Earth and Planetary Sciences 5, 397–447.

Evans, B.W., 2004. The serpentinite multisystem revisited: chrysotile is metastable. 46, 479–506.

Evans, B.W., Dyar, M.D., Kuehner, S.M., 2012. Implications of ferrous and ferric iron in antigorite. American Mineralogist 97, 184–196.

Frost, B.R., 1985. On the stability of sulfides, oxides, and native metals in serpentinite. Journal of Petrology 26, 31–63.

Fudral, S., Deville, E., Pognante, U., Gay, M., Fregolent, G., Lorenzoni, S., Robert, D., Nicoud, G., Blake, C., Jayko, A., Jaillard, É., Bertrand, J.-M., Forno, M.G., Massazza, G., 1993. Carte géologique de la France (1/50.000°), feuille Lanslebourg - Mont d'Ambin (776). Notice explicative par Fudral, S. Deville, E., Nicoud G., Pognante U., Guillot P.-L., Jaillard É., BRGM publ., Orléans.

Gasc, J., Schubnel, A., Brunet, F., Guillon, S., Mueller, H.J., Lathe, C., 2011. Simultaneous acoustic emissions monitoring and synchrotron X-ray diffraction at high pressure and temperature: calibration and application to serpentinite dehydration. Physics of the Earth and Planetary Interiors 189, 121–133.

Guillot, S., Hattori, K., de Sigoyer, J., Nagler, T., Auzende, A.L., 2001. Evidence of hydration of the mantle wedge and its role on the exhumation of eclogites. Earth and Planetary Science Letters 193, 115–127.

Hacker, B.R., Peacock, S.M., Abers, G.A., Holloway, S.D., 2003. Subduction factory 2. Are intermediate-depth earthquakes in subducting slabs linked to metamorphic dehydration reactions? Journal of Geophysical Research: Solid Earth 108, 11-1–11-8.

Hattori, K.H., Guillot, S., 2007. Geochemical character of serpentinites associated with high- to ultrahigh-pressure metamorphic rocks in the Alps, Cuba, and the Himalayas: recycling of elements in subduction zones. Geochemistry, Geophysics, Geosystems 8, 9.

Holland, T.J.B., Powell, R., 1998. An internally consistent thermodynamic data set for phases of petrological interest. Journal of Metamorphic Geology 16, 309–343.

Jarosewich, E., 2002. Smithsonian microbeam standards. Journal of Research of the National Institute of Standards and Technology 107, 681.

Lamberg, P., Hautala, P., Sotka, P., Saavalainen, S., 1997. Mineralogical balances by dissolution methodology. Paper Presented at IMA Commission on Ore Mineralogy Short Course, S. Mamede de Infesta, Portugal, pp. 1–29.

Li, X.-P., Rahn, M., Bucher, K., 2004. Serpentinites of the Zermatt–Saas ophiolite complex and their texture evolution. Journal of Metamorphic Geology 22, 159–177.

Marcaillou, C., Muñoz, M., Vidal, O., Parra, T., Harfouche, M., 2011. Mineralogical evidence for H_2 degassing during serpentinization at 300 °C/300 bar. Earth and Planetary Science Letters 303, 281–290.

Marchesi, C., Garrido, C.J., Padrón-Navarta, J.A., López Sánchez-Vizcaíno, V., Gómez-Pugnaire, M.T., 2013. Element mobility from sea floor serpentinization to high-pressure dehydration of antigorite in subducted serpentinite: insights from the Cerro del Almirez ultramafic massif (southern Spain). Lithos 178, 128–142.

Mellini, M., Trommsdorff, V., Compagnoni, R., 1987. Antigorite polysomatism: behaviour during progressive metamorphism. Contributions to Mineralogy and Petrology 97, 147–155.

Merkulova M.V., Muñoz M., Brunet F., Vidal O., Hattori K., Vantelon D., Trcera N., Huthwelker T., Consequences of Fe and S reduction during serpentinite dehydration: experimental study, (in preparation).

Muñoz, M., Vidal, O., Marcaillou, C., Pascarelli, S., Mathon, O., Farges, F., 2013. Iron oxidation state in phyllosilicate single crystals using Fe–K pre-edge and XANES spectroscopy: effects of the linear polarization of the synchrotron X-ray beam. American Mineralogist 98, 1187–1197.

Ogorodova, L., Melchakova, L., Kiseleva, I., Korytkova, E., 2009. Enthalpies of formation of minerals of serpentine group. Vestnik Otdelenia Nauk O Zemle RAN 1, 2–3.

O'Hanley, D.S., Wicks, F.J., 1995. Conditions of formation of lizardite, chrysotile and antigorite, Cassiar, British Columbia. The Canadian Mineralogist 33, 753–773.

Okazaki, K., Hirth, G., 2016. Dehydration of lawsonite could directly trigger earthquakes in subducting oceanic crust. Nature 530, 81–84.

Padrón-Navarta, J.A., Hermann, J., Garrido, C.J., López Sánchez-Vizcaíno, V., Gomez-Pugnaire, M.T., 2010. An experimental investigation of antigorite dehydration in natural silica-enriched serpentinite. Contributions to Mineralogy and Petrology 159, 25–42.

Padrón-Navarta, J.A., López Sánchez-Vizcaíno, V., Garrido, C.J., Gomez-Pugnaire, M.T., 2011. Metamorphic record of high-pressure dehydration of antigorite serpentinite to chlorite harzburgite in a subduction setting (Cerro del Almirez, Nevado–Filabride Complex, Southern Spain). Journal of Petrology 52, 2047–2078.

Padrón-Navarta, J.A., López Sánchez-Vizcaíno, V., Hermann, J., Connolly, J.a.D., Garrido, C.J., Gómez-Pugnaire, M.T., Marchesi, C., 2013. Tschermak's substitution in antigorite and consequences for phase relations and water liberation in high-grade serpentinites. Lithos 178, 186–196.

Peacock, S.M., 2001. Are the lower planes of double seismic zones caused by serpentine dehydration in subducting oceanic mantle? Geology 29, 299.

Perrillat, J., Daniel, I., Koga, K., Reynard, B., Cardon, H., Crichton, W., 2005. Kinetics of antigorite dehydration: a real-time X-ray diffraction study. Earth and Planetary Science Letters 236, 899–913.

Rebay, G., Spalla, M.I., Zanoni, D., 2012. Interaction of deformation and metamorphism during subduction and exhumation of hydrated oceanic mantle: insights from the Western Alps. Journal of Metamorphic Geology 30, 687–702.

Rüpke, L., Morgan, J.P., Hort, M., Connolly, J.A.D., 2004. Serpentine and the subduction zone water cycle. Earth and Planetary Science Letters 223, 17–34.

Scambelluri, M., Hoogerduijn Strating, E.H., Piccardo, G.B., Vissers, R.L.M., Rampone, E., 1991. Alpine olivine- and titanian clinohumite-bearing assemblages in the Erro–Tobbio peridotite (Voltri Massif, NW Italy). Journal of Metamorphic Geology 9, 79–91.

Scambelluri, M., Müntener, O., Ottolini, L., Pettke, T.T., Vannucci, R., 2004. The fate of B, Cl and Li in the subducted oceanic mantle and in the antigorite breakdown fluids. Earth and Planetary Science Letters 222, 217–234.

Schwartz, S., Guillot, S., Reynard, B., Lafay, R., Debret, B., Nicollet, C., Lanari, P., Auzende, A.L., 2013. Pressure–temperature estimates of the lizardite/antigorite transition in high pressure serpentinites. Lithos 178, 197–210.

Sillitoe, R., 2008. Major gold deposits and belts of the North and South American Cordillera: distribution, tectonomagmatic settings, and metallogenic considerations. Economic Geology 103, 663–687.

Spandler, C., Pirard, C., 2013. Element recycling from subducting slabs to arc crust: a review. Lithos 170–171, 208–223.

Stern, R.J., 2002. Subduction zones. Reviews of Geophysics 40, 1012.

Stern, R.J., Fouch, M.J., Klemperer, S.L., 2003. An overview of the Izu–Bonin–Mariana subduction factory. Inside the subduction factory. Geophysical Monograph Series 138, 175–222.

Stern, R.J., Kohut, E., Bloomer, S.H., Leybourne, M., Fouch, M., Vervoort, J., 2006. Subduction factory processes beneath the Guguan cross-chain, Mariana Arc: no role for sediments, are serpentinites important? Contributions to Mineralogy and Petrology 151, 202–221.

Syracuse, E.M., van Keken, P.E., Abers, G.A., 2010. The global range of subduction zone thermal models. Physics of the Earth and Planetary Interiors 183, 73–90.

Trommsdorff, V., Evans, B.W., 1972. Progressive metamorphism of antigorite schist in the Bergell tonalite aureole (Italy). American Journal of Science 272, 423–437.

Trommsdorff, V., Evans, B.W., 1974. Alpine metamorphism of peridotitic rocks. Schweizerische Mineralogische und Petrographische Mitteilungen 54, 333–354.

Trommsdorff, V., Lòpez Sànchez-Vizcaíno, V.L., Gómez-Pugnaire, M.T., Müntener, O., 1998. High pressure breakdown of antigorite to spinifex-textured olivine and orthopyroxene, SE Spain. Contributions to Mineralogy and Petrology 132, 139–148.

Truckenbrodt, J., Ziegenbein, D., Johannes, W., 1997. Redox conditions in piston cylinder apparatus: the different behavior of boron nitride and unfired pyrophyllite assemblies. American Mineralogist 82, 337–344.

Ulmer, P., Trommsdorff, V., 1995. Serpentine stability to mantle depths and subduction-related magmatism. Science 268, 858–861.

van Keken, P.E., Hacker, B.R., Syracuse, E.M., Abers, G.A., 2011. Subduction factory: 4. Depth-dependent flux of H_2O from subducting slabs worldwide. Journal of Geophysical Research: Solid Earth 116, B01401.

Wunder, B., Schreyer, W., 1997. Antigorite: high-pressure stability in the system. Lithos 41, 213–227.

Wunder, B., Wirth, R., Gottschalk, M., 2001. Antigorite: pressure and temperature dependence of polysomatism and water content. European Journal of Mineralogy 13, 485–495.

Chapter 3 Behavior of Fe and S during serpentinite dehydration

3.1. Introduction

Subduction zones are main global element cycling systems. The main element-transport agent in subduction zones is widely assumed to be an aqueous fluid released due to dehydration of oceanic lithosphere. The mobility and compatibility of fluid mobile elements strongly depends on P-T conditions and oxygen fugacity (fO_2) of the zone where H_2O is released. While pressure and temperature conditions of various depths in the slab and along the slab are well established, information about fO_2 of subduction zones is hardly provided. The fO_2 of subduction zones and upper mantle in general may vary by 6 orders of magnitude (Frost and McCammon, 2008). The understanding of fO_2 conditions in mantle and in subduction zones in particular includes investigation of slab lithologies and their relations between each other and a mantle wedge. The fact that mantle wedge peridotites are more oxidized than abyssal peridotites brings compelling evidence that oxidized subducted slab influences the redox state of the overlying mantle. Composition of the slab and speciation of elements capable for electron exchange, Fe and S in particular, are the principal parameters which are controlled by fO_2 in subduction zones. The evolution of Fe^{3+}/Fe_{total} ratio and S speciation in serpentinites may provide invaluable information about fO_2 in subduction zones.

In this chapter the behavior of Fe and S, main redox sensitive elements in serpentinites, and the redox capacity of different in composition serpentinites are investigated. Accurate X-ray absorption spectroscopy measurements, applied in this study, allows to quantify Fe^{3+}/Fe_{total} in all *ex-situ* and *in-situ* experimental products. The discussion about oxidizing properties of released fluids is provided. In addition, the influence of neighboring lithologies on reduction/oxidation of serpentinites and the role of serpentinites in mantle wedge oxidation is discussed.

Sulfur may be not only oxidized/reduced during serpentinite dehydration, but also can be volatilized. The speciation of volatile sulfur and understanding the mechanism of S release from subducting slab is important regarding the ability of sulfur complexes transport economically important elements to the mantle wedge and continental crust. Experimental results of this chapter demonstrate the speciation and loss of S during serpentinite dehydration and allow to speculate about analogous processes in natural settings.

3.2 Consequences of Fe and S reduction during serpentinite dehydration: experimental study

Margarita Merkulova[1*], Manuel Muñoz[1], Fabrice Brunet[1,2], Olivier Vidal[1,2], Keiko Hattori[3], Delphine Vantelon[4], Nicolas Trcera[4], Thomas Huthwelker[5]

[1]*Univ. Grenoble Alpes, ISTerre, F-38041 Grenoble, France*

[2]*CNRS, ISTerre, F-38041 Grenoble, France*

[3]*Department of Earth Sciences, University of Ottawa, Ottawa, Canada*

[4]*Synchrotron SOLEIL, l'Orme des Merisiers, BP 48, 91192 Gif-sur-Yvette, France*

[5]*Swiss Light Source, Paul Scherrer Institute, WLGA 212, 5232 Villigen –PSI, Switzerland*

An article to be submitted to Earth and Planetary Science Letters

Abstract

Dehydration of serpentinites produces a large amount of H_2O at elevated P-T conditions relevant for subduction settings. Our results identified that this aqueous fluid has a different redox capacity at intermediate and high P-T conditions due to different degree of Fe and S reduction.

The progress of the redox reactions during serpentinite dehydration was constrained by experimental approach. Experiments were performed in piston-cylinder apparatus. Three serpentinites compositions varied in terms of bulk Fe, Fe^{3+} and S contents were used. Intrinsic oxygen fugacity (fO_2) of the experimental setup was stable at fO_2 ~QFM-2, close to conditions of subduction settings. Experimental results demonstrated decrease of an initial high bulk Fe^{3+}/Fe_{total} ratios (0.9) of serpentinites down to ~0.2 in anhydrous high temperature assemblages through magnetite and Fe^{3+}-bearing antigorite breakdown. Serpentinites without magnetite are shown to drastically reduce their Fe^{3+}/Fe_{total} ratio at 650°C. Magnetite is occurred to be crucial for production of highly oxidized fluids and volatile sulfur species which can be transported from the subducting slab to the mantle wedge. The presence of pyrite, which transforms to pyrrhotite below 450°C, imposes a release of ¼ of initial sulfur, most-likely in H_2S form.

The experimental approach and detailed characterization of mineral assemblages and bulk Fe and S speciation allowed to estimate quantitatively the amount of released H_2O and redox potential of the released fluid at different steps of dehydration process. The extrapolation of experimental results to natural settings was accomplished with the help of thermodynamic modeling. We suggested that the presence of reduced species (e.g., sulfur and carbon) in subducting slab may drive elemental reduction in serpentinites. The demonstrated great oxidizing power of serpentinites could explain why mantle wedge peridotites and arc magmas are more oxidized compared to the upper mantle in other geological settings.

Key words: iron, sulfur, serpentinite, subduction zone, redox reaction, mantle oxidation

3.2.1 Introduction

Subduction of sediments, metabasalts and serpentinites comprising oceanic lithosphere is accompanied by a release of aqueous fluid, which is widely known to be a cause of partial melting in the mantle wedge, arc magma formation and generation of earthquakes. Dehydration of oceanic subducting slab is also an important process regarding global geochemical cycling of elements. It is well established that fore-arc mantle rocks and arc magmas inherit part of their geochemical composition from oceanic slab via the release of aqueous fluids from dehydrating subducting lithologies (e.g., Plank and Langmuir, 1998; Kerrick and Connoly, 2001a; Kessel et al., 2005). Each of the slab lithological components, i.e. sediments, metabasalts or serpentinites, releases fluids to a different extent and in different ranges of subduction depths. Sediments and metabasalts which compose the upper layers of the slab, dehydrate at depths of about 50-80 km (e.g., Syracuse et al., 2010) and mainly contribute to the hydration of fore-arc mantle, before the front of arc-magmas generation (Kerrick and Connolly, 2001a; Evans, 2012). Serpentinites, in their turn, dehydrate at greater depths, due to the successive breakdown of antigorite, the main high-pressure and high-temperature serpentine variety (Ulmer and Trommsdorff, 1995), and clinochlore (Bromiley and Pawley, 2003). Contribution of serpentinites to the slab water budget is important since serpentinites contain 8 wt.% of H_2O in average (Hacker, 2003) whereas metabasalts and sediments host about 3 wt.% (Kerrick and Connolly, 2001b) and 5 wt.% (Kerrick and Connolly, 2001a), respectively.

The dehydration of serpentinites causes the mobilization of FME (fluid-mobile elements) (Hattori and Guillot, 2007; Evans, 2012) potentially in their oxidized form (e.g., Evans, 2012; Debret et al., 2016). Release and migration of slab-derived fluids is potentially a way to modify the redox conditions occurring in the mantle wedge. Indeed, arc magmas were shown to be more oxidized than MORB and OIB (Parkinson and Arculus, 1999; Kelley and Cottrell, 2008). In addition, serpentinites forming in a mantle wedge were shown to be oxidized and enriched in FME (e.g., Hattori and Guillot, 2007) which could have been transported by aqueous fluids from the slab serpentinites to the mantle wedge.

The oxidizing/reducing capacity of a rock is determined by the presence of elements capable for electron exchange, such as Fe and S (Evans, 2012). Oceanic serpentinites are mainly produced by the hydrothermal alteration of the oceanic lithosphere which involves redox reactions. Globally, ferrous iron from oceanic mantle peridotites oxidizes while the alteration fluid is reduced (Evans, 2013). At slow spreading centers for example, olivine and pyroxene from abyssal peridotites are transformed into ferric serpentine (lizardite) and magnetite while H_2-bearing fluids are produced (Marcaillou et al., 2011). It can be anticipated that the process of dehydration of serpentinized peridotites will conversely produce oxidized fluids while ferric iron in serpentine and magnetite reduces back to ferrous in olivine-pyroxene assemblages. Actually, the Fe^{3+}/Fe_{tot} ratio of natural serpentinites is shown to decrease during serpentinite dehydration in a fossilized subduction setting from western Alps (Debret et al., 2014, 2015). As it was demonstrated by Debret et al. (2014), modal abundance of magnetite, together with bulk ferric iron, decreases progressively during serpentine breakdown. Consequently, we must consider iron reduction (Fe^{3+} 🎭 Fe^{2+}) as a half-reaction of oxidation with the potential of oxidizing the serpentinite environment.

Sulfur is another element capable for electron exchange in subducted rocks. A number of natural and thermodynamic modeling studies demonstrated a possible sulfur loss from deep parts of the slab. Release of sulfur is often proposed to be associated with redox reactions producing volatile (e.g., H_2S) or soluble sulfur-bearing species (e.g., SO_4^{2-}), as the reduction of sulfates to sulfides (Evans, 2014), the reduction of pyrite to pyrrhotite (Hall, 1986; Evans et al., 2015) or the oxidation of sulfides to sulfates (Debret et al., 2016). In serpentinites, sulfur is mostly hosted by sulfides (reference). The stability of sulfides at P-T-fO_2 conditions relevant to subduction zones is however mostly unknown and, hence, the observed transfer of sulfur from sulfide to S-bearing volatile species is still poorly understood (see Frost, 1985 for the sulfur behavior at shallow depths in subduction zones).

Serpentinites composition with respect to these two elements with variable oxidation states, iron and sulfur, is somehow variable. Total iron content in serpentinites can range from ~4 wt.% (Guillot et al., 2001) to ~12 wt.% (Li et al., 2004). A range of Fe^{3+}/Fe_{total} in serpentinites is found to be about 0.7-0.8 (Evans, 2008; Debret et al. 2014; 2015). Sulfur content in serpentinites changes from ~0.03 to ~1 wt.% (Alt et al., 2013). Consequently, different oceanic serpentinites may produce different types of fluids with potentially different redox potentials.

Based on our recent experimental results, reduction of iron in serpentinites begins at low temperatures, when magnetite destabilizes (Merkulova et al., 2016). Iron reduction proceeds up to 700°C, when Fe^{3+}-antigorite breakdown is completed. Sulfur reduction is likely to occur in narrower and lower temperature range compared to Fe (Frost, 1985; Hall, 1986).

Considering the slab being an open or closed system it may have major implications regarding processes of slab dehydration. According to several authors (e.g., Marchesi et al., 2013; Evans et al., 2014), the open system should be favored, meaning that the formed fluids leave the system, and do not impact the forthcoming mineral reactions, especially in terms of redox conditions. Based on this assumption, released fluids potentially escape to upper parts of the slab or ascent to the mantle wedge.

Hence, possible liberation of oxygen, due to potential Fe and S reduction in the open-system conditions of subduction, leads to the oxidation of upper layers of the slab and the mantle wedge, provides oxidized conditions for arc magma formation, and affects mobility of FME. However, no experimental work has been done in order to estimate quantitatively the effect of transition elements reduction on the release of oxidizing fluids.

The goal of the present work is to examine the redox behavior of iron and sulfur during the dehydration of simplified serpentinite compositions at the P-T conditions of subduction zones and fO_2 ~QFM. Our approach is to combine experimental results and thermochemical modeling in order to evaluate the reducing/oxidizing potential of the aqueous fluid released coincidentally. Three different starting compositions were chosen for experiments in the piston-cylinder apparatus (PC): 1) Fe^{3+}-bearing antigorite; 2) mixture of Fe^{3+}-antigorite and magnetite; 3) mixture of Fe^{3+}-antigorite and pyrite. Such a choice of starting materials allows to investigate the effect of magnetite and sulfide on the phase relationships of antigorite as a function of temperature at 2 GPa. We show that fO_2 conditions in our experiments are controlled by the PC cell assembly and, thus, thermodynamic modeling is used to extrapolate the experimental results to a range of naturally relevant redox conditions. Experimental products were characterized by X-ray diffraction, electron microprobe and X-ray absorption near edge structure (XANES) spectroscopy at both the Fe and S *K*-edges.

3.2.2 Methods

Three starting materials containing antigorite as major component were used: (1) 100 wt.% natural antigorite; (2) 95 wt.% natural antigorite + 5 wt.% magnetite (Magnox powder, 99% purity); (3) 97 wt.% natural antigorite + 3 wt.% natural pyrite. Experiments performed with these starting materials will be referred to as “set#1”, “set#2” or “set#3”, respectively. The same natural antigorite was used in all three starting mixtures, antigorite was collected at the Mont-Cenis massif, French Alps (Muñoz et al., 2013). Muñoz et al. (2013) determined a Fe^{3+}/Fe_{total} of 0.97 ratio for this antigorite sample which is relevant to the Fe^{3+}/Fe_{total} ratio encountered for lizardite in general and for lizardite from serpentinized peridotite in particular (e.g., Evans et al., 2012; Debret et al., 2014). Furthermore, this antigorite sample was selected because of its homogeneity and availability in sufficient quantity for experimental petrology. The relatively high amount of pyrite in set#3, which is 3 times higher than in natural serpentinites (Delacour et al., 2008), is aimed at performing sulfur elemental analysis and XANES measurements at S *K*-edge on the run products with sufficient resolution.

The major-element composition of starting materials was measured by X-ray fluorescence using (XRF) EDAX Eagle III spectrometer (ISTerre, Grenoble) and mineral abundance was determined using X-ray powder diffraction (XRPD). Minor amounts of andradite and clinochlore were observed in all starting mixtures, which account for the presence of CaO and Al_2O_3 (2.43 wt.% and 1.92 wt.%, respectively) in the starting antigorite. Bulk oxide compositions of the three starting materials are shown in Table 3.2-2 together with Fe^{3+}/Fe_{total} ratios obtained from XANES spectroscopy measurements at Fe *K*-edge.

Experiments were carried out in an end-loaded piston-cylinder apparatus at pressures from 1.5 to 2 GPa and temperatures from 450 to 900°C, with experimental durations ranging from 4.5 to 9 days. The detailed experimental procedure is described in Merkulova et al. (2016). The oxygen fugacity (fO_2) was imposed by the cell assembly and no fO_2 mineral buffer was added. The permeability of gold capsule to hydrogen, produced by the graphite furnace oxidation (Chou., 1986), imposes, at least transiently, a fO_2 between QFM and QFM-2 (e.g., Truckenbrodt et al., 1997). The capacity of our cell assembly to produce H_2 has been tested (see hereafter).

Table 3.2-1 summarizes the P-T conditions, durations, starting material and mineral assemblages observed in run products for three experimental sets.

Table 3.2-1. P-T conditions, durations, starting materials and mineral assemblage in run products for three sets of piston-cylinder experiments.

Run #	T, °C	P, GPa	Starting material	Duration, days	Solid run products
Set#1					
Atg_15	600	2	Atg 100%	7	Atg, Ol, Clc, Cpx
Atg_16	700	2	Atg 100%	5	Ol, Clc, Opx, Cpx
Atg_17	800	2	Atg 100%	6	Ol, Opx, Clc, Cpx
Atg_18	550	2	Atg 100%	7	Atg, Ol, Clc
Atg_19	650	2	Atg 100%	5	Atg, Ol, Clc, Cpx, Tr
Atg_20	850	2	Atg 100%	6	Ol, Cpx, Opx, Clc
Atg_22	875	2	Atg 100%	7	Ol, Cpx, Opx, Clc
Set#2					
Ant_Mgt5_01	600	2	Atg 95%, Mag 5%	9	Atg, Clc, Ol, Cpx
Ant_Mgt5_02	700	2	Atg 95%, Mag 5%	5	Ol, Opx, Tr, Clc
Ant_Mgt5_03	650	2	Atg 95%, Mag 5%	6	Atg, Ol, Cpx, Clc, Adr
Ant_Mgt5_06	750	2	Atg 95%, Mag 5%	4.5	Ol, Opx, Clc, Cpx
Ant_Mgt5_07	800	2	Atg 95%, Mag 5%	4.5	Ol, Opx, Clc, CPx
Ant_Mgt5_08	675	2	Atg 95%, Mag 5%	4.5	Atg, Ol, Clc, Tr, Cpx
Ant_Mgt5_09	725	2	Atg 95%, Mag 5%	4.5	Ol, Opx, Clc, Cpx
Ant_Mgt5_11	850	2	Atg 95%, Mag 5%	4.5	Ol, Opx, Prp
Ant_Mgt5_12	550	2	Atg 95%, Mag 5%	5	Atg, Clc, Ol
Set#3					
Atg_Py_15	550	2	Atg 98.5%, Py 1.5%	4.5	Atg, Clc, Po
Atg_Py_16	700	2	Atg 98.5%, Py 1.5%	5	Atg, Tr, Clc, Ol, Cpx Po
Atg_Py_17	850	2	Atg 98.5%, Py 1.5%	6	Ol, Opx, Cpx, Clc, Po
Atg_Py_18	450	1.5	Atg 98.5%, Py 1.5%	8	Atg, Ol, Cpx, Clc, Py, Po
Atg_Py_19	600	2	Atg 98.5%, Py 1.5%	6	Atg, Ol, Cpx, Clc, Po
Atg_Pyt_20	900	2	Atg 98.5%, Py 1.5%	6	Fo, Opx, Cpx, Po, Prp

After each run, the recovered capsule was pierced to check whether the water produced during mineral reactions, if any, had not escaped in the course of the experiment. “Rotten egg” smell was sensed after capsules of set#3 experiments were pierced, characterizing the presence of H_2S gas.

One third of the recovered powder sample was crushed in an agate mortar for XRPD characterization. Another third of the sample was mounted in epoxy and polished for electron probe micro-analysis (EPMA) and scanning electron microscope (SEM) observations. The remaining part of the sample was finely crushed and prepared as a 5 mm diameter pellet for XANES spectroscopy measurements. Samples containing sulfide (set#2) were crushed in a glove bag filled with He/Ar gas to prevent oxidation of sulfides.

The methods of X-ray diffraction characterization of experimental products and electron probe micro-analysis (EPMA) of individual mineral phases performed at ISTerre (Grenoble, France) are identical to those described in Merkulova et al. (2016).

The phase abundances in each experimental product were estimated from mass balance calculations using the average individual mineral compositions measured by EPMA (Table 3.2-S1) and the bulk composition of starting materials (Table 3.2-2). Modal abundances were derived following the method described by Lamberg et al. (1997). Estimated deviations from average values are ± 1-20 %.

Table 3.2-2. Composition of starting materials for three experimental sets.

Oxide, wt%	Set#1	Set#2	Set#3
SiO_2	44.12	39.02	38.99
TiO_2	0.02	0.45	0.00
Al_2O_3	0.72	1.92	1.66
FeO	1.37	6.07	3.24
MgO	41.49	38.52	40.71
CaO	0.01	2.43	0.99
Cr_2O_3	0.00	0.16	0.16
NiO	0.00	0.04	0.00
H_2O	12.14	11.50	12.00
SO_3	0.00	0.00	2.20
Total	100.00	100.12	100.00
Fe^{3+}/Fe_{tot}	0.96	0.96	0.82

XANES analyses were performed at Phoenix beamline of SLS (Swiss Light Source) synchrotron and at LUCIA beamline of SOLEIL synchrotron (France). Experimental products from set#2 were analyzed at the Fe *K*-edge at the Phoenix beamline. Incident energy was scanned from 7050 eV to 7290 eV using Si(111) double-crystal monochromator. The spot size on the sample was 1.4 x 1.4 mm. XANES spectra were collected in fluorescence mode using a 1-element silicon-drifted diode (SDD) located at 90° from the incident X-ray beam direction.

XANES spectra of experimental products from set#1 and set#3 were collected at LUCIA beamline. Fe K-edge XANES spectra were acquired between 7050 and 7600 eV, using a Si(311) fixed-exit double-crystal monochromator, and the S K-edge XANES spectra were acquired between 2400 and 2600 eV using the same monochromator equipped with KTP(011) crystals. The beam size on the sample was ~1 mm in diameter. In order to prevent beam damage and possible changes in valence for iron and sulfur (i.e., photo-oxidation/reduction) during measurements, XANES spectra were collected in a primary vacuum chamber cooled at -70°C using a liquid nitrogen cryostat. Spectra were collected in fluorescence mode using 4-elements silicon drifted diode (SDD) located at 86° from the incident beam.

XANES spectra were normalized using the Athena software (Ravel and Newville, 2005). Quantitative bulk rock Fe^{3+}/Fe_{tot} was obtained from Fe-K pre-edge analysis, which includes baseline subtraction and fitting the pre-peak region of the spectra using a Matlab routine from the XasMap package (Muñoz at al., 2006; 2008). The Fe^{3+}/Fe_{tot} quantification was based on the pre-edge centroid energy calibration (see Wilke et al., 2001) using the following model phases: olivine, staurolite, andradite and sanidine (Muñoz et al., 2013).

The determination of sulfur concentration in starting material and 3 experimental products of the set#3 was performed at G.G. Hatch Lab (Ottawa, Canada). Detailed procedure of elemental analysis can be found in Operating Instructions vario EL (2005) and in supplementary material of this article.

3.2.3 Results

Mineral assemblages

Diffraction patterns (Fig. 3.2-S1) confirmed the starting materials mineralogical content along with minor clinochlore (Clc) and andradite (Adr). As the run temperature increases, the diffraction peaks of Atg decrease in intensity and disappear at 700°C in set#1 and #2 indicating complete breakdown of antigorite. Peaks of Atg are still present on diffraction pattern of 700°C experimental product of the set#3. The intensity of Clc reflections increases at 700°C and decreases at 850-900°C. Tremolite (Tr) peak is observed only at 700°C. XRD patterns of 450-700°C experimental products of all three sets demonstrate the growth of olivine (Ol), clinopyroxene (Cpx) and orthopyroxene (Opx). Assemblages observed for the experiments performed at the highest temperatures (875-900°C) are composed of Ol, Cpx, Opx and pyrope (Prp) according to XRPD.

Mineral chemistry

Mg# defined as Mg/(Mg+Fe), is observed to change significantly in the mineral products as a function of run temperature. Figures 3.2-1a, b and c show three plots of Mg# of mineral phases *vs.* temperature from the three sets of experiments. Two different temperature ranges are distinguished in each plot (Fig. 3.2-1a, b, c). In the lower temperature experiments (<700°C), Mg# of olivine increases whereas Mg# of clinopyroxene decreases. Note, that Mg# of antigorite in the set#2 also decreases similarly to Mg# of clinopyroxene. Such a reverse evolution of Mg# of olivine and clinopyroxene/antigorite can be explained by Fe-Mg exchange between coexisting minerals below 700°C (Merkulova et al., 2016). Minerals recovered from higher temperatures (>700°C) do not vary in composition and have nearly constant Mg#, 0.97 on average for Ol, Cpx, Opx, Clc and 0.88 for garnet (Grt) in set#1, 0.91 for Ol, Cpx, Opx, Clc and 0.78 for Grt in set#2 and between 0.91 (Grt) and 0.96 (Clc) in set#3.

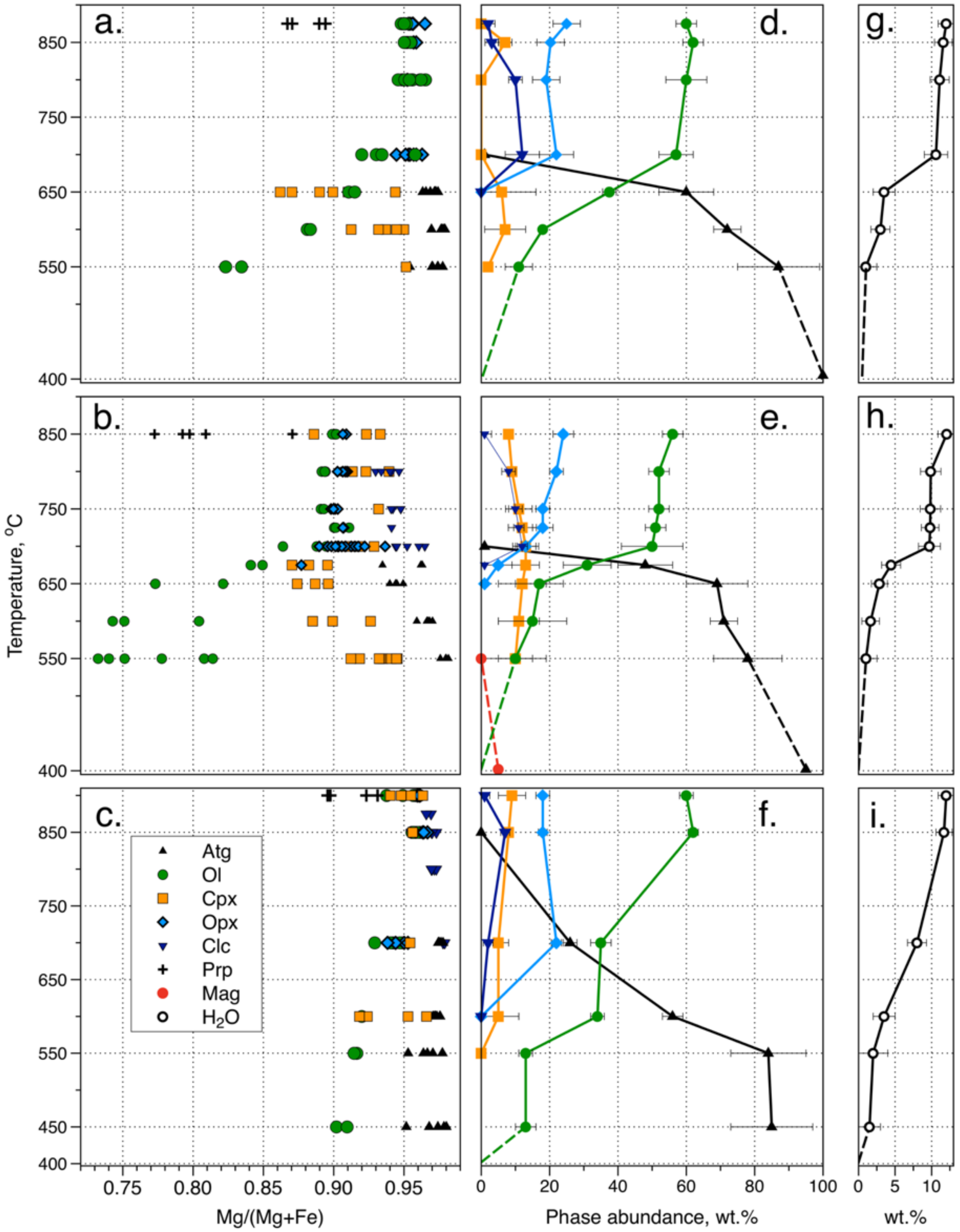

Figure 3.2-1. Mg# index of observed minerals in experimental products as a function of temperature of the experimental a) set#1, b) set#2, c) set#3. Green circles indicate Mg# of olivine, black triangles –Mg# of antigorite, orange squares – Mg# of clinopyroxene, light blue diamonds – Mg# of orthopyroxene, blue triangles – Mg# of clinochlore, crosses – Mg# of garnet. Evolution of mineral phase abundances during dehydration at experimental d) set#1, e) set#2, f) set#3; Integrated amount of released water calculated by mass balance for g) set#1, h) set#2; i) set#3.

Mass balance calculations

The change of phase abundances in three experimental sets obtained from mass balance calculations is shown in Figures 3.2-1d, e, f as a function of run temperature.

Although minor clinochlore and andradite were detected by XRD in the starting materials, they were not accessible for EPMA analyses due to low amount and small grain size. Therefore, andradite and clinochlore were not considered to be present in starting material in mass balance calculations. Pyrite and pyrrhotite were not measured by EPMA and, thus, their abundances were not calculated.

Figure 3.2-1d, e, f, g, h and i show the calculated mineral abundances and the amount of aqueous fluid liberated by the experimental charge. Antigorite abundance is shown to decrease from 95-100 wt.% at ambient temperature to about 60 wt.% at 600-650°C in the three experimental sets. Antigorite disappears at 700°C in set#1 and #2; however, it is still present at 700°C in set#3 where it amounts to 26 wt.% before vanishing at higher temperature. Magnetite was not detected in any of the experimental products of set#2 suggesting that it breaks down at temperature <550°C. Olivine progressively increases in abundance from about 10 wt.% at 450-550°C to ~60 wt.% at 700°C and above. Clinopyroxene appears at 550°C and reaches 10-12 wt.% at most (in set#2). Both orthopyroxene and clinochlore appear above 650°C. Opx remains present at the highest temperatures investigated here, i.e. 875-900°C, whereas clinochlore has a maximum abundance of 12 wt.% at 700°C in set#1 and set#2, set#3 and breaks down at 850 or 900°C depending on the set of experiments.

The water content of the starting materials, as initially stored in antigorite, is 12.14 wt.% (set#1), 11.50 wt.% (set#2) and 12 wt.% (set#3) (Table 3.2-2). With increasing temperature, water is liberated in the experimental charge as antigorite breaks down. Based on mineral modes, it can be shown that at 650°C already about 3 wt.% H_2O has been released by antigorite. At 700-800°C, antigorite has been consumed and most of the water/hydroxyl groups contained in mineral phases has been released as a fluid phase. Actually, depending on the experimental set, a few more wt.% H_2O are finally produced upon clinochlore thermal decomposition at 875-900°C.

Bulk Fe speciation

XANES (X-ray Absorption Near Edge Structure) spectra were measured at the Fe K-edge on experimental products from three sets of experiments (Figure 3.2-2 a, b and c). As a general observation, each series of XANES spectra show systematic shift towards lower energies with increasing temperature. In a first approximation, such a shift most likely traduces a reduction of the valence of iron, from ferric to ferrous.

Regarding set#1 and set#3 (Fig. 3.2-2a, c), the white line of the starting material spectrum shows a doublet with the main peak located at 7134 eV, indicated as a B feature on Fig. 3.2-2. While at 700°C and higher temperature the white line shifts towards lower energies (line A in Fig. 3.2-2a).

XANES spectra collected for the set#2 are summarized in Figure 3.2-2b. Energies of the set#2 XANES spectra are slightly lower than energies for set#1 and set#3 due to different analytical conditions on the two synchrotron beamlines. The starting material spectrum of the set#2 has a white line (feature B in Fig. 3.2-2b) at 7132.3 eV which shifts towards lower energies with increasing temperature. XANES spectrum of the set#2 run performed at 550°C exhibits an intermediate white line energy. For set#2 run products obtained at 600°C and above, white line of the corresponding spectra is further shifted to lower energies, as indicated by feature A on Fig. 3.2-2b.

Pre-peaks of Fe *K*-edge XANES spectra were subtracted and fitted (Figure 3.2-2 d, e, f). Pre-edge centroid energies were calibrated using model reference minerals and Fe^{3+}/Fe_{total} ratio was quantified. Bulk Fe^{3+}/Fe_{total} values are shown in Figures 3.2-3 as a function of run temperature.

The Fe^{3+}/Fe_{total} ratio of set#1 reduces from 0.97 in the starting material to 0.85 in the 550°C run product. Fe^{3+}/Fe_{total} sharply decreases to 0.42 in the 600°C sample and down to 0.17 and 0.18 in 700°C and 875°C run products, respectively.

Fe^{3+}/Fe_{total} ratio of the antigorite - magnetite starting mixture (i.e., set#2) equals to 0.96. It decreases drastically down to 0.42 in the 550°C run (set#2) and decreases further to reach values from 0.14 to 0.28 for runs performed at T > 600°C.

The set#3 starting material has the lowest Fe^{3+}/Fe_{total} ratio (0.82) due to the addition of pyrite. The sample produced at 450°C has still bulk Fe redox state (Fe^{3+}/Fe_{total} = 0.78) close to that of the starting material. With increasing the run temperature, the Fe^{3+}/Fe_{total} ratio gradually reduces to 0.62 (550°C), 0.25 (700°C), and 0.15 (900°C run).

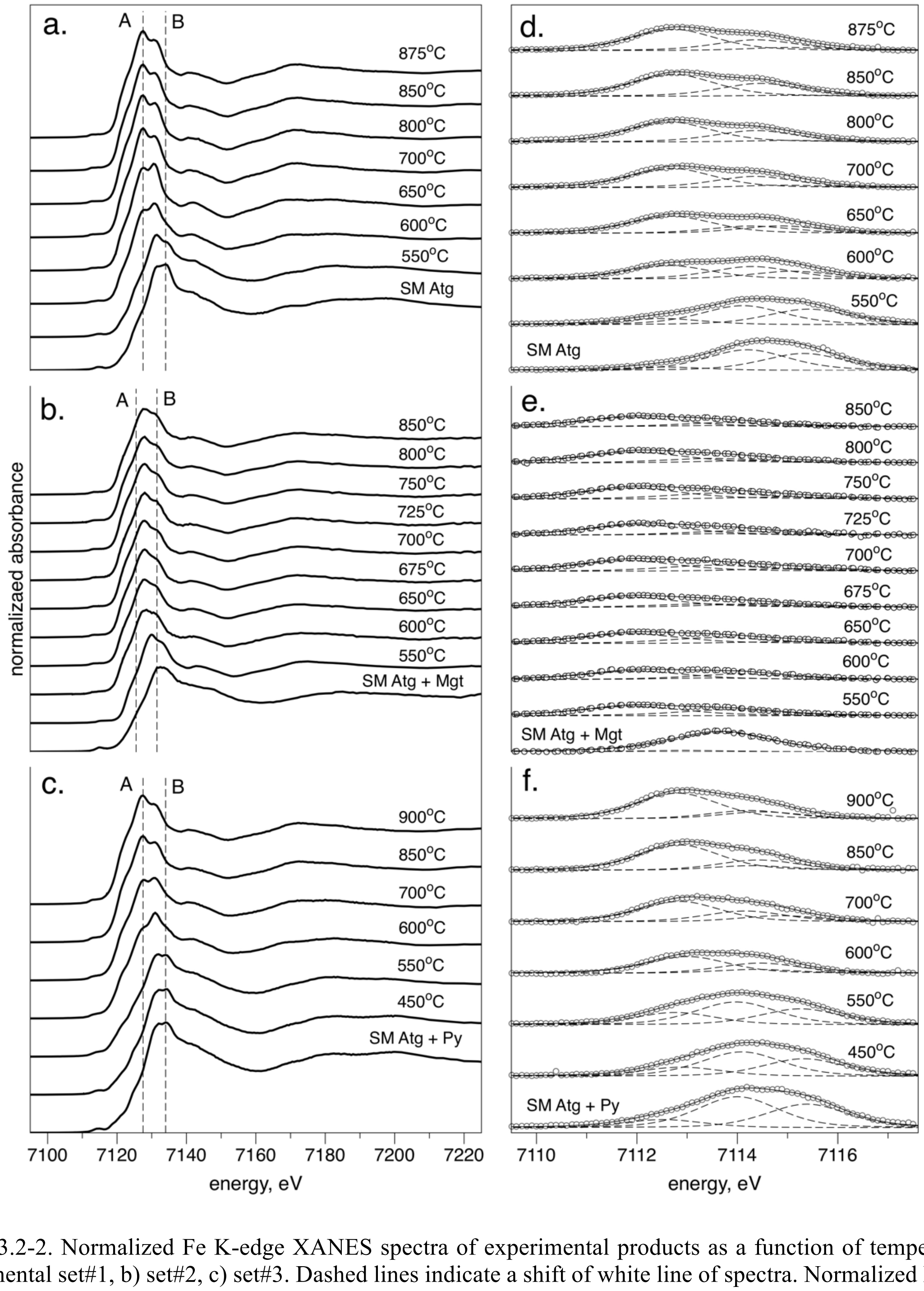

Figure 3.2-2. Normalized Fe K-edge XANES spectra of experimental products as a function of temperature. a) experimental set#1, b) set#2, c) set#3. Dashed lines indicate a shift of white line of spectra. Normalized Fe-K pre-edge spectra of the experimental products of d) set#1, e) set#2, f) set#3. Open circles represent pre-edge fits.

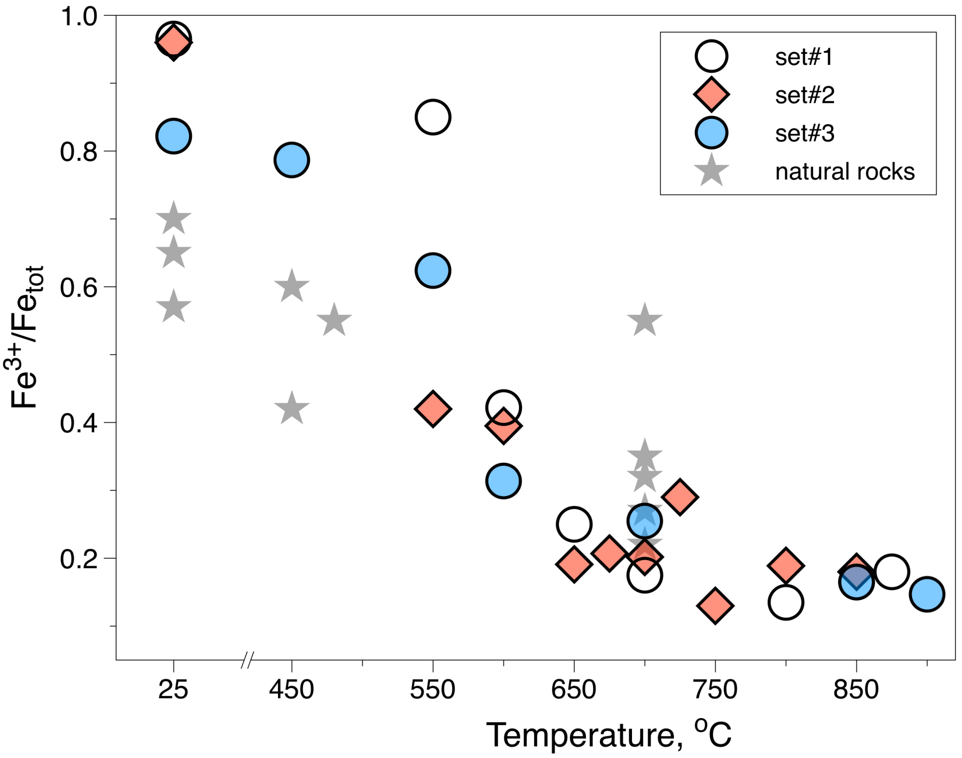

Figure 3.2-3. Evolution of Fe^{3+}/Fe_{total} as a function of temperature in experimental set#1 (white circles), set#2 (red diamonds), set#3 (blue circles) and natural serpentinites (grey stars). Values of Fe^{3+}/Fe_{total} for natural serpentinites are taken from Debret et al., 2014 and 2015.

Bulk S speciation

The S K-edge XANES spectra of set#3 are shown in Figure 3.2-4 together with a spectrum of the starting material and a reference spectrum of pyrrhotite (FeS). The starting material spectrum shows a typical signature of pyrite, in which sulfur has a negative charge (S^-). The white line of the starting material spectrum is characterized by a sharp single peak located at 2471.1 eV (feature b on Fig. 3.2-4). Pyrrhotite reference spectrum displays an absorption edge located at lower energy, which is consistent with its formal oxidation state (S^{2-}). The white line of pyrrhotite spectrum is characterized by a wide peak located at 2469.5 eV (feature a, Fig. 3.2-4). A high-energy peak (feature c, Fig. 3.2-4) on a wide shoulder of the starting material spectrum is attributed to an iron sulfate phase, which was not detected by other analytical methods (XRD, EPMA). Hence, this Fe-sulfate is interpreted as a sample preparation artifact. Although the sample was crushed under anoxic conditions, part of the pyrite could have been oxidized in air after sample removal from a glove bag. Additionally, pyrite oxidation could occur under the X-ray beam during XANES acquisition.

The shape of the white line (a and b features in Fig. 3.2-4) is found to evolve between the starting material and the run product obtained at 550°C. The spectrum corresponding to the 450°C sample displays both a and b features which indicate the presence of both, pyrite (44 wt. %, LCF) and pyrrhotite (66 wt.%, LCF; Fig. 3.2-4).

The spectrum of the 550°C experimental product indicates that pyrrhotite is the only sulfur-bearing phase in this sample. Consequently, S K-edge XANES spectroscopy demonstrates a reduction of sulfur from S^- to S^{2-} between ambient conditions and 550°C/2 GPa with a transitional assemblage at 450°C/2 GPa, which contains both pyrite and pyrrhotite. In samples obtained at higher T (>550°C), pyrrhotite remains the only S-bearing mineral (Fig. 3.2-4). Thus, no further change in sulfur oxidation state (S^{2-}) is observed in the solid fraction of samples produced at temperatures above 550°C.

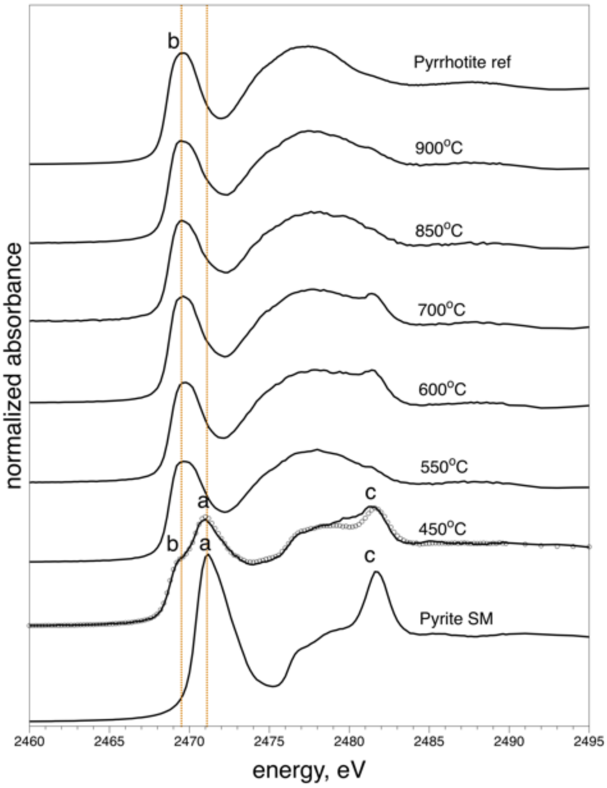

Figure 3.2-4. Evolution of S K-edge XANES spectra as a function of temperature in the experimental set#2. Orange dotted lines indicate a white line shift. Open circles represent fit of the 450°C spectrum obtained by linear combination. Features a, b and c are discussed in the text.

<u>*Bulk S concentration*</u>

Elemental analysis of S was performed on three set#3 samples and the corresponding starting material (Table 3.2-3). The starting material contains 1.65 wt.% total sulfur in the form of pyrite. In the set#3 sample run at 450°C where both pyrite and pyrrhotite are present (see section "*Bulk S speciation*"), total sulfur amounts to 1.21 wt.% and implying thus a loss of 0.35 mg of sulfur during the experiments. Combining this result with concentration of sulfur in the experimental product amount of pyrite corresponds to 0.44 wt.% and pyrrhotite to 1.04 wt.%. Set#3 samples produced at 850°C and 900°C contain 1.26 wt.% sulfur, which is close to that of the 450°C sample. Overall, about 25% of bulk initial sulfur content is transferred from sulfide to a volatile S-rich phase and lost during the serpentinite dehydration at 450°C or below.

Table 3.2-3. Wt.% of sulfur, moles of pyrite, pyrrhotite and O_2 per kg of solid rock calculated based on S reduction.

Experiment	**T, °C**	**S, wt.%**	**FeS_2, moles/kg**	**FeS, moles/kg**	**H_2S moles/kg**	**O_2 Reaction (3.2-2), moles/kg**	**O_2 Reaction (3.2-3), moles/kg**	**O_2 total, moles/kg**
Atg_Py SM	25	1.65	1.03	0	0	0	0	0
Atg_Py_18	450	1.21	0.33	0.2	0.28	4.24	0.14	4.38
Atg_Py_17	850	1.26	0	0.39	0	3.12	0	3.12
Atg_Py_20	900	1.26	0	0.39	0	0	0	0

Oxygen transfer in the RedOx reactions

Based on the observed bulk Fe^{3+} reduction, it can be considered that oxygen is produced according to the following simplified half reaction of reduction:

$$[Fe_2O_3]^{\text{mineral reactant}} = [FeO]^{\text{mineral product}} + O_2 \qquad (3.2\text{-}1)$$

This reaction is only virtual since a coupled oxidation half-reaction proceeds at the same time, here, the oxidation of the cell assembly (see section 3.2.4 Discussion). Based on Reaction (3.2-1), the Fe^{3+}/Fe_{total} ratio can therefore be translated into an amount of transferred oxygen as a function of run temperature (Fig. 3.2-5). About 2.7 moles of O_2 are released in total after complete dehydration of 1 kg of our antigorite starting material, i.e., in set#1. Calculations based on results of set#2, which contained 5 wt.% magnetite in the starting material, show that total amount of transferred O_2 is 13.9 moles per kg of starting material (Fig. 3.2-5), which is almost 5 times more than in set#1 (Fig. 3.2-5). This difference is obviously due to the breakdown of magnetite (Fe^{3+}/Fe_{total} ratio of 2/3). The amount of oxygen transferred in set#3 experiments equals to 5.8 moles per kg of starting material (Fig. 3.2-5), i.e., 2.5 times less than for set#2.

Similarly, virtual oxygen production associated with S reduction was calculated from Reactions (3.2-2) and (3.2-3) based on the S content and the Py/Po ratio of the experimental products (Table 3.2-3 and Fig. 3.2-5). A total of 4.38 mole/kg of O_2 is potentially formed at 450°C and 3.12 mole/kg of O_2 formed at 550°C. Note, that higher S concentration in the set#3 compared to natural rocks should be taken into account when applying the results to natural settings, and thus the amount of produced oxygen by S reduction should be divided by 3.

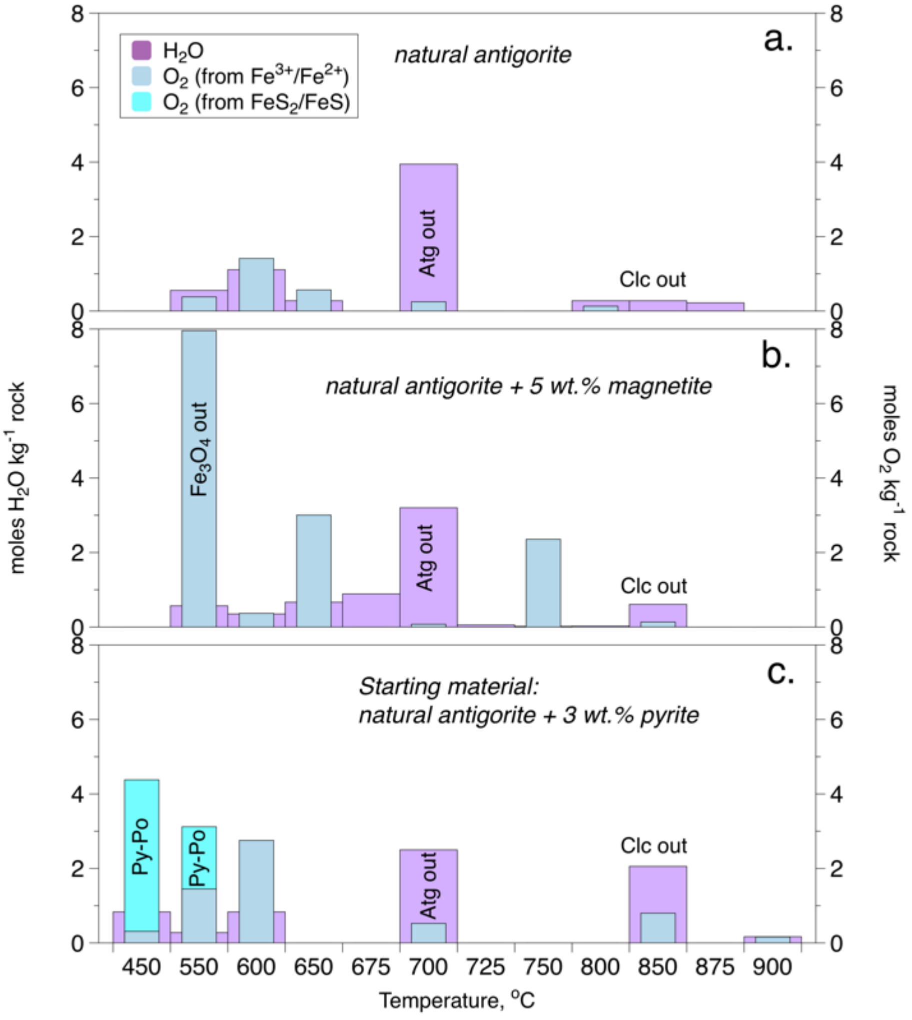

Figure 3.2-5. Calculated moles of released H_2O (purple) and O_2 (bright blue and mild blue) per kg of solid rock at a single T for a). experimental set#1, b). set#2, c). set#3. "Fe_3O_4 out" indicates temperature of magnetite-out reaction, "Atg out" – antigorite breakdown, "Clin out" – clinochlore breakdown, "Py-Po" – temperatures of pyrite-pyrrhotite transition.

3.2.4 Discussion

S reduction and mobility in experiment

Pyrite, contained in set#3, is found to transform into pyrrhotite between 450 and 550°C at 2 GPa. This mineral change occurs coincidently with olivine crystallization and Fe depletion in the coexisting silicates, mostly olivine (Fig. 3.2-1c). We therefore propose that pyrite reacted with antigorite to produce pyrrhotite and olivine with a Mg# lower than that of the starting antigorite. The corresponding water- and oxygen-producing reaction can be summarized as follows:

$$2(Mg_2Fe^{3+})(Fe^{3+}Si)O_5(OH)_4 + 4FeS_2 = 2Mg_2SiO_4 + 4H_2O + 3O_2 + 8FeS \quad (3.2\text{-}2)$$

Fe^{3+}-Atg pyrite forsterite water oxygen pyrrhotite

The process of Fe remobilization from silicate minerals to sulfides during metamorphism was described in a number of studies (e.g. Hall, 1986; Alonso-Azcarate et al., 1999) and thus, is likely to occur is subducting serpentinites. It should be noted that Reaction (2) does not imply a release of sulfur in a fluid phase, but results in Fe and S reduction between 450-550°C, which occur due to low fO_2 of the experimental setup.

On the other hand, sulfur elemental analysis of the solid products of set#3 runs indicated that about 25 % of the sulfur initially present in pyrite has been lost from the solid, i.e. volatilized, below or at 450°C during dehydration. Regarding the relatively low fO_2 of the present experiments, and the stability of pyrrhotite, reduced fluid S species, such as H_2S, are expected to be in equilibrium with pyrrhotite. This assumption is supported by the phase diagram of iron sulfides proposed by Frost (1985) and extended here to 800°C and 2 GPa (Fig. 3.2-S2). Consequently, following reaction may be responsible for S volatilization:

$$FeS_2 + H_2O = H_2S + FeS + 1/2O_2 \quad (3.2\text{-}3)$$

pyrite water hydrogen sulfide pyrrhotite oxygen

These experimental results can have important consequences for S behavior in natural settings. Natural rock studies (e.g., Alt et al., 2012, Evans et al., 2014) on sulfur isotopic composition showed that sulfur loss from subducting serpentinites takes place at conditions relevant for serpentine dehydration. These studies claim that sulfur is likely to be volatilized in oxidized form, sulfate or SO_2. According to our results, significant sulfur can be released in the form of H_2S (or related sulfide species) provided that fO_2 is below QFM. In other words, S release in serpentinites does not necessarily implies sulfur oxidation. However, in addition, dehydration experiments comprising magnetite and sulfides together are required to investigate the behavior and release of S in the presence of magnetite. Sulfur speciation in supercritical fluids from subduction zone is far from being understood. As an example, sulfur species like S^{3-} which was recently reported in synthetic high P-T fluids (Pokrovski and Dubrovinsky, 2011; Manning, 2011) to coexist with H_2S and sulfate complexes (Pokrovski and Dubessy, 2015) might actually be relevant S-bearing serpentinites in subduction zones.

Moreover, a release of O_2 from dehydrating S-bearing serpentinites is demonstrated in Reactions (3.2-2) and (3.2-3). In case of the present experimental conditions, oxygen is transferred from serpentinites to the fluid to form H_2O due to “unlimited” source of H_2 in the experimental setup. And this way, uptake of O_2 by present H_2 in the capsule drives reduction of S. However, natural environment case may not have such a source of H_2. Natural scenario will be discussed later.

Magnetite destabilization in experimental conditions

Due to its relatively high Fe^{3+} content, magnetite can promote oxidizing conditions through Fe^{3+} reduction into ferric iron and subsequent oxygen release (Figure 3.2-5). The stability of magnetite in the synthetic serpentinite, set#2, is displayed on a T-log(aO_2) pseudosection (Fig. 3.2-6) has been calculated with Theriak-Domino program using the thermodynamic dataset of Holland and Powell (1998), complemented with Fe-antigorite end-member (Merkulova et al., 2016). From Fig. 3.2-6, it can be seen that the disappearance of magnetite observed in set#2 can be a result of (1) fO_2 decrease, (2) temperature increase, or (3) both of them. Since magnetite is absent in set#2 experiments at 550°C, it can be inferred from the computed pseudosection (Fig. 3.2-6) that fO_2 should be at least higher than QFM-2. This value is in line with reported fO_2 in pressure cells with carbon heaters. The “unlimited” source of H_2 in the experimental setup imposes an fO_2~QFM-2 during the whole run duration and thus temperature should be the controlling factor for magnetite breakdown in our experiments.

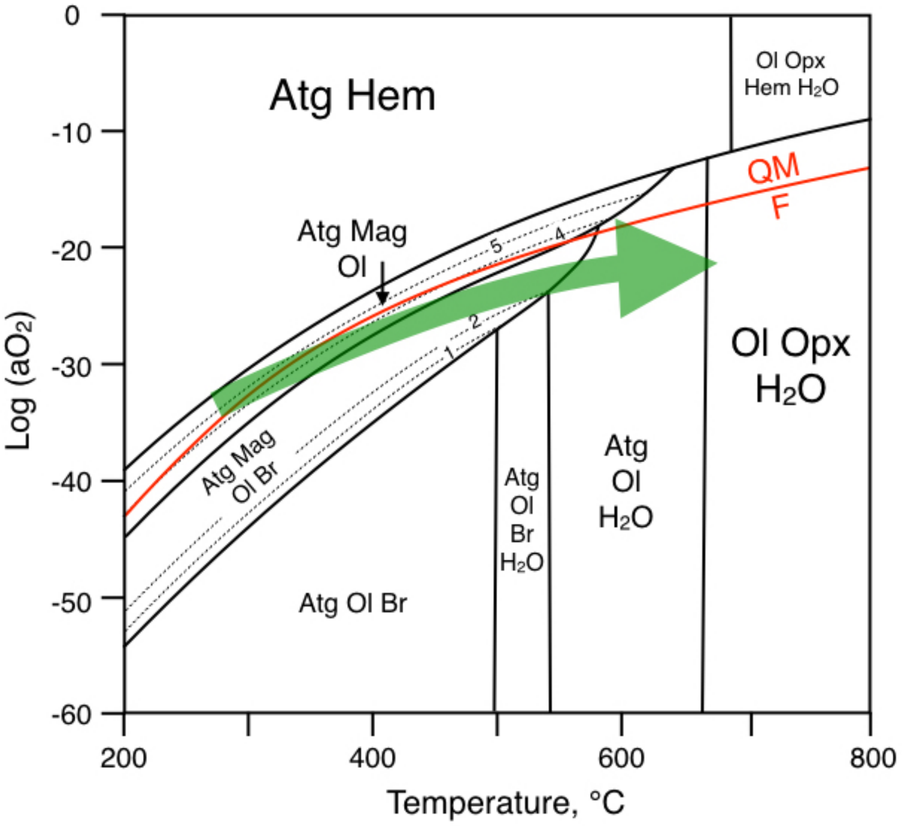

Figure 3.2-6. Log(aO_2)-T isobaric (P = 2 GPa) pseudosection for bulk composition corresponding to the starting material of the experimental set#2. Pseudosection computed with software Theriak-Domino (de Capitani and Petrakakis; 2010). Red line indicate the QFM buffer. Dashed lines are isopleths of magnetite wt.%. Green arrow indicates proposed evolution of natural serpentinites during dehydration. Atg – antigorite, Mag – magnetite, Hem – hematite, Ol – olivine, Br – brucite, Opx – orthopyrotxene.

Redox reactions

The redox magnetite-out reaction which consumes antigorite and produces olivine and an aqueous fluid can be summarized as follows:

$$6Mg_3Si_2O_5(OH)_4 + 2Fe_3O_4 = 12(Mg_{1.5}Fe_{0.5})SiO_4 + O_2 + 12H_2O \qquad (3.2\text{-}4)$$

antigorite magnetite olivine oxygen water

Since antigorite also contains Fe^{3+}, other reduction reactions must proceed in set#2:

$$6Fe_2Si_2O_5(OH)_4 + 4Fe_3O_4 = 5O_2 + 12H_2O + 12Fe_2SiO_4 \qquad (3.2\text{-}5)$$

Fe^{3+}-Atg Magnetite oxygen water fayalite

and

$2Fe_2Si_2O_5(OH)_4 = 4FeSiO_3 + O_2 + H_2O$ (3.2-6)

Fe^{3+}-Atg ferrosilite oxygen water

The lack of thermochemical data for Fe^{3+}-bearing antigorite precludes to model the respective contribution of (3.2-5) and (3.2-6) as well as the temperatures at which they will occur. As it was discussed previously, Reactions (3.2-2), (3.2-3), (3.2-4), (3.2-5) and (3.2-6) are most likely driven by the oxidation of the cell heater.

Transposed to subduction settings, these results suggest that as long as a redox couple is effective, the fluid produced below 550°C thanks to the breakdown of magnetite by Reaction (3.2-4), and possibly (3.2-5), has a great oxidation capacity (Fig. 3.2-5). The main event of aqueous fluid release will occur at higher T, between 675 and 700°C (Merkulova et al., 2016), i.e., deeper, wih a potentially lower oxidation capacity (Fig. 3.2-5). Applying these observations to nature, the higher fO_2 in natural settings (e.g., Frost and McCammon, 2008) should be kept in mind. Increase of fO_2 from QFM-2 to QFM+1 expands magnetite stability field by ~100°C. 100°C. Therefore, the temperature-range mismatch between magnetite reduction and antigorite breakdown may cause a release of chemically different fluids at shallow (lower T) and deep (higher T) parts of subduction (Fig. 3.2-7).

Comparison to natural data from the Western Alps

Our experimental results performed at the fO_2 imposed by the cell assembly show obvious similarity with some natural observations. Evolution of the Fe^{3+}/Fe_{total} ratio in serpentinites from the western Alps sampled along a metamorphic transect, was found to decrease from 0.5 and 0.8 (e.g., Evans, 2008; Debret et al., 2014) down to 0.2-0.4 at the highest grade where serpentinites are no longer stable (Debret et al., 2014; 2015). A very similar trend is observed in set#2 as a function of run temperature (Fig. 3.2-3).

Debret et al. (2014; 2015) linked this trend to a decrease in magnetite abundance from ~6 wt.% down to ~1 wt.% in serpentinites metamorphosed at 600°C. The persistence of magnetite observed by these authors may merely indicate differences in fO_2 between their samples and our experiments where magnetite has already fully disappeared at 550°C. As it is shown in Figure 3.2-6, in order to decrease the modal abundance of magnetite from 6 to 1 wt.% in serpentinite between 300 and 500°C, fO_2 of mineral assemblage should change from

~QFM+1 value to QFM-2. Magnetite-hematite reaction is taken as an upper bound to the *f*O_2 in metaserpentinites from subduction-collision zones since metamorphic hematite is barely described (Debret et al., 2014) in these rocks.

What controls fO_2 in subducted serpentinites?

If the reduction of the synthetic serpentinite of set#2 is driven by the cell assembly oxidation, what controls the *f*O_2 drop by ca. three orders of magnitude in subducted serpentinites from the Western Alps as inferred from published natural data?

The first hypothesis that can be considered is an internal redox equilibration at the serpentinte scale. In serpentinites, Alt et al. (2012) reported that magnetite coexists with pentlandite and pyrrhotite, i.e. two sulfides containing reduced S^{2-} ; at higher grade, beyond the antigorite stability field, they are no longer present and, instead, pyrite (S^{1-}), coexists with lower amount of magnetite. Moreover, Alt et al. (2013) demonstrated a sulfur loss in serpentinites during their dehydration occur in a form of sulfates. Thus, it could be argued that achievement of internal chemical equilibrium in subducted serpentinites operates by oxidation of primary sulfides into pyrite and sulfates coupled to ferric iron reduction by breakdown of both, magnetite and antigorite. Although, the stability of sulfates in the mantle conditions are not well constrained, few studies showed that sulfate is stable at *f*O_2 relative to QFM+2 (Mungall, 2002) and even higher, at ~QFM+5 (Fujii, 2015) at mantle P-T. This way, slab serpentinites should have higher *f*O_2 compared to that of for example serpentinites studied in Debret et al. (2014) (Fig. 3.2-6) in order to compensate Fe reduction by sulfate/SO_2 formation.

Simple calculations of pyrrhotite amount required to react with O_2, formed by magnetite breakdown (experimental set#2), in order to form sulfate, reveal that at least 4 wt.% sulfide should be present in serpentinites. Such a high S content has not been reported in natural serpentinites. Thus, only part of oxygen may be used to form sulfates with a proviso that *f*O_2 is high enough. And most probable S oxidation in this case occurs through pyrrhotite to pyrite reaction (e.g., Evans and Powell, 2015), which in turn do not require such a great source of O_2 as it provided by magnetite breakdown.

Combining experimental results with discussed above S oxidation and natural rock observation (Alt et al., 2012), first pyrite-to-pyrrhotite reduction may occur at T<450°C with a release of H_2S. Second, Fe reduction taking place at T>500C is balanced by pyrrhotite-to-pyrite reaction with a sulfate/SO_2 formation. Such a sequence suggests a narrow temperature window of pyrrhotite existence, and a change in fO_2 conditions from <QFM to >QFM. Ultimately, other reduced species, besides S, must balance/drive Fe reduction at T>500°C.

Similarly to what happened in our experiments, the oxidation of reduced carbon can potentially drive ferric Fe reduction. In the altered oceanic crust, carbon is mainly found in carbonates (Alt and Teagle, 2003; Alt et al., 2013), and thus cannot be oxidized. However, Hayes and Waldbauer (2006) demonstrated that oceanic sediments also carry organic carbon down to deep subduction. Their work showed that oceanic crust has a significant reducing power by means of reduced C species which requires reverse oxidizing power. Our experimental results demonstrate that Fe-bearing serpentinites can be a source of the oxidizing power. The input of organic carbon within oceanic sediment into subduction was estimated by Wallman (2001) based on average sediment composition (Plank and Langmuir, 1998), the flux of organic carbon equals to 0.45 moles per kg of sediment. Taking in account that 1 mole of O_2 is needed to oxidize 1 mole of C into CO_2, amount of reduced C in sediments is insufficient for consumption of O_2 produced by Fe reduction (Fig. 3.2-5).

Thus, natural serpentinites and overlying crust do not have enough large source of reduced species (e.g., H_2, S^{2-}, C^0, Fe^{2+}), the oxidation of that could drive decrease of bulk ferric Fe. Although, Fe reduction observed in natural settings is similar to that in the present experiments, it does not progress to the same degree. Following evidences justify the above mentioned statement.

First, initial Fe^{3+}/Fe_{total} in natural serpentinites is lower than in the starting material of the present experiments. Difference of ~0.2 between Fe^{3+}/Fe_{total} between experimental starting material and natural serpentinites (e.g., Debret et al., 2014) may reduce the redox capacity of the natural rock by ~30%. Second, the presence of Cr- and Ti-bearing magnetite (Trommsdorff, 1998) and high amount of Fe^{3+}-bearing chlorite in natural harzburgites explains higher Fe^{3+}/Fe_{total} in natural prograde metamorphic rocks in comparison with anhydrous experimental assemblages. Fe^{3+}/Fe_{total} of natural serpentinites and their dehydrated lithologies are superimposed with experimentally obtained values in Figure 3.2-3. Thus, the amount of oxygen "released" during dehydration of serpentinites in natural settings is about half less than in experiment. Consequently, 1 wt.% of reduced sulfides (pentlandite, pyrrhotite) in natural serpentinites (Delacour et al., 2008), 2.5 wt.% of sulfides in neighbored metabasalts (Jego and Dasgupta, 2013) and ~0.3 wt.% of organic C in sediments (Plank and Langmuir, 1998) can be enough to be oxidized by Fe reduction in magnetite-bearing serpentinites.

Changing to a large-scale view, reduction of Fe may transfer redox potential from subducting slab to the mantle wedge. Comparison of redox state in mantle wedge peridotite and in peridotites from other tectonic settings can illustrate such a transport. Average ridge peridotite records fO_2 of QFM-1 (e.g. Lopez et al., 2012), whereas mantle wedge peridotites are more oxidized, with fO_2 ranging from QFM to QFM+1 (Frost and McCammon, 2008). Fluids rising from subducting slab can be responsible for oxidation of overlying mantle. The experimental results demonstrate that aqueous fluid formed by slab dehydration is released continuously along 400°C range, however the redox power of the fluid formed at 450°C and 900°C is different (Fig. 3.2-5). Figure 3.2-7 schematically illustrates the distribution of the fluid with a different redox power along a part of subduction zone. A portion of aqueous fluid released below 650°C has a high oxidizing potential and may carry oxidized FME. The largest portion of the aqueous fluid is liberated at deeper parts of the slab corresponding to 700°C isotherm. If one assumes that all oxygen, formed by Fe reduction, “transfers” from serpentinite to the fluid, this aqueous fluid may be 15 times less oxidized relative to the low-temperature fluid. Last part of H_2O, released by chlorite breakdown, is intermediate in terms of redox potential. To summarize, such a differentiated composition and distribution of the fluid flow rising from dehydrating serpentinites along the slab may result in (1) a different degree of mantle wedge hydration, (2) different composition and redox state of mantle wedge rocks and magmas forming above the dehydration front at shallow and deep parts of a fore-arc mantle.

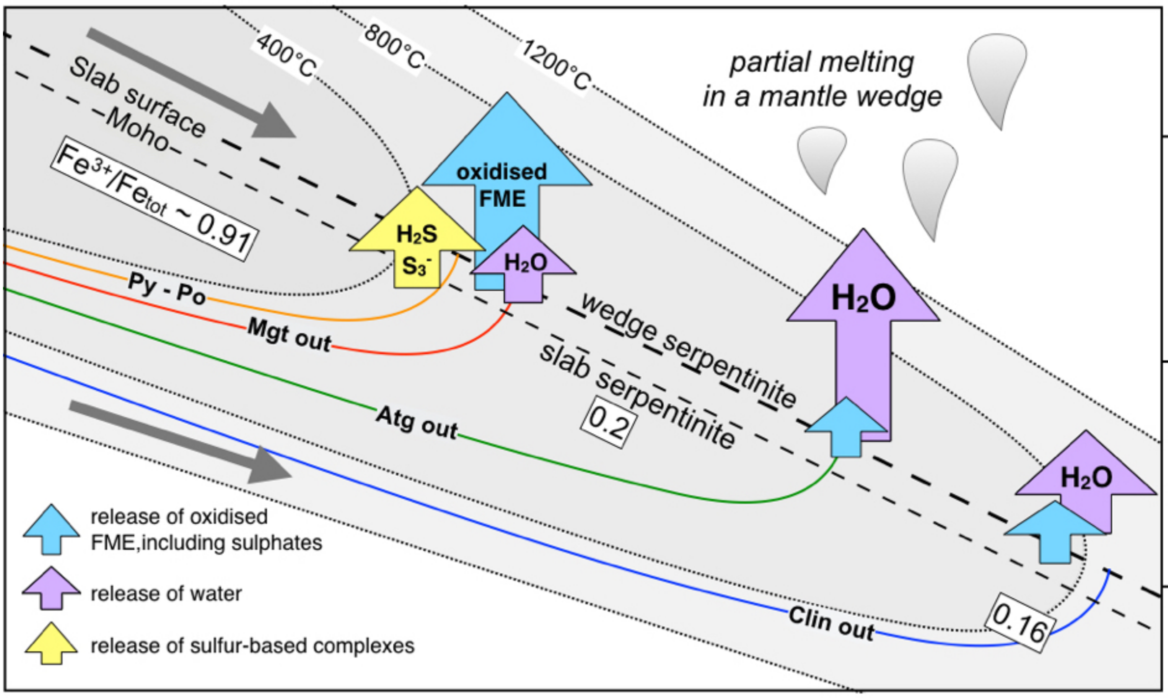

Figure 3.2-7. Schematic diagram summarizing processes in subduction zone: break down of mineral phases (color lines), movements of the slab and in a mantle wedge (grey arrows), reduction of Fe, release of fluids (thick blue, purple and yellow arrows), partial melting. The depths are taken from the Syracuse et al. (2010) for the average "hot" subduction.

3.2.5 Conclusions

Serpentinites have a great oxidizing power that stored in Fe^{3+}-bearing minerals, Fe^{3+}-antigorite and magnetite. The experimental results showed the importance of magnetite in serpentinites, since magnetite increases oxidizing capacity of the rock by 15 times. Redox balance can be accomplished by a transfer of electrons from serpentinites to reduced species, mainly S and C, present in subducting slab. The present study demonstrated that oxygen fugacity is one of the most important parameters which controls behavior of Fe and S in dehydrating serpentinites. Temperature of complete magnetite decomposition, i.e. Fe reduction, may vary by 100°C depending on fO_2. Moreover, at high fO_2, >QFM, S can be oxidized to sulfate/SO_2, whereas, at fO_2 <QFM pyrite, present in serpentinites, may increase oxidizing capacity of the oceanic lithosphere and can be reduced to pyrrhotite accompanying by a release of H_2S at $T<450°C$.

Redox reaction occurred in subducting slab are not only fO_2 dependent, but also P-T-dependent. The extrapolation of experimental results to subduction zone settings demonstrates, that at constant fO_2, fluid released at depths ~70 km within flat subduction geotherm is about 15 times more oxidized in comparison with the fluid formed at deeper levels (~120 km) of subduction. Such a different composition of released aqueous fluid along subducting slab may explain a wide range of redox conditions from fore-arc to deep mantle.

3.3. Reduction of Fe during serpentine dehydration: *in-situ* observations

3.3.1 HDAC experiments

Results

In-situ experiments and observations in hydrothermal diamond-anvil cell (HDAC) were performed at BM23 beamline at ESRF (Grenoble, France). The main goal of the experiments was to monitor Fe speciation change in mineral phases during serpentine dehydration. Two types of serpentine minerals were used as a starting material: antigorite and lizardite. Five experimental runs were completed. For clarity purposes, experimental runs shown in this chapter will be called run#1, run#2, run#3, run#3, run#4, run#5. Table 3.3.-1 summarizes temperature and starting materials for the 5 runs. Water was loaded to the sample chamber together with samples in run#1 and #2. However, because of the poor optical visibility of the sample chamber during the experiments, air bubble could not be monitored and pressure could not be defined. Run#3, #4 and #5 were loaded without water. Experiments in HDAC were assumed to be performed at pressures between 0 and ~ 6 GPa (the upper pressure stability limit of serpentine minerals). It should be noted that the temperatures of reported experiments are estimated based on temperature calibration (Chapter 1.1.2), but due to technical problems and weak electrical connections, real temperature in the sample chamber could be different from the calculated one. Therefore, the reported temperatures are necessarily overestimated and it should be taken in account that real temperatures can be 100 to 300°C less than the ones indicated, especially in run#3, #4 and #5.

In-situ measurements in HDAC consisted of XANES spectra acquisition at Fe *K*-edge and X-ray diffraction. Low quality of the spectra, caused by diluted amount of Fe in sample and by numerous Bragg peaks/glitches occurring from diamond anvils, limited the quantification of Fe^{3+}/Fe_{tot}. Thus, XANES spectra were analyzed qualitatively by describing shift of the white line of the spectra and changes in spectral shape.

Table 3.3.-1. Temperature ranges and mineral composition of starting material for the experimental runs performed in HDAC.

Run#	T (°C)	Starting material
run#1	25-500	atg grain, H_2O
run#2	25-600	atg powder, H_2O
run#3	25-1000	crashed crystal of atg
run#4	25-800	lizardite M1 grain
run#5	25-650	lizardite+ antigorite M16 grains

Experimental Run#1

Starting material used for the run#1 is composed of the natural antigorite from Mont Cenis massif (French Alpes, Munoz et al., 2013). The antigorite contains 1.37 wt.% of total FeO, most of which is Fe_2O_3. Fe^{3+}/Fe_{total} ratio of this antigorite is 0.96 based on previous XANES measurements (Munoz et al., 2013). Figures 3.3.-1a and b demonstrate XRD patterns and XANES spectra at Fe *K*-edge obtained for the starting material and experimental products of run#1. The quenched sample could not be analyzed because gold foil, used to isolate sample from Re gasket, filled the sample chamber when the sample was quenched. The experiment was carried out in 10 hours, temperature of 400°C was reached in 6 hours after the experiments was started.

XRD pattern of the starting material displays main peaks of antigorite and low-intensity peaks of andradite, which indicates that andradite is present in the starting material in trace amount. As temperature of experiment increases, double peak of antigorite at 7° 2θ-angle decreases in intensity and 12°-2θ peak become the most intense. Different relative intensities of antigorite peaks demonstrate changes in crystal orientation, which occur because of the pressurizing. XRD patterns at 400°C and 500°C show three peaks of olivine at around 22°-2θ. Intensity of all antigorite peaks decreased at 500°C, which may indicate a decrease in antigorite abundance. Andradite is always present at all temperatures.

Fig. 3.3.-1b comprises XANES spectra at Fe *K*-edge. Spectra show no change between 25 and 400°C, and all of them match the Fe spectral signature in starting antigorite. The white line of the spectrum at 500°C shifted towards low energies indicating a slight reduction of Fe.

Experimental Run#2

The starting material used for run#2 is the same natural antigorite as for run#1. XRD pattern of starting material at 25°C shows peaks of antigorite and clinochlore (Fig. 3.3.-1c and d). Clinochlore is present in the sample due to natural origin of antigorite and thus, minor phases like clinochlore and andradite may be present. During the heating up to 600°C the mineral assemblage did not change, and antigorite and clinochlore remain the only phases identified at 600°C as well as after quenching. In parallel, XANES spectra demonstrate a shift of the white line towards lower energies, representing a reduction of Fe in the assemblage between 25°C and 500°C. XANES spectrum was not acquired at 600°C due to the failure of the heater after XRD pattern acquisition.

Experimental Run#3

Figures 3.3.-1 e and f display a sequence of diffraction and XANES spectra obtained between 25°C and 1000°C. As it was already mentioned, due to experimental issues, temperature was overestimated during the run and temperature indicated in Figures 3.3.-1e and f is about 200°C higher than real temperature in the sample chamber. The starting material used in the run#3 consisted of natural antigorite, same as in run#1 and run#2, including minor clinochlore amounts. The sample was placed in the sample chamber as a few single grains. Intensities of main diffraction peaks of antigorite change as temperature increase, most likely due to changes in preferential orientation of single crystals. Clinochlore is systematically present at all temperatures. Diffraction pattern of the quenched sample shows peaks of antigorite and a very intense peak of andradite (18.1°-2θ), which begin to be visible at 400°C. According to bulk powder XRD of the starting material (Fig. 1.1.-2) andradite could be already present in the sample of the run#3. Such an intense andradite peak on a quenched sample XRD pattern (Fig. 3.3.-1e) could appear because of the sample movement due to temperature decrease and therefore, part of the sample with andradite grain could be under the X-ray beam. XANES spectra do not show any significant change between 25°C and 1000°C. XANES spectrum of the quenched sample is identical to the one of the starting material.

Experimental Run#4

Run#4 shows the most interesting results among the five experimental runs. Figure 3.3.-1 demonstrates XRD patterns and XANES spectra at Fe *K*-edge of sample at temperatures between 25°C and 800°C and a quenched material. The temperature overestimation is applied to run#4, consequently, real temperatures are ~200°C less than indicated. The starting material used for the run#4 consisted of lizardite single crystal (Table 3.3.-2). XRD pattern acquired at 25°C demonstrates typical lizardite diffraction peaks. A single peak positioned at 7.5°-2θ together with a peak at 14°-2θ characterizes lizardite diffraction pattern. At 400°C another peak appears on the right from the 7.5°-2θ peak. Such a doublet indicates the presence of antigorite in the sample (Mellini, 1982; Capitani and Mellini, 2004). As temperature increases, the doublet become more distinct. XRD results clearly evidence the lizardite-to-antigorite replacement. However, pattern of the quenched sample shows typical Bragg peaks of lizardite, with no evidence for the presence of antigorite. XANES spectra display a slight shift of the white line from 7133.4 eV to 7131.4 eV at temperatures relevant to antigorite appearance. A shift of the white line of the spectra may indicate a reduction of Fe.

Experimental Run#5

Starting material for the run#5 is represented by a mixture of antigorite and lizardite grains (Table 3.3.-2). No changes in XRD and XANES spectra were observed during the run between 25°C and 650°C. Spectra of the quenched sample match spectra of the starting material. Thus, no mineral reaction and no speciation change occurred during the experiment.

Table 3.3.-2. Major-oxide composition of starting material samples used in HDAC *in-situ* experiments.

	Atg Mt Cenis	**M1 Liz**	**M16 Liz+Atg**
SiO_2	44.12	43.39	41.70
TiO_2	0.02	0.02	0.02
Al_2O_3	0.72	0.38	0.28
FeO	1.37	0.90	2.14
MgO	41.49	42.64	42.34
CaO	0.01	0.08	0.01
Cr_2O_3	0.00	0.00	0.03
NiO	0.00	0.00	0.00
(OH)	12.14	12.64	13.55
Total	100.00	100.00	100.00
Fe^{3+}/Fe_{tot}	0.96	0.96	0.94

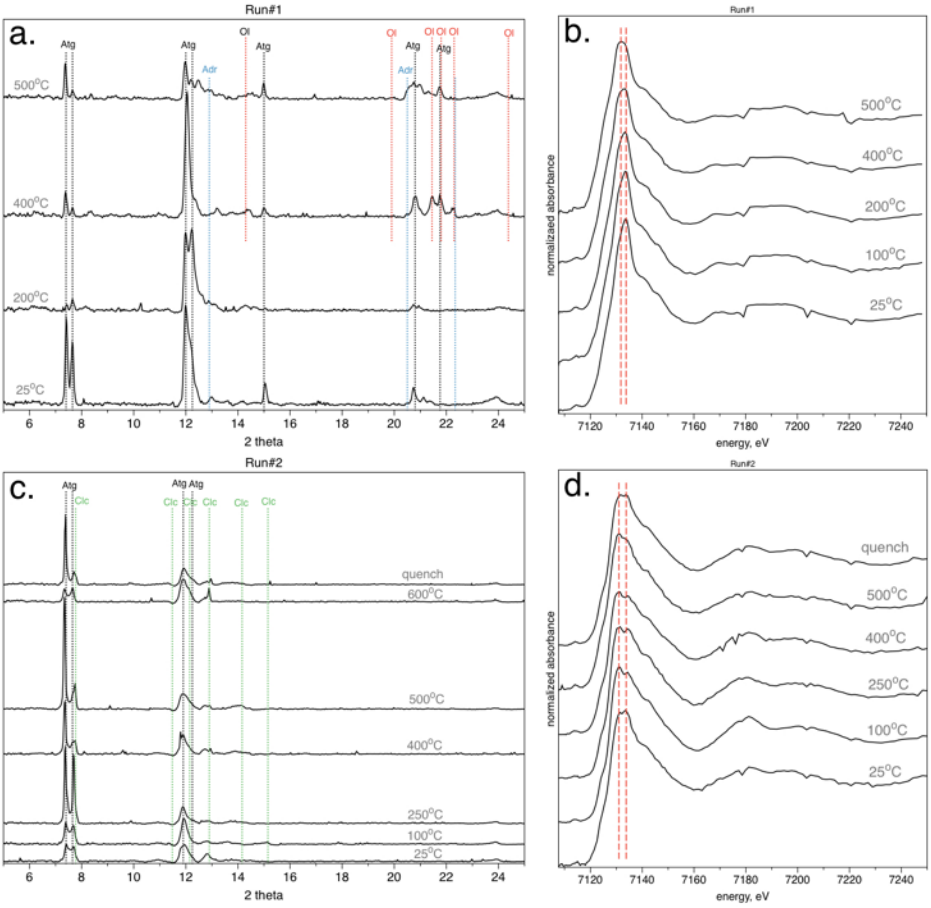

Fig. 3.3.-1. Description is on the next page.

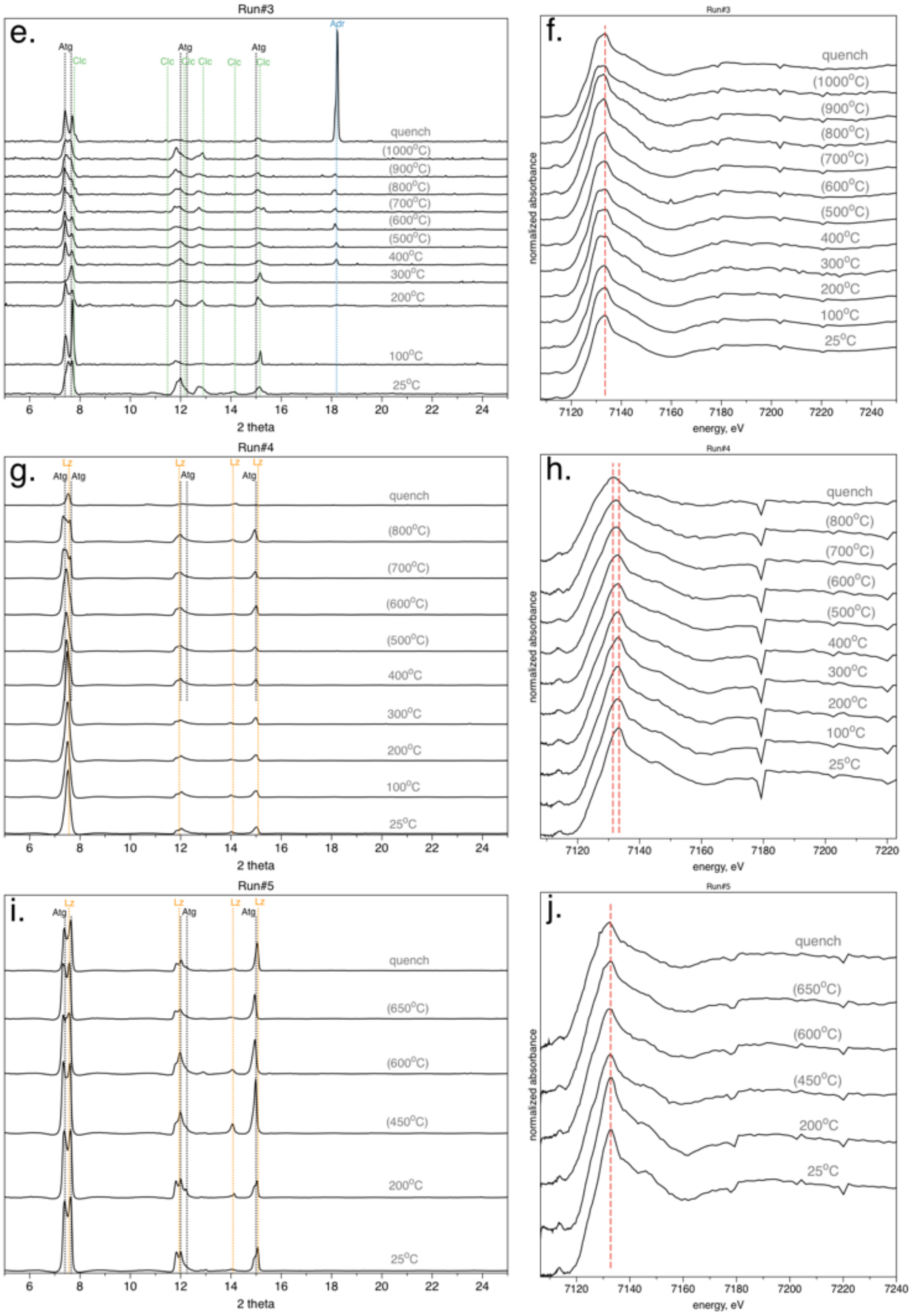

Fig. 3.3.-1. a., c., e., g. and i. XRD patterns as temperature series for run#1, #2, #3, #4 and #5 respectively. Dashed lines indicate diffraction peaks of mineral phases. Mineral name abbreviations: Atg – antigorite, Clc – clinochlore, Adr – andradite, Ol – olivine, Lz – lizardite. b., d., f., h. and j. XANEs spectra at Fe K-edge as temperature series for run#1, #2, #3, #4 and #5 respectively. Red dashed lines indicate energies of white lines of the spectra. Numbers in parenthesis – overestimated experimental temperatures.

Discussion

The reported results of five *in-situ* XRD and XANES experiments performed using HDAC show almost no change in mineralogy and Fe oxidation state from ambient condition to high temperature. However, two experiments, run#1 and run#4, are considered to be successful. The results of experimental run#1 reveal the crystallization of olivine at 400°C, which indicates destabilization of antigorite, needed for olivine formation, and release of H_2O. Initial water, presented in the sample chamber, does not influence thermal stability of antigorite compared to dry starting material assemblages (Chapter 3.2). The formation of olivine in the run#1 is associated with a reduction of Fe, as evidenced by XANES measurements at Fe *K*-edge. Thus, antigorite composition is likely to influence the composition of the newly formed olivine. Moreover, Run#1 demonstrated that olivine crystallization is a relatively fast process, since olivine formed in 8 hours after the experiment had been started. This way, the rate of olivine nucleation is not a limitation factor for one-day *in-situ* experiments.

One of the goals of these experimental runs was to test the influence of the starting material grain size on kinetics of antigorite breakdown. Although sample in run#2 comprised antigorite powder, and consequently smaller grain size, no mineral reaction was observed. But the absence of reaction could result in some external reasons such as the deviation of heaters electric power from the calibration due to changes in resistivity, and therefore overestimation of temperature values.

Run#4 demonstrates the most interesting results showing the crystallization of antigorite from lizardite. Antigorite formed at 400°C become more abundant at higher temperatures, however it disappears in the quenched sample. The absence of antigorite after quenching may result either from metastability of antigorite or movement of the sample during quenching and therefore change of the X-ray position on the sample. The replacement of lizardite by antigorite is accompanied with slight changes in Fe speciation, possibly a slight reduction from ferric to ferrous iron. Change in Fe speciation implies change in position of Fe in the lattice, and therefore would not support the assumption to consider lizardite and antigorite as two polymorphs.

The change in Fe speciation, in particular change from Fe^{3+} to Fe^{2+}, demands the formation of other phases or ions, such as O_2. The actual reaction responsible for lizardite-antigorite transition and corresponding to our experimental observations can be following reaction:

$3Mg_2Fe_2SiO_9H_4 + 3SiO_2 = 3Mg_2FeSi_2O_9H_4 + O_2 + Fe_3O_4$ (4.3.-1)

Reaction (.4.3.-1) requires SiO_2 coexisting with lizardite. However, we don't have an evidence of SiO_2 in the starting material, such phases as chlorite, andradite, olivine known to be present in trace amounts in serpentinites may play a role of SiO_2 source for the Reaction (4.3.-1). Magnetite was not detected either, which could happen because of a very moderate amount.

Reactions of lizardite-antigorite replacement suggested by Evans (2004) do not include Fe incorporation in minerals, therefore cannot be applied to present experiments:

17Liz/Chr = Atg + 3Brc (4.3.-2)

16Liz/Chr + $2SiO_{2, aq}$ = Atg + H_2O (4.3.-3)

20Chr/Liz = Atg + 6Fo + $9H_2O$ (4.3.-4)

Note, formulas of lizardite and antigorite are $Mg_3Si_2O_5(OH)_4$ and $Mg_{48}Si_{34}O_{85}(OH)_{62}$ respectively. All reactions mentioned in the discussion must be though taken into account in preparation of future experiments.

Run#1 and Run#4 are excellent complements to each other if we apply the results to subduction zones. Lizardite, used as a starting mineral in the Run#4, is the most common serpentine mineral in oceanic peridotites, consequently lizardite enters a subduction zone within serpentinized oceanic lithosphere. When pressure and temperature conditions increase, lizardite destabilizes and is replaced by antigorite, high-P high-T serpentine variety. This replacement occurs at temperatures around 400°C with slight reduction of Fe according to our results, and consequently with a release of an oxidizing fluid. Further existence of antigorite lasts until Fe-bearing olivine forms on the basis of antigorite. According to the results of the Run#1 olivine growth begins at 400°C. Such an overlap in temperature of lizardite-to-antigorite and antigorite-to-olivine reactions indicates that antigorite may exist in a narrow temperature range. However, only part of antigorite breaks down to olivine at temperature before 700°C, according to piston-cylinder experiments (Chapter 3.2.). And thus, antigorite formed due to lizardite destabilization then breaks down gradually until complete disappearance at around 700°C.

Besides the obtained results on evolution of serpentine minerals at high temperature, present *in-situ* HDAC runs are also valuable for preparation of future experiments. Following issues should be taken in account for future experiments:

1. The additional source of SiO_2 placed together with lizardite may speed up transition of lizardite to antigorite.
2. The example of three starting materials with different Fe contents show that XANES spectra of Run#5 have the most intense pre-edge region (~7115 eV).
3. Since peaks of antigorite and lizardite overlap on diffraction patterns, Raman spectroscopy measurements can be a possible solution to distinguish lizardite and antigorite.
4. The new heating technique with the use of WTi coated diamonds was tested in the described experiments. The heating appears easy to perform, diamonds can be removed easily without dismounting the whole cell assembly and moreover, diamonds can be re-used several times after experiments. However, some improvements should be applied for future runs, such as better maintenance of electrical connections inside the cell body, the use of direct temperature measurements during the sample heating.

3.3.2 *In-situ* XANES and XRD experiments on lizardite-antigorite transition

The experiment was performed at BM23 beamline using RH-DAC. The starting material used for the experiment comprised serpentine M16 (Table 3.3.-2). As it was shown in Chapter 3.3.1. (run#5) starting material M16 consists of a mixture between lizardite and antigorite. Starting material was prepared as a homogeneous powder and loaded to the sample chamber in the RH-DAC together with a chip of NaCl and gold powder, which were used as pressure calibrants. XANES measurements were performed at Fe *K*-edge and were accompanied by XRD characterization of the sample. Experiment was conducted at temperatures from 25°C to 450°C and pressure from 0 to 2.3 GPa. Starting material and the quenched experimental product were analyzed by high-resolution X-ray diffraction at ID27 beamline (ESRF, Grenoble) in order to perform Rietveld refinement on high-resolution XRD patterns.

Results

Fig. 3.3.-2. demonstrates XRD patterns for starting material and quenched experimental product. Peaks of antigorite and lizardite are present on both diffraction patterns with similar relative ratios of the peak height. An intense peak of gold on the pattern of the quenched sample appears because the gold powder used as a pressure marker is dispersed in the sample chamber. In order to quantify antigorite and lizardite abundances Rietveld refinement was performed (Table 3.3.-3). Starting material, which was assumed to mostly contain lizardite, occurred to be composed of 87 wt.% of antigorite and 13 wt.% of lizardite. The mineral composition of the quenched sample is similar to that of the starting material, however, amounts of antigorite and lizardite changed during the heating and equal to 92 wt.% for antigorite and 8 wt.% for lizardite in the quenched material. Thus, XRD results show slight changes in sample mineralogy after increase of pressure and temperature conditions to 450°C and 2.3 GPa, respectively.

XANES spectra acquired at different P-T conditions during the experiment are shown in Fig. 3.3.-3. and demonstrate slight changes in shape. The white line of the spectra shows an intense peak at around 7132 eV, which shifts from 7133.5 eV at 25°C to 7132.35 eV at 450°C and 2.1 GPa. This spectral feature also evolves in intensity and become less intense at high temperature. Such changes in spectral shape most likely reveal changes in Fe speciation, i.e. reduction of Fe.

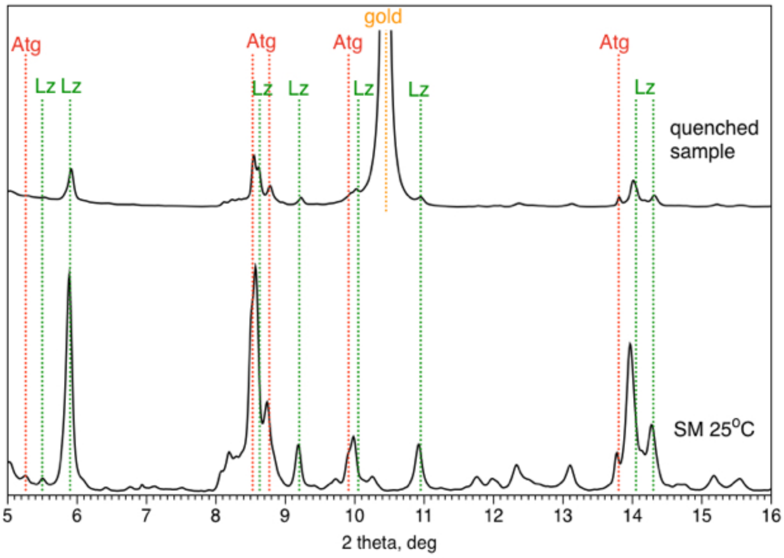

Fig. 3.3.-2. XRD patterns for staring material and quenched experimental product obtained at ID27 beamline (ESRF) using high-resolution XRD. Dotted lines indicate peaks of mineral phases: green – lizardite, red – antigorite, yellow – gold.

Table 3.3.-3. Wt.% of antigorite and lizardite for starting material and quenched experimental product obtained from Rietveld refinement of XRD patterns.

	wt.% obtained from refinement	
	starting material	reacted sample
Antigorite	86.96	91.86
Lizardite	13.04	8.14
Total	100.00	100.00

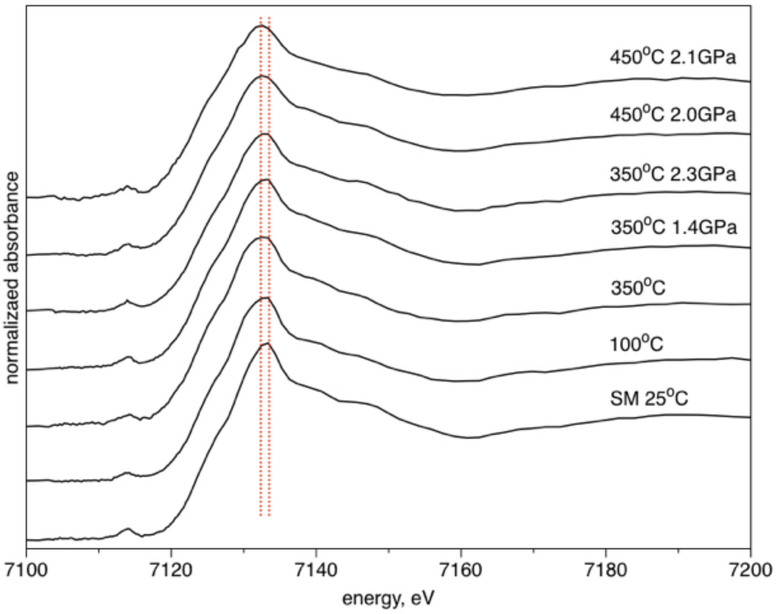

Fig. 3.3.-3. XANES spectra at Fe K-edge acquired at different pressure-temperature conditions during the experiment. Dotted red lines indicate energies of the white line of spectra.

Discussion

Serpentinization of peridotites involving mainly the lizardite variety is known to occur at mid-ocean ridge settings, and is likely to occur during slab subduction until temperature reaches about 300°C (Evans, 2010). At higher temperatures, 300-400°C lizardite was shown to destabilize and form either olivine or other serpentine mineral, antigorite (e.g., O'Hanley and Wicks, 1995; Evans, 2010). Antigorite, in turn, is stable up to 700°C (e.g. Ulmer and Trommsdorff, 1995; O'Hanley and Wicks, 1995). Taking in account mentioned statements, lizardite is supposed to breakdown either into olivine or antigorite at temperature >300°C. Natural observations (O'Hanley and Wicks, 1995; Schwartz et al., 2013) evidenced that the transition of lizardite to antigorite occurs between 250°C and 390°C. Our experimental results confirm the occurrence of the lizardite-antigorite transition, which occurs below 450°C. However, the rate of the reaction is relatively slow. Although the starting material contained small amounts of antigorite, which is supposed to speed up the reaction, only 5 wt.% of lizardite was consumed to produce secondary antigorite during 12 hours of the experiment.

Schwartz et al. (2013) and Evans (2004) proposed that lizardite-to-antigorite transition should occur in the presence of additional SiO_2. The additional SiO_2 is required for the antigorite formation due to the higher Si/Mg ratio in antigorite ($Mg_{48}Si_{34}O_{147}H_{62}$) than in lizardite ($Mg_3Si_2O_9H_4$). Taking this into consideration, another ultimate way to produce antigorite may be applied, such as a lizardite breakdown leading to formation of antigorite and another Mg-bearing phase, brucite or forsterite. The formation of a second Mg-phase is required in order to liberate excessive Mg, not incorporated into antigorite. Consequently, as it was already shown in Chapter 3.3.1., following reactions in $MgO\text{-}SiO_2\text{-}H_2O$ system may be responsible for lizardite-antigorite transition:

$$17\text{Liz/Chr} = \text{Atg} + 3\text{Brc} \qquad (4.3.\text{-}2)$$

$$16\text{Liz/Chr} + 2SiO_{2,\ aq} = \text{Atg} + H_2O \qquad (4.3.\text{-}3)$$

$$20\text{Chr/Liz} = \text{Atg} + 6\text{Fo} + 9H_2O \qquad (4.3.\text{-}4)$$

However, our experimental results do not show any evidence for the presence of Brc, SiO_2 or Fo. Our starting material already contained antigorite together with lizardite, and in this case we assume that no additional source of SiO_2 is needed, since antigorite itself acts as a source of SiO_2. Moreover, Reaction (4.3.-2), (4.3.-3), and (4.3.-4) describe processes in MSH system. If we transfer the reactions in Fe-bearing system, they will become more complex, considering possible changes in Fe speciation.

Indeed, iron speciation was shown to change during the lizardite-antigorite transition. In particular, Fe reduction was demonstrated by an energy shift and shape change of the XANES spectra. The iron reduction should imply a release of oxygen, or other oxidizing agent during the lizardite replacement, in order to compensate for the gain of electrons. The experimental observations present a realistic picture taking into consideration that most of natural lizardite is found to have much higher Fe^{3+}/Fe_{total} ratios compared to that of common natural antigorite.

To summarize, the replacement of low-temperature serpentine is a complex process, which cannot be described by simplified reactions in MSH system. Since Fe was shown to reduce during lizardite-antigorite transition, this process should result in release of oxidized fluid or solid phase. In subduction zone, this transition occurs at depths around 20-30 km in the narrow temperature range and may contribute to the oxidation of the overlying crust.

3.4. Sulfur mobility during serpentinite dehydration

3.4.1 Introduction

Sulfides are the main sulfur-bearing phases in oceanic serpentinites. Most common sulfides found in natural serpentinite rocks are pyrite, chalcopyrite, pyrrhotite and pentlandite (e.g., Alt et al., 2012; Alt et al., 2013). Frost (1985) and Evans et al. (2015) noted that pyrite is the predominant sulfide in carbonate- and talc-bearing rocks, whereas pyrrhotite and heazlewoodite becomes principal sulfides in carbonate-free serpentinites and their lithologies. However, pyrite is reported to be the major sulfide phase in most natural oceanic serpentinites (e.g., Frost., 1985; Delacour et al., 2008; Alt et al., 2012; Alt et al., 2013).

When serpentinite experience a prograde metamorphism during subduction, destabilization of pyrite and consequently formation of other sulfide phases with a potential release of sulfur-bearing fluids can occur. The fate of sulfides and the principal pyrite breakdown reaction during metamorphism of serpentinites in subduction zones is still a debated topic. We showed in Chapter 3.2. that the observed pyrite-pyrrhotite transition during serpentinite dehydration occurs because of the sequestration of Fe from Fe-bearing silicates, such as antigorite and olivine. This reaction does not imply any mobility of sulfur from the rock, but sulfur liberation from subducted serpentinites was reported by a number of studies (e.g., Evans et al., 2015; Alt et al., 2012). Thus, we can assume that in addition to the reaction of pyrrhotite formation through depletion of Fe from silicates, another S-liberation reaction takes place at the same temperature range, between 400 and 500°C. The simplest pyrite-breakdown reaction which releases S and occur with an increase of temperature is a transition of pyrite to pyrrhotite with a release of S_2 (Toulmin and Barton, 1964):

$$FeS_2 = FeS + 1/2S_2 \qquad (3.4.\text{-}1)$$

But in natural settings the mobilization of sulfur most probably happens by more complicated reactions, than Reaction (3.4.-1). Because serpentine breaks down at temperatures from ~400 to 850°C (Ulmer and Trommsdorff, 1996; Bromiley and Pawley, 2003; Merkulova et al., 2016) a release of H_2O can trigger destabilization of pyrite and formation of pyrrhotite by following reactions:

$$FeS_2 + H_2O = FeS + H_2S + 1/2O_2 \qquad (3.4.\text{-}2)$$

$$3FeS_2 + 2H_2O = 3FeS + SO_2 + 2H_2S \qquad (3.4.\text{-}3)$$

As it was shown by Tomkins (2010) both reactions, Reaction (3.4.-2) and (3.4.-3), become more significant at temperature between 400 and 600°C. Assuming that in natural settings pyrite is not isolated from the surrounding rock and interacts with released H_2O, then Reaction (3.4.-2) and (3.4.-3) are more likely to occur during serpentinite dehydration. Recent study by Alt et al. (2013) on sulfur isotopic ratios in serpentinites and their dehydrated lithologies demonstrated that the loss of sulfur coincides with a decrease in $\delta^{34}S$ from serpentinites to meta-peridotites. Such a change in $\delta^{34}S$, derived from fractionation of sulfur isotopes during metamorphism, implies a formation of oxidized sulfur (e.g., sulfate, SO_2), which has higher $\delta^{34}S$ compared to sulfides (Jager and Hunziker, 1979). The loss of oxidized form of sulfur could result in decreasing of heavy ^{34}S isotope in newly formed sulfides. This notion excludes reaction (3.4.-2) since no oxidized sulfur is formed in this reaction. This way, Reaction (3.4.-3) must be responsible for breakdown of pyrite and formation of pyrrhotite, together with a release of H_2S and SO_2 in a fluid.

In this chapter, we show the results of sulfur isotope measurements coupled with sulfur concentrations analysis in serpentinites, meta-peridotites and intermediate assemblages produced in piston-cylinder experiments (set#2). The starting serpentinite was mixed with ~3 wt.% of natural pyrite. Experimental technique is described in Chapter 1.1.2. and analytical procedure of sulfur isotope ratio measurements and elemental analysis is described in Chapter 1.2. The results show that sulfur-bearing serpentinite dehydration in conditions relevant for subduction zone results in loss of 25% of total sulfur with higher $\delta^{34}S$ than the host rock, which may indicate the presence of potentially oxidized S in gas/fluid phase with a proviso that fO_2 >QFM. Moreover, these results indicate that about 75% of the initial sulfur contained in oceanic serpentinites remains in the slab and sinks deep into the mantle, whereas 25% of sulfur is mobilized and may be transported from the slab to the overlying mantle.

3.4.2 Results and discussion

A set of experiments was performed in piston-cylinder apparatus on serpentinite dehydration. Starting material for all experiments in this experimental set (set#2, see Chapter 1.1.2.) was composed of natural antigorite, with minor chlorite and andradite, and pyrite. The experiments were carried out at temperature from 450 to 900°C at pressure of 2 GPa.

The results of XANES spectroscopic measurements of experimental products are demonstrated and discussed in Chapter 3.2. Pyrite presented in starting serpentinite transforms to pyrrhotite at temperature below 550°C. This transformation indicates a reduction of sulfur from S^{1-} to S^{2-}. Electron microprobe analysis revealed a depletion in Fe of silicate phases produced in the experiments. Consequently, the reduction of sulfur is associated with an iron depletion in silicates as well as a release of O_2 folowing Reaction (3.2-5) (Chapter 3.2.).

Since XANES spectroscopy shows only relative proportions of mineral phases in the assemblages, elemental analysis of S was performed on starting material and 3 experimental products in order to show a loss of sulfur, if any occurred during dehydration. The result of S concentration analysis is shown in Table 3.4.-1. The starting serpentinites contain 1.65% total sulfur, which is represented by pyrite, the amount of which is 3 wt.% according to calculations. The assemblages produced at 450°C has 1.21 wt.% total sulfur and implies loss of 0.35 mg of sulfur during the experiments. Analysis of XANES spectra at S K-edge (Fig. 3.2-7 in Chapter 3.2) and XRD results (Fig. 3.2-1 in Chapter 3.2) indicate the presence of two sulfur-bearing phases in the solid rock produced at 450°C. According to linear combination fit (LCF) of XANES spectra pyrite to pyrrhotite ratio equals to 0.44/0.56.Coupling this results with concentration of sulfur in the experimental product the percentage of pyrite corresponds to 0.44 wt.% and pyrrhotite to 1.04 wt.%. The assemblages from 850°C and 900°C contain 1.262 wt.% and 1.267 wt.% of sulfur respectively, which indicates a loss of about 0.31 mg sulfur. At high temperature, sulfur is only present in pyrrhotite, the amount of which is 3.46 wt.% and 3.48 wt.% in the 850°C and 900°C assemblages, respectively. In spite of expecting lower concentration of S at higher temperature, compared to 450°C, we observe the opposite trend. This trend may be explained by a slight difference in sulfur concentration in starting materials for 450°C and for 850/900°C experiments. As the volume of starting materials for experiments is about 0.2 cm^3, even minor heterogeneities in the prepared powdered mixture could lead to different total sulfur concentration. Despite these uncertainties, serpentinites loose around 0.32

mg of sulfur on average during the dehydration between 450 and 900°C, which is about 25 % of total sulfur.

Concentration of sulfur in an aqueous fluid at different experimental temperatures was calculated based on the amount of released sulfur, shown in this Chapter, combined with amount of released H_2O obtained from mass balance calculations (Chapter 3.2.). The concentration of S in H_2O equals to 5.5 mol/kg in the fluid formed at 450°C, 1.1 mol/kg at both temperatures, 850°C and 900°C. To compare, Wallace (2005) showed S and H_2O contents in melt inclusions from different arc volcanoes, with maximum concentration of S in H_2O = 3.1 mol/L. Thus, concentration in the fluid released from dehydrated serpentinites on average is similar to that in arc magmas. Although the amount of pyrite is twice lower in natural antigorite than in our starting material, we can claim that serpentinites contribute significantly to sulfur recycling in subduction zones.

The $\delta^{34}S$ values obtained by IRMS measurements are shown in Table 3.4.-1. Starting material, composed of antigorite and pyrite, has $\delta^{34}S=8.18‰$. The experimental products has lower $\delta^{34}S$ values, 7.52‰, 7.03‰ and 7.07‰ at 450°C, 800°C and 900°C respectively. The obtained $\delta^{34}S$ values for staring material and experimental products fit the range of of isotopic ratios of sulfides (Jager and Hunziker, 1979), which is consistent with XRD and XANES results (Chapter 3.2.).

Table 3.4.-1. Sulfur isotope ratios ($\delta^{34}S$) and S concentration (wt.%) in starting material and experimental products of the set#2.

Run#	Experimental T	$\delta^{34}S$ vcdt ‰	% S
Atg_Py SM	25	8.18	1.65
Atg_Py_18	450	7.52	1.21
Atg_Py_17	850	7.03	1.26
Atg_Py_20	900	7.07	1.27

Sulfur isotope fractionation clearly occurs during the serpentinite dehydration, since all $\delta^{34}S$ values of experimental products are lower than that of starting material. Applied mass balance calculations show that the lost sulfur species have $\delta^{34}S=11‰$. The loss of heavy-isotope-rich ^{34}S is consistent with the liberation of oxidized form of sulfur, such as for example SO_4^{2-} or SO_2 (Ohmoto and Rye, 1979; Seal et al., 2006; Alt et al., 2012). Both species enriched in ^{34}S and consequently their release from the assemblage may cause depletion in heavy ^{34}S isotope of the solid rock. Reaction responsible for the release of oxidized sulfur is most likely Reaction (3.4.-3). This reaction can be advanced if we take in account the reduction of pyrrhotite through sequestration of Fe from silicates, described in Chapter 3.2. Then the more complex reaction may take place:

$$\underset{Fe^{3+}\text{-antigorite}}{2Mg_2Fe_2SiO_9H_4} + \underset{\text{pyrite}}{7FeS_2} = \underset{\text{pyrrhotite}}{11FeS} + \underset{\text{S-dioxide}}{3SO_2} + \underset{\text{forsterite}}{2Mg_2SiO_4} + \underset{\text{water}}{4H_2O} \qquad (3.4.\text{-}4.)$$

However, the Reaction (3.4.-3) and Reaction (3.2-5) in Chapter 3.2. may occur one after the other. First, reaction of pyrrhotite formation through sequestration of Fe from silicates and release of H_2O and O_2; and second, reaction of pyrite with H_2O, formed due to partial breakdown of antigorite. The second reaction leads to a release of H_2S and SO_2.

Whatever the process of pyrite breakdown during serpentinite dehydration, SO_2 and H_2O may form. When transferring the results of thermodynamic modelling provided in Chapters 3.2. and 4, high fO_2 is required in order to stabilize oxidized forms of S, sulfate and SO_2. However, little is known about the thermodynamic properties of sulfates as well as about the fractionation of sulfur isotopes at different P-T and fO_2 conditions. And this way, the assumption that loss of heavy sulfur isotopes from a rock resulted from a release of oxidized forms of sulfur should be verified in future studies.

Projecting the results to subduction zone settings, a release of oxidized sulfur species, possibly together with H_2S, should occur at temperatures between ~400°C and 550°C at 2 GPa, which corresponds to conditions of flat and “hot” subduction (Fig. 3.2-7 in Chapter 3.2). This process is accompanied by pyrite-reduction which involves Fe-silicates with the possible release of O_2. Although, our experiments were carried out at 2 GPa, we can assume that in conditions of steep and “cold” subduction the process of pyrite reduction is the same as in “hot” subduction.

With a proviso that fO_2 in upper layers of subducting slab >QFM the release of oxidized form of sulfur together with aqueous fluid from serpentinites can contribute to mantle wedge oxidation. Arc magmas, generated in the mantle wedge due to partial melting driven by serpentinite dehydration are found to be more sulfur-rich compared to MORB magmas (Jego and Dasgupta. 2013) and therefore serpentinites may be considered as sulfur source. Sulfur isotope ratio values of arc magmas vary from -3 to 9.8‰ (de Hoog et al., 2001; Mandeville et al., 2010), such a wide range of $\delta^{34}S$ can be explained by fractionation of isotopes during melting, sulfides extraction from melts. Fractionation mechanisms of S isotopes during various processes in magma chambers are poorly constrained and for this reason it would be incorrect to claim that $\delta^{34}S$ of arc magmas are inherited from released from the slab S. However, it should be noted that $\delta^{34}S$ in nature can vary from -50 in marine sediments to 40 in evaporates. Taking in account such a wide scale, $\delta^{34}S$ obtained in this work for released S lay in the same range as values for arc magmas.

Sulfur recycling from mantle peridotites through subduction and volcanism to the crust is a complex process which may involve several chemical reactions. Sulfur reduction demonstrated by the transition from pyrite to pyrrhotite affects the composition of silicate phases, by uptake of Fe, and therefore their stability. This way, presence of S-bearing phases in serpentinites may affect dehydration temperatures of antigorite, one of the main sources of H_2O in subduction. Moreover, our results show that pyrite-pyrrhotite transition is accompanied by release of O_2, H_2O, H_2S and potentially SO_2 at temperatures below 550°C. In context of subduction zone, the released fluids would oxidize surrounding rocks and overlying mantle wedge. The comparison of sulfur concentration in released aqueous fluid and in melt inclusions from arc magmas shows that pyrite-bearing serpentinites can be an important source of sulfur for arc magmas.

Chapter 4 Thermodynamic modeling

4.1. Introduction

Oceanic lithosphere sinking into subduction zone undergoes metamorphism along hundreds of kilometers. Most of metamorphic reactions within a subducting lithosphere are dehydration reactions of sediments, metabasalts and serpentinized peridotites. Sediments experience dehydration at relatively low depths, from few kilometers to 55 km (Vidal and Dubacq, 2009; Stern, 2002). The underlying metabasalts dehydrate at depths of 40-80 km (Abers et al., 2013), and serpentinized peridotites at depths between 50 km to about 100-200 km depending on the age and descending angle of the slab (Merkulova et al., 2016). The metamorphic processes occurring in subduction are established first on the basis of field observations. Ophiolite complexes, fragments of the oceanic crust exposed on the Earth's surface, give a good picture of mineral reactions of subduction zone metamorphism. A number of ophiolite complexes (e.g., Cerro del Almirez, Spain; ophiolites of Western Alpes) preserved transitions between hydrous rocks formed during alteration of the oceanic lithosphere before subduction to their high-pressure high-temperature anhydrous metamorphic lithologies (e.g., Padron-Navarta et al., 2011; Debret et al., 2014). However, field evidences of subducting slab dehydration do not give a comprehensive image of metamorphic reactions that can occur along the wide range of pressures and temperatures. This image can be improved by combining natural observations with experiments conducted at controlled pressure, temperature and rock composition. Experimental data can be used to interpret conditions of metamorphism at different geological settings, but this must be done carefully since conditions inside the experimental setup may differ from those in nature. For example, parameters as oxygen fugacity, fluid pressure, stress and open or closed system conditions may vary in orders of magnitude in natural settings. Experimentalists use simple chemical systems to control precisely these different parameters and extrapolate to more complex and realistic compositions and P-T conditions using thermodynamics.

Thermodynamics has been first applied to geosciences about one hundred years ago by Victor Goldschmidt (1888 - 1947) and Pentti Eskola (1883 – 1964) to calculate equilibrium reactions between minerals. Nowadays, thermodynamics is an important tool to interpreting and predicting conditions, mineral reactions, mineral and fluid compositions in various geological processes and settings. Since the present work is dedicated to mineralogical and chemical changes during dehydration of serpentinites, application of thermodynamics only to ultramafic compositions relevant for subduction zone settings will be discussed in this Chapter.

In order to model dehydration reactions within ultramafic composition at elevated pressure and temperature conditions, the thermodynamic properties (entropy, enthalpy, volume) of at least antigorite and chrysotile are needed. The thermodynamic data set of Holland and Powell (1998) includes thermodynamic properties of Mg-antigorite and -chrysotile consistent with the properties of other silicates and oxides of petrological interest. The Holland and Powell (1998) data set is also consistent with recent calorimetric data, including work of Ogorodova et al (2009), which provided the most recent enthalpies of formation for antigorite, chrysotile and lizardite. However, natural serpentine was shown to comprise not only Mg-end member, but also Al (Tschermak substitution) and Fe (ferric and ferrous) (e.g., Uehara and Shirozu, 1985). The incorporation of Al increases thermal stability of antigorite as it was shown in experimental work of Bromiley and Pawley (2003) and thermodynamic model of Padron-Navarta et al. (2013). The effect of ferric Fe is believed (Padron-Navarta et a., 2013, Evans et al., 2013) to influence the antigorite thermal stability the same way as Al, i.e. expands stability field. In contrast, an increase of Fe-content decreases the thermal stability of antigorite (see Chapter 2). Fe and Al contents affect not only the stability of antigorite, but also the presence or absence other phases, such as chlorite, magnetite, brucite, garnet. A number of studies report P-T phase diagrams (pseudosections) for common serpentinite compositions in MSH (MgO-SiO_2-H_2O) system (e.g., Hacker et al., 2003; Rupke, 2004; Peacock et al., 2005; Nestola et al., 2010). By comparison, very few models were calculated for systems including Fe and/or Al (Lopez Sanchez-Vizcaino et al., 2005; Padron-Navarta et al., 2013; Evans et al., 2013, 2015).

The aim of this chapter is: (1) to develop ferrous- and ferric-antigorite end-members and a solid-solution model consistent with Holland and Powell (1998) thermodynamic data set and with the experimental results presented in Chapters 2 and 3; (2) to model dehydration reactions in CFMASH (CaO - FeO (Fe_2O_3) – MgO – Al_2O_3 – SiO_2 – H_2O) and CFMASH + S systems at conditions relevant to slab subduction; (3) to apply the results of modeling to natural rocks and discuss their P-T conditions of formation. A pseudosection approach is used to calculate metamorphic phase assemblages, phase compositions and water release. All thermodynamic calculations of the present study carried out using Theriak-Domino software (de Capitani and Petrakakis, 2010) with the Holland and Powell (1998) thermodynamic database.

4.2. Methods

The Theriak-Domino software package used for thermodynamic calculations and modeling consists of two principal programs: Theriak and Domino. Theriak calculates the stable mineral assemblage and phase compositions for a given bulk rock composition at specified pressure (P) and temperature (T) conditions or along a specified PT-path. Theriak combines linear programming with energy minimization of single thermodynamic functions to calculate the most stable (lowest free energy) mineral assemblage even for complex and non-ideal systems (de Capitani and Brown, 1987). Domino calculates equilibrium assemblage phase diagrams, pseudo-binary or pseudo-ternary phase diagrams, pixelmaps for all thermodynamic variables or isolines of several thermodynamic properties for bulk rock, non-solution and solution phases.

Theriak-Domino programs are based on Gibbs free energy minimization The thermodynamic database (Holland and Powell, 1998) provides the following parameters for all mineral end-members:

1. $\Delta fH°$ [J/mol], standard state enthalpy of formation
2. $S°$ [J/(K.mol)], third law molar entropy
3. $V°$ [J/(bar.mol)], molar volume
4. Heat capacity (Cp) function coefficients
5. Thermal expansion (α) and compressibility (β) V(P,T) function coefficients

Solid solution information, such as type of the solution (ideal, non-ideal) and Margules parameters for non-ideal solutions are also incorporated in the database. The molar Gibbs free energy of any phase ($\Delta G^{T,P}$) at given P and T is calculated by following equation:

$$\Delta G^{T,P} = \Delta_f H^{T0,P0} + \int_{T0}^{T} Cp dT - TS^{T0,P0} - T\int_{T0}^{T} \frac{Cp}{T} dT + \int_{P0}^{P} V(P,T) dP \quad (4.2.-1)$$

Equation (4.2.-1) is used to minimize the Gibbs free energy of the system at given bulk composition:

$$G = \sum_{k-1}^{N} n_k G_k \quad (4.2.-2)$$

where n_k is number of moles of phase k, G_k is the molar Gibbs free energy and N is total number of coexisting phases. Thus, the program reduces the Gibbs free energy of a system with fixed composition until a minimum is reached, which corresponds to chemical equilibrium (de Capitani and Brown, 1987).

The thermodynamic database lists the thermodynamic properties of rock-forming and accessory mineral phases as well as aqueous species and gases. However, the variety of natural mineral compositions is much larger than it can be described with the data set of Holland and Powell (1998), which needs to be complemented with additional phases, end-members and solid solutions. To model serpentinite dehydration at the conditions of subduction zones, antigorite is needed to be introduced. The solid solution created for the present study comprises the following antigorite end-members:

Table 4.2.-1. Composition of antigorite end-members and sources of their standart-state properties used in the present study antigorite solid solution.

Name	Abbreviation	M0	M1	T1	Formula	source
Mg-antigorite	Atg	Mg Mg	Mg	Si Si	$Mg_3Si_2O_5(OH)_4$	Holland and Powell (1998)
Fe^{2+}-antigorite	Fe-Atg	Fe Fe	Fe	Si Si	$Fe_3Si_2O_5(OH)_4$	This study
Tschermak antigorite	Mg-Tsch.Atg	Mg Mg	Al	Al Si	$Mg_2Si_1Al_2O_5(OH)_4$	Padron-Navarta et al. (2013)
Fe^{3+}-antigorite	Fe^{3+}-Atg	Mg Mg	Fe^{3+}	Fe^{3+} Si	$Mg_2Fe_2SiO_5(OH)_4$	Evans et al. (2013)
Fe-tschermak antigorite	Fe-Tsch.Atg	Fe Fe	Al	Al Si	$Fe_2SiAl_2O_5(OH)_4$	This study

Two main approaches are commonly used to estimate the standard-state thermodynamic properties of phases:

-The first approach is based on oxide summation technique, which allows estimation of standard state enthalpy of formation (ΔH°_f), third law entropy (S°), volume (V°) and heat capacity (Cp). This method is suitable for low-temperature and low-pressure systems and the technique was used successfully to discuss the conditions of stability and hydration of smectites (Vidal and Dubacq, 2009).

-The second approach estimates the thermodynamic properties from exchange reactions. ΔH°_f, S°, V° and Cp are constrained from the difference between standard-state properties of phases participating in exchange reaction. For example, the thermodynamic properties of Fe-antigorite $(Fe)_3Si_2O_5(OH)_{3.7}$ were estimated using the standard-state properties of Mg-antigorite and the difference between those of Fe- and Mg-talc :

$$(\Delta H^\circ_f, S^\circ, V^\circ, Cp)\text{Fe-antigorite} = (\Delta H^\circ_f, S^\circ, V^\circ, Cp)\text{Mg-antigorite} + (\Delta H^\circ_f, S^\circ, V^\circ, Cp)(\text{Fe-Talc} - \text{Mg-Talc}) \quad (4.2.-3)$$

according to the exchange reaction:

Mg-talc + Fe-antigorite = Fe-talc + Mg-antigorite (4.2.-4)

($\Delta H°_f$, S°, V°,Cp)Mg-antigorite are the original properties reported by Holland and Powell (1998) for the $Mg_{48}Si_{34}O_{85}(OH)_{62}$ structural formula divided by 17. ($\Delta H°_f$, S°, V°,Cp)Fe-Talc and Mg-Talc are the original properties for talc end-members from Holland and Powell (1998).

Similarly, standard state properties of other antigorite end-members were estimated from respective mineral reactions. Table 4.2.-2 summarizes the antigorite end-members and reactions used to estimate the relevant thermodynamic properties. The $\Delta H°_f$ of Mg-antigorite was corrected to that determined using a calorimetric method by Ogorodova et al. (2009). $\Delta H°_f$ of other antigorite end-members were slightly adjusted in order to reproduce experimental observations. Since Al and Fe^{3+} occupy the octahedral and tetrahedral sites of antigorite, Tschermak and Tschermak-like substitutions are considered in Mg-Tschermak-antigorite and Fe^{3+}-antigorite end-members. The antigorite solid solution was assumed to be ideal.

Table 4.2.-2. End-member and respective theoretical mineral reactions used for thermodynamic properties estimations. Mg-atg – Mg-antigorite; Clin – clinochlore; Br – brucite; Fo – forsterite; En – enstatite; Mg-Tscher.pyx - ; Acm – acmite; Jd – jadeite; Fe-atg – Fe-antigorite. Thermodynamic data for Mg-atg, Fe-talc, Mg-talc, Clin, Br, Mg-Tscher.pyx, En, Fo, H_2O, Acm and Jd are from Holland and Powell (1998).

Name	**hypothetical mineral reactions**		**source**
Fe^{2+}-antigorite	1/17Mg-atg + Fe-talc - Mg-talc		This study
Tschermak antigorite	4/17Clin + 1/32Mg-atg − 1/12Br	4/17Clin + 6/17Fo + 6/17En + 15/17H_2O *	Padron-Navarta et al. (2013)
Fe^{3+}-antigorite	Mg-Atg + Mg-Tscher.pyx - En + 2Acm - 2 Jd		Evans et al. (2013)
Fe-tschermak antigorite	Mg-Tscher.Atg - 2/3Mg-Ag + 2/3Fe-Atg		This study

Thermodynamic modeling for CFMASH system with sulfur was performed with the internally consistent database of Holland and Powell (1998) complemented with mentioned above antigorite end-members, assuming an ideal antigorite solid solution, and with sulfur-bearing phases (H_2S, SO_2, pyrite and pyrrhotite) and their respective thermodynamic standard state properties ($\Delta H°_f$, S°, V° and Cp function coefficients) obtained from thermodynamic data set of Robie and Hemingway (1995). Calculations were performed for systems at oxygen activity relative to the QFM (quartz-fayalite-magnetite) redox buffer, in order to be comparable to experimental conditions and natural subduction settings.

4.3. Modeling CFMASH and CFMASH-Sulfur systems relative to experiments

CFMASH system

Some results of thermodynamic modeling with the reduced Fe^{2+}-Mg antigorite solid-solution are discussed in Chapter 2.2. A P-T pseudosection calculated with this reduced solid-solution is shown in Figure 4.3.-1a and compared with pseudosections computed with the complete solid-solution (including Fe^{3+} and Al) for two starting bulk compositions used in the piston-cylinder experiments described in Chapter 2.2 and 3.2. (Fig. 4.3.-1b and c).

Figure 4.3.-1a and b show that the phase assemblages and mineral reactions computed with the reduced and complete solid solutions are similar. However, the antigorite compositions computed with both models are different. The isopleths of Fe^{3+}-antigorite end-member activity (Figure 4.3.-2) show that Fe^{3+} in antigorite first increases from X(Fe^{3+}-atg) = 0.035 to 0.044 between 350°C to 500°C at 2 GPa and then drops down to 0.004 at 550°C. A gradual decrease of X(Fe^{3+})-atg is observed with further increase of temperature. The value of X(Fe^{3+})-atg in experiments could not be measured. However, the measured and calculated bulk Fe^{3+}/Fe_{total} show similar features (Table 4.3.-1). The same decreasing trends are observed from about 0.8-0.9 below at 550°C down to ~0.2 at 675°C. At T > 700°C, the computed assemblages are free of Fe^{3+} because no Fe^{3+}-bearing chlorite end-member is present in the thermodynamic data base, whereas experimental products show that ferric iron is present in chlorite.

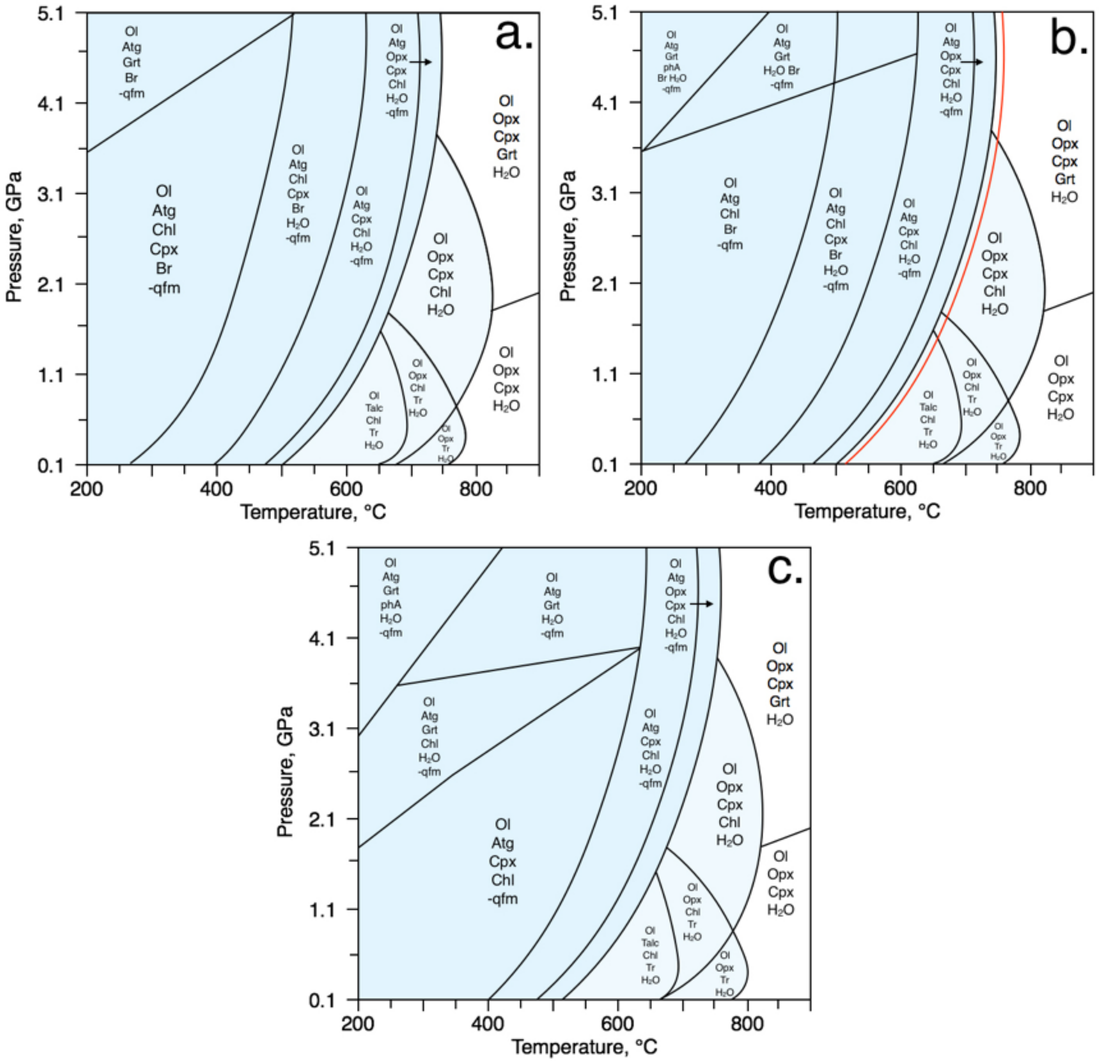

Fig. 4.3.-1. P-T pseudosections a) for bulk composition of serpentinites with 6 wt.% FeO_{total} computed with the use of Fe-Mg antigorite solid solution; b) for bulk composition of serpentinites with 6 wt.% FeO_{total} computed with the use of completed antigorite solid solution; c) for bulk composition of serpentinites with 1.3 wt.% FeO_{total} computed with the use of completed antigorite solid solution. Blue fields indicate assemblages with antigorite, light blue field indicates assemblages with only clinochlore as a main hydrous mineral. Red solid line represent Atg-out reaction in the system with 1.3 wt.% FeO_{total}.

Calculated pseudosections in Figures 4.3.-1a, b and c show that with increasing temperature, assemblages with Fe^{3+}-bearing antigorite transform into assemblages free of Fe^{3+}-bearing phases. Since the calculations were made at QFM buffer oxygen fugacity conditions, the change in redox state of the serpentinite composition is illustrated by the disappearance of the "–qfm" phase from the mineral assemblages. "-qfm" indicates that the oxygen fugacity of the buffer has to be lower than qfm in order to compensate the oxygen fugacity of the input serpentinite composition. After antigorite breaks down, the fO_2 of the system is maintained at QFM buffer level since no Fe^{3+}-bearing phases is present.

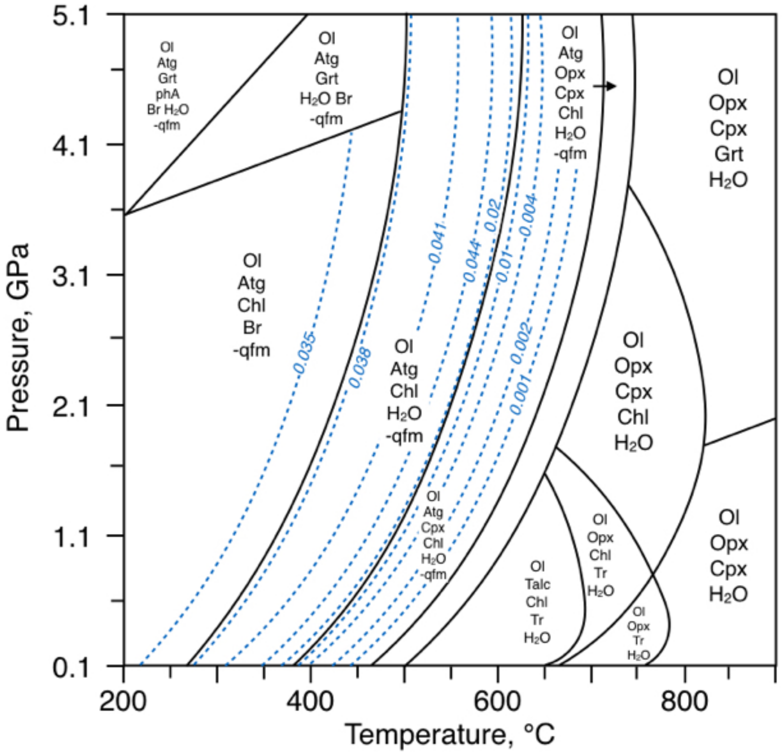

Fig. 4.3.-2. P-T pseudosection for serpentinite composition (set#2; 6 wt.% FeO). Dashed blue lines indicate activity of Fe^{3+}-antigorite end-member.

Table 4.3.-1. Comparison of computed by Theriak and measured in experimental samples Fe^{3+}/Fe_{total} ratios in bulk rock in starting composition and at temperatures from 400°C to 700°C. SM – starting material.

	Fe^{3+}/Fe_{total} bulk rock	
Temperature, °C	Computed	Measured
SM	0.6	0.96
400	0.76	-
450	0.75	-
500	0.83	-
550	0.84	0.42
600	0.41	0.395
650	0.20	0.191
675	0.16	0.207
700	0.00	0.20

The Fe^{3+}-antigorite and magnetite breakdown in subduction zones plays an important role regarding potential release of oxidized fluids (Chapter 3.2.) in deep parts of subduction. The reduction of Fe and consequent release of oxidized fluid depend on the fO_2 of the system. Since the pseudosections discussed above were computed at QFM buffer, no magnetite was present in the calculated assemblages because it is included in the buffer. Figure 4.3.-3 depicts the evolution of mineral assemblages with temperature and activity of oxygen (proportional to oxygen fugacity). Calculated pseudosection presents that antigorite contains Fe^{3+} only at aO_2 at or above QFM value. In assemblages forming at log $a(O_2)$ lower than that of QFM, antigorite is Fe^{3+}-free and the only Fe^{3+}-bearing phase is magnetite. Magnetite is absent in assemblages stable below log $a(O_2)$ ~QFM-10. Experimental results showed that Fe^{3+} was present in antigorite after magnetite destabilization and until complete antigorite breakdown (Chapter 2.2). Natural observations, on the other hand demonstrated that Fe3+-antigorite coexists with magnetite. However, computed log $a(O_2)$-T isobaric pseudosection (Fig. 4.3-3) shows that Fe^{3+}-bearing antigorite does not coexist with magnetite. Such a discrepancy between experiment, natural observations and model may be originated from yet poorly constrained thermodynamic parameters for Fe^{3+}-antigorite end-member, and different fO_2 conditions in the experiment and natural settings.

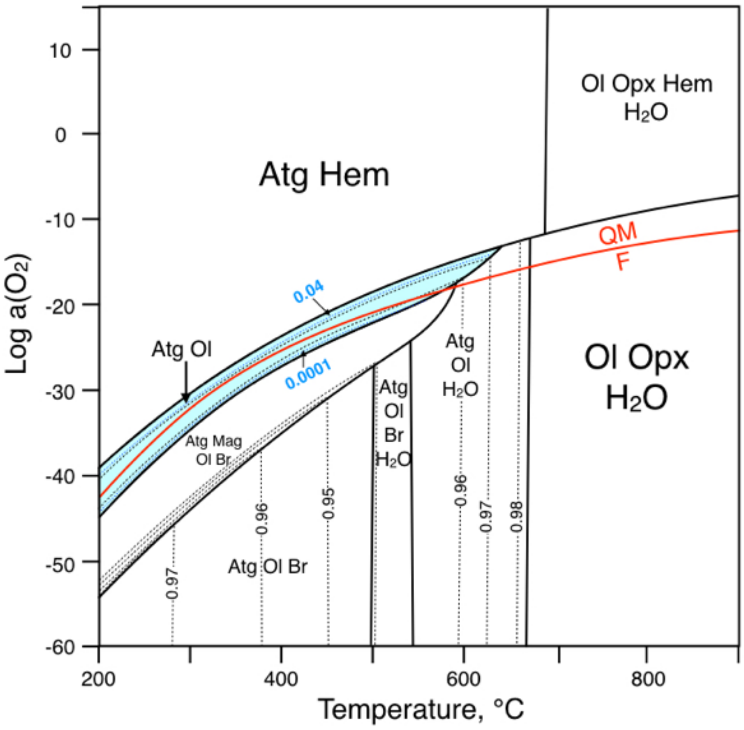

Fig. 4.3.-3. Log $a(O_2)$-T isobaric pseudosection at 2 GPa for serpentinite composition comprising 6 wt.% FeO_{total}. Red solid line indicates activity of oxygen relative to QFM buffer. Dashed black lines indicate Mg# of antigorite; dashed blue lines and blue labels indicate activity of Fe^{3+}-antigorite end-member. Blue field represent stability of Fe^{3+}-antigorite.

The new antigorite solid-solution was also tested with serpentinite composition containing 1.3 wt.% FeO_{total}, which represents the bulk composition of experimental set#1 (Chapter 3.2). Figures 4.1.-1 b and c show P-T pseudosections computed for Fe-rich and Fe-poor systems, respectively. Low-temperature assemblages show slight changes in mineral abundances. Brucite does not appear in the system with 1.3 wt.% FeO_{total}, but in system with 6 wt.%. This difference can be explained by the formation of Fe-richer antigorite in Fe-rich system (Fig. 4.3.-1b). The excess Mg not incorporated in antigorite is incorporated in brucite. No significant changes in mineral assemblages are revealed at high temperatures.

As discussed in Chapter 2, the Fe-content of serpentinites affects thermal stability of antigorite and the temperature of water release associated with the antigorite breakdown. Figure 4.3.-1b demonstrates that the breakdown of antigorite in Fe-poor systems occurs at 10 to 20°C higher than in Fe-rich systems. Consequently, the main portion of water released by antigorite breakdown is liberated at higher P-T conditions and deeper parts of subducting slab.

An isobaric X-T pseudosection is shown in Figure 4.3.-4, where X is bulk FeO_{total} in serpentinite. Serpentinite with 6 wt.% FeO_{total} is projected on the left part of the pseudosection, serpentinite with 1.3 wt.% of FeO_{total} is on the right part of the pseudosection. An increase of FeO from 1.3 wt.% to 6 wt.% decreases the temperature of antigorite breakdown (Reaction 1 in Fig. 4.3.-4) by 100°C. Reaction 1 represents breakdown of Atg to Ol and H_2O. However, reaction lines at higher temperature are less inclined, which means that Fe component affects these reactions in smaller extent. For example, reaction 2 (complete antigorite breakdown) changes its temperature from 690°C to 670°C in composition with 1.3 wt.% FeO and 6 wt.% FeO, respectively. Antigorite breakdown reactions are responsible for H_2O release, consequently FeO_{total} content will affect H_2O release. As it was already showed in P-T pseudosections (Fig. 4.3.-1), dehydration occurs at lower temperature in Fe-rich systems. Isopleths of H_2O projected in Figure 4.3.-4 also reveal that dehydration is progressive between Reaction 1 and Reaction 3, and occurs at water content decreasing from ~12 to 9 wt.% between 500°C and 650°C. H_2O content in a rock decreases sharply in a narrow temperature range, between ~650°C and ~700°C.

A more detailed discussion regarding the effect of Fe on water release in serpentinites can be found in Chapter 2.

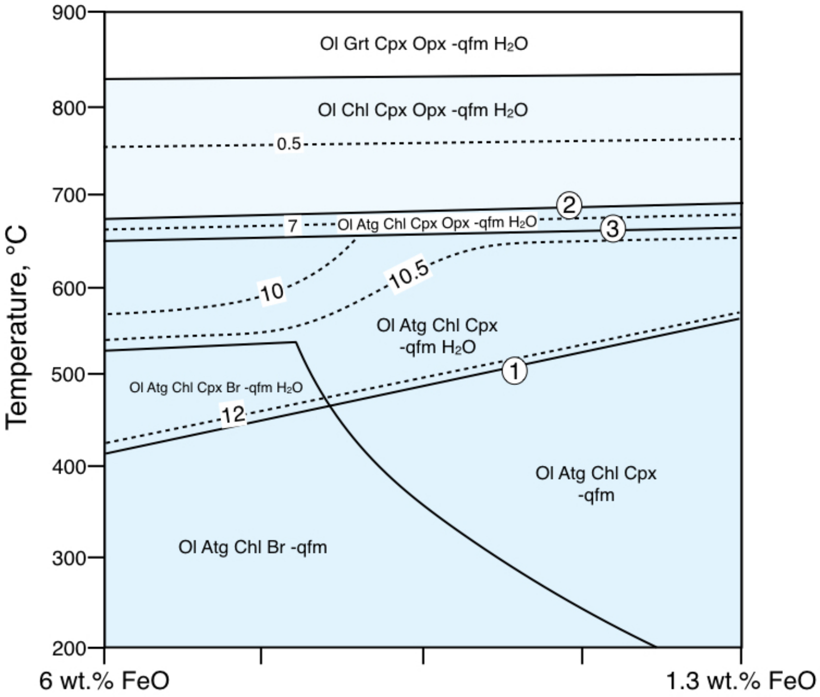

Figure 4.3.-4. X-T isobaric pseudosection at 2 GPa. X axis is FeO_{total} in bulk serpentinite. Solid lines indicate mineral reactions; dashed curves indicate wt.% of H_2O in the solid rock. White circles with numbers represent mineral reactions: 1. Onset of antigorite breakdown, 2. Complete antigorite breakdown. Blue field indicate assemblages with antigorite, light blue field indicates assemblages with only clinochlore as a main hydrous mineral.

The results of modeling demonstrate that incorporation of Fe^{3+} in antigorite does not influence its thermal stability, compared to Fe^{2+}, which in its turn decreases the antigorite thermal stability. However, the incorporation of Fe^{3+} in antigorite is more significant regarding changes in redox state of the rock and fluid.

Tschermak substitution is known to increase the thermal stability of antigorite (Padron-Navarta et al., 2013), however, it is not discussed here, since Al component is negligible in antigorite in computed assemblages. The average apfu value of Al in antigorite is 0.001, but antigorite from experimental products contains about 0.06 apfu Al. The possible reason of such low Al in modelled antigorite can mean that Fe^{3+}-end-member is too stable compared to Al-end-member.

Thermodynamic modeling complemented with new developed antigorite solid solution introduced by Holland and Powell (1998) data set was shown to be relatively compatible with experimental results. Computations were performed for oxygen activity relative to QFM buffer, however, further modeling is required in order to test antigorite solid solution with different buffers. Also compatibility of Al and Fe^{3+} incorporation should be modified and tested.

CFMASH + Sulfur system

Serpentinites usually contain ~ 1 wt.% sulfur, which is mainly found in form of pyrite in low-grade serpentinites (e.g., Delacour et al., 2008). The experimental results (Chapter 3.2.) revealed that pyrite reduces to pyrrhotite between 450°C and 550°C at 2 GPa with the release of ¼ of sulfur initially contained in pyrite. The stability of sulfide at P-T-fO_2 conditions relevant to subduction zones is mostly unknown and, hence, the observed transfer of sulfur from sulfide to S-bearing volatile species is still poorly understood (see Frost, 1985). In order to constrain stability of sulfur phases in a fluid coexisting with pyrrhotite, thermodynamic modeling is required, since fluid composition analysis cannot be performed in piston-cylinder experiments. Here we show the results of thermodynamic modeling in sulfur-bearing systems with the use of Holland and Powell (1998) data set complemented with thermodynamic parameters for pyrite, pyrrhotite, SO_2 and H_2S taken from Robie and Hemingway (1995).

Figure 4.3.-5 shows phase diagrams for two chemical systems Fe-S-O-H and Fe-Mg-Si-O-H plotted in terms of log of activity of oxygen and activity of sulfur. The stability of pyrrhotite, which is the principal sulfide mineral in experimental products (Chapter 3.2.), is limited by log of activity of oxygen relative to QFM buffer at 450°C/2 GPa and to QFM+6 at 800°C/2 GPa. Sulfur concentration analysis of experimental products (Chapter 3.2.) revealed the loss of sulfur, i.e. volatilization of a part of sulfur, took place during experiments. Figure 4.3.-5 demonstrates that the only sulfur-bearing volatile (i.e. gas) phase coexisting with pyrrhotite at P-T conditions relevant to experiment is H_2S. The stability field of pyrrhotite and H_2S is relatively narrow in terms of sulfur activity. However, in terms of activity of oxygen (i.e. oxygen fugacity) pyrrhotite+H_2S stability field has a wide range of values from about QFM buffer and lower. The experiments described in Chapter 3.2. are reported to be performed at fO_2 between ~QFM and QFM-2, which indicates that the possible volatile sulfur phase in experiment was H_2S.

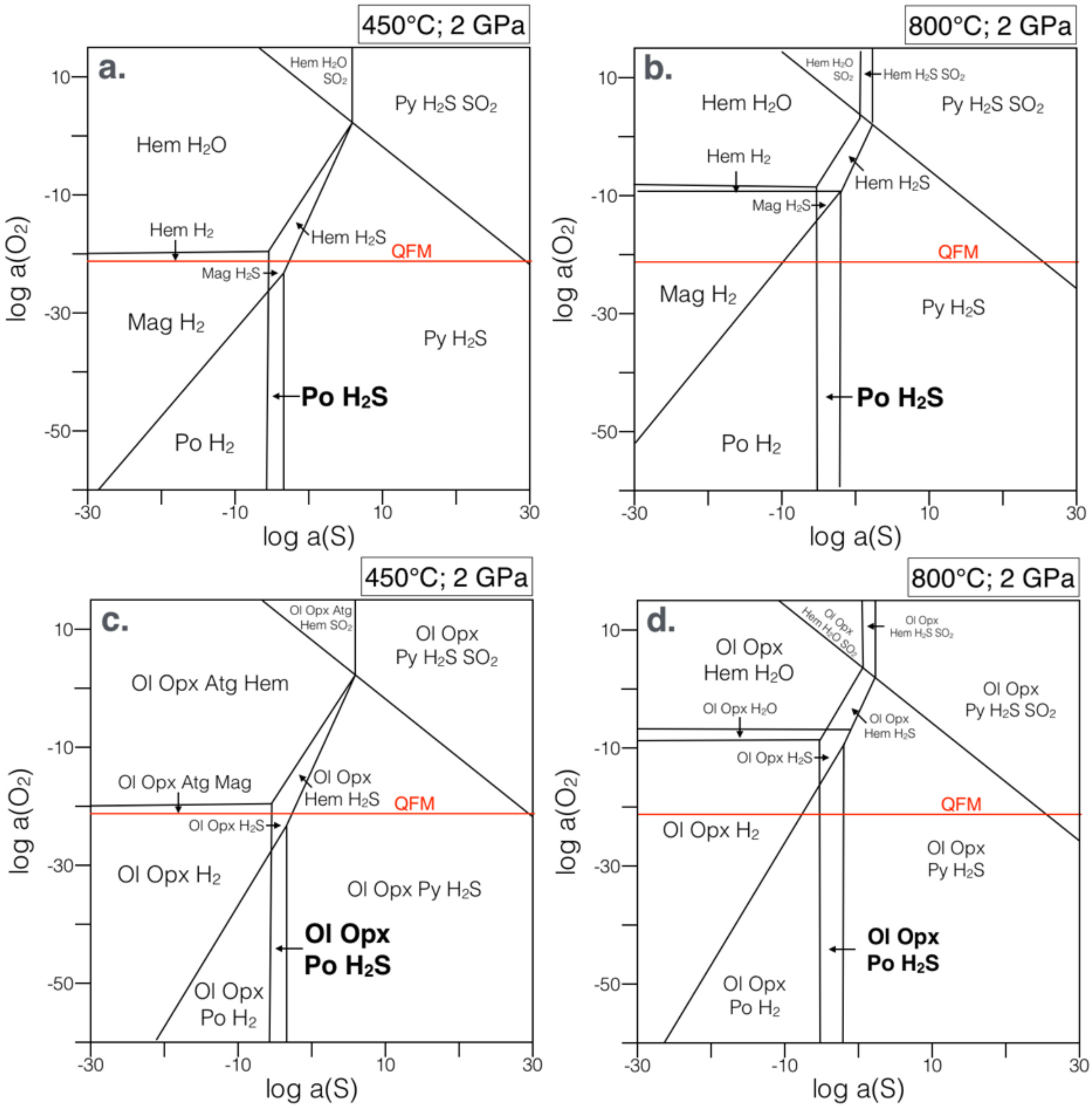

Fig. 4.3.-5. Isothermic and isobaric Log(a_{O2})-log(a_S) sections showing phase stabilities in a). Fe-S-O-H system at 450°C and 2 GPa; b). Fe-S-O-H system at 800°C and 2 GPa; c). Fe-Mg-Si-O-H system at 800°C and 2 GPa; d). Fe-Mg-Si-O-H system at 450°C and 2 GPa Red line represents a(O_2) of QFM buffer. Diagrams were made using Theriak-Domino software (de Capitani and Petrakakis; 2010). Thermodynamic properties of silicate and oxides were taken from Holland and Powell (1998) data set; properties of sulfides, SO_2 and H_2S were taken from Robie and Hemingway (1995). The field indicated with bold text font represent stability of pyrrhotite together with H_2S.

4.4. Conclusions

Taking into account variability of natural rock compositions, models of subduction zone processes, especially dehydration, will vary depending on the extension, in terms of solid solution development, of thermodynamic data sets. For example, thermal structures of subduction zones (e.g., Peacock et al., 2005; Syracuse et al., 2010) will be different depending on bulk serpentinite composition: more ferrous systems produce more ferrous antigorite which dehydrate at shallower depths and consequently melting may happen at shallower levels in the mantle wedge. At the same time, incorporation of ferric iron in antigorite affects the composition of released fluid. Since antigorite which contains Fe^{3+} breaks down at ~700°C, oxygen should be released and thus, oxygen activity of a solid rock should decrease. Thus, development of completed antigorite solid solution is necessary not only to model the regime of H_2O release, but also to understand changes in oxygen activity in subducting slab.

The solid solution model for antigorite, used in this study, was shown to change slightly the phase relations in the CFMASH system compared to the use of Fe^{2+}-Mg –antigorite solid solution. The new model provides information on the changes in antigorite composition with P and T, which is in agreement with experimental results. The use of advanced antigorite solid solution permits modeling of systems with different Fe and Al contents. The increase of bulk FeO was shown to decrease the thermal stability of antigorite and consequently the temperature of water release.

Moreover, serpentinites contain ~1 wt.% of sulfur (Alt et al., 2013). Transition of pyrite to pyrrhotite during the dehydration is demonstrated experimentally in Chapter 3.2. The lower amount of sulfur (Chapter 3.2.) and different sulfur isotope ratio (Chapter 3.4.) in dehydrated assemblages compared to serpentinites reveal the loss of sulfur during dehydration. It is difficult to estimate the speciation of volatilized sulfur due to limitations of fluid phase composition analysis in piston-cylinder experiment, however thermodynamic approach helped to constrain stability of pyrrhotite and volatile sulfur in form of H_2S. Models of sulfur-bearing systems demonstrates that sulfur might not necessary be oxidized in order to be released from serpentinites. Modeling shows that mobilization of sulfur can occur in a wide range of fO_2, but the speciation of volatilized S is dictated by fO_2 and activity of sulfur.

Equilibrium calculations, in our case with the use of Theriak-Domino suit, are powerful tools to help understanding natural processes and experimental results, help to develop new equations of state and solution models for more advanced modeling and also help to plan future experimental work.

4.5 Application of thermodynamics to natural systems modeling

Mantle wedge peridotite metamorphism above subduction zone: hydration in lithospheric mantle.

Savelieva G.N.[1], Raznitzin Y.N.[1], Merkulova M.V.[2]

[1] *Geological Institute Russian Academy of Sciences, Moscow, Russia, e-mail: razn46@mail.ru;*

[2] *Univ. Grenoble Alpes, ISTerre, F-38041 Grenoble, France*

Published article

Doklady Akademii Nauk (Russian: Доклады Академии Наук) (2016) 468, 1, 62-64

DOI: 10.7868/S0869565216130181

ISSN 1028-334X, Doklady Earth Sciences, 2016, Vol. 468, Part 1, pp. 438–440. © Pleiades Publishing, Ltd., 2016.
Original Russian Text © G.N. Savelieva, Yu.N. Raznitsin, M.V. Merkulova, 2016, published in Doklady Akademii Nauk, 2016, Vol. 468, No. 1, pp. 62–64.

GEOLOGY

Metamorphism of Peritotites in the Mantle Wedge above the Subduction Zone: Hydration of the Lithospheric Mantle

G. N. Savelieva[a], Yu. N. Raznitsin[a], and M. V. Merkulova[b]

Presented by Academician Yu.M. Pushcharovsky January 14, 2016

Received January 11, 2016

Abstract—Two areas with different types of hydration (serpentinization), which occurred in two settings distinct in temperatures, pressures, and stresses, are spatially individualized in the ophiolitic ultramafic massifs of the Polar Urals. The high-temperature hydration of ultramafic rocks occurred in the lithosphere of the mantle wedge directly above the subducted slab. The initial conditions of hydration are limited to 1.2–2 GPa and 650–700°C; a stable assemblage of olivine + antigorite + magnetite → amphibole → talc → chlorite was formed at 0.9–1.2 GPa and 550–600°C. The low-temperature mesh lizardite–chrysotile serpentinization occurred in the crustal, near-surface conditions. Both types of hydration were accompanied by release of hydrogen, which participates in abiogenic CH_4 synthesis in the presence of CO_2 dissolved in water.

DOI: 10.1134/S1028334X16050068

In the opinion of many researchers, olivine–antigorite rocks after peridotites are exclusively formed in suprasubduction settings, which is supported by numerous findings of antigorite serpentinites in the present-day deep-sea trenches and their absence in the mid-oceanic ridges. While submerging, the serpentinized peridotites undergo deserpentinization and metamorphism in the slab structure with formation of new high-temperature hydroxyl-bearing minerals: amphibole, talc, antigorite, and Mg-chlorite [11, 12, 14].

In ophiolitic allochthons of the Polar Urals, first of all, the Voykar–Synya massif, the spatial interrelations of the high-temperature metamorphic (olivine–antigorite ± amphibole ± talc) and low-temperature (lizardite–chrysotile) ultramafic rocks are well mapped. Peridotites with structures of a viscous–plastic mantle flow are subjected to uneven mesh serpentinization, which keeps the structures of rocks. The zones of ultramafic metamorphic amphibole–antigorite–olivine rocks cut these deformation textures and are concordant with the high-grade metamorphic rocks in the allochthon foot. This indicates a link between the formation of ultramafic metamorphic rocks and the movement of peridotites from the mantle to the crust.

The zones of the olivine–antigorite metamorphic rocks are asymmetric: fresh peridotites surrounded by massive amphibole ± talc–antigorite–olivine rocks occur at the top, whereas gneisslike, intensely deformed olivine–(antophyllite)–antigorite schists are developed at the foot. The asymmetric structure of zones and sharply intense foliation of the rocks at their foot are more evidence of the causation between transportation of mantle masses, hydration of peridotites, and the formation of ultramafic metamorphic rocks.

The following series of alternating mineral assemblages are identified: olivine + enstatite + diopside ± pargasite → secondary olivine + amphibole (antophyllite, tremolite) + talc + olivine → talc + antigorite + olivine ± diopside → antigorite–olivine rock → antigorite–olivine schist. This series has previously been considered as reverse (progressive), probably, with complete dehydration of rocks and the formation of absolutely fresh peridotites [5]. New analytical data have shown that the petrography and geochemistry of fresh nonserpentinized harzburgites and lherzolites are similar to those of typical abyssal mantle peridotites, whereas the geochemistry of dunites, pyroxenite veins in the mantle section, and adjacent peridotites is typical of rocks formed in the suprasubduction zone [1, 7]. Taking into account this and the structural interrelations (e.g., the mesh of talc and antigorite veinlets in fresh peridotites), we ascribe the fresh harzburgites to the primary rocks that were involved in regressive high-temperature dehydration. The geological and geochemical data on the Voykar–Synya massif [1, 5, 7] indicate that the mantle ultramafic rocks of the Polar Urals were formed in the forearc basin. After the early stage of the formation of the mantle section, the mantle masses moved to the trench. Thus, the lithospheric mantle in the suprasubduction zone could be a possible zone of starting the hydration process.

---

[a] *Geological Institute, Russian Academy of Sciences, Pyzhevskii per. 7, Moscow, 119017 Russia*
e-mail: razn46@mail.ru
[b] *ISTerre, Universite Joseph Fourier, Grenoble, France*

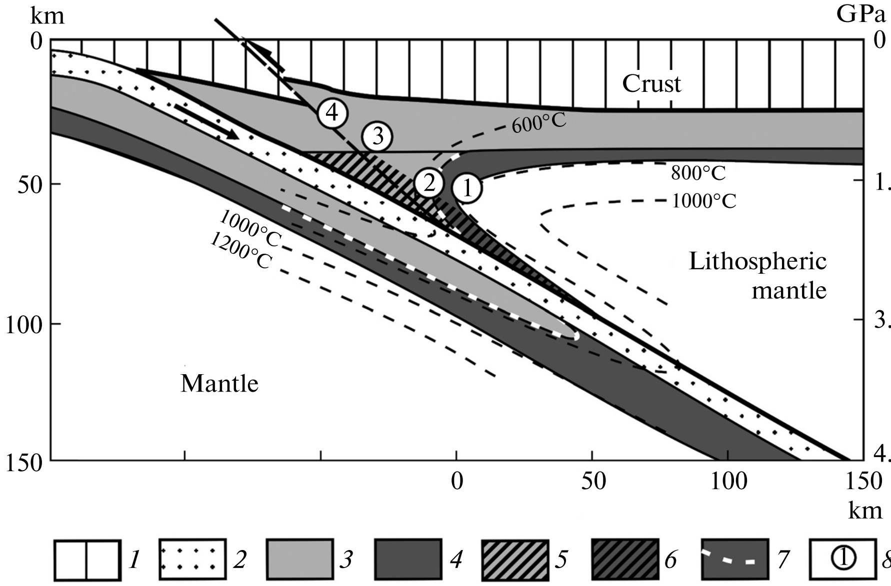

Position of the area of formation of ultramafic metamorphic rocks in the suprasubduction mantle wedge. The areas of stability of antigorite serpentinites and chlorite harzburgites are after [9–11]. (*1*) Island arc crust, (*2*) oceanic crust of slab, (*3*) serpentinized (antigorite) ultramafic rocks [9, 10], (*4*) chlorite harzburgite with spinifex and hornfels textures [9, 11], (*5*, *6*) the areas of stability of antigorite (*5*) and Mg-chlorite (*6*) in the mantle harzburgite of the suprasubduction wedge according to numerical modeling [9], (*7*) boundary of decomposition of antigorite, and (*8*) areas of the lithospheric mantle with known PT-conditions of hydration.

The stability of antigorite in the $MgO–SiO_2–H_2O$ and $MgO–Al_2O_3–SiO_2–H_2O$ systems (reaction: antigorite = forsterite + clinoenstatite + water) is limited under the H_2O-saturated conditions by 630–650°C and 1.6 GPa and 620–660°C and 2.5 GPa. In the presence of Al_2O_3, this reaction occurs at 660–700°C and 2.0 GPa and 660–680°C and 2.9 GPa [8]. Similar restrictions for the stability of antigorite were obtained by other researchers [9, 10, 12], who showed its decomposition (transit to chlorite) at 680–710°C and 1.6–1.9 GPa.

The metamorphic conditions inferred from the study of real geological objects [11, 12] are quite consistent with the results of experiments and numerical modeling of hydration of ultramafic rocks at various temperature and pressures [9, 10, 14]. The olivine–antigorite and olivine–chlorite assemblages are formed and remain stable at depths up to 100 km at temperatures up to 650–700°C and represent the most typical ultramafic metamorphic rocks of the subducted slab along with chlorite and amphibole–olivine rocks.

Such a high-temperature metamorphism of peridotites is considered by these works as a progressive process, which occurs in the course of submergence of the rocks with an increase in temperature and pressure.

Dehydration of serpentinites and sediments in the slab causes the formation of the H_2O-dominant volatile flow. It rises to the rocks of the mantle wedge above the slab and stimulates the high-temperature hydration of peridotites at depths of 100–20 km. The change in the $\mathrm{Ol}_{\mathrm{Mg\#90{-}91}} + \mathrm{En}_{\mathrm{Mg\#90{-}91}} \pm \mathrm{Prg}_{\mathrm{Mg\#91{-}94}}$ to $\mathrm{Ol}_{\mathrm{Mg\#87{-}88}} \pm \mathrm{Prg}_{\mathrm{Mg\#94}} \pm \mathrm{Trem}_{\mathrm{Mg\#96}} \pm \mathrm{Antg}_{\mathrm{Mg\#94{-}95}}$ assemblage is one of the earliest metamorphic reactions in peridotites of the Voykar–Synya massif. The minerals were analyzed on a JEOL-8230 microprobe (ISTerre, Grenoble, France, analyst V.G. Batanova). On the basis of this composition, thermodynamic calculations by M.V. Merkulova (the Theriak-Domino software package for thermodynamic modeling on the basis of the Gibbs energy minimization) showed that harzburgites and lherzolites with rare pargasite are stable at 1.5–1.2 GPa and 900–850°C. In the presence of water vapors, the decrease in the temperature and pressure results in the formation of metamorphic assemblages, whose stability is limited to 1.2–0.9 GPa and 600–550°C.

Figure schematically shows the location of the areas of formation of ultramafic metamorphic rocks in the suprasubduction mantle wedge and the areas of stability of anrigorite serpentinites and chlorite harzburgites after [9–11]. Taking into consideration the estimations of hydration of peridotites and the above data on the Polar Urals, we may state that the early hydration reaction of primary peridotites starts at ~1.5 GPa (depth of 50–60 km) and 650–600°C. The position of the mantle domain, where the hydration of peridotites began in the mantle wedge, is marked by circles 1 and 2 (figiure). The close position of domains 1 and 2 reflects the sharp (within several meters) change in the metamorphic assemblages in the top of the zones where the amphibole–antigorite–olivine rocks were replaced by talc–antigorite–olivine rocks with various amounts of two–three generations of high-Mg amphibole and two generations of olivine. Areas 3 and 4 demonstrate the mantle domains at the depths of 30–35 and 20–15 km above the subducted slab. They are mostly composed of antigorite–olivine rocks: massive with small relics of fresh peridotites (domain 3) and olivine–antigorite schists (domain 4).

The formation of the hydration front was accompanied by an increase in the volume of rocks and temperature. These processes increase the ductility of the mantle masses, and the ductile olivine–antigorite schists served as the "rails" for the extrusion of the mantle deep masses to the upper crustal horizons. In the numerical model of layering and uplift of the oceanic crust in the suprasubduction area, the leading role belongs to the weakened serpentinite horizon [15]. Our case is principally distinct from this model in that the detachment process at the crust–mantle boundary occurs in the mantle wedge in the suprasubduction zone rather than in the subducted slab. Most likely, this explains the presence of the giant poorly disintegrated masses of mantle peridotites in the Polar Ural ophiolites. As peridotites are extruded to the crust, the temperature and the total pressure of hydration decrease, but the fluid pressure and stress in the local near-foot zones increase.

The generalized serpentinization reaction olivine + enstatite + H_2O = serpentine + magnetite + H_2 in the $MgO–FeO–SiO_2–H_2O$ system is accompanied by release of hydrogen both in the crustal conditions (low-temperature lizardite–chrysotile serpentinization) and, probably, the lithospheric mantle of the subduction area, where antigorite is formed (high-temperature serpentinization). This hydrogen takes part in abiogenic synthesis of methane in the presence of CO_2 dissolved in water and also initiates hydrogen metabolism in marine conditions: its consumption by prokaryotes with further release of methane [6, 13]. This affects greatly the increase in the amount of methane generated during serpentinization of peridotites in the ocean and backarc and forearc basins in the suprasubduction geodynamic setting.

The formation of hydrogen and methane during serpentinization of mantle peridotites is used by many researchers for substantiation of the hypothesis of the abiogenic origin of oil and interpretation of the geodynamic models of the petroleum potential of various basins [2–4].

ACKNOWLEDGMENTS

This work was supported by the Russian Foundation for Basic Research (project no. 13-05-136) and the Leading Scientific Schools (project no. NSh-2981.2014.5).

REFERENCES

1. I. A. Belousov, V. G. Batanova, G. N. Savelieva, and A. V. Sobolev, Dokl. Earth Sci. **429** (8), 238–243 (2009).
2. L. V. Dmitriev, B. A. Bazylev, M. V. Borisov, et al., Ross. Zh. Nauk Zemle **1** (6), 1–13 (1999).
3. V. P. Gavrilov, Geol. Nefti Gaza, No. 3, 60–68 (2012).
4. Yu. N. Raznitsin, Geotectonics **46** (1), 1–15 (2012).
5. G. N. Savelieva, "Ural gabbro-ultrabasite complexes of ophiolites and their analogues in recent oceanic crust," in *Scientific Works of Geological Institute of the USSR Acad. Sci.* (Nauka, Moscow, 1987), Issue 404 [in Russian].
6. M. A. Fedonkin, in *Problems on Genesis and Evolution of Biosphere*, Ed. by E. M. Galimov (Librokom, Moscow, 2008), pp. 417–437 [in Russian].
7. V. Batanova, I. Belousov, G. Savelieva, and A. Sobolev, J. Petrol. **52** (12), 2483–2521 (2011).
8. G. D. Bromiley and A. R. Pawley, Am. Mineral. **88**, 99–108 (2003).
9. T. V. Gerya and D. A. Yuen, Earth Planet. Sci. Lett. **212**, 47–62 (2003).
10. B. R. Hacker, S. M. Peacock, G. A. Abers, and S. D. Holloway, J. Geophys. Res.: Solid Earth **108** (B1), 2029 (2003).
11. J. A. Padron-Navarta, V. L. Sancehz-Vizchaino, C. J. Garrido, and M.-T. Gomez-Pugnaire, J. Petrol. **19**, 1–32 (2011).
12. F. Rossetti, J. Glodny, T. Theyec, and M. Maggi, Lithos, No. 218/219, 99–116 (2015).
13. N. H. Sleep, A. Melbom, Th. Fridriksson, R. G. Coleman, and D. K. Bird, Proc. Natl. Acad. Sci. USA **101** (35), 12818–12823 (2004).
14. V. Trommsdorff, V. Lopez Sanchez-Vizcano, M. T. Gomez-Pugnair, and O. Muntener, Contrib. Mineral. Petrol. **132**, 139–148 (1998).
15. K. Vogt and T. V. Gerya, Geology **42** (8), 723–726 (2014). doi: 10.1130/G35565.1

Translated by I. Melekestseva

Conclusions and perspectives

Conclusions

The main goal of this PhD thesis was to understand the mechanisms of serpentinite dehydration, the chemistry of the slab-derived fluid and the redox conditions in subduction zones. The experimental approach with well-defined P-T and fO_2 conditions of experimental runs and numerous analytical methods allowed to accurately describe mineral modes, mineral chemistry, bulk rock composition and speciation of Fe and S in the *ex-situ* and *in-situ* produced assemblages. The experimental results were extrapolated to natural subduction zone settings.

Main results and conclusions obtained in the present work are summarized in the following paragraphs:

Modelling of Fe-bearing systems

Detailed P-T diagram in CFMASH (CaO-FeO-MgO-Al_2O_3-SiO_2-H_2O) system for ultramafic phase relations was defined experimentally and thermodynamically with introduced Fe-bearing antigorite. CFMASH chemical system corresponds to natural serpentinized peridotite compositions and includes such common in metaperidotites minerals as clinopyroxene, chlorite and garnet. Stability of Fe-bearing antigorite was constrained and Fe content was demonstrated to reduce the upper thermal stability limit of antigorite compared to that in pure Mg-systems.

Effect of bulk composition on serpentinite dehydration

Increase of bulk Fe content was shown to decrease temperature of serpentinite dehydration and consequently depths of water release. The presence of Al in serpentinites was shown to stabilize chlorite up to 800°C. The higher thermal stability of chlorite compared to that of antigorite implies the retain of H_2O in metaperidotites after antigorite breakdown and release of 20 % H_2O initially contained in serpentinite at deep parts of subduction.

Assessment of potential correlation between dehydration regimes and seismicity

Thermodynamic models of water release regime at two common geothermal gradients corresponding to “hot” and “cold” subduction zones were constrained. The comparison between water-release depth profiles and focal depths in two different subduction zones demonstrated that, depending on the angle of subduction and the PT conditions in the slab, the contribution of serpentinite dehydration to seismicity can be highly contrasted. A clear correlation between depths of dehydration and of peak seismic activity in hot subduction zones strongly contrasts with the absence of such a correlation in cold subduction zones.

Speciation of Fe during serpentinite dehydration

Progressive reduction of Fe in experiments at relatively low fO_2 (QFM-2) was observed during dehydration of serpentinites. Main Fe^{3+}-bearing phases, magnetite and antigorite, break down at 550°C and 700°C respectively at 2 GPa, and form Fe^{2+}-bearing assemblages of mainly olivine and orthopyroxene. Initially high Fe^{3+}/Fe_{total}, equaled to 0.9, of serpentinites drops down to 0.15 in fully dehydrated metaperidotites. The Fe reduction progresses in a lower extent in nature, however, the trend of the reduction and redox reactions, involving antigorite and magnetite, are similar to those in experiment.

Speciation and mobility of S during serpentinite dehydration

Sulfur, present in serpentinites in form of pyrite, was shown to be reduced at 450°C. Reduction of S occurs through pyrite-to-pyrrhotite reaction. In addition, 25% of S was mobilized, i.e. volatilized, most-likely in form of H_2S, according to experimental and thermodynamic results. These results provide evidence that sulfur might not necessary be oxidized in order to be released from serpentinites, however, fO_2 for such a release should be below QFM buffer.

Consequences of Fe and S reduction

Reduction of Fe and S during serpentinite dehydration was shown to be driven by the presence of reduced species in both, experimental setup and in natural conditions. Oxygen was assumed to be the main electron-transfer. Thus, the oxidizing potential of serpentinites was quantified by means of oxygen, transferred from initially oxidized serpentinites to reduced species. Demonstrated high redox capacity of oceanic serpentinites might result in a release of oxidized fluid at depths relevant for serpentinite dehydration. Moreover, fluid released at depths of ~70 km is about 15 times more oxidized and may carry more fluid mobile elements in comparison to the fluid formed at deeper levels (~120 km) of a common flat ("hot") subduction. Such a different composition of released aqueous fluid along subducting slab may explain a wide range of redox conditions from fore-arc to deep mantle.

Importance of subduction zone redox cycle

Compilation of all redox processes including oceanic peridotite serpentinization, serpentinite dehydration and mantle wedge hydration implies a large-scale subduction zone redox cycle. Aqueous fluid is the main agent that transports the redox potential from one part of subduction zone to another, and plays a major role in a number of subduction zone processes. In particular, the ability of oxidized aqueous fluid to transport elements of economic interest (e.g., Au, Pt, Cu, Ag, W, Mo, U) from subducted slab to the overlying mantle leads to ore-deposits formation. The volatilization of sulfur species in the fluid facilitates the mobility of mentioned elements in form of sulfur complexes. The hydration and oxidation of the mantle wedge is accompanied by a release of hydrogen in fore-arc settings and may lead to abiogenic synthesis of methane and genesis of oil. Not less important, the release of aqueous fluid from the slab is linked to generation of subduction zone seismicity. In addition, the large volume of the aqueous fluid liberated at deep parts of subduction results in partial melting of mantle and a birth of arc volcanism.

In conclusion, this study demonstrates that experimental approach can be successfully applied to investigate mechanisms of serpentinite dehydration and redox changes in subduction zones. Precise knowledge about experimental setup conditions, such as pressure, temperature and fO_2, are required to extrapolate laboratory observations to natural settings.

Perspectives

A number of studies, including the present thesis, has uncovered questions regarding dehydration process and redox changes in subduction zones. However, many unsolved problems still remain on the subject. Few suggestions for future investigations and possible technical improvements are listed as follows:

1. Dehydration of Fe^{3+}-bearing serpentinites should be examined experimentally at various oxygen fugacity conditions. Present experimental work demonstrated results obtained at fO_2 QFM-2. However, fO_2 in subduction zone settings can vary from QFM+1 to QFM-2. Such a range of fO_2 might cause significant discrepancies in mineral chemistry, redox reactions and water release between assemblages produced in reduced and oxidized conditions.

2. Evolution of serpentinite, containing magnetite together with sulfides (pyrite, pyrrhotite), must be investigated at the conditions of subduction zone dehydration. Coexistence of magnetite and sulfide phase in serpentinite may cause oxidation of sulfur to sulfate/SO_2, if fO_2 > QFM. Another possible scenario is that pyrite+pyrrhotite+magnetite (PPM buffer) assemblage will be stable along the whole range of P-T conditions relevant for subduction zones. The latter statement indicates that in case of coexisting magnetite with sulfide, the redox evolution of serpentinite may have a totally different trend in comparison with results presented in this work.

3. Relations between serpentinites with overlying sediments and metabasalts have to be investigated. As it was shown in the present work, serpentinites have a great redox potential and may be capable to oxidize overlying crust. The presence of reduced species (S, C, Fe, H) in oceanic crust may drive reduction of Fe in serpentinites. Thus, assessment of oceanic crust reducing potential will demonstrate the proposed hypothesis. Additionally, buffered experiments on dehydration of serpentinite, placed in contact with a block of sediment/metabasalt, can be carried out. Coincident reduction of serpentinite and oxidation of sediments will proove the suggested above assumption.

4. Lizardite-antigorite transition, another intriguing observation, which was not completely understood within the present study, has to be studied in more details. Heterogeneity of natural serpentine samples, slow kinetics of the transition and difficulties in lizardite and antigorite analytical discrimination complicate and limit *in-situ* experimental observations. The choice of pure lizardite starting material and the use of Raman spectroscopy together with *in-*

situ XAS measurements may facilitate characterization of two minerals. The author has an opportunity to perform in-situ experiments on lizardite-antigorite transition with suggested improvements during the beamtime (ESRF, Grenoble) in October 2016. Moreover, ex-situ experiments can be performed, which allow the use of bigger sample volume, and can be carried out with long duration.

5. *In-situ* dehydration experiments in diamond-anvil cells still remain challenging because of big uncertainties on P and T, slow kinetics of some mineral reactions, small sample size and therefore low element (in particular Fe) concentration. Moreover, diamond anvils significantly absorb X-rays at energies of Fe K-edge, which lower the quality of XANES spectra. And the use of single-crystal diamonds-anvils may cause appearance of unwanted Bragg peaks on XANES spectra. Thus, the implication of perforated nano-crystal diamonds, more concentrated samples and improvements in P and T maintenance will provide invaluable results obtained from in-situ dehydration experiments.

6. To investigate the fractionation of sulfur isotopes in subduction zone settings future experiments and measurements are required to be performed. No accurate data is available to describe loss/gain of heavy sulfur isotope. Experiments on reduction/oxidation of sulfur and further sulfur isotope measurements of experimental products will provide helpful information about the sulfur volatile species formed during serpentinite dehydration.

To constrain different types of pseudosections describing realistic dehydration of serpentinite, antigorite solid solution should be improved, Fe^{3+}-bearing chlorite and sulfates should be introduced to the datasets. Thermodynamic modeling is a necessary tool that supports experimental results. Mentioned advances in thermodynamic calculations and thermodynamic datasets will upgrade the level of the modeling.

References

Abers, G.A., Nakajima, J., van Keken, P.E., Kita, S., Hacker, B.R., 2013. Thermal-petrological controls on the location of earthquakes within subducting plates. Earth and Planetary Science Letters 369-370, 178-187.

Alonso-Azcarate, J., Rodas, M., Bottrell, S.H., Raiswell, R., Velasco, F., Mas, J.R., 1999. Pathways and distances of fluid flow during low-grade metamorphism: evidence from pyrite deposits of the Cameros Basin, Spain. Journal of Metamorphic Geology 17, 339-348.

Alt, J.C., Garrido, C.J., Shanks, W.C., Turchyn, A., Padrón-Navarta, J.A., López Sánchez-Vizcaíno, V., Gómez Pugnaire, M.T., Marchesi, C., 2012. Recycling of water, carbon, and sulfur during subduction of serpentinites: A stable isotope study of Cerro del Almirez, Spain. Earth and Planetary Science Letters 327-328, 50-60.

Alt, J.C., Schwarzenbach, E.M., Früh-Green, G.L., Shanks, W.C., Bernasconi, S.M., Garrido, C.J., Crispini, L., Gaggero, L., Padrón-Navarta, J.a., Marchesi, C., 2013. The role of serpentinites in cycling of carbon and sulfur: Seafloor serpentinization and subduction metamorphism. Lithos 178, 40-54.

Andreani, M., Muñoz, M., Marcaillou, C., Delacour, A., 2013. µXANES study of iron redox state in serpentine during oceanic serpentinization. Lithos 178, 70-83.

Arculus, R.J., 1985. Oxidation status of the mantle: past and present. Annual Review of Earth and Planetary Sciences 13, 75-95.

Auzanneau, E., Schmidt, M.W., Vielzeuf, D., D Connolly, J.A., 2010. Titanium in phengite: A geobarometer for high temperature eclogites. Contributions to Mineralogy and Petrology 159, 1-24.

Bach, W., Paulick, H., Garrido, C.J., Ildefonse, B., Meurer, W.P., Humphris, S.E., 2006. Unraveling the sequence of serpentinization reactions: Petrography, mineral chemistry, and petrophysics of serpentinites from MAR 15??N (ODP Leg 209, Site 1274). Geophysical Research Letters 33, 4-7.

Bali, E., Audetat, A., Keppler, H., 2011. The mobility of U and Th in subduction zone fluids : an indicator of oxygen fugacity and fluid salinity. Contributions to Mineralogy and Petrology 161, 597-613.

Bassett, W.A., Shen, A.H., Bucknum, M., Chou, I.-M., 1993. A new diamond anvil cell for hydrothermal studies to 2.5 GPa and from −190 °C to 1200 °C. Review of Scientific Instruments 64, 2340-2345.

Bassett, W.A., Wu, T.C., Chou, I.-M., Haselton, H.T., Jr., Frantz, J., Mysen, B.O., Huang, W.L., Sharma, K., Schiferl, D., 1996. The hydrothermal diamond anvil cell (HDAC) and its applications, 261–272 in: Mineral spectroscopy: A Tribute to Roger G. Burns (M.D. Dyar, C. McCammon & M.W. Schaefer, editors), The Geochemical Society, Special Publication no. 5.

Batanova, V.G., Belousov, I.a., Savelieva, G.N., Sobolev, a.V., 2011. Consequences of Channelized and Diffuse Melt Transport in Supra-subduction Zone Mantle: Evidence from the Voykar Ophiolite (Polar Urals). Journal of Petrology 52, 2483-2521.

Beard, J.S., Frost, B.R., Fryer, P., McCaig, a., Searle, R., Ildefonse, B., Zinin, P., Sharma, S.K., 2009. Onset and progression of serpentinization and magnetite formation in olivine-rich troctolite from IODP hole U1309D. Journal of Petrology 50, 387-403.

Bergmann, J., Friedel, P., Kleeberg, R., 1998. BGMN - a new fundamental parameters based Rietveld program for laboratory X-ray sources, it's use in quantitative analysis and structure investigations. Commission on powder Diffraction Newsletter 20, 5-8.

Bose, K., Ganguly, J., 1995. Antigorite and phase A at high pressures with applications to subduction processes. Earth and Planetary Science Letters 136, 109-121.

Boudier, F., Nicolas, A., 1985. Harzburgite and lherzolite subtypes in ophi- olitic and oceanic environments. Earth and Planetary Science Letters 76, 84-92.

Brandon, A.D., Draper, D.S., 1996. Constraints on the origin of the oxidation state of mantle overlying subduction zones: An example from Simcoe, Washington, USA. Geochimica et Cosmochimica Acta 60, 1739-1749.

Bromiley, G.D., Pawley, A.R., 2003. The stability of antigorite in the systems Mg-SiO_2-H_2O (MSH) and MgO-Al_2O_3-SiO_2-H_2O (MASH): The effects of Al^{3+} substitution on high-pressure stability. American Mineralogist 88, 99-108.

Brunet, F., Bagdassarov, N., Miletich, R., 2003. $Na_3Al_2(PO_4)_3$, a fast sodium conductor at high pressure: *In-situ* impedance spectroscopy characterisation and phase diagram up to 8 GPa. Solid State Ionics 159, 35-47.

Bunker, G., 2010. Introduction to XAFS - A practical guide to X-ray absorption fine structure spectroscopy. Cambridge Press.

Capitani, C.D.E., Brown, T.H., 1987. The computation of chemical equilibrium in complex systems containing non-ideal solutions. Geochimica et Cosmochimica Acta 51, 2639-2652.

Capitani, G., Mellini, M., 2004. The modulated crystal structure of antigorite: the m= 17 polysome. American Mineralogist 89, 147-158.

Chou, I.-M., 1986. Permeability of precious metals to hydrogen at 2 kb total pressure and elevated temperatures. American Journal of Science 286, 638-658.

Christensen, N.I., 1972. The abundance of serpentinites in the oceanic crust. Journal of Geology 80, 709-719.

Cooke, D., Simmons, S.F., 2000. Characteristics and genesis of epithermal gold deposits. Reviews in Economic Geology 13, 221-244.

de Capitani, C., Petrakakis, K., 2010. The computation of equilibrium assemblage diagrams with Theriak/Domino software. American Mineralogist 95, 1006-1016.

de Hoog, J.C.M., Hattori, K., Jung, H., 2014. Titanium- and water-rich metamorphic olivine in high-pressure serpentinites from the Voltri Massif (Ligurian Alps, Italy): evidence for deep subduction of high-field strength and fluid-mobile elements. Contributions to Mineralogy and Petrology 167, 990.

de Hoog, J.C.M., Mason, P.R.D., van Bergen, M.J., 2001. Sulfur and chalcophile elements in subduction zones: constraints from a laser ablation ICP-MS study of melt inclusions from Galunggung Volcano, Indonesia. Geochimica et Cosmochimica Acta 65, 3147-3164.

Debelmas, J., Giraud, P., Sacchi, R., 1980. Excursion 25 Géologie structurale des Alpes franco-italiennes. Geologie Alpine 56, 99-117.

Debret, B., Andreani, M., Muñoz, M., Bolfan-Casanova, N., Carlut, J., Nicollet, C., Schwartz, S., Trcera, N., 2014. Evolution of Fe redox state in serpentine during subduction. Earth and Planetary Science Letters 400, 206-218.

Debret, B., Bolfan-Casanova, N., Padrón-Navarta, J.A., Martin-Hernandez, F., Andreani, M., Garrido, C.J., López Sánchez-Vizcaíno, V., Gómez-Pugnaire, M.T., Muñoz, M., Trcera, N., 2015. Redox state of iron during high-pressure serpentinite dehydration. Contributions to Mineralogy and Petrology 169:36.

Debret, B., Millet, M.-A., Pons, M.-L., Bouilhol, P., Inglis, E., Williams, H., 2016. Isotopic evidence for iron mobility during subduction. Geology 44, 215-218.

Du, Z.X., Miyagi, L., Amulele, G., Lee, K.K.M., 2013. Efficient graphite ring heater suitable for diamond-anvil cells to 1300 k. Review of Scientific Instruments 84, 024502.

Delacour, A., Früh-Green, G.L., Bernasconi, S.M., 2008. Sulfur mineralogy and geochemistry of serpentinites and gabbros of the Atlantis Massif (IODP Site U1309). Geochimica et Cosmochimica Acta 72, 5111-5127.

Deschamps, F., Godard, M., Guillot, S., Chauvel, C., Andreani, M., Hattori, K., Wunder, B., France, L., 2012. Behavior of fluid-mobile elements in serpentines from abyssal to subduction environments: Examples from Cuba and Dominican Republic. Chemical Geology 312-313, 93-117.

Deschamps, F., Godard, M., Guillot, S., Hattori, K., 2013. Geochemistry of subduction zone serpentinites: A review. Lithos 178, 96-127.

Diener, J.F.a., Powell, R., 2010. Influence of ferric iron on the stability of mineral assemblages. Journal of Metamorphic Geology 28, 599-613.

Eiler, J. (Ed.), 2003. Inside the Subduction Factory, GeophysicalMonograph Series, 138. AGU, Washington D.C., 293–309.

Elliott, T., Plank, T., Zindler, A., White, W., Bourdon, B., 1997. Element transport from slab to volcanic front at the Mariana arc. Journal of geophysical research 102, 14991-15019.

Evans, B.W., 2004. The Serpentinite Multisystem Revisited: Chrysotile Is Metastable. International Geology Review 46, 479-506.

Evans, B.W., 2008. Control of the products of serpentinization by the $Fe^{2+}Mg_{-1}$ exchange potential of olivine and orthopyroxene. Journal of Petrology 49, 1873-1887.

Evans, B.W., 2010. Lizardite versus antigorite serpentinite: Magnetite, hydrogen, and life(?). Geology 38, 879-882.

Evans, B.W., Dyar, M.D., Kuehner, S.M., 2012. Implications of ferrous and ferric iron in antigorite. American Mineralogist 97, 184-196.

Evans, B.W., Johannes, W., Oterdom, H., Trommsdor, V., 1976. Stability of chrysotile and antigorite in the serpentinite multisystem. Schweizerische Mineralogische und Petrographische Mitteilungen 56, 79-93.

Evans, K.A., 2012. The redox budget of subduction zones. Earth Science Reviews 113, 11-32.

Evans, K.A., Elburg, M.A., Kamenetsky, V.S., 2012b. Oxidation state of subarc mantle. Geology 40, 783-786.

Evans, K.A., Powell, R., 2015. The effect of subduction on the sulphur, carbon and redox budget of lithospheric mantle. Journal of Metamorphic Geology 33, 649-670.

Evans, K.A., Powell, R., Frost, B.R., 2013. Using equilibrium thermodynamics in the study of metasomatic alteration, illustrated by an application to serpentinites. Lithos 168-169, 67-84.

Evans, K.A., Tomkins, A.G., Cliff, J., Fiorentini, M.L., 2014. Insights into subduction zone sulfur recycling from isotopic analysis of eclogite-hosted sulfides. Chemical Geology 365, 1-19.

Faccenda, M., Gerya, T.V., Mancktelow, N.S., Moresi, L., 2012. Fluid flow during slab unbending and dehydration: Implications for intermediate-depth seismicity, slab weakening and deep water recycling. Geochemistry, Geophysics, Geosystems 13.

Frost, B.R., 1985. On the stability of sulfides, oxides, and native metals in serpentinite. Journal of Petrology 26, 31-63.

Frost, D.J., Mccammon, C.A., 2008. The Redox State of Earth’s Mantle. Annual Review of Earth and Planetary Sciences 36, 389-420.

Fujii, T., 2015. The fate of sulfate mineral during subduction to the deep mantle. The 432 Geodynamics seminar.

Funamori, N., Sato, T., 2008. A cubic boron nitride gasket for diamond-anvil experiments. Review of Scientific Instruments 79, 053903. doi: 053910.051063/053901.2917409.

Ganguly, J., 2008. Thermodynamics in Earth and Planetary Sciences.

Gasc, J., Schubnel, A., Brunet, F., Guillon, S., Mueller, H.J., Lathe, C., 2011. Simultaneous acoustic emissions monitoring and synchrotron X-ray diffraction at high pressure and temperature: Calibration and application to serpentinite dehydration. Physics of the Earth and Planetary Interiors 189, 121-133.

Gerya, T., Yuen, D.A., 2003. Rayleigh–Taylor instabilities from hydration and melting propel ‘cold plumes’ at subduction zones. Earth and Planetary Science Letters 212, 47-62.

Guillot, S., Hattori, K., de Sigoyer, J., Nagler, T., Auzende, A.L., 2001. Evidence of hydration of the mantle wedge and its role on the exhumation of eclogites. Earth and Planetary Science Letters 193, 115-127.

Hacker, B.R., 2003. Subduction factory 1. Theoretical mineralogy, densities, seismic wave speeds, and H 2 O contents. Journal of Geophysical Research 108, 2029.

Hacker, B.R., Peacock, S.M., Abers, G.A., Holloway, S.D., 2003. Subduction factory 2. Are intermediate-depth earthquakes in subducting slabs linked to metamorphic dehydration reactions? Journal of Geophysical Research: Solid Earth 108, 11-1-11-8.

Hall, A.J., 1986. Pyrite-Pyrrhotine Redox Reactions in Nature. Mineralogical Magazine 50, 223-229.

Hattori, K.H., Guillot, S., 2003. Volcanic fronts form as a consequence of serpentinite dehydration in the forearc mantle wedge. Geology 31, 525-528.

Hattori, K.H., Guillot, S., 2007. Geochemical character of serpentinites associated with high- to ultrahigh-pressure metamorphic rocks in the Alps, Cuba, and the Himalayas: Recycling of elements in subduction zones. Geochemistry, Geophysics, Geosystems 8:9.

Holland, T.J.B., 1989. Dependence of entropy on volume for silicate and oxide minerals; a review and predictive model. American Mineralogist 74, 5-13.

Holland, T.J.B., Powell, R., 1998. An internally consistent thermodynamic data set for phases of petrological interest. Journal of Metamorphic Geology 16, 309-343.

Jager, E., Hunziker, J.C., 1979. Lectures in Isotope Geology. Springer.

Jarosewich, E., 2002. Smithsonian Microbeam Standards. Journal of Research of the National Institute of Standards and Technology 107, 681.

Jeanloz, R., Heinz, D.L., 1984. Experiments at high temperature and pressure: laser heating through the diamond cell. Journal de Physique Colloques 45, C8-83-C88-92.

Jégo, S., Dasgupta, R., 2013. Fluid-present melting of sulfide-bearing ocean-crust: Experimental constraints on the transport of sulfur from subducting slab to mantle wedge. Geochimica et Cosmochimica Acta 110, 106-134.

Kelemen, P.B., Hanghøj, K., Greene, a.R., 2013. One View of the Geochemistry of Subduction-Related Magmatic Arcs, with an Emphasis on Primitive Andesite and Lower Crust. Treatise on Geochemistry: Second Edition 4, 749-806.

Kelley, K.A., Cottrell, E., 2009. Water and the Oxidation State of Subduction Zone Magmas, Science, pp. 605-607.

Kerrick, D., 2002. Geology. Serpentinite seduction. Science 298, 1344-1345.

Kerrick, D.M., Connolly, J.A.D., 2001a. Metamorphic devolatilization of subducted marine sediments and the transport of volatiles into the Earth ' s mantle. 36, 293-296.

Kerrick, D.M., Connolly, J.A.D., 2001b. Metamorphic devolatilization of subducted oceanic metabasalts: implications for seismicity, arc magmatism and volatile recycling. Earth and Planetary Science Letters 189, 19-29.

Kessel, R., Schmidt, M.W., Ulmer, P., Pettke, T., 2005. Trace element signature of subduction-zone fluids, melts and supercritical liquids at 120-180 km depth. Nature 437, 724-727.

King, R.L., Bebout, G.E., Kobayashi, K., Nakamura, E., van der Klauw, S.N.G.C., 2004. Ultrahigh-pressure metabasaltic garnets as probes into deep subduction zone chemical cycling. Geochemistry, Geophysics, Geosystems 5, Q12J14.

Krishnakanta Singh, a., 2013. Petrology and geochemistry of Abyssal Peridotites from the Manipur Ophiolite Complex, Indo-Myanmar Orogenic Belt, Northeast India: Implication for melt generation in mid-oceanic ridge environment. Journal of Asian Earth Sciences 66, 258-276.

Lamberg, P., Hautala, P., Sotka, P., Saavalainen, S., 1997. Mineralogical balances by dissolution methodology. Paper presented at IMA Commission on Ore Mineralogy Short Course, S. Mamede de Infesta, Portugal, 1-29.

Letoullec, R., Pinceaux, J.P., Loubeyre, P., 1988. The membrane diamond anvil cell: A new device for generating continuous pressure and temperature variations. High Pressure Research 1, 77-90.

Li, X.-P., Rahn, M., Bucher, K., 2004. Serpentinites of the Zermatt-Saas ophiolite complex and their texture evolution. Journal of Metamorphic Geology 22, 159-177.

López Sánchez-Vizcaíno, V., Trommsdorff, V., Gómez-Pugnaire, M.T., Garrido, C.J., Müntener, O., Connolly, J.a.D., 2005. Petrology of titanian clinohumite and olivine at the high-pressure breakdown of antigorite serpentinite to chlorite harzburgite (Almirez Massif, S. Spain). Contributions to Mineralogy and Petrology 149, 627-646.

Lopez, O.G., Cottrell, E., Warren, J.M., Sciences, P., 2012. T51D-2632: Upper mantle oxygen fugacity in ridge and subduction zone settings recorded by spinel peridotite. AGU Fall meeting, 2012.

Loubeyre, P., Occelli, F., LeToullec, R., 2002. Optical studies of solid hydrogen to 320 GPa and evidence for black hydrogen. Nature 416, 613-617.

Mandeville, C.W., 2010. Sulfur: a ubiquitous and useful tracer in Earth and planetary sciences. Elements 6, 75-80.

Manning, C.E., 2011. Sulfur Surprises in Deep Geological Fluids. Science 331, 1018 - 1019.

Marcaillou, C., Muñoz, M., Vidal, O., Parra, T., Harfouche, M., 2011. Mineralogical evidence for H2 degassing during serpentinization at 300°C/300bar. Earth and Planetary Science Letters 303, 281-290.

Marchesi, C., Garrido, C.J., Padrón-Navarta, J.A., López Sánchez-Vizcaíno, V., Gómez-Pugnaire, M.T., 2013. Element mobility from seafloor serpentinization to high-pressure dehydration of antigorite in subducted serpentinite: Insights from the Cerro del Almirez ultramafic massif (southern Spain). Lithos 178, 128-142.

Masanori, M., Yuji, H., Yoshihiro, O., Tetsuo, I., Ken Ichi, F., 2012. Simultaneous sound velocity and density measurements of NaCl at high temperatures and pressures: Application as a primary pressure standard. American Mineralogist 97, 1670-1675.

Mellini, M., 1982. The crystal structure of lizardite-1T: Hydrogen bonds and polytypism. American Mineralogist 67, 587-598.

Mellini, M., Trommsdorff, V., Compagnoni, R., 1987. Antigorite polysomatism: behaviour during progressive metamorphism. Contributions to Mineralogy and Petrology 97, 147-155.

Merkel, S., Wenk, H.R., Shu, J., Shen, G., Philippe, G., Mao, H.-k., Hemley, R.J., 2002. Deformation of polycrystalline MgO at pressures of the lower mantle. Journal of Geophysical Research 107, 2271.

Merkulova, M., Muñoz, M., Vidal, O., Brunet, F., 2016. Role of iron content on serpentinite dehydration depth in subduction zones: experiments and thermodynamic modeling. Lithos 264, 441-452.

Mével, C., 2003. Serpentinization of abyssal peridotites at mid-ocean ridges. Comptes Rendus Geoscience 335, 825-852.

Moore, G., Roggensack, K., Klonowski, S., 2008. A low-pressure-high- temperature technique for the piston-cylinder. American Mineralogist 93, 48-52.

Morard, G., Mezouar, M., Rey, N., Poloni, R., Merlen, A., Le Floch, S., Toulemonde, P., Pascarelli, S., San-Miguel, A., Sanloup, C., Fiquet, G., 2007. Optimization of Paris-Edinburgh press cell assemblies for *in-situ* monochromatic X-ray diffraction and X-ray absorption. High Pressure Research 27, 223-233.

Mungall, J.E., 2002. Roasting the mantle : Slab melting and the genesis of major Au and Au-rich Cu deposits. Geology 30, 915-918.

Muñoz, M., De Andrade, V., Vidal, O., Lewin, E., Pascarelli, S., Susini, J., 2006. Redox and speciation micromapping using dispersive X-ray absorption spectroscopy: application to iron in chlorite mineral of a metamorphic rock thin section. Geochemistry, Geophysics, Geosystems 7, 1-10.

Muñoz, M., Pascarelli, S., Aquilanti, G., Narygina, O., Kurnosov, A., Dubrovinsky, L., 2008. Hyperspectral μ -XANES mapping in the diamond-anvil cell : analytical procedure applied to the decomposition of (Mg , Fe) -ringwoodite at the upper / lower mantle boundary. High Pressure Research 28, 665-673.

Muñoz, M., Vidal, O., Marcaillou, C., Pascarelli, S., Mathon, O., Farges, F., 2013. Iron oxidation state in phyllosilicate single crystals using Fe-K pre-edge and XANES spectroscopy: Effects of the linear polarization of the synchrotron X-ray beam. American Mineralogist 98, 1187-1197.

Nestola, F., Angel, R.J., Zhao, J., Garrido, C.J., Sánchez-Vizcaíno, V.L., Capitani, G., Mellini, M., 2010. Antigorite equation of state and anomalous softening at 6 GPa: An in situ single-crystal X-ray diffraction study. Contributions to Mineralogy and Petrology 160, 33-43.

O'Hanley, D.S., Wicks, F.J., 1995. Conditions of formation of lizardite, chrysotile and antigorite, Cassiar, British Columbia. Canadian Mineralogist 33, 753-773.

Ogorodova, L., Melchakova, L., Kiseleva, I., Korytkova, E., 2009. Enthalpies of formation of minerals of serpentine group. Vestnik Otdelenia nauk o Zemle RAN 1, 2-3.

Ohmoto, H., Rye, R.O., 1979. Isotopes of sulfur and carbon. In: Barnes, H.L. (Ed.), Geochemistry of Hydrothermal Ore Deposits. John Wiley and Sons, New York. 509-567.

Okazaki, K., Hirth, G., 2016. Dehydration of lawsonite could directly trigger earthquakes in subducting oceanic crust. Nature 530, 81-84.

Padrón-Navarta, J.A., Hermann, J., Garrido, C.J., López Sánchez-Vizcaíno, V., Gómez-Pugnaire, M.T., 2010. An experimental investigation of antigorite dehydration in natural silica-enriched serpentinite. Contributions to Mineralogy and Petrology 159, 25-42.

Padrón-Navarta, J.A., Lopez Sanchez-Vizcaíno, V., Garrido, C.J., Gomez-Pugnaire, M.T., 2011. Metamorphic Record of High-pressure Dehydration of Antigorite Serpentinite to Chlorite Harzburgite in a Subduction Setting (Cerro del Almirez, Nevado-Filabride Complex, Southern Spain). Journal of Petrology 52, 2047-2078.

Padrón-Navarta, J.A., Sánchez-Vizcaíno, V.L., Hermann, J., Connolly, J.a.D., Garrido, C.J., Gómez-Pugnaire, M.T., Marchesi, C., 2013. Tschermak's substitution in antigorite and consequences for phase relations and water liberation in high-grade serpentinites. Lithos 178, 186-196.

Parkinson, I.J., Arculus, R.J., 1999. The redox state of subduction zones: insights from arc-peridotites. Chemical Geology 160, 409-423.

Peacock, S.M., 2001. Are the lower planes of double seismic zones caused by serpentine dehydration in subducting oceanic mantle? Geology 29, 299.

Peacock, S.M., van Keken, P.E., Holloway, S.D., Hacker, B.R., Abers, G.A., Fergason, R.L., 2005. Thermal structure of the Costa Rica – Nicaragua subduction zone. Physics of the Earth and Planetary Interiors 149, 187-200.

Perrillat, J., Daniel, I., Koga, K., Reynard, B., Cardon, H., Crichton, W., 2005. Kinetics of antigorite dehydration: A real-time X-ray diffraction study. Earth and Planetary Science Letters 236, 899-913.

Petitgirard, S., Jacobs, J., Garbarino, G., Dabin, Y., Perrillat, J.-P., Vitoux, H., Aracne, C., Farber, D.L., Mezouar, M., 2015. In preparation.

Plank, T., Langmuir, C.H., 1998. The chemical composition of subducting sediment and its consequences for the crust and mantle. Chemical Geology 145, 325-394.

Plümper, O., Beinlich, A., Bach, W., Janots, E., Austrheim, H., 2014. Garnets within geode-like serpentinite veins: Implications for element transport, hydrogen production and life-supporting environment formation. Geochimica et Cosmochimica Acta 141, 454-471.

Pokrovski, G.S., Dubrovinsky, L., 2011. The S3- ion is stable in geological fluids at elevated temperatures and pressures. Science 331, 1052-1054.

Pokrovski, G.S., Kokh, M.A., Guillaume, D., Borisova, A.Y., Gisquet, P., Hazemann, J.-l., Lahera, E., Del, W., Proux, O., Testemale, D., Haigis, V., Jonchière, R, Seitsonend, A.P, Ferlate, G, Vuilleumierd, R, Saittae, A.M, Boiron, M-C, Dubessy, J, 2015. Sulfur radical species form gold deposits on Earth. Proceedings of the National Academy of Science 112, 13484-13489.

Prescher, C., Prakapenka, V.B., 2015. DIOPTAS: a program for reduction of two-dimensional X-ray diffraction data and data exploration. High Pressure Research 7959, 1-8.

Ranero, C.R., Morgan, J.P., McIntosh, K., Reichert, C., 2003. Bending-related faulting and mantle serpentinization at the Middle America trench. Nature 425, 367-373.

Ravel, B., Newville, M., 2005. ATHENA, ARTEMIS, HEPHAESTUS: data analysis for X-ray absorption spectroscopy using IFEFFIT. Journal of Synchrotron Radiation 12, 537-541.

Ravna, E.J.K., Andersen, T.B., Jolivet, L., de Capitani, C., 2010. Cold subduction and the formation of lawsonite eclogite - constraints from prograde evolution of eclogitized pillow lava from Corsica. Journal of Metamorphic Geology 28, 381-395.

Ribeiro, J.M., Stern, R.J., Kelley, K.A., Martinez, F., Ishizuka, O., Manton, W.I., Ohara, Y., 2013. Nature and distribution of slab-derived fluids and mantle sources beneath the Southeast Mariana forearc rift. Geochemistry, Geophysics, Geosystems 14, 4585-4607.

Ribeiro, J.M., Stern, R.J., Kelley, K.A., Shaw, A.M., Martinez, F., Ohara, Y., 2015. Composition of the slab-derived fluids released beneath the Mariana forearc: Evidence for shallow dehydration of the subducting plate. Earth and Planetary Science Letters 418, 136-148.

Robie, R.A., Hemingway, B.S., 1995. Thermodynamic properties of minerals and related substances at 298.15 K and 1 bar (105 Pascals) pressure and higher temperatures. U.S. Geological survey Bulletin 2131, 458.

Rosa, A., Hilairet, N., Ghosh, S., Merkel, S., 2015. In situ monitoring of phase transformation microstructures at Earth's mantle pressure and temperature using multi-grain XRD. Journal of Applied Crystallography 48, 1-9.

Rosa, A., Sanchez-Valle, C., Nisr, C., Evans, S.R., Debord, R., Merkel, S., 2013. Shear wave anisotropy in textured phase D and constraints on deep water recycling in subduction zones. Earth and Planetary Science Letters 377, 13-22.

Rossetti, P., Glodny, J., Theye, T., Maggi, M., 2015. Pressure-temperature-deformation-time of the ductile Alpine shearing in Corsica: From orogenic construction to collapse. Lithos 218-219, 99-116.

Rüpke, L., 2004. Serpentine and the subduction zone water cycle. Earth and Planetary Science Letters 223, 17-34.

Scambelluri, M., Müntener, O., Ottolini, L., Pettke, T.T., Vannucci, R., 2004. The fate of B, Cl and Li in the subducted oceanic mantle and in the antigorite breakdown fluids. Earth and Planetary Science Letters 222, 217-234.

Schwartz, S., Guillot, S., Reynard, B., Lafay, R., Debret, B., Nicollet, C., Lanari, P., Auzende, A.L., 2013. Pressure–temperature estimates of the lizardite/antigorite transition in high pressure serpentinites. Lithos 178, 197-210.

Seal, R.R., 2006. Sulfur isotope geochemistry of sulfide minerals. Reviews in Mineralogy and Geochemistry 61, 633-677.

Shilling, F.R., Wunder, B., 2004. Temperature distribution in piston-cylinder assemblies: Numerical simulations and laboratory experiments. European Journal of Mineralogy 16, 7-14.

Shim, S.-H., Duffy, T.S., Takemura, K., 2002. Equation of state of gold and its application to the phase boundaries near 660 km depth in Earth’s mantle. Earth and Planetary Science Letters 203, 729-739.

Sillitoe, R., 2008. Major gold deposits and belts of the North and South American Cordillera: distribution, tectonomagmatic settings, and metallogenic considerations. Economic Geology 103, 663-687.

Sleep, N.H., Meibom, A., Fridriksson, T., Coleman, R.G., Bird, D.K., 2004. H2-rich fluids from serpentinization: geochemical and biotic implications. Proceedings of the National Academy of Science 101, 12818–12823.

Spandler, C., Pirard, C., 2013. Element recycling from subducting slabs to arc crust: A review. Lithos 170-171, 208-223.

Staudigel, H., Schreyer, W., 1977. Mineralogy and The Upper Thermal Stability of Clinochlore, $Mg_5AI[AISi_3O_{10}](OH)_8$, at 10-35 kb PH_2O. Contributions to Mineralogy and Petrology 198, 187-198.

Stern, R.J., 2002. Subduction zones. Reviews of Geophysics 40, 1012.

Stern, R.J., Fouch, M.J., Klemperer, S.L., 2003. An overview of the Izu-Bonin-Mariana Subduction Factory. Inside the Subduction Factory. Geophysical Monograph Series 138, 175-222.

Stern, R.J., Kohut, E., Bloomer, S.H., Leybourne, M., Fouch, M., Vervoort, J., 2006. Subduction factory processes beneath the Guguan cross-chain, Mariana Arc: No role for sediments, are serpentinites important? Contributions to Mineralogy and Petrology 151, 202-221.

Syracuse, E.M., van Keken, P.E., Abers, G.a., 2010. The global range of subduction zone thermal models. Physics of the Earth and Planetary Interiors 183, 73-90.

Tatsumi, Y., Nakamura, N., 1986. Composition of aqueous fluid from serpentinite in the subducted lithosphere. Geochemical Journal 20, 191-196.

Tenthorey, E., Hermann, J., 2004. Composition of fluids during serpentinite breakdown in subduction zones: Evidence for limited boron mobility. Geology 32, 865-868.

Tomkins, A.G., 2010. Windows of metamorphic sulfur liberation in the crust: Implications for gold deposit genesis. Geochimica et Cosmochimica Acta 74, 3246-3259.

Toulmin, P., Barton, P.B., 1964. A thermodynamic study of pyrite and pyrrhotite. Geochimica et Cosmochimica Acta 28, 641-671.

Trommsdorff, V., Lopez Sanchez-Vizcaino, V., Gomez-Pugnaire, M.T., Muntener, O., 1998. High pressure breakdown of antigorite to spinifex-textured olivine and orthopyroxene, SE Spain. Contributions to Mineralogy and Petrology 132, 139-148.

Truckenbrodt, J., Ziegenbein, D., Johannes, W., 1997. Redox conditions in piston cylinder apparatus: The different behavior of boron nitride and unfired pyrophillite assemblies. American Mineralogist 82, 337-344.

Uehara, S., Shirozu, H., 1985. Variations in chemical composition and structural properties of antigorites. Mineralogical Magazine 12, 299-318.

Ulmer, P., Trommsdorff, V., 1995. Serpentine stability to mantle depths and subduction-related magmatism. Science 268, 858-861.

van Keken, P.E., Hacker, B.R., Syracuse, E.M., Abers, G.A., 2011. Subduction factory: 4. Depth-dependent flux of H2O from subducting slabs worldwide. Journal of Geophysical Research: Solid Earth 116, B01401.

Vidal, O., Dubacq, B., 2009. Thermodynamic modelling of clay dehydration, stability and compositional evolution with temperature, pressure and H_2O activity. Geochimica et Cosmochimica Acta 73, 6544-6564.

Vogt, K., Gerya, T., 2014. Deep plate serpentinization triggers skinning of subducting slabs. Geology 42, 723-726.

Wallace, P.J., 2005. Volatiles in subduction zone magmas: Concentrations and fluxes based on melt inclusion and volcanic gas data. Journal of Volcanology and Geothermal Research 140, 217-240.

Wang, J., Hattori, K.H., Kilian, R., Stern, C.R., 2007. Metasomatism of sub-arc mantle peridotites below southernmost South America: Reduction of fO2 by slab-melt. Contributions to Mineralogy and Petrology 153, 607-624.

Wang, L., Yang, W., Xiao, Y., Liu, B., Chow, P., Shen, G., Mao, W., Mao, H., 2011. Application of a new composite cubic-boron nitride gasket assembly for high pressure inelastic x-ray scattering studies of carbon related materials. Review of Scientific Instruments 82, 073902.

Wicks, F.J., O'Hanley, D.S., 1988. Serpentine minerals; structures and petrology. Reviews in Mineralogy and Geochemistry 19, 91-167.

Wilke, M., Arges, F., Petit, P.-E., Gordon, E.B.J., Martin, F., 2001. Oxidation state and coordination of Fe in minerals : An Fe K- XANES spectroscopic study. American Mineralogist 86, 714-730.

Wunder, B., Schreyer, W., 1997. Antigorite : High-pressure stability in the system. Lithos 41, 213-227.

Wunder, B., Wirth, R., Gottschalk, M., 2001. Antigorite: Pressure and temperature dependence of polysomatism and water content. European Journal of Mineralogy 13, 485-495.

Zeng, Z., Wang, Q., Wang, X., Chen, S., Yin, X., Li, Z., 2012. Geochemistry of abyssal peridotites from the super slow-spreading Southwest Indian Ridge near 65°E: Implications for magma source and seawater alteration. Journal of Earth System Science 121, 1317-1336.

Белоусов, И.А., Батанова, В.Г., Савельева, Г.Н., А.В, С., 2009. Свидетельства надсубдукционной природы мантийных пород Войкаро-Сыньинского массива, Полярный Урал. Доклады РАН 421, 238-243.

Гаврилов, В.П., 2012. Геодинамическая модель нефтегазоносности Западной Сибири Геология нефти и газа 3, 60-68.

Дмитриев, Л.В., Базылев, Б.А., Борисов, М.В, 1999. Образование водорода и метана при серпентинизации мантийных гипербазитов океана и происхождение нефти. Российский журнал наук о земле 1, 1-13.

Разницин, Ю.Н., 2012. Геодинамика офиолитов и формирование месторождений углеводородов на шельфе Восточного Сахалина. Геотектоника 1, 3-18.

Савельева, Г.Н., 1987. Габбро ультрабазитовые комплексы офиолитов Урала и их аналоги в современной океанической коре Тр. ГИН АН СССР В. 404, 243.

Федонкин, М.А., 2008. Проблемы зарождения и эволюции биосферы. М.: Кн. дом “Либроком”.

Annex

(Supplementary material)

Fig. 1-S1a

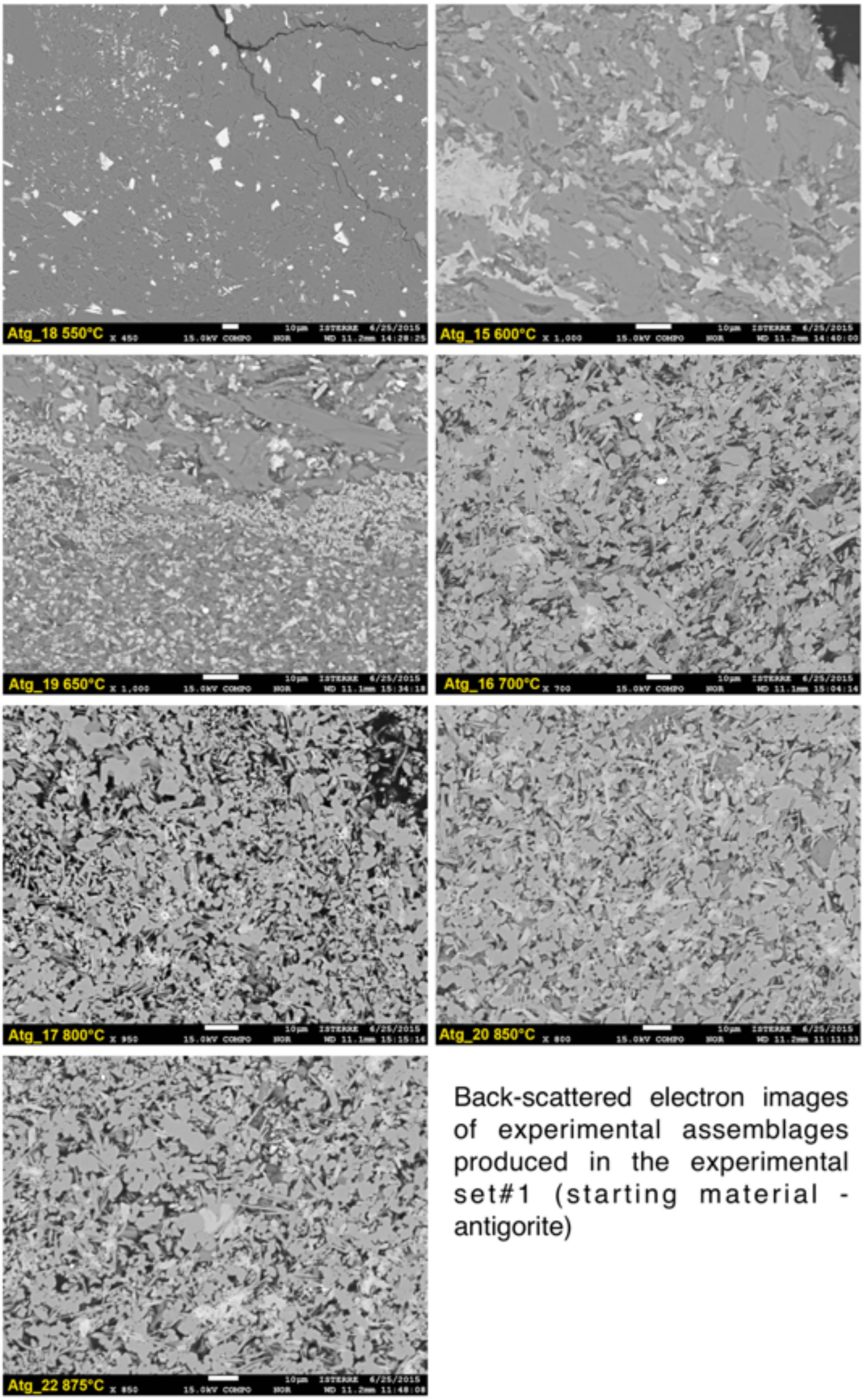

Back-scattered electron images of experimental assemblages produced in the experimental set#1 (starting material - antigorite)

Fig. 1-S1b

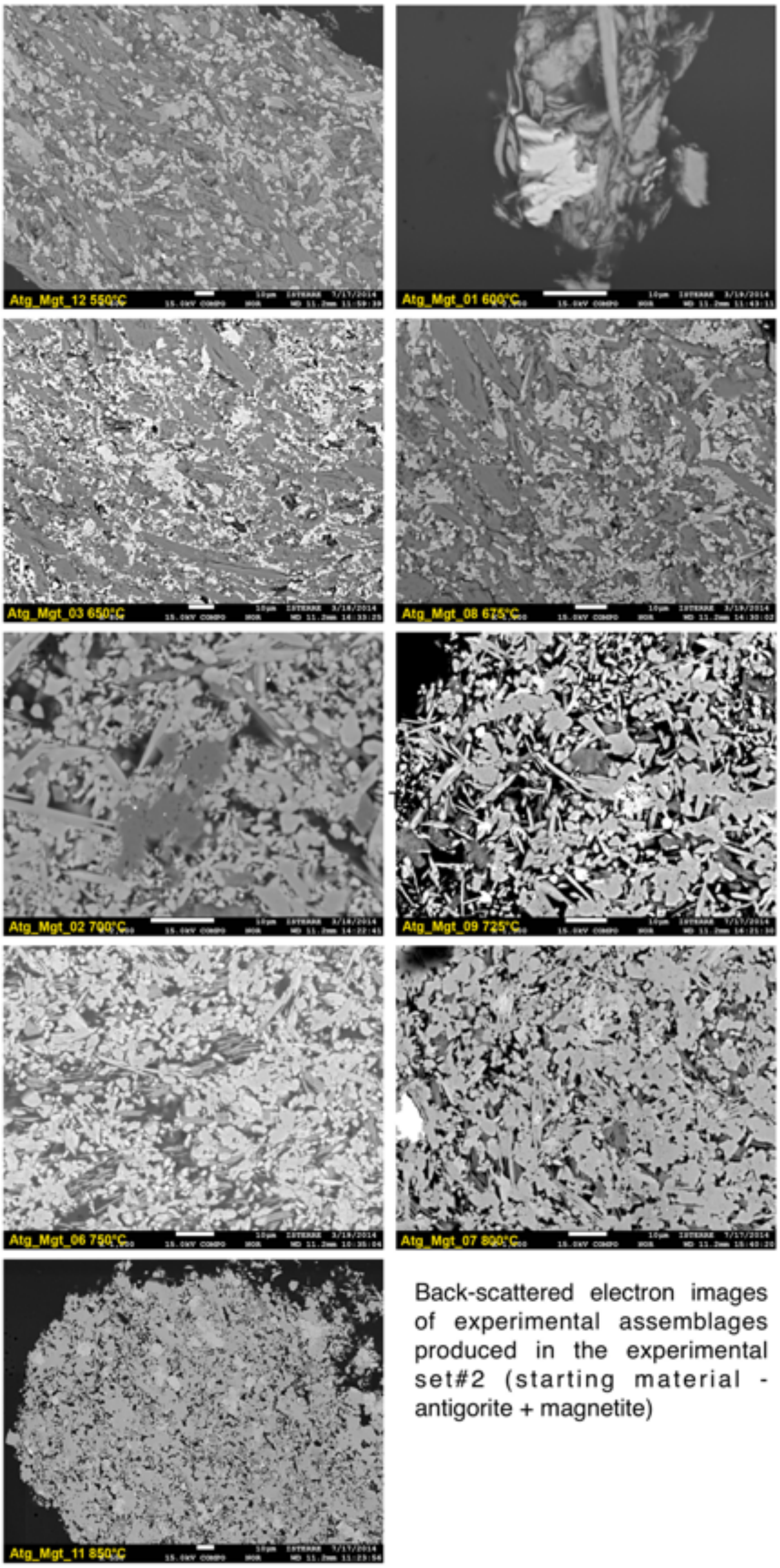

Back-scattered electron images of experimental assemblages produced in the experimental set#2 (starting material - antigorite + magnetite)

Fig. 1-S1c

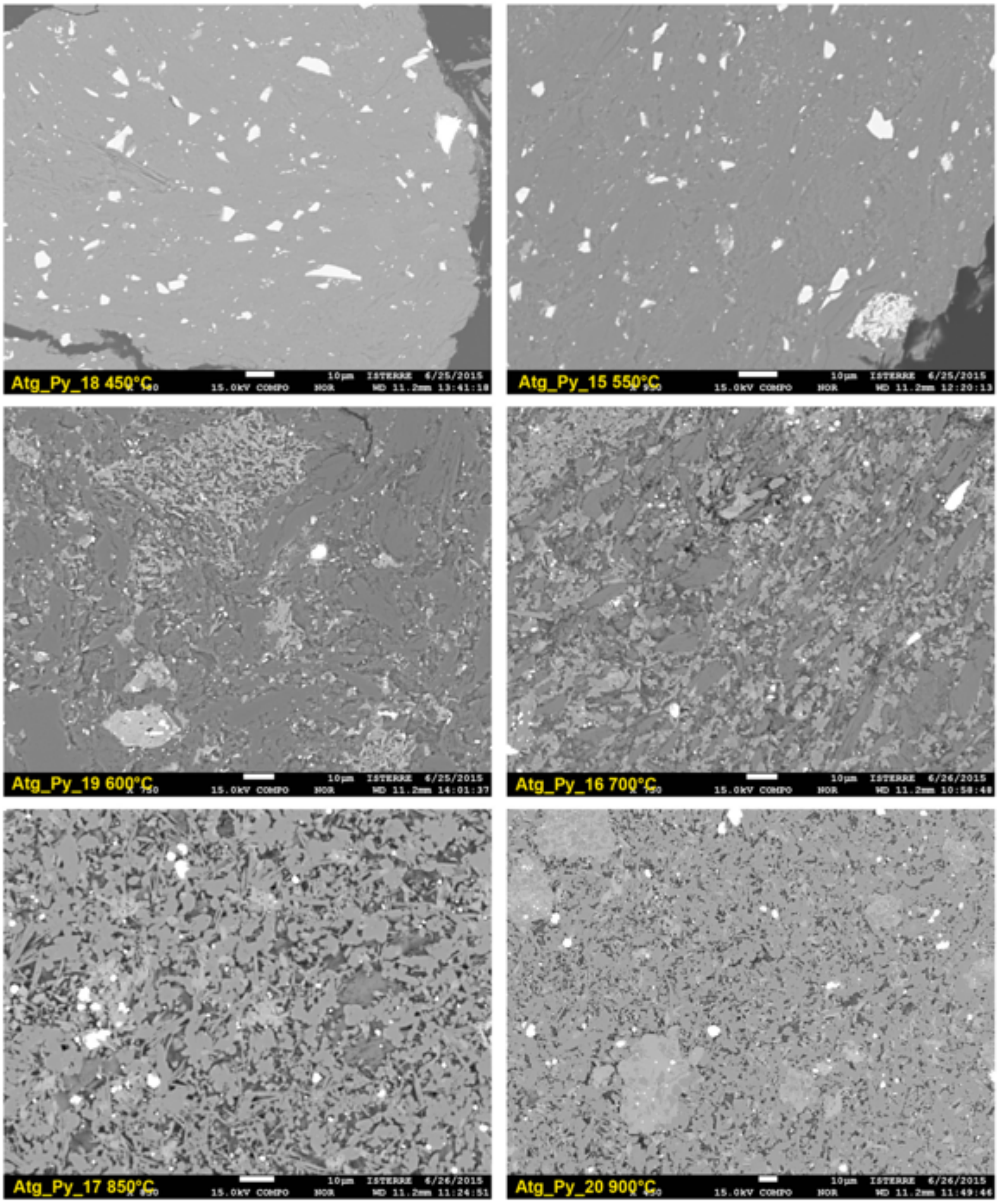

Back-scattered electron images of experimental assemblages produced in the experimental set#3 (starting material – antigorite + pyrite)

Table 2-S1a. Composition of antigorite produced in experiments (set#2)

T, ^{o}C	**550**	**550**	**550**	**550**	**550**	**600**	**600**	**600**	**600**	**600**	**650**	**650**	**650**	**650**	**675**	**675**	**675**
Major elements (wt.%)																	
SiO_2	44.32	47.75	47.75	48.13	47.57	44.57	44.72	44.95	44.84	44.92	45.82	44.82	45.67	44.09	44.75	45.69	46.90
TiO_2	0.04	0.02	0.01	0.03	0.01	0.00	0.01	0.01	0.01	0.02	0.02	0.00	0.03	0.03	0.02	0.02	0.09
Al_2O_3	0.86	1.33	0.85	0.80	1.03	1.07	0.74	1.15	1.45	1.21	1.06	0.93	1.34	1.54	1.08	1.10	1.00
FeO t	1.51	1.25	1.22	1.29	1.57	2.09	2.90	2.40	2.45	2.51	4.25	3.91	3.97	3.53	2.73	2.49	3.25
MnO	0.07	0.08	0.07	0.09	0.10	0.09	0.07	0.09	0.09	0.11	0.10	0.10	0.08	0.07	0.09	0.08	0.10
MgO	41.43	33.68	36.64	35.55	35.57	38.34	38.16	40.98	40.28	40.30	37.25	37.62	37.57	37.13	38.75	38.59	26.11
CaO	0.20	0.11	0.03	0.06	0.10	0.10	0.02	0.01	0.01	0.05	0.10	0.02	0.05	0.06	0.03	0.03	11.20
Na_2O	0.02	0.04	0.04	0.02	0.03	0.00	0.00	0.01	0.01	0.00	0.00	0.00	0.00	0.00	0.00	0.01	0.02
Cr_2O_3	0.03	0.07	0.01	0.02	0.06	0.04	0.01	0.05	0.06	0.08	0.04	0.01	0.04	0.12	0.37	0.03	0.02
NiO	0.00	0.03	0.02	0.03	0.05	0.07	0.05	0.00	0.00	0.00	0.05	0.05	0.06	0.08	0.05	0.06	0.04
OH	11.53	15.64	13.35	13.98	13.92	13.61	13.33	10.36	10.81	10.80	11.33	12.53	11.20	13.35	12.14	11.90	11.27
Total	100	100	100	100	100	100	100	100	100	100	100	100	100	100	100	100	100
apfu																	
Si	1.96	2.17	2.12	2.15	2.13	2.01	2.02	1.97	1.97	1.98	2.03	2.01	2.02	2.00	1.99	2.02	2.12
Ti	0.00	0.00	0.00	0.00	0.00	0.00	0.00	0.00	0.00	0.00	0.00	0.00	0.00	0.00	0.00	0.00	0.00
Al	0.04	0.07	0.04	0.04	0.05	0.06	0.04	0.06	0.08	0.06	0.06	0.05	0.07	0.08	0.06	0.06	0.05
Fe^{3+}	0.04	0.05	0.05	0.05	0.06	0.08	0.10	0.06	0.07	0.07	0.12	0.10	0.12	0.11	0.09	0.09	0.12
Fe^{2+}	0.01	0.00	0.00	0.00	0.00	0.00	0.01	0.03	0.02	0.02	0.03	0.04	0.03	0.03	0.01	0.00	0.00
Mn	0.00	0.00	0.00	0.00	0.00	0.00	0.00	0.00	0.00	0.00	0.00	0.00	0.00	0.00	0.00	0.00	0.00
Mg	2.74	2.28	2.43	2.37	2.38	2.58	2.57	2.68	2.64	2.64	2.46	2.52	2.47	2.51	2.58	2.55	1.76
Ca	0.01	0.01	0.00	0.00	0.00	0.00	0.00	0.00	0.00	0.00	0.00	0.00	0.00	0.00	0.00	0.00	0.54
Na	0.00	0.00	0.00	0.00	0.00	0.00	0.00	0.00	0.00	0.00	0.00	0.00	0.00	0.00	0.00	0.00	0.00
Cr	0.00	0.00	0.00	0.00	0.00	0.00	0.00	0.00	0.00	0.00	0.00	0.00	0.00	0.00	0.01	0.00	0.00
Ni	0.00	0.00	0.00	0.00	0.00	0.00	0.00	0.00	0.00	0.00	0.00	0.00	0.00	0.00	0.00	0.00	0.00
Fe^{3+}/Fe_{tot}	0.77	1.00	1.00	1.00	1.00	1.00	0.93	0.65	0.77	0.74	0.79	0.70	0.81	0.79	0.92	1.00	1.00
Mg #	98.00	97.96	98.16	98.00	97.58	97.03	95.91	96.82	96.71	96.62	93.99	94.49	94.40	94.94	96.20	96.51	93.47

Table 2-S1b. Composition of olivine produced in experiments (set#2)

T, °C	**550**	**550**	**550**	**550**	**550**	**550**	**600**	**600**	**600**	**650**	**650**	**675**	**675**	**700**	**700**	**700**	**700**
Major elements (wt.%)																	
SiO_2	38.98	38.59	37.67	38.08	39.01	39.55	39.10	38.87	37.93	39.97	39.29	39.61	39.82	40.96	41.44	40.31	40.49
TiO	0.00	0.00	0.00	0.00	0.00	0.00	0.00	0.00	0.00	0.02	0.00	0.00	0.00	0.00	0.00	0.00	0.00
Al_2O_3	0.00	0.00	0.00	0.00	0.00	0.00	0.00	0.00	0.00	0.03	0.00	0.00	0.00	0.00	0.00	0.00	0.00
FeO t	20.19	22.80	23.76	23.09	17.48	16.76	18.49	22.63	23.36	16.74	20.55	14.02	14.91	12.58	9.62	10.82	10.40
MnO	0.39	0.30	1.23	0.23	0.61	0.17	0.24	0.25	0.15	0.25	0.25	0.21	0.21	0.21	0.16	0.18	0.16
MgO	39.66	38.67	36.52	36.93	41.97	41.70	42.65	38.33	37.87	43.22	39.33	44.38	44.30	44.82	50.02	48.15	49.66
CaO	0.14	0.09	0.50	0.26	0.06	0.06	0.02	0.02	0.04	0.08	0.12	0.05	0.06	0.09	0.03	0.04	0.03
Cr_2O_3	0.16	0.17	0.12	0.15	0.15	0.12	0.04	0.03	0.19	0.07	0.05	0.08	0.11	0.21	0.07	0.06	0.09
NiO	0.16	0.32	0.19	0.24	0.15	0.13	0.14	0.18	0.22	0.23	0.09	0.15	0.21	0.30	0.11	0.15	0.24
Total	99.62	100.82	99.82	98.78	99.29	98.30	100.68	100.31	99.76	100.61	100.70	98.50	99.61	100.17	101.45	99.69	101.07
apfu																	
Si	1.01	1.00	0.99	1.01	1.00	1.01	0.99	1.01	1.00	1.01	1.01	1.01	1.00	1.02	1.00	1.00	0.99
Ti	0.00	0.00	0.00	0.00	0.00	0.00	0.00	0.00	0.00	0.00	0.00	0.00	0.00	0.00	0.00	0.00	0.00
Al	0.00	0.00	0.00	0.00	0.00	0.00	0.00	0.00	0.00	0.00	0.00	0.00	0.00	0.00	0.00	0.00	0.00
Fe	0.44	0.49	0.52	0.51	0.37	0.36	0.39	0.49	0.51	0.35	0.49	0.30	0.31	0.26	0.19	0.22	0.21
Mn	0.01	0.01	0.03	0.01	0.01	0.00	0.01	0.01	0.00	0.01	0.01	0.00	0.00	0.00	0.00	0.00	0.00
Mg	1.53	1.49	1.44	1.45	1.60	1.60	1.61	1.48	1.48	1.62	1.47	1.68	1.66	1.66	1.80	1.77	1.80
Ca	0.00	0.00	0.01	0.01	0.00	0.00	0.00	0.00	0.00	0.00	0.00	0.00	0.00	0.03	0.00	0.00	0.00
Cr	0.00	0.00	0.00	0.00	0.00	0.00	0.00	0.00	0.00	0.00	0.00	0.00	0.00	0.00	0.00	0.00	0.00
Ni	0.00	0.01	0.00	0.01	0.00	0.00	0.00	0.00	0.00	0.00	0.00	0.00	0.00	0.01	0.00	0.00	0.00
Mg #	77.78	75.14	73.25	74.02	80.79	81.41	80.43	75.12	74.29	82.14	77.32	84.95	84.11	86.40	90.26	88.80	89.48

Table 2-S1b (continued)

T, ^{o}C	**725**	**725**	**725**	**750**	**750**	**800**	**800**	**800**	**800**	**800**	**850**	**850**	**850**	**850**	**850**
Major elements (wt.%)															
SiO_2	41.35	42.01	40.65	41.26	40.98	40.09	40.80	40.84	40.80	40.80	40.67	40.96	40.82	40.99	40.58
TiO_2	0.00	0.00	0.00	0.00	0.00	0.00	0.00	0.00	0.00	0.00	0.00	0.00	0.00	0.00	0.00
Al_2O_3	0.00	0.00	0.00	0.00	0.00	0.00	0.00	0.00	0.00	0.00	0.00	0.00	0.00	0.00	0.00
FeO t	9.70	9.60	8.56	10.74	10.41	10.57	9.24	10.29	10.51	10.31	9.52	9.60	9.51	9.77	9.59
MnO	0.16	0.18	0.15	0.14	0.19	0.18	0.17	0.15	0.17	0.18	0.15	0.14	0.13	0.16	0.14
MgO	49.23	49.26	49.14	49.25	48.80	50.14	50.24	48.52	48.51	48.68	48.82	48.82	48.79	48.80	49.41
CaO	0.05	0.06	0.03	0.03	0.04	0.04	0.04	0.03	0.04	0.03	0.09	0.03	0.04	0.05	0.03
Cr_2O_3	0.06	0.11	0.09	0.05	0.07	0.03	0.08	0.11	0.10	0.02	0.05	0.02	0.03	0.02	0.03
NiO	0.16	0.12	0.13	0.16	0.13	0.14	0.13	0.16	0.18	0.10	0.15	0.20	0.15	0.16	0.16
Total	100.49	101.10	98.50	101.64	100.62	101.19	100.71	100.09	100.31	100.13	99.46	99.76	99.47	99.95	99.95
apfu															
Si	1.02	1.00	1.01	1.00	1.00	0.98	0.99	1.00	1.00	1.00	1.00	1.00	1.00	1.00	0.99
Ti	0.00	0.00	0.00	0.00	0.00	0.00	0.00	0.00	0.00	0.00	0.00	0.00	0.00	0.00	0.00
Al	0.00	0.00	0.00	0.00	0.00	0.00	0.00	0.00	0.00	0.00	0.00	0.00	0.00	0.00	0.00
Fe	0.36	0.20	0.19	0.22	0.21	0.22	0.19	0.21	0.22	0.21	0.20	0.20	0.20	0.20	0.20
Mn	0.00	0.00	0.00	0.00	0.00	0.00	0.00	0.00	0.00	0.00	0.00	0.00	0.00	0.00	0.00
Mg	1.60	1.78	1.77	1.78	1.78	1.82	1.82	1.77	1.77	1.78	1.79	1.79	1.79	1.78	1.81
Ca	0.00	0.00	0.00	0.00	0.00	0.00	0.00	0.00	0.00	0.00	0.00	0.00	0.00	0.00	0.00
Cr	0.00	0.00	0.00	0.00	0.00	0.00	0.00	0.00	0.00	0.00	0.00	0.00	0.00	0.00	0.00
Ni	0.00	0.00	0.00	0.00	0.00	0.00	0.00	0.00	0.00	0.00	0.00	0.00	0.00	0.00	0.00
Mg #	90.04	90.15	91.10	89.10	89.31	89.42	90.65	89.37	89.16	89.38	90.14	90.06	90.14	89.90	90.18

Table 2-S1c. Composition of clinopyroxene produced in experiments. (set#2)

T, ^{o}C	**550**	**550**	**550**	**550**	**550**	**550**	**550**	**550**	**600**	**600**	**600**	**650**	**650**	**650**
Major elements (wt.%)														
SiO_2	55.92	55.37	55.65	55.45	58.44	55.26	55.37	55.01	53.59	55.30	52.49	54.14	53.73	54.23
TiO_2	0.14	0.09	0.07	0.10	0.13	0.00	0.05	0.18	0.09	0.10	0.10	0.13	0.15	0.14
Al_2O_3	1.16	1.40	1.10	0.81	2.24	0.00	1.06	1.45	0.33	0.24	1.79	0.84	0.96	0.66
FeO t	2.36	2.86	2.16	2.22	2.34	2.24	2.01	3.11	3.87	2.48	3.74	3.84	3.93	4.87
MnO	0.08	0.04	0.01	0.04	0.02	0.07	0.04	0.05	0.06	0.08	0.08	0.06	0.12	0.09
MgO	18.98	18.08	19.31	17.42	22.72	17.34	19.23	18.16	16.70	17.52	18.77	18.60	17.29	18.99
CaO	21.53	20.71	21.65	23.75	10.23	23.65	21.51	20.64	24.27	24.50	21.57	21.77	22.51	19.06
Na_2O	0.93	1.06	0.88	0.47	3.14	0.00	0.76	1.13	0.00	0.00	0.03	0.02	0.01	0.03
Cr_2O_3	0.02	0.05	0.00	0.03	0.18	0.09	0.03	0.19	0.17	0.07	0.17	0.15	0.12	0.21
NiO	0.05	0.05	0.02	0.00	0.05	0.02	0.00	0.00	0.04	0.01	0.00	0.04	0.00	0.26
Total	101.16	99.71	100.84	100.31	99.50	98.75	99.36	99.11	99.13	100.31	98.68	99.58	98.82	98.54
apfu														
Si	1.99	2.00	1.98	2.00	2.03	2.03	1.99	1.99	1.99	2.00	1.92	1.98	1.98	2.00
Ti	0.00	0.00	0.00	0.00	0.00	0.00	0.00	0.00	0.00	0.00	0.00	0.00	0.00	0.00
Al	0.05	0.06	0.05	0.03	0.09	0.00	0.04	0.06	0.01	0.01	0.08	0.04	0.04	0.03
Fe	0.07	0.09	0.06	0.07	0.07	0.07	0.06	0.09	0.12	0.08	0.12	0.12	0.12	0.15
Mn	0.00	0.00	0.00	0.00	0.00	0.00	0.00	0.00	0.00	0.00	0.00	0.00	0.00	0.00
Mg	1.01	0.97	1.03	0.94	1.18	0.95	1.03	0.98	0.92	0.95	1.06	1.01	0.95	1.04
Ca	0.82	0.80	0.83	0.92	0.38	0.93	0.83	0.80	0.96	0.95	0.87	0.85	0.89	0.75
Na	0.05	0.06	0.05	0.03	0.17	0.00	0.04	0.06	0.00	0.00	0.00	0.00	0.00	0.00
Cr	0.00	0.00	0.00	0.00	0.01	0.00	0.00	0.01	0.00	0.00	0.00	0.00	0.00	0.01
Ni	0.00	0.00	0.00	0.00	0.00	0.00	0.00	0.00	0.00	0.00	0.00	0.00	0.00	0.00
Mg #	93.49	91.85	94.10	93.32	94.53	93.23	94.47	91.23	88.51	92.63	89.93	89.62	88.69	87.41
Wo	43.25	43.06	43.13	47.76	23.43	47.76	43.17	42.70	48.04	48.21	42.62	42.99	45.36	38.67
En	53.06	52.30	53.52	48.75	72.38	48.71	53.68	52.28	45.99	47.97	51.60	51.09	48.47	53.61
Fs	3.69	4.64	3.35	3.49	4.19	3.53	3.14	5.02	5.97	3.81	5.78	5.92	6.18	7.72
Jad	5.85	6.84	5.53	2.79	30.64	0.00	4.84	7.28	0.00	0.00	0.20	0.13	0.04	0.25
Di	94.15	93.16	94.47	97.21	69.36	100.00	95.16	92.72	100.00	100.00	99.80	99.87	99.96	99.75

Table 2-S1c (continued)

T, °C	**675**	**675**	**675**	**700**	**700**	**700**	**700**	**750**	**800**	**800**	**800**	**850**	**850**	**850**
Major elements (wt.%)														
SiO_2	54.13	52.94	54.91	57.02	55.88	55.30	54.34	54.37	54.44	55.51	54.24	54.19	53.94	52.50
TiO_2	0.08	0.07	0.10	0.15	0.13	0.07	0.08	0.11	0.13	0.12	0.00	0.15	0.17	0.10
Al_2O_3	1.18	1.63	0.45	1.00	0.90	1.36	1.56	1.08	1.22	1.50	1.30	2.37	3.89	1.04
FeO t	4.39	5.13	6.10	4.50	3.89	2.84	2.80	2.56	2.24	3.39	2.75	4.45	2.91	2.70
MnO	0.08	0.10	0.18	0.10	0.09	0.10	0.10	0.09	0.09	0.13	0.12	0.08	0.09	0.12
MgO	21.18	19.33	25.71	25.61	23.67	17.86	20.51	19.71	19.47	20.04	18.48	19.42	19.64	21.20
CaO	15.64	19.12	12.03	11.29	14.50	21.90	19.10	21.41	22.65	19.96	22.46	21.45	18.77	21.15
Na_2O	0.05	0.03	0.02	0.03	0.01	0.05	0.07	0.01	0.02	0.02	0.00	0.03	0.06	0.01
Cr_2O_3	0.16	0.31	0.25	0.17	0.18	0.02	0.10	0.16	0.35	0.20	0.35	0.09	0.44	0.48
NiO	0.10	0.05	0.03	0.11	0.07	0.04	0.01	0.00	0.00	0.00	0.02	0.00	0.00	0.00
Total	97.01	98.71	99.80	100.00	99.34	99.55	98.68	99.36	100.39	100.65	99.71	101.56	99.24	98.58
apfu														
Si	2.00	1.94	1.97	2.01	2.00	2.00	1.98	1.99	1.96	1.98	1.97	1.93	1.94	1.93
Ti	0.00	0.00	0.00	0.00	0.00	0.00	0.00	0.00	0.00	0.00	0.00	0.00	0.00	0.00
Al	0.05	0.07	0.02	0.04	0.04	0.06	0.07	0.05	0.05	0.06	0.06	0.10	0.16	0.04
Fe	0.14	0.16	0.18	0.13	0.12	0.09	0.09	0.08	0.07	0.10	0.08	0.13	0.09	0.08
Mn	0.00	0.00	0.01	0.00	0.00	0.00	0.00	0.00	0.00	0.00	0.00	0.00	0.00	0.00
Mg	1.17	1.08	1.38	1.35	1.26	0.96	1.11	1.00	1.05	1.07	1.00	1.03	1.05	1.16
Ca	0.62	0.77	0.46	0.43	0.56	0.85	0.74	0.84	0.88	0.76	0.88	0.82	0.72	0.83
Na	0.00	0.00	0.00	0.00	0.00	0.00	0.00	0.00	0.00	0.00	0.00	0.00	0.00	0.00
Cr	0.00	0.02	0.02	0.00	0.01	0.00	0.00	0.00	0.00	0.03	0.00	0.03	0.03	0.04
Ni	0.00	0.00	0.00	0.00	0.00	0.00	0.00	0.00	0.00	0.00	0.00	0.00	0.00	0.00
Mg #	89.57	87.04	88.25	91.02	91.56	91.81	92.88	93.21	93.94	91.34	92.30	88.60	92.33	93.32
Wo	32.23	38.24	22.89	22.39	28.74	44.73	38.34	43.73	43.99	39.54	44.63	41.30	38.81	40.09
En	60.70	53.76	68.05	70.64	65.25	50.75	57.28	51.90	52.62	55.22	51.11	52.01	56.50	55.91
Fs	7.07	8.00	9.06	6.97	6.01	4.52	4.39	4.37	3.39	5.23	4.26	6.69	4.69	4.00
Jad	0.46	0.24	0.24	0.44	0.14	0.33	0.55	0.10	0.13	0.12	0.00	0.22	0.44	0.08
Di	99.54	99.76	99.76	99.56	99.86	99.67	99.45	99.90	99.87	99.88	100.00	99.78	99.56	99.92

Table 2-S1d. Composition of orthopyroxene produced in experiments (set#2)

T, °C	**675**	**700**	**700**	**700**	**700**	**700**	**700**	**700**	**700**	**700**	**700**	**700**	**700**	**700**
Major elements (wt.%)														
SiO_2	54.52	58.86	57.82	58.11	58.28	57.29	57.69	56.97	58.58	56.86	58.65	58.58	58.38	57.86
TiO_2	0.07	0.07	0.04	0.08	0.08	0.09	0.08	0.09	0.09	0.10	0.06	0.08	0.09	0.05
Al_2O_3	0.35	0.50	0.48	0.80	0.62	0.85	0.84	1.21	0.52	0.58	0.51	0.71	0.65	0.51
FeO t	8.90	6.66	7.40	5.90	6.18	7.17	6.46	5.62	5.63	7.01	5.58	4.32	6.59	4.90
MnO	0.29	0.17	0.20	0.17	0.18	0.14	0.15	0.12	0.19	0.20	0.22	0.18	0.16	0.20
MgO	34.56	34.77	33.55	34.53	34.41	34.61	33.99	30.31	34.04	34.81	34.90	35.80	33.77	32.57
CaO	0.82	0.17	0.48	1.35	0.18	0.21	0.42	3.81	1.79	0.21	0.26	0.14	0.25	3.66
Na_2O	0.00	0.00	0.00	0.00	0.00	0.01	0.06	0.29	0.00	0.00	0.01	0.00	0.00	0.00
Cr_2O_3	0.18	0.12	0.27	0.18	0.18	0.18	0.22	0.23	0.14	0.11	0.18	0.08	0.16	0.27
NiO	0.05	0.04	0.03	0.04	0.05	0.24	0.04	0.02	0.02	0.08	0.05	0.01	0.07	0.06
Total	97.74	101.38	100.27	101.15	100.17	100.78	99.97	98.67	101.00	99.97	100.44	99.91	100.14	100.10
apfu														
Si	0.98	1.00	1.00	0.99	1.00	0.99	1.00	1.00	1.00	0.99	1.00	1.00	1.01	1.00
Ti	0.00	0.00	0.00	0.00	0.00	0.00	0.00	0.00	0.00	0.00	0.00	0.00	0.00	0.00
Al	0.01	0.01	0.01	0.02	0.01	0.02	0.02	0.03	0.01	0.01	0.01	0.01	0.01	0.01
Fe	0.13	0.09	0.11	0.08	0.09	0.10	0.09	0.08	0.08	0.10	0.08	0.06	0.09	0.07
Mn	0.00	0.00	0.00	0.00	0.00	0.00	0.00	0.00	0.00	0.00	0.00	0.00	0.00	0.00
Mg	0.87	0.88	0.87	0.88	0.88	0.89	0.88	0.80	0.87	0.90	0.89	0.91	0.87	0.84
Ca	0.02	0.00	0.01	0.02	0.00	0.00	0.01	0.07	0.03	0.00	0.00	0.00	0.00	0.07
Na	0.00	0.00	0.00	0.00	0.00	0.00	0.00	0.02	0.00	0.00	0.00	0.00	0.00	0.00
Cr	0.00	0.00	0.01	0.00	0.00	0.00	0.00	0.00	0.01	0.00	0.00	0.00	0.00	0.01
Ni	0.00	0.00	0.00	0.00	0.00	0.01	0.00	0.00	0.00	0.00	0.00	0.00	0.00	0.00
Mg #	87.38	90.29	88.98	91.25	90.84	89.58	90.36	90.58	91.51	89.85	91.76	93.66	90.13	92.21
Wo	1.55	0.32	0.90	2.49	0.35	0.39	0.80	7.56	3.34	0.38	0.50	0.27	0.47	6.93
En	85.36	90.00	88.18	88.98	90.53	89.24	89.64	83.73	88.46	89.50	91.31	93.41	89.71	85.82
Fs	13.09	9.68	10.92	8.53	9.12	10.37	9.56	8.71	8.20	10.11	8.20	6.32	9.82	7.25

Table 2-S1d (continued).

T, ^{o}C	**725**	**725**	**750**	**750**	**750**	**750**	**800**	**800**	**800**	**800**	**850**	**850**
Major elements (wt.%)												
SiO_2	57.69	56.47	57.33	53.23	55.23	56.12	54.95	54.35	55.70	52.15	55.84	58.88
TiO_2	0.08	0.10	0.00	0.09	0.12	0.13	0.11	0.15	0.09	0.08	0.11	0.00
Al_2O_3	0.69	1.07	0.00	1.00	1.70	1.77	3.44	4.16	1.64	2.06	4.15	2.00
FeO t	6.50	6.42	6.70	6.99	6.43	6.55	6.31	6.01	6.34	7.46	5.29	5.90
MnO	0.16	0.15	0.16	0.20	0.11	0.13	0.15	0.18	0.18	0.13	0.09	0.13
MgO	35.69	35.00	34.27	34.60	33.59	33.02	35.70	33.44	34.51	38.88	29.67	32.09
CaO	0.39	1.17	0.62	2.09	0.77	0.30	0.40	0.53	0.30	0.28	4.80	0.67
Na_2O	0.02	0.01	0.00	0.01	0.01	0.00	0.00	0.00	0.00	0.01	0.02	0.00
Cr_2O_3	0.21	0.26	0.20	0.24	0.26	0.22	0.34	0.11	0.32	0.31	0.30	0.35
NiO	0.00	0.00	0.04	0.04	0.01	0.00	0.00	0.00	0.00	0.00	0.08	0.03
Total	101.42	100.67	99.33	98.50	98.23	98.26	101.44	98.97	98.11	101.29	100.39	100.04
apfu												
Si	0.98	0.97	1.00	0.95	0.98	0.99	0.94	0.95	0.97	0.91	0.97	1.01
Ti	0.00	0.00	0.00	0.00	0.00	0.00	0.00	0.00	0.00	0.00	0.00	0.00
Al	0.01	0.02	0.00	0.02	0.04	0.04	0.07	0.09	0.03	0.04	0.08	0.00
Fe	0.09	0.09	0.10	0.11	0.10	0.10	0.09	0.09	0.09	0.11	0.08	0.09
Mn	0.00	0.00	0.00	0.00	0.00	0.00	0.00	0.00	0.00	0.00	0.00	0.00
Mg	0.91	0.90	0.89	0.93	0.88	0.87	0.91	0.87	0.90	1.01	0.77	0.88
Ca	0.01	0.02	0.01	0.04	0.01	0.01	0.01	0.01	0.01	0.01	0.09	0.01
Na	0.00	0.00	0.00	0.00	0.00	0.00	0.00	0.00	0.00	0.00	0.00	0.00
Cr	0.00	0.01	0.00	0.01	0.01	0.00	0.02	0.00	0.02	0.02	0.02	0.02
Ni	0.00	0.00	0.00	0.00	0.00	0.00	0.00	0.00	0.00	0.00	0.00	0.00
Mg #	90.72	90.66	90.11	89.82	90.30	89.99	90.98	90.84	90.66	90.28	90.90	90.65
Wo	0.70	2.13	1.15	3.75	1.46	0.58	0.72	1.03	0.56	0.47	9.56	1.34
En	90.09	88.74	89.08	86.45	88.98	89.47	90.32	89.91	90.15	89.86	82.22	89.44
Fs	9.21	9.13	9.77	9.80	9.56	9.95	8.96	9.07	9.29	9.67	8.23	9.22

Table 2-S1e. Composition of clinochlore produced in experiments (set#2)

T, °C	**700**	**700**	**700**	**700**	**700**	**725**	**750**	**750**	**750**	**750**	**800**	**800**	**800**	**800**	**800**
Major elements (wt.%)															
SiO_2	37.69	38.30	32.48	32.67	34.03	33.74	33.13	33.85	32.76	31.90	31.18	33.90	33.68	31.41	40.98
TiO_2	0.06	0.06	0.02	0.05	0.05	0.04	0.06	0.06	0.05	0.05	0.08	0.08	0.08	0.09	0.07
Al_2O_3	16.59	13.35	12.97	15.77	15.31	14.08	15.51	16.05	15.04	15.03	15.78	13.48	17.29	14.89	15.61
FeO t	2.00	2.29	3.88	3.14	3.23	3.66	3.71	3.39	3.83	3.54	3.93	4.72	3.65	4.16	2.66
MnO	0.04	0.02	0.03	0.04	0.03	0.01	0.04	0.05	0.05	0.01	0.03	0.09	0.01	0.02	0.03
MgO	30.79	31.34	36.81	35.19	31.07	32.90	33.93	34.58	34.24	36.08	35.38	35.12	28.99	36.52	26.39
CaO	0.02	0.04	0.06	0.08	0.06	0.04	0.04	0.13	0.04	0.03	0.06	0.14	0.04	0.03	0.13
Na_2O	0.02	0.02	0.04	0.07	0.04	0.01	0.00	0.00	0.00	0.00	0.00	0.01	0.00	0.00	0.00
K_2O	0.02	0.01	0.00	0.00	0.01	0.01	0.00	0.00	0.00	0.00	0.00	0.00	0.00	0.00	0.02
Cr_2O_3	1.09	1.00	0.90	1.05	1.12	1.10	1.57	1.42	1.28	1.22	1.45	1.13	1.51	1.45	1.27
NiO	0.08	0.05	0.00	0.00	0.06	0.00	0.00	0.00	0.00	0.00	0.00	0.00	0.10	0.00	0.04
OH	11.60	13.54	12.81	11.93	14.97	14.41	12.01	10.47	12.71	12.14	12.12	11.33	14.64	11.43	12.81
Total	100.00	100.00	100.00	100.00	100.00	100.00	100.00	100.00	100.00	100.00	100.00	100.00	100.00	100.00	100.00
apfu															
Si	3.41	3.55	3.05	3.04	3.25	3.23	3.10	3.11	3.10	2.98	2.92	3.16	3.19	2.92	3.72
Ti	0.00	0.00	0.00	0.00	0.00	0.00	0.00	0.00	0.00	0.00	0.01	0.01	0.01	0.01	0.01
Al	1.77	1.46	1.44	1.73	1.72	1.59	1.71	1.74	1.67	1.65	1.74	1.48	1.93	1.63	1.67
Fe^{3+}	0.05	0.08	0.00	0.00	0.18	0.08	0.02	0.03	0.00	0.10	0.02	0.00	0.26	0.00	0.06
Fe^{2+}	0.05	0.11	0.46	0.29	0.08	0.22	0.27	0.23	0.32	0.30	0.41	0.41	0.03	0.48	0.14
Mn	0.00	0.00	0.00	0.00	0.00	0.00	0.00	0.00	0.00	0.00	0.00	0.01	0.00	0.00	0.00
Mg	4.16	4.33	5.16	4.88	4.42	4.69	4.74	4.73	4.82	5.02	4.94	4.89	4.10	5.06	3.58
Ca	0.00	0.00	0.01	0.01	0.01	0.00	0.00	0.01	0.00	0.00	0.01	0.01	0.00	0.00	0.01
Na	0.00	0.00	0.01	0.01	0.01	0.00	0.00	0.00	0.00	0.00	0.00	0.00	0.00	0.00	0.00
K	0.00	0.00	0.00	0.00	0.00	0.00	0.00	0.00	0.00	0.00	0.00	0.00	0.00	0.00	0.00
Cr	0.08	0.07	0.07	0.08	0.08	0.08	0.12	0.10	0.10	0.09	0.11	0.08	0.11	0.11	0.09
Ni	0.01	0.00	0.00	0.00	0.00	0.00	0.00	0.00	0.00	0.00	0.00	0.00	0.01	0.00	0.00
Fe^{3+}/Fe_{tot}	0.52	0.42	0.00	0.00	0.68	0.26	0.08	0.13	0.00	0.24	0.06	0.00	0.90	0.00	0.30
Mg #	96.49	96.07	94.41	95.23	94.49	94.12	94.22	94.78	94.09	94.77	94.13	92.99	93.39	94.00	94.65

Table 2-S1f. Composition of garnets produced in experiments (set#2)

T, °C	**850**	**850**	**850**	**850**	**850**
Major elements (wt.%)					
SiO_2	41.12	41.4	41.06	41.09	41.74
TiO_2	0.52	0.69	0.63	0.58	0.73
Al_2O_3	21.55	22.1	20.68	22.36	21.89
Cr_2O_3	2.22	0.95	1.69	0.69	1.45
FeO t	9.02	8.71	9.34	7.91	7.53
MnO	0.4	0.42	0.39	0.4	0.37
MgO	18.31	16.37	19.26	16.37	14.74
CaO	8.27	11	8.73	10.81	12.63
Total	101.42	101.63	101.77	100.21	101.1
apfu					
Si	2.98	2.99	2.94	3	3
Ti	0.03	0.04	0.03	0.03	0.04
Al	1.78	1.84	1.7	1.88	1.85
Cr	0.12	0.05	0.09	0.04	0.08
Fe^{3+}	0.08	0.06	0.26	0.03	0
Fe^{2+}	0.45	0.45	0.29	0.44	0.46
Mn	0.02	0.03	0.02	0.02	0.02
Mg	1.91	1.72	2.01	1.74	1.58
Ca	0.62	0.83	0.65	0.82	0.97
Mg#	78.33	77	78.61	78.67	77.72
Fe^{3+}/Fe_{tot}	0.15	0.124	0.47	0.064	0
Almandine	15	14.9	9.7	14.6	15.3
Spessartine	0.8	0.8	0.8	0.8	0.8
Pyrope	63.6	56.8	67.5	57.4	52
Grossular	18.5	25.8	18.2	26.3	30.6
Andradite	0.8	0.9	2.7	0.4	0
Uvarovite	1.3	0.7	1	0.5	1.4

Appendix 3.2-A: Definition of the experimental *f*O_2 upper limit

1. The upper limit of *f*O_2 which may be reached in the present experiments within graphite-NaCl-pyrophyllite cell assemblies is QFM +4, which was calculated based on the equilibrium between ferrosilite, magnetite, fayalite and oxygen:

$6FeSiO_3 + 2Fe_3O_4 = 6FeSiO_4 + O_2$ (1)

In the described experiments magnetite was never found to be in equilibrium with olivine, this observation indicates that *f*O_2 of the experiments is lower than in Reaction (1).

2. We performed an additional experiment on verification of gold capsules permeability for hydrogen and estimation of the amount of diffused hydrogen. Starting material for this experiment was prepared as a mixture of synthetic hematite (93 wt.%) and natural magnetite (7 wt.%) with a drop of water. Temperature and pressure of the experiment were 700°C and 2 GPa respectively. In order to reach an equilibrium, the experiment duration was 6 days, which is comparable to dehydration experimental runs. Experimental product was characterized by XRD. Rietveld refinement reveals that the run product consists of 25 wt.% hematite and 75 wt.% magnetite. Such a reduction of hematite to magnetite suggests that the fO2 conditions in the capsule are below HM buffer, i.e. below QFM +6, since the following equilibrium is shifted to the left side:

$4Fe_3O_4 + O_2 = 6Fe_2O_3$ (2)

And hence O_2 which may be present in the capsule is bond to hydrogen coming from the cell assembly in order to maintain proportion of magnetite to hematite below HM buffer.

Reduction of magnetite to hematite may also happen by following reaction:

$3Fe_2O_3 + H_2 = 2Fe_3O_4 + H_2O$ (3)

Reaction (3) also reveals the presence of H_2 in the capsule. Obtained results of Rietveld refinement allows to calculate moles of H_2 required for hematite-to-magnetite transition based on Reaction (3). Thus, $9x10^{-5}$ moles of H_2 are needed to reduce 68 wt.% of hematite. Further calculations of oxygen amount produced in the experiments will show, that the maximum value is $5x10^{-5}$ moles of oxygen per sample, which is enough to be coupled with H_2 coming from the outside of the capsule. Following reaction is responsible for the mentioned O_2 consumption:

$1/2O_2 + H_2 = H_2O$ (4)

Consequently, the potential hydrogen "reservoir" of the cell assembly can be considered as unlimited, and therefore, intrinsic *f*O_2 does not vary from one experiment to another.

Appendix 3.2-B: Sulfur elemental analysis method

The procedure of sulfur elemental analysis consisted of mixing a sample with tungsten oxide (in proportion 1:2) and placing the mixture in a tin capsule, which was loaded to Vario Micro Cube (Elementar, Germany) for S% analysis using calibration with internal standards. The detailed description of the method can be found in Operating Instructions vario EL (2005).

Appendix 3.2-C: Details on mineral formula calculations

The structural formulae of antigorite were calculated based on the ideal antigorite mineral formula $M_{3m-3}T_{2m}O_{5m}(OH)_{4m-6}$ for the most commonly observed m = 17 polysome (i.e., number of SiO_4 tetrahedra in a single chain defined by the antigorite wavelength; Mellini et al., 1987) and was normalized to 6.825 oxygen atoms. Water contents in hydrous minerals were calculated from the difference from 100 wt.% after ZAF correction. Mineral formulae of antigorite, clinochlore and garnet were first calculated with Fe^{2+} as total Fe, then Fe^{3+} was calculated using deficiencies in the sum of cations, taking into account that Fe^{3+} occurs in both T (Si, Al, Ti, Cr, Fe^{3+}) and M (Mg, Fe^{2+}, Mn, Ca, Na, Ni, Fe^{3+}) sites for antigorite, in M1 (Mg, Fe^{2+}, Mn, Ni, Fe^{3+}) and in M2 (Mg, Al, Cr, Fe^{3+}) for chlorite, and in one site Y (Al, Cr, Fe^{3+}) for the garnet. The structural formulae of chlorite were calculated on the basis of 14 anhydrous oxygen atoms.

Appendix 3.2-D: XRD patterns

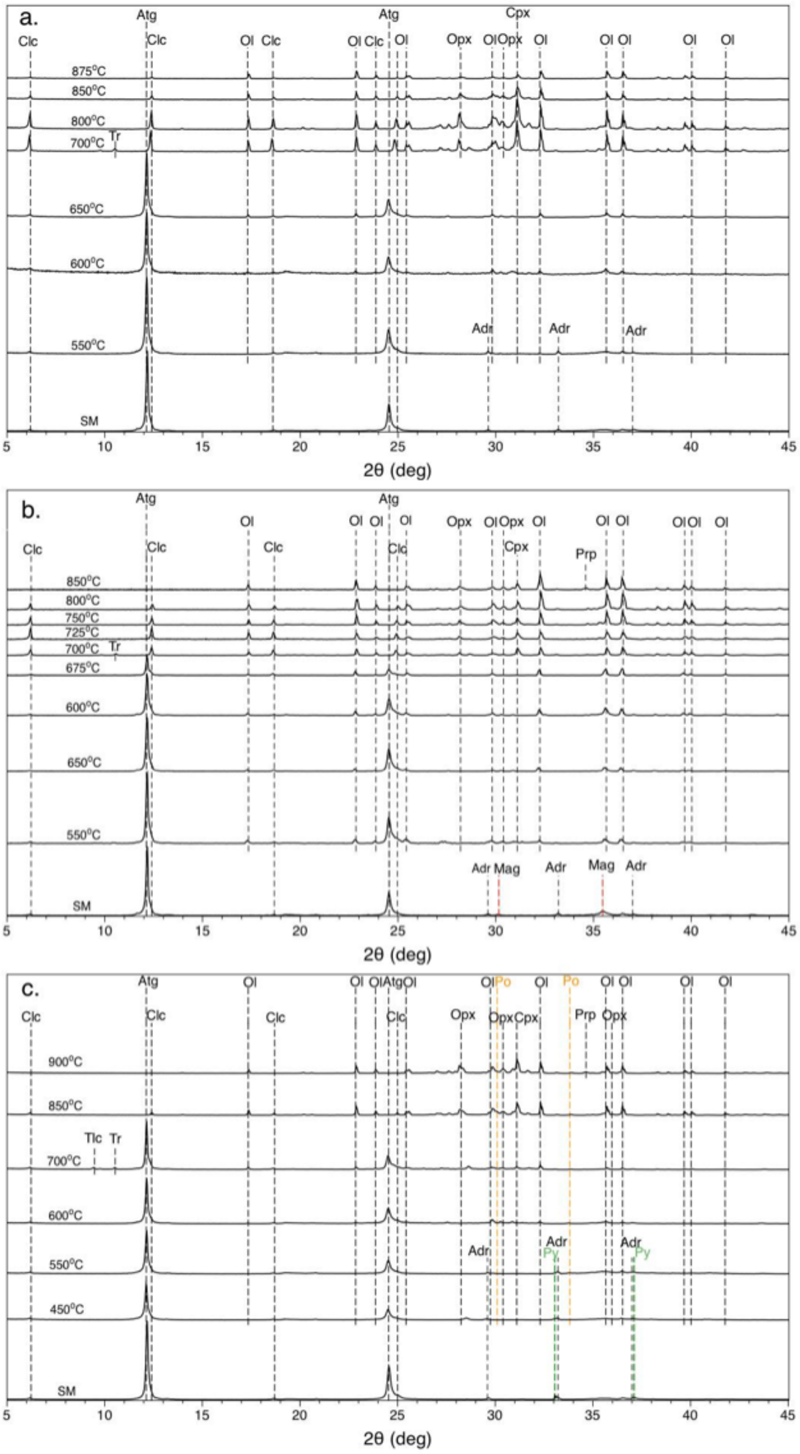

Figure 3.2-S1. XRD patterns of starting materials (SM) and experimental products for the set#1 (a), set#2 (b), and set#3 (c). Dashed lines indicate diffraction peaks corresponding to the mineral phases observed. Atg – antigorite, Clc – clinochlore, Mag – magnetite, Adr – andradite, Ol – olivine, Opx – orthopyroxene, Cpx – clinopyroxene, Prp – pyrope, Tr – tremolite, Tlc – talc, Py – pyrite, Po – pyrrhotite.

Appendix 3.2-E:

Table 3.2-S1. Fe^{3+}/Fe_{total}, wt.% of FeO and H_2O and moles of O_2 and H_2O calculated per kg of solid rock based on Fe reduction.

$Fe_2O_3 = 2FeO + 1/2O_2$ **Atg 100%**	**Fe^{3+}/Fe_{tot}**	**FeO total, wt.%**	**O_2, moles/kg**	**H_2O, wt%**	**H_2O, moles/kg**
SM	0.97	1.37	0.00	0.00	0.00
550	0.85	1.37	0.38	1.00	0.56
600	0.42	1.37	1.41	2.00	1.11
650	0.25	1.37	0.57	0.50	0.28
700	0.18	1.37	0.25	7.10	3.94
800	0.14	1.37	0.13	0.50	0.28
850	0.17	1.37	0.00	0.50	0.28
875	0.18	1.37	0.00	0.40	0.22
Atg+Mgt 5%					
SM	0.96	6.10	0.00	0.00	0.00
550	0.42	6.10	7.96	1.03	0.57
600	0.40	6.10	0.37	0.63	0.35
650	0.19	6.10	3.01	1.20	0.67
675	0.21	6.10	0.00	1.60	0.89
700	0.20	6.10	0.07	5.24	2.91
725	0.29	6.10	0.00	0.10	0.06
750	0.13	6.10	2.36	0.03	0.02
800	0.19	6.10	0.00	0.04	0.03
850	0.18	6.10	0.13	2.19	1.22
Atg+Py 3%					
SM	0.82	3.68	0.00	0.00	0.00
450	0.79	3.68	0.31	1.50	0.83
550	0.62	3.68	1.45	0.50	0.28
600	0.31	3.68	2.76	1.50	0.83
700	0.26	3.68	0.52	4.50	2.50
850	0.17	3.68	0.80	3.70	2.06
900	0.15	3.68	0.16	0.30	0.17

Appendix 3.2-F: Log(a_{O_2})-log(a_S) diagrams

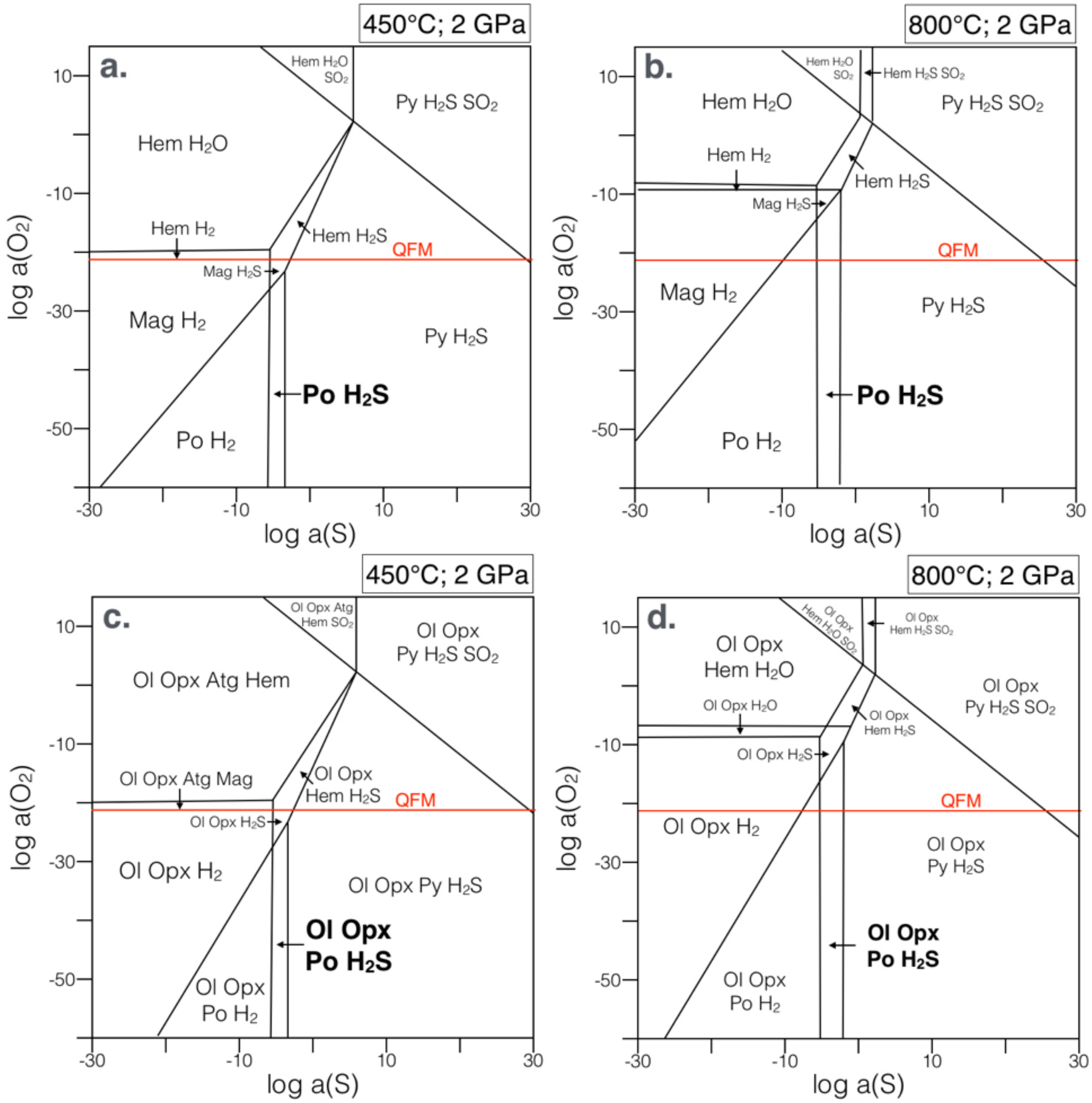

Figure 3.2-S2. Isothermic and isobaric Log(a_{O2})-log(a_S) sections showing phase stabilities in a). Fe-S-O-H system at 450°C and 2 GPa; b). Fe-S-O-H system at 800°C and 2 GPa; c). Fe-Mg-Si-O-H system at 800°C and 2 GPa; d). Fe-Mg-Si-O-H system at 450°C and 2 GPa. Red line represents log(aO_2) of QFM buffer. Diagrams were made using Theriak-Domino software (de Capitani and Petrakakis; 2010). Thermodynamic properties of silicate and oxides were taken from Holland and Powell (1998) data set; properties of sulfides, SO_2 and H_2S were taken from Robie and Hemingway

(1995).

de Capitani, C., Petrakakis, K., 2010. The computation of equilibrium assemblage diagrams with Theriak/Domino software. American Mineralogist 95, 1006-1016.

Holland, T.J.B., Powell, R., 1998. An internally consistent thermodynamic data set for phases of petrological interest. Journal of Metamorphic Geology 16, 309-343.

Robie, R.A., Hemingway, B.S., 1995. Thermodynamic properties of minerals and related substances at 298.15 K and 1 bar (105 Pascals) pressure and at higher temperatures. U.S. Geol Survey Bull No. 2131, 461p.

Appendix F: Table 3.2-S2. Major-oxide mineral composition

Table 3.2-S2. Composition of antigorite produced in experimental set#1.

T, ^{o}C	**500**	**500**	**500**	**500**	**500**	**500**	**600**	**600**	**600**	**600**	**600**	**600**	**650**	**650**	**650**	**650**	**650**	**650**	**650**
SiO2	45.33	45.66	44.06	43.79	43.66	34.43	43.43	45.44	45.01	44.85	44.88	44.64	45.44	44.53	43.67	43.22	44.55	44.49	43.92
TiO2	0.01	0.01	0.01	0.04	0.00	0.03	0.04	0.03	0.02	0.01	0.00	0.03	0.03	0.01	0.07	0.06	0.03	0.01	0.02
Al2O3	1.03	0.92	0.91	1.24	1.65	14.11	1.50	0.78	1.13	1.11	0.97	1.13	1.15	0.95	2.50	1.64	0.84	1.15	1.28
FeO	1.97	1.72	1.97	2.28	2.27	3.01	2.28	1.74	1.64	1.56	1.79	1.57	2.10	1.97	2.59	2.55	2.15	2.05	2.36
MnO	0.10	0.09	0.11	0.09	0.12	0.03	0.13	0.14	0.08	0.09	0.13	0.08	0.10	0.09	0.06	0.09	0.12	0.11	0.08
MgO	41.18	42.06	41.79	41.27	41.71	35.05	40.69	41.82	41.32	41.18	41.40	41.23	41.22	41.59	40.74	37.57	41.25	41.10	41.07
CaO	0.04	0.02	0.04	0.08	0.05	0.04	0.09	0.03	0.04	0.05	0.04	0.05	0.03	0.04	0.53	2.36	0.03	0.02	0.06
Na2O	0.00	0.00	0.01	0.00	0.00	0.00	0.04	0.02	0.02	0.01	0.03	0.00	0.00	0.01	0.00	0.00	0.00	0.01	0.00
K2O	0.00	0.00	0.00	0.02	0.00	0.00	0.00	0.00	0.00	0.01	0.01	0.01	0.00	0.00	0.00	0.01	0.01	0.00	0.00
Cr2O3	0.26	0.16	0.05	0.18	0.08	0.71	0.20	0.00	0.35	0.04	0.02	0.06	0.05	0.03	0.22	0.18	0.02	0.03	0.08
NiO	0.06	0.06	0.07	0.09	0.08	0.16	0.11	0.06	0.08	0.05	0.04	0.04	0.09	0.04	0.07	0.10	0.06	0.09	0.05
(OH)	9.88	9.13	10.99	10.91	10.38	12.43	11.36	9.81	10.16	11.03	10.70	11.16	9.68	10.66	9.54	12.22	10.93	10.94	11.08
Total	100.00	100.00	100.00	100.00	100.00	100.00	100.00	100.00	100.00	100.00	100.00	100.00	100.00	100.00	100.00	100.00	100.00	100.00	100.00
apfu																			
Si	1.97	1.97	1.95	1.94	1.92	1.57	1.94	1.98	1.97	1.97	1.97	1.97	1.97	1.96	1.91	1.95	1.97	1.96	1.95
Ti	0.00	0.00	0.00	0.00	0.00	0.00	0.00	0.00	0.00	0.00	0.00	0.00	0.00	0.00	0.00	0.00	0.00	0.00	0.00
Al	0.05	0.05	0.05	0.06	0.09		0.08	0.04	0.06	0.06	0.05	0.06	0.06	0.05	0.13	0.09	0.04	0.06	0.07
Fe3+	0.06	0.06	0.03	0.03	0.02	0.01	0.03	0.05	0.06	0.06	0.05	0.05	0.06	0.04	0.03	0.06	0.05	0.05	0.04
Fe2+	0.01	0.01	0.05	0.05	0.06	0.10	0.05	0.01	0.00	0.00	0.01	0.00	0.01	0.03	0.06	0.04	0.03	0.03	0.05
Mn	0.00	0.00	0.00	0.00	0.00	0.00	0.00	0.01	0.00	0.00	0.00	0.00	0.00	0.00	0.00	0.00	0.00	0.00	0.00
Mg	2.67	2.71	2.76	2.73	2.74	2.38	2.70	2.71	2.69	2.70	2.71	2.71	2.67	2.73	2.66	2.53	2.71	2.70	2.71
Ca	0.00	0.00	0.00	0.00	0.00	0.00	0.00	0.00	0.00	0.00	0.00	0.00	0.00	0.00	0.02	0.11	0.00	0.00	0.00
Na	0.00	0.00	0.00	0.00	0.00	0.00	0.00	0.00	0.00	0.00	0.00	0.00	0.00	0.00	0.00	0.00	0.00	0.00	0.00
K	0.00	0.00	0.00	0.00	0.00	0.00	0.00	0.00	0.00	0.00	0.00	0.00	0.00	0.00	0.00	0.00	0.00	0.00	0.00
Cr	0.01	0.01	0.00	0.01	0.00	0.03	0.01	0.00	0.01	0.00	0.00	0.00	0.00	0.00	0.01	0.01	0.00	0.00	0.00
Ni	0.00	0.00	0.00	0.00	0.00	0.01	0.00	0.00	0.00	0.00	0.00	0.00	0.00	0.00	0.00	0.00	0.00	0.00	0.00
Fe3+/Fetot	0.89	0.89	0.38	0.36	0.25	0.12	0.39	0.85	0.98	1.00	0.78	0.95	0.83	0.57	0.37	0.61	0.57	0.65	0.42
Mg#	97.39	97.75	97.42	96.99	97.03	95.41	96.95	97.72	97.83	97.91	97.64	97.91	97.22	97.42	96.56	96.33	97.16	97.27	96.87

Table 3.2-S2. Composition of olivine produced in experimental set#1.

T, °C	**550**	**550**	**600**	**600**	**650**	**650**	**700**	**700**	**700**	**700**	**700**	**800**	**800**	**800**	**800**	**800**	**800**	**800**
SiO2	39.21	39.58	40.50	40.33	40.21	41.2551	41.04	40.02	41.14	41.24	40.91	43.79	43.63	43.35	43.56	42.09	41.70	41.52
Al2O3	0.02	0.09	0.05	0.05	0.28	0.18	0.05	0.19	0.02	0.13	0.08	0.03	0.05	0.05	0.03	0.05	0.06	0.13
FeO	16.27	15.75	11.40	11.57	8.68	8.18	7.83	6.44	6.89	4.17	6.40	5.12	4.91	5.26	4.85	3.44	3.78	4.29
MnO	1.76	0.15	0.22	0.21	0.27	0.28	0.24	0.17	0.17	0.14	0.16	0.18	0.16	0.18	0.16	0.11	0.17	0.14
MgO	42.52	44.59	47.47	48.95	49.72	49.17	50.51	51.08	51.59	53.44	51.16	53.11	52.14	51.60	52.40	53.76	53.00	52.42
CaO	0.09	0.05	0.04	0.02	0.03	0.04	0.04	0.06	0.04	0.05	0.03	0.04	0.04	0.06	0.02	0.03	0.05	0.05
Na2O	0.00	0.00	0.03	0.01	0.00	0.00	0.00	0.00	0.00	0.00	0.00	-0.01	0.01	-0.01	0.00	0.00	0.00	0.00
K2O	0.00	0.00	0.00	0.00	0.00	0.00	0.00	0.00	0.00	0.00	0.00	0.00	0.00	0.00	0.00	0.00	0.00	0.00
Cr2O3	0.01	0.05	0.11	0.10	0.07	0.06	0.04	0.11	0.12	0.05	0.08	0.03	0.15	0.10	0.04	0.02	0.02	0.20
NiO	0.00	0.00	0.22	0.10	0.37	0.17	0.13	0.17	0.14	0.15	0.41	0.12	0.24	0.19	0.18	0.06	0.13	0.21
Total	99.93	100.32	100.43	101.41	99.71	99.33	100.04	98.46	100.29	100.00	100.00	102.53	101.49	101.17	101.63	100.00	100.00	100.00
apfu																		
Si	1.00	0.99	1.00	0.98	0.99	1.01	1.00	0.99	0.99	0.99	1.00	1.02	1.03	1.03	1.03	1.01	1.00	1.00
Al	0.00	0.00	0.00	0.00	0.01	0.01	0.00	0.01	0.00	0.00	0.00	0.00	0.00	0.00	0.00	0.00	0.00	0.00
Fe	0.35	0.33	0.24	0.24	0.18	0.17	0.16	0.13	0.14	0.08	0.13	0.10	0.10	0.10	0.10	0.07	0.08	0.09
Mn	0.04	0.00	0.00	0.00	0.01	0.01	0.00	0.00	0.00	0.00	0.00	0.00	0.00	0.00	0.00	0.00	0.00	0.00
Mg	1.61	1.67	1.75	1.78	1.82	1.79	1.83	1.88	1.86	1.92	1.86	1.85	1.83	1.83	1.84	1.91	1.90	1.89
Ca	0.00	0.00	0.00	0.00	0.00	0.00	0.00	0.00	0.00	0.00	0.00	0.00	0.00	0.00	0.00	0.00	0.00	0.00
Cr	0.00	0.00	0.00	0.00	0.00	0.00	0.00	0.00	0.00	0.00	0.00	0.00	0.00	0.00	0.00	0.00	0.00	0.00
Ni	0.00	0.00	0.00	0.00	0.01	0.00	0.00	0.00	0.00	0.00	0.01	0.00	0.00	0.00	0.00	0.00	0.00	0.00
Mg#	82.32	83.45	88.12	88.29	91.08	91.46	92.00	93.39	93.03	95.80	93.44	94.86	94.98	94.59	95.06	96.53	96.15	95.61

Table 3.2-S2. Composition of olivine produced in experimental set#1.

T, ^{o}C	**800**	**800**	**800**	**850**	**850**	**850**	**850**	**850**	**850**	**850**	**875**	**875**	**875**	**875**	**875**	**875**
SiO2	41.66	42.14	41.76	41.83	42.00	41.90	41.95	41.54	41.93	41.72	41.41	41.96	41.76	41.75	41.26	41.89
Al2O3	0.11	0.08	0.03	0.08	0.08	0.03	0.11	0.33	0.07	0.06	0.03	0.06	0.04	0.07	0.04	0.03
FeO	4.40	3.75	4.56	4.72	4.82	4.75	4.40	4.81	4.51	4.89	4.96	4.99	4.87	4.80	5.16	4.94
MnO	0.16	0.19	0.18	0.15	0.14	0.16	0.11	0.13	0.13	0.15	0.14	0.16	0.14	0.11	0.16	0.08
MgO	53.38	53.56	52.85	53.02	52.70	53.10	52.72	51.71	53.31	52.39	52.91	52.10	52.90	53.34	52.85	52.82
CaO	0.05	0.05	0.05	0.08	0.07	0.04	0.07	0.09	0.05	0.17	0.04	0.32	0.03	0.08	0.06	0.06
Na2O	0.00	0.00	0.00	0.00	0.00	0.01	0.00	0.00	0.00	0.00	0.00	0.00	0.00	0.01	0.00	0.00
K2O	0.00	0.01	0.01	0.01	0.00	0.00	0.00	0.00	0.00	0.00	0.00	0.00	0.01	0.01	0.00	0.00
Cr2O3	0.01	0.02	0.14	0.09	0.02	0.01	0.02	0.14	0.03	0.02	0.07	0.04	0.07	0.07	0.04	0.07
NiO	0.11	0.09	0.13	0.14	0.08	0.12	0.09	0.18	0.16	0.10	0.13	0.20	0.13	0.07	0.21	0.17
Total	100.00	100.00	99.79	100.20	100.00	100.19	100.00	100.00	100.25	100.00	100.00	100.00	100.03	100.40	100.00	100.16
apfu																
Si	1.00	1.01	1.00	1.00	1.01	1.00	1.01	1.01	1.00	1.00	1.00	1.01	1.00	1.00	0.99	1.00
Al	0.00	0.00	0.00	0.00	0.00	0.00	0.00	0.01	0.00	0.00	0.00	0.00	0.00	0.00	0.00	0.00
Fe	0.09	0.07	0.09	0.09	0.10	0.09	0.09	0.10	0.09	0.10	0.10	0.10	0.10	0.10	0.10	0.10
Mn	0.00	0.00	0.00	0.00	0.00	0.00	0.00	0.00	0.00	0.00	0.00	0.00	0.00	0.00	0.00	0.00
Mg	1.91	1.90	1.89	1.89	1.88	1.89	1.89	1.87	1.90	1.88	1.90	1.87	1.89	1.90	1.90	1.89
Ca	0.00	0.00	0.00	0.00	0.00	0.00	0.00	0.00	0.00	0.00	0.00	0.01	0.00	0.00	0.00	0.00
Cr	0.00	0.00	0.00	0.00	0.00	0.00	0.00	0.00	0.00	0.00	0.00	0.00	0.00	0.00	0.00	0.00
Ni	0.00	0.00	0.00	0.00	0.00	0.00	0.00	0.00	0.00	0.00	0.00	0.00	0.00	0.00	0.00	0.00
Mg#	95.58	96.22	95.39	95.24	95.11	95.22	95.52	95.04	95.47	95.02	95.00	94.90	95.09	95.19	94.80	95.01

Table 3.2-S2. Composition of clinopyroxene produced in experimental set#1.

T, ^{o}C	**550**	**600**	**600**	**600**	**600**	**600**	**600**	**650**	**650**	**650**	**650**	**650**	**650**	**650**	**850**
SiO2	53.04	52.78	54.79	54.41	54.31	51.19	52.77	52.75	53.91	53.86	51.94	49.36	55.09	52.26	51.65
Al2O3	2.41	1.31	0.32	0.21	0.26	0.68	0.57	0.54	0.55	0.97	0.62	0.23	0.56	0.74	0.98
FeO	1.71	3.33	1.83	2.07	1.92	3.02	2.35	4.82	4.70	3.23	4.77	6.76	2.06	6.45	2.08
MnO	0.28	0.09	0.07	0.11	0.14	0.13	0.11	0.11	0.15	0.11	0.15	0.34	0.12	0.15	0.09
MgO	18.86	19.52	19.50	17.34	18.38	23.20	19.69	16.88	23.61	18.41	17.97	30.72	19.44	16.03	25.04
CaO	22.47	20.01	23.04	24.50	23.89	18.95	21.65	23.51	17.51	22.68	20.53	12.40	20.42	21.73	18.32
Na2O	0.04	0.14	0.03	0.05	0.04	0.06	0.06	0.00	0.00	0.01	0.00	0.00	0.00	0.00	0.10
K2O	0.00	0.00	0.00	0.00	0.00	0.00	0.00	0.00	0.00	0.00	0.01	0.01	0.00	0.01	0.00
Cr2O3	0.03	0.44	0.08	0.18	0.19	0.20	0.21	0.43	0.33	0.02	0.26	0.06	0.08	0.30	0.35
NiO	0.04	0.00	0.00	0.00	0.06	0.04	0.02	0.03	0.05	0.02	0.00	0.00	0.00	0.00	0.00
Total	99.04	97.85	99.76	99.08	99.47	97.79	97.64	99.20	101.27	99.66	96.74	99.95	97.90	98.08	98.76
apfu															
Si	1.94	1.96	1.99	2.00	1.99	1.90	1.96	1.96	1.93	1.97	1.97	1.80	2.02	1.97	1.89
Al	0.10	0.06	0.01	0.01	0.01	0.03	0.03	0.02	0.02	0.04	0.03	0.01	0.02	0.03	0.04
Fe	0.05	0.10	0.06	0.06	0.06	0.09	0.07	0.15	0.14	0.10	0.15	0.21	0.06	0.20	0.06
Mn	0.01	0.00	0.00	0.00	0.00	0.00	0.00	0.00	0.00	0.00	0.00	0.01	0.00	0.00	0.00
Mg	1.03	1.08	1.05	0.95	1.00	1.29	1.09	0.94	1.26	1.00	1.02	1.67	1.06	0.90	1.36
Ca	0.88	0.79	0.89	0.96	0.94	0.75	0.86	0.94	0.67	0.89	0.83	0.49	0.80	0.88	0.72
Cr	0.00	0.01	0.00	0.01	0.01	0.01	0.01	0.01	0.01	0.00	0.01	0.00	0.00	0.01	0.01
Ni	0.00	0.00	0.00	0.00	0.00	0.00	0.00	0.00	0.00	0.00	0.00	0.00	0.00	0.00	0.00
Mg#	95.15	91.25	95.00	93.72	94.47	93.19	93.76	86.20	89.95	91.03	87.04	89.00	94.39	81.57	95.55
En	52.44	54.57	52.58	48.02	50.19	60.23	53.85	46.27	60.80	50.40	50.77	70.74	55.12	45.45	63.59
Fs	2.67	5.23	2.76	3.22	2.94	4.40	3.60	7.41	6.79	4.96	7.55	8.74	3.27	10.27	2.96
Wo	44.89	40.20	44.66	48.77	46.88	35.37	42.55	46.32	32.40	44.63	41.68	20.52	41.61	44.28	33.45
Aeg	0.00	0.00	0.00	0.00	0.00	0.00	0.00	0.00	0.00	0.00	0.00	0.00	0.00	0.00	0.00
Jad	0.00	0.00	0.00	0.00	0.00	0.00	0.00	0.00	0.00	0.00	0.00	0.00	0.00	0.00	0.00
Di	1.00	1.00	1.00	1.00	1.00	1.00	1.00	1.00	1.00	1.00	1.00	1.00	1.00	1.00	1.00

Table 3.2-S2. Composition of orthopyroxene produced in experimental set#1.

T, ^{o}C	**700**	**700**	**700**	**700**	**700**	**700**	**700**	**800**	**850**	**850**	**875**	**875**	**875**	**875**	**875**
SiO2	60.42	58.43	58.97	57.82	58.80	56.83	57.79	55.19	54.34	56.30	53.92	57.94	51.70	55.27	54.80
Al2O3	0.33	0.56	0.30	0.26	0.44	0.40	0.59	3.86	2.89	3.40	2.93	2.21	3.26	5.26	3.74
FeO	2.59	3.26	3.84	3.06	2.81	3.44	2.97	3.04	2.76	2.75	2.87	2.37	3.58	2.92	2.96
MnO	0.11	0.17	0.24	0.17	0.13	0.20	0.17	0.10	0.12	0.15	0.11	0.13	0.08	0.12	0.13
MgO	37.66	37.35	36.83	35.99	36.73	37.72	36.95	34.26	34.34	35.86	35.41	36.67	40.99	34.48	36.11
CaO	0.10	0.14	0.14	1.88	0.59	0.12	0.16	0.36	1.03	0.43	1.57	0.29	0.38	0.38	0.42
Na2O	0.00	-0.01	0.00	0.00	0.00	0.00	0.00	0.00	0.00	0.01	0.00	0.00	0.01	0.00	0.00
K2O	0.00	0.00	0.00	0.00	0.00	0.00	0.00	0.00	0.00	0.01	0.00	0.01	0.00	0.00	0.00
Cr2O3	0.20	0.18	0.11	0.16	0.12	0.17	0.10	0.25	0.20	0.07	0.13	0.03	0.22	0.19	0.18
NiO	0.03	0.05	0.06	0.09	0.00	0.00	0.00	0.04	0.00	0.00	0.07	0.00	0.00	0.00	0.00
Total	101.54	100.28	100.60	100.00	99.67	98.95	98.79	97.23	95.77	99.07	100.00	99.70	100.34	98.75	98.46
apfu															
Si	1.01	0.99	1.00	0.99	1.00	0.98	0.99	0.96	0.97	0.97	0.95	0.98	0.89	0.95	0.95
Al	0.01	0.01	0.01	0.01	0.01	0.01	0.01	0.08	0.06	0.07	0.06	0.04	0.07	0.11	0.08
Fe	0.04	0.05	0.05	0.04	0.04	0.05	0.04	0.04	0.04	0.04	0.04	0.03	0.05	0.04	0.04
Mn	0.00	0.00	0.00	0.00	0.00	0.00	0.00	0.00	0.00	0.00	0.00	0.00	0.00	0.00	0.00
M	0.93	0.94	0.93	0.92	0.93	0.97	0.95	0.89	0.91	0.92	0.93	0.93	1.05	0.88	0.93
Ca	0.00	0.00	0.00	0.03	0.01	0.00	0.00	0.01	0.02	0.01	0.03	0.01	0.01	0.01	0.01
Cr	0.00	0.00	0.00	0.00	0.00	0.00	0.00	0.00	0.00	0.00	0.00	0.00	0.00	0.00	0.00
Ni	0.00	0.00	0.00	0.00	0.00	0.00	0.00	0.00	0.00	0.00	0.00	0.00	0.00	0.00	0.00
Mg#	96.29	95.33	94.47	95.44	95.88	95.12	95.68	95.25	95.69	95.87	95.65	96.49	95.33	95.46	95.61
En	96.11	95.08	94.23	92.14	94.84	94.92	95.40	94.57	93.75	95.10	92.82	95.98	94.73	94.75	94.86
Fs	3.71	4.66	5.51	4.40	4.07	4.86	4.31	4.71	4.22	4.09	4.22	3.48	4.64	4.50	4.35
Wo	0.18	0.26	0.26	3.46	1.09	0.21	0.30	0.72	2.03	0.81	2.97	0.54	0.64	0.75	0.79

Table 3.2-S2. Composition of clinochlore produced in experimental set#1.

T, ^{o}C	**700**	**700**	**800**	**800**	**800**	**800**	**800**	**850**	**850**	**850**	**850**	**875**	**875**
SiO2	34.68	34.47	32.83	33.46	32.72	34.87	34.40	35.05	31.81	31.68	34.72	31.78	34.11
TiO2	0.03	0.04	0.09	0.11	0.09	0.08	0.07	0.08	0.10	0.08	0.06	0.11	0.07
Al2O3	13.41	13.72	16.05	16.48	16.33	14.86	15.34	11.70	15.59	17.77	14.95	17.08	15.83
FeO	1.49	1.47	1.84	1.85	1.74	1.85	1.84	2.54	2.14	1.82	2.46	1.84	2.20
MnO	0.00	0.00	0.02	0.02	0.04	0.03	0.03	0.08	0.07	0.04	0.04	0.02	0.04
MgO	36.94	38.39	33.34	35.56	35.19	33.04	32.82	39.05	38.44	33.03	31.80	32.52	34.99
CaO	0.05	0.05	0.05	0.07	0.07	1.31	1.25	0.09	0.03	0.05	0.10	0.07	0.07
Na2O	0.01	0.00	0.01	0.00	0.01	0.01	0.02	0.00	0.00	0.00	0.00	0.00	0.00
K2O	0.00	0.00	0.00	0.00	0.00	0.00	0.00	0.00	0.00	0.01	0.00	0.01	0.00
Cr2O3	0.97	1.05	1.04	1.23	1.69	1.02	1.11	0.95	1.22	0.82	0.66	1.36	0.99
NiO	0.05	0.12	0.11	0.12	0.14	0.11	0.09	0.09	0.09	0.12	0.17	0.11	0.22
(OH)	12.38	10.69	14.61	11.10	11.98	12.82	13.04	10.38	10.50	14.58	15.05	15.10	11.48
Total	100.00	100.00	100.00	100.00	100.00	100.00	100.00	100.00	100.00	100.00	100.00	100.00	100.00
apfu													
Si	3.22	3.14	3.12	3.07	3.04	3.25	3.21	3.19	2.89	3.01	3.30	3.04	3.14
Ti	0.00	0.00	0.01	0.01	0.01	0.01	0.01	0.01	0.01	0.01	0.00	0.01	0.00
Al	1.47	1.47	1.80	1.78	1.79	1.63	1.69	1.26	1.67	1.99	1.67	1.93	1.72
Fe3+	0.00	0.00	0.08	0.02	0.00	0.12	0.12	0.00	0.00	0.06	0.19	0.08	0.05
Fe2+	0.12	0.18	0.07	0.12	0.13	0.02	0.02	0.30	0.33	0.09	0.01	0.07	0.12
Mn	0.00	0.00	0.00	0.00	0.00	0.00	0.00	0.01	0.01	0.00	0.00	0.00	0.00
Mg	5.11	5.21	4.73	4.87	4.88	4.59	4.57	5.30	5.21	4.68	4.50	4.64	4.80
Ca	0.00	0.00	0.01	0.01	0.01	0.13	0.12	0.01	0.00	0.01	0.01	0.01	0.01
Na	0.00	0.00	0.00	0.00	0.00	0.01	0.01	0.00	0.00	0.00	0.00	0.00	0.00
K	0.00	0.00	0.00	0.00	0.00	0.00	0.00	0.00	0.00	0.00	0.00	0.00	0.00
Cr	0.07	0.08	0.08	0.09	0.12	0.08	0.08	0.07	0.09	0.06	0.05	0.10	0.07
Ni	0.00	0.01	0.01	0.01	0.01	0.01	0.01	0.01	0.01	0.01	0.01	0.01	0.02
Total	18.01	16.09	17.90	17.98	18.00	17.84	15.84	18.14	18.22	17.92	17.74	15.89	17.94
Mg#	97.78	97.90	97.00	97.16	97.30	96.95	96.96	96.48	96.97	96.99	95.85	96.93	96.59

Table 3.2-S2. Composition of garnet produced in experimental set#1.

T, °C	**875**	**875**	**875**	**875**
SiO2	43.29	42.72	43.32	42.63
TiO2	0.41	0.21	0.39	0.24
Al2O3	21.54	19.53	21.26	20.26
Cr2O3	1.38	1.12	1.46	1.20
FeO	5.46	5.42	5.28	5.30
MnO	0.74	0.60	0.67	0.71
MgO	20.00	25.69	19.92	23.97
CaO	8.28	5.65	8.04	6.01
Total	101.13	100.99	100.34	100.32
apfu				
Si	3.04	2.94	3.06	2.97
Ti	0.02	0.01	0.02	0.01
Al	1.78	1.59	1.77	1.66
Cr	0.08	0.06	0.08	0.07
Fe3+	0.02	0.45	0.00	0.31
Fe2+	0.30	0.00	0.33	0.00
Mn	0.04	0.04	0.04	0.04
Mg	2.09	2.64	2.10	2.49
Ca	0.62	0.42	0.61	0.45
Mg#	86.70	89.41	87.05	88.97
Fe^{3+}/Fe_{tot}	0.06	1.00	0.00	0.99
Almandine	9.85	0.00	10.61	0.07
Spessartine	1.43	1.19	1.30	1.40
Pyrope	68.38	85.60	68.10	83.47
Grossular	19.30	9.79	19.11	12.30
Andradite	0.21	3.02	0.00	2.27
Uvarovite	0.83	0.41	0.88	0.49

Table 3.2-S2. Composition of antigorite produced in experimental set#3.

T, °C	**450**	**450**	**450**	**450**	**450**	**550**	**550**	**550**	**550**	**550**	**550**	**600**	**600**	**600**	**600**	**600**	**600**
SiO2	41.83	43.22	44.28	44.79	44.62	43.95	42.94	38.30	33.93	44.00	44.23	44.19	44.48	44.61	44.78	44.32	44.07
TiO2	0.05	0.05	0.01	0.00	0.00	0.04	0.04	0.03	0.05	0.03	0.01	0.01	0.00	0.02	0.01	0.00	0.02
Al2O3	2.58	2.18	0.85	0.73	0.71	1.26	2.30	9.14	13.01	1.23	0.71	0.77	0.74	0.97	0.90	0.74	0.98
FeO	3.66	2.40	1.62	1.54	1.96	2.19	2.45	2.55	3.22	1.73	1.74	2.09	2.22	1.86	1.87	2.18	2.03
MnO	0.07	0.10	0.09	0.07	0.13	0.11	0.12	0.09	0.01	0.11	0.14	0.16	0.16	0.08	0.08	0.11	0.11
MgO	40.40	40.66	40.98	42.40	41.43	40.51	39.73	38.14	36.54	41.60	42.16	41.26	41.15	41.43	42.04	41.93	41.53
CaO	0.24	0.15	0.16	0.04	0.03	0.14	0.17	0.06	0.05	0.06	0.05	0.04	0.03	0.05	0.10	0.03	0.18
Na2O	0.02	0.00	0.02	0.00	0.01	0.00	0.00	0.00	0.00	0.01	0.00	0.01	0.01	0.00	0.00	0.00	0.00
K2O	0.01	0.00	0.00	0.00	0.00	0.00	0.00	0.00	0.00	0.01	0.01	0.00	0.00	0.00	0.01	0.00	0.00
Cr2O3	0.14	0.28	0.01	0.03	0.02	0.08	0.24	1.09	0.97	0.12	0.00	0.03	0.01	0.05	0.00	0.00	0.17
NiO	0.20	0.31	0.12	0.02	0.06	0.13	0.08	0.17	0.16	0.11	0.04	0.03	0.08	0.09	0.06	0.06	0.09
(OH)	10.79	10.64	11.87	10.38	11.03	11.58	11.93	10.42	12.07	10.99	10.90	11.41	11.12	10.84	10.16	10.63	10.84
Total	100.00	100.00	100.00	100.00	100.00	100.00	100.00	100.00	100.00	100.00	100.00	100.00	100.00	100.00	100.00	100.00	100.00
apfu																	
Si	1.87	1.91	1.97	1.96	1.97	1.96	1.92	1.70	1.54	1.94	1.95	1.96	1.97	1.96	1.96	1.95	1.95
Ti	0.00	0.00	0.00	0.00	0.00	0.00	0.00	0.00	0.00	0.00	0.00	0.00	0.00	0.00	0.00	0.00	0.00
Al	0.14	0.11	0.04	0.04	0.04	0.07	0.12	0.48	0.70	0.06	0.04	0.04	0.04	0.05	0.05	0.04	0.05
Fe3+	0.00	0.03	0.05	0.03	0.04	0.05	0.05	0.01	0.00	0.03	0.03	0.04	0.04	0.05	0.04	0.03	0.03
Fe2+	0.14	0.06	0.01	0.02	0.03	0.03	0.05	0.08	0.15	0.03	0.04	0.04	0.04	0.02	0.03	0.05	0.04
Mn	0.00	0.00	0.00	0.00	0.00	0.00	0.00	0.00	0.00	0.00	0.01	0.01	0.01	0.00	0.00	0.00	0.00
Mg	2.70	2.68	2.72	2.77	2.73	2.69	2.65	2.53	2.48	2.74	2.78	2.73	2.71	2.72	2.74	2.76	2.74
Ca	0.01	0.01	0.01	0.00	0.00	0.01	0.01	0.00	0.00	0.00	0.00	0.00	0.00	0.00	0.00	0.00	0.01
Na	0.00	0.00	0.00	0.00	0.00	0.00	0.00	0.00	0.00	0.00	0.00	0.00	0.00	0.00	0.00	0.00	0.00
K	0.00	0.00	0.00	0.00	0.00	0.00	0.00	0.00	0.00	0.00	0.00	0.00	0.00	0.00	0.00	0.00	0.00
Cr	0.01	0.01	0.00	0.00	0.00	0.00	0.01	0.04	0.03	0.00	0.00	0.00	0.00	0.00	0.00	0.00	0.01
Ni	0.01	0.01	0.00	0.00	0.00	0.00	0.00	0.01	0.01	0.00	0.00	0.00	0.00	0.00	0.00	0.00	0.00
Fe3+/Fetot	0.00	0.35	0.80	0.62	0.61	0.59	0.50	0.15	0.00	0.52	0.40	0.50	0.53	0.68	0.54	0.34	0.42
Mg#	95.16	96.79	97.84	98.01	97.41	97.05	96.66	96.38	95.29	97.72	97.74	97.24	97.06	97.55	97.57	97.17	97.34

Table 3.2-S2. Composition of antigorite produced in experimental set#3.

T, ^{o}C	**700**	**700**	**700**	**700**	**700**	**700**	**700**	**700**
SiO2	42.79	43.20	41.29	44.39	44.70	43.73	44.17	43.92
TiO2	0.03	0.01	0.01	0.02	0.02	0.03	0.01	0.03
Al2O3	1.05	0.97	1.40	1.41	1.22	1.03	1.13	1.01
FeO	1.62	1.82	1.77	1.76	1.77	1.86	1.87	1.91
MnO	0.13	0.08	0.08	0.07	0.08	0.08	0.08	0.07
MgO	40.01	40.04	39.02	40.57	40.96	40.30	40.72	40.77
CaO	0.04	0.02	0.04	0.04	0.09	0.04	0.05	0.04
Na2O	0.00	0.00	0.00	0.00	0.00	0.00	0.00	0.00
K2O	0.00	0.01	0.00	0.00	0.00	0.00	0.00	0.00
Cr2O3	0.30	0.03	0.06	0.11	0.13	0.03	0.04	0.02
NiO	0.03	0.04	0.05	0.05	0.06	0.04	0.04	0.10
(OH)	14.00	13.79	16.27	11.59	10.99	12.86	11.90	12.13
Total	100.00	100.00	100.00	100.00	100.00	100.00	100.00	100.00
apfu								
Si	1.95	1.97	1.94	1.96	1.97	1.97	1.97	1.96
Ti	0.00	0.00	0.00	0.00	0.00	0.00	0.00	0.00
Al	0.06	0.05	0.08	0.07	0.06	0.05	0.06	0.05
Fe3+	0.04	0.05	0.03	0.06	0.06	0.05	0.05	0.05
Fe2+	0.02	0.02	0.04	0.00	0.01	0.02	0.02	0.03
Mn	0.00	0.00	0.00	0.00	0.00	0.00	0.00	0.00
Mg	2.72	2.72	2.73	2.68	2.69	2.70	2.70	2.72
Ca	0.00	0.00	0.00	0.00	0.00	0.00	0.00	0.00
Na	0.00	0.00	0.00	0.00	0.00	0.00	0.00	0.00
K	0.00	0.00	0.00	0.00	0.00	0.00	0.00	0.00
Cr	0.01	0.00	0.00	0.00	0.00	0.00	0.00	0.00
Ni	0.00	0.00	0.00	0.00	0.00	0.00	0.00	0.00
Fe3+/Fetot	0.72	0.70	0.50	0.96	0.91	0.76	0.76	0.65
Mg#	97.78	97.51	97.51	97.63	97.64	97.48	97.48	97.44

Table 3.2-S2. Composition of olivine produced in experimental set#3.

T, ^{o}C	**450**	**450**	**550**	**550**	**600**	**700**	**700**	**700**	**700**	**700**	**700**	**700**	**850**	**850**	**850**	**850**	**850**	**850**	**850**
SiO2	41.08	40.86	40.07	42.92	42.92	41.64	41.69	42.73	42.62	43.59	42.29	41.50	41.55	42.05	41.77	41.92	41.36	42.25	41.64
Al2O3	0.02	0.06	0.02	0.02	0.00	0.11	0.59	0.42	0.22	0.40	0.14	0.30	0.08	0.06	0.10	0.05	0.07	0.09	0.02
FeO	9.60	8.95	8.05	8.00	7.70	5.47	5.68	5.14	6.97	5.63	4.93	5.06	3.85	3.65	4.23	4.27	4.40	4.07	4.35
MnO	0.16	0.06	0.07	0.18	0.05	0.15	0.25	0.24	0.24	0.13	0.18	0.17	0.14	0.17	0.13	0.13	0.16	0.11	0.14
MgO	49.62	50.62	49.25	48.56	50.16	50.81	51.57	48.46	51.36	49.76	51.49	50.84	53.75	53.62	53.21	53.78	53.24	53.49	53.91
CaO	0.10	0.02	0.05	0.00	0.00	0.05	0.11	1.22	0.07	0.07	0.20	0.04	0.06	0.06	0.05	0.05	0.05	0.07	0.07
Na2O	0.00	0.00	0.00	0.00	0.00	0.00	0.01	0.00	0.00	0.00	0.00	0.00	0.00	0.00	0.00	0.00	0.00	0.00	0.00
K2O	0.00	0.00	0.00	0.00	0.00	0.01	0.00	0.01	0.00	0.00	0.00	0.00	0.00	0.00	0.00	0.01	0.00	0.00	0.00
Cr2O3	0.02	0.06	0.03	0.00	0.00	0.08	0.13	0.10	0.02	0.14	0.07	0.09	0.06	0.03	0.03	0.03	0.03	0.05	0.07
NiO	0.36	0.15	0.46	0.25	0.35	0.03	0.13	0.10	0.06	0.09	0.04	0.05	0.07	0.05	0.06	0.05	0.05	0.07	0.06
Total	100.97	100.77	98.00	99.94	101.19	98.49	100.32	100.00	101.69	100.00	100.00	100.00	100.00	100.00	100.00	100.35	100.00	100.27	100.41
apfu																			
Si	1.00	0.99	1.00	1.04	1.03	1.02	1.00	1.04	1.01	1.04	1.02	1.01	1.00	1.00	1.00	1.00	1.00	1.01	0.99
Al	0.00	0.00	0.00	0.00	0.00	0.00	0.02	0.01	0.01	0.01	0.00	0.01	0.00	0.00	0.00	0.00	0.00	0.00	0.00
Fe	0.19	0.18	0.17	0.16	0.15	0.11	0.11	0.10	0.14	0.11	0.10	0.10	0.08	0.07	0.08	0.09	0.09	0.08	0.09
Mn	0.00	0.00	0.00	0.00	0.00	0.00	0.01	0.00	0.00	0.00	0.00	0.00	0.00	0.00	0.00	0.00	0.00	0.00	0.00
Mg	1.80	1.83	1.83	1.75	1.79	1.85	1.85	1.76	1.82	1.77	1.85	1.85	1.92	1.91	1.90	1.91	1.91	1.90	1.92
Ca	0.00	0.00	0.00	0.00	0.00	0.00	0.00	0.03	0.00	0.00	0.01	0.00	0.00	0.00	0.00	0.00	0.00	0.00	0.00
Cr	0.00	0.00	0.00	0.00	0.00	0.00	0.00	0.00	0.00	0.00	0.00	0.00	0.00	0.00	0.00	0.00	0.00	0.00	0.00
Ni	0.01	0.00	0.01	0.00	0.01	0.00	0.00	0.00	0.00	0.00	0.00	0.00	0.00	0.00	0.00	0.00	0.00	0.00	0.00
Mg#	90.20	90.97	91.60	91.54	92.07	94.30	94.18	94.38	92.92	94.03	94.91	94.71	96.13	96.32	95.73	95.73	95.57	95.91	95.67

Table 3.2-S2. Composition of olivine produced in experimental set#3.

T, ^{o}C	**900**	**900**	**900**	**900**	**900**	**900**	**900**	**900**	**900**	**900**	**900**
SiO2	42.13	42.40	42.04	42.81	50.99	44.63	42.62	42.69	41.36	43.10	42.11
Al2O3	8.43	14.38	0.20	0.16	1.51	0.65	0.10	0.16	0.13	0.29	0.09
FeO	4.02	3.95	4.10	4.02	3.09	3.77	4.03	4.25	3.94	3.99	3.93
MnO	0.22	0.21	0.13	0.12	0.10	0.13	0.13	0.14	0.12	0.11	0.15
MgO	42.22	33.37	52.67	52.49	42.88	50.41	53.30	52.73	53.41	52.39	53.85
CaO	3.74	6.79	0.12	0.23	0.26	0.16	0.05	0.05	0.04	0.10	0.06
Na2O	0.00	0.00	0.00	0.00	0.01	0.02	0.00	0.00	0.00	0.00	0.01
K2O	0.00	0.00	0.00	0.00	0.01	0.00	0.00	0.00	0.01	0.01	0.00
Cr2O3	0.34	0.62	0.09	0.03	0.32	0.11	0.06	0.09	0.07	0.07	0.01
NiO	0.05	0.03	0.06	0.02	0.07	0.04	0.00	0.04	0.08	0.07	0.02
Total	101.50	102.11	100.00	100.00	100.00	100.02	100.35	100.27	100.00	100.20	100.27
apfu											
Si	0.99	0.99	1.01	1.02	1.19	1.06	1.01	1.02	1.00	1.02	1.00
Al	0.23	0.40	0.01	0.00	0.04	0.02	0.00	0.00	0.00	0.01	0.00
Fe	0.08	0.08	0.08	0.08	0.06	0.07	0.08	0.08	0.08	0.08	0.08
Mn	0.00	0.00	0.00	0.00	0.00	0.00	0.00	0.00	0.00	0.00	0.00
Mg	1.48	1.16	1.88	1.86	1.49	1.78	1.89	1.87	1.92	1.85	1.91
Ca	0.09	0.17	0.00	0.01	0.01	0.00	0.00	0.00	0.00	0.00	0.00
Cr	0.01	0.01	0.00	0.00	0.01	0.00	0.00	0.00	0.00	0.00	0.00
Ni	0.00	0.00	0.00	0.00	0.00	0.00	0.00	0.00	0.00	0.00	0.00
Mg#	94.92	93.77	95.82	95.88	96.11	95.97	95.93	95.67	96.03	95.90	96.07

Table 3.2-S2. Composition of clinopyroxene produced in experimental set#3.

T, ^{o}C	**600**	**600**	**600**	**600**	**600**	**700**	**850**	**900**	**900**	**900**	**900**
SiO2	53.78	55.04	54.98	51.68	53.80	53.47	54.37	52.74	55.37	51.19	53.43
Al2O3	0.25	0.13	0.16	0.43	0.26	1.98	2.62	1.72	1.86	3.15	2.24
FeO	4.26	2.56	2.89	1.94	1.29	2.08	1.54	1.85	2.51	1.65	1.74
MnO	0.16	0.20	0.35	0.21	0.19	0.13	0.08	0.13	0.10	0.11	0.12
MgO	15.13	17.44	18.22	22.03	20.57	24.42	18.86	18.94	22.16	24.31	20.77
CaO	24.91	24.11	22.78	20.84	21.49	17.98	19.90	21.21	16.53	18.21	20.07
Na2O	0.02	0.00	0.00	0.01	0.01	0.04	0.02	0.01	0.00	0.01	0.02
K2O	0.01	0.01	0.00	0.00	0.01	0.02	0.01	0.01	0.01	0.00	0.00
Cr2O3	0.09	0.00	0.03	0.21	0.03	0.19	0.40	0.41	0.38	0.42	0.24
NiO	0.00	0.00	0.00	0.00	0.00	0.09	0.05	0.04	0.00	0.04	0.08
Total	98.70	99.54	99.53	97.66	97.81	100.39	98.04	97.30	99.12	99.32	98.86
apfu											
Si	2.00	2.01	2.00	1.92	1.98	1.94	1.98	1.96	1.98	1.85	1.94
Al	0.01	0.01	0.01	0.02	0.01	0.09	0.11	0.08	0.08	0.13	0.10
Fe	0.13	0.08	0.09	0.06	0.04	0.07	0.05	0.06	0.08	0.05	0.05
Mn	0.01	0.01	0.01	0.01	0.01	0.00	0.00	0.00	0.00	0.00	0.00
Mg	0.84	0.95	0.99	1.22	1.13	1.40	1.02	1.05	1.18	1.31	1.12
Ca	0.99	0.94	0.89	0.83	0.85	0.49	0.78	0.84	0.63	0.71	0.78
Cr	0.00	0.00	0.00	0.01	0.00	0.01	0.01	0.01	0.01	0.01	0.01
Ni	0.00	0.00	0.00	0.00	0.00	0.00	0.00	0.00	0.00	0.00	0.00
Mg#	86.37	92.40	91.84	95.29	96.61	95.44	95.62	94.80	94.03	96.34	95.51
En	42.71	48.18	50.32	57.83	55.99	71.41	55.43	53.76	62.52	63.44	57.42
Fs	6.74	3.96	4.47	2.85	1.97	3.41	2.54	2.95	3.97	2.41	2.70
Wo	50.55	47.86	45.20	39.32	42.04	25.18	42.03	43.29	33.51	34.15	39.88
Aeg	0.00	0.00	0.00	0.00	0.00	0.00	0.00	0.00	0.00	0.00	0.00
Jad	0.00	0.00	0.00	0.00	0.00	0.00	0.00	0.00	0.00	0.00	0.00
Di	1.00	1.00	1.00	1.00	1.00	1.00	1.00	1.00	1.00	1.00	1.00

Table 3.2-S2. Composition of orthopyroxene produced in experimental set#3.

T, °C	**700**	**700**	**700**	**700**	**850**	**850**	**80**	**900**	**900**	**900**
SiO2	58.42	58.48	56.98	55.19	55.46	56.60	56.09	55.88	57.22	56.78
Al2O3	0.35	0.41	0.42	0.40	3.84	4.00	2.69	2.61	2.58	2.30
FeO	3.44	3.95	3.10	4.48	2.31	2.12	2.46	2.70	2.40	2.60
MnO	0.21	0.23	0.18	0.20	0.09	0.12	0.16	0.11	0.10	0.13
MgO	36.88	37.39	35.14	38.25	34.09	34.51	37.11	37.92	31.93	35.73
CaO	0.35	0.10	2.24	0.55	0.38	0.41	0.30	0.33	3.34	0.39
Na2O	0.00	0.00	0.00	0.01	0.00	0.00	0.00	0.00	0.01	0.00
K2O	0.01	0.01	0.01	0.00	0.00	0.00	0.00	0.00	0.00	0.01
Cr2O3	0.16	0.20	0.18	0.19	0.12	0.18	0.09	0.27	0.25	0.24
NiO	0.01	0.02	0.00	0.05	0.02	0.00	0.05	0.00	0.04	0.00
Total	99.86	100.85	98.31	99.42	96.39	98.06	99.00	99.94	98.00	98.29
apfu										
Si	1.00	0.99	0.99	0.96	0.97	0.97	0.96	0.95	0.99	0.98
Al	0.01	0.01	0.01	0.01	0.08	0.08	0.05	0.05	0.05	0.05
Fe	0.05	0.06	0.05	0.07	0.03	0.03	0.04	0.04	0.03	0.04
Mn	0.00	0.00	0.00	0.00	0.00	0.00	0.00	0.00	0.00	0.00
Mg	0.94	0.94	0.91	0.99	0.89	0.89	0.95	0.96	0.83	0.92
Ca	0.01	0.00	0.04	0.01	0.01	0.01	0.01	0.01	0.06	0.01
Cr	0.00	0.00	0.00	0.00	0.00	0.00	0.00	0.00	0.00	0.00
Ni	0.00	0.00	0.00	0.00	0.00	0.00	0.00	0.00	0.00	0.00
Mg#	95.02	94.41	95.28	93.83	96.34	96.67	96.41	96.15	95.96	96.08
En	94.42	94.24	91.30	92.93	95.61	95.88	95.87	95.58	89.50	95.36
Fs	4.95	5.58	4.52	6.11	3.63	3.30	3.57	3.82	3.77	3.89
Wo	0.64	0.19	4.18	0.97	0.77	0.82	0.56	0.60	6.73	0.75

Table 3.2-S2. Composition of clinochlore produced in experimental set#3.

T, ^{o}C	**850**	**850**	**850**	**850**
SiO2	34.05	31.87	31.05	33.07
TiO2	0.05	0.12	0.11	0.06
Al2O3	15.95	19.04	18.94	16.82
FeO	2.81	1.69	1.68	2.67
MnO	0.01	0.06	0.03	0.02
MgO	33.54	34.43	30.67	34.39
CaO	0.07	0.03	0.08	0.03
Na2O	0.00	0.00	0.01	0.01
K2O	0.00	0.00	0.00	0.00
Cr2O3	0.33	1.38	1.41	0.75
NiO	0.18	0.02	0.03	0.16
(OH)	13.02	11.36	16.00	12.01
Total	100.00	100.00	100.00	100.00
apfu				
Si	3.18	2.93	2.99	3.07
Ti	0.00	0.01	0.01	0.00
Al	1.76	2.06	2.15	1.84
Fe3+	0.09	0.03	0.14	0.03
Fe2+	0.13	0.10	0.00	0.18
Mn	0.00	0.00	0.00	0.00
Mg	4.67	4.72	4.40	4.76
Ca	0.01	0.00	0.01	0.00
Na	0.00	0.00	0.00	0.00
K	0.00	0.00	0.00	0.00
Cr	0.02	0.10	0.11	0.06
Ni	0.01	0.00	0.00	0.01
Total	17.88	15.97	17.81	17.96
Mg#	95.51	97.31	97.01	95.82
Fe3+/Fetot	0.40	0.20	1.00	0.13

Table 3.2-S2. Composition of garnet produced in experimental set#3.

T, °C	**900**	**900**	**900**	**900**	**900**
SiO2	48.40	42.48	42.68	42.61	42.48
TiO2	0.19	0.45	0.45	0.71	0.28
Al2O3	13.01	22.92	23.07	23.20	15.39
Cr2O3	1.06	1.27	1.21	0.65	0.80
FeO	2.96	4.26	4.19	3.91	4.25
MnO	0.32	0.51	0.56	0.39	0.40
MgO	20.00	20.55	20.62	18.80	32.30
CaO	14.04	8.05	8.08	10.83	4.64
Total	100.01	100.50	100.89	101.14	100.56
apfu					
Si	3.45	2.98	2.98	2.98	2.87
Ti	0.01	0.02	0.02	0.04	0.01
Al	1.09	1.89	1.90	1.91	1.23
Cr	0.06	0.07	0.07	0.04	0.04
Fe3+	0.00	0.03	0.02	0.01	0.97
Fe2+	0.24	0.22	0.22	0.22	0.00
Mn	0.02	0.03	0.03	0.02	0.02
Mg	2.12	2.15	2.15	1.96	3.25
Ca	1.07	0.60	0.60	0.81	0.34
Mg#	92.32	89.58	89.76	89.56	93.12
Almandine	7.07	7.31	7.34	7.39	0.00
Spessartine	0.55	1.01	1.10	0.76	0.63
Pyrope	61.40	71.54	71.45	64.96	90.08
Grossular	31.20	19.13	19.19	26.32	5.09
Andradite	0.00	0.30	0.25	0.07	4.02
Uvarovite	1.71	0.71	0.67	0.50	0.18

Supplementary material for Chapter 3.3

Amorphous boron composite gaskets for *in situ* high pressure and high temperature studies.

A.D. Rosa[1,*], M. Merkulova[2], G. Garbarino[1], V. Svitlyk[1], J. Jacobs[1], C. Sahle[1], O. Mathon[1], M. Munoz[2], S. Merkel[3]

[1] European Synchrotron Radiation Facility, ESRF, 71 rue des Martyrs, Grenoble, 38000, France

[2] Univ. Grenoble Alpes, ISTerre, F-38041 Grenoble, France

[3] Unité Matériaux et Transformations, ENSCL, CNRS, Université Lille1, Villeneuve d'Ascq, 59655, France

*correspondence e-mail: arosa@esrf.fr

Published article
High Pressure Research (2016)
DOI: 10.1080/08957959.2016.1245297

HIGH PRESSURE RESEARCH, 2016
http://dx.doi.org/10.1080/08957959.2016.1245297

Amorphous boron composite gaskets for *in situ* high-pressure and high-temperature studies

A. D. Rosa[a], M. Merkulova[b], G. Garbarino[a], V. Svitlyk[a], J. Jacobs[a], Ch.J. Sahle[a], O. Mathon[a], M. Munoz[c] and S. Merkel[d,e]

[a]European Synchrotron Radiation Facility, ESRF, Grenoble, France; [b]France Univ. Grenoble Alpes, Grenoble, France; [c]Univ. Montpellier, UMR 5243, Géosciences Montpellier, F-34095 Montpellier, France; [d]Univ. Lille, CNRS, INRA, ENSCL, UMR 8207 - UMET - Unité Matériaux et Transformations, F-59000 Lille, France; [e]Institut Universitaire de France, Paris, France

ABSTRACT
The diamond anvil cell (DAC) is a fundamental device used to explore the properties of materials under extreme pressure and temperature (*P/T*) conditions. In the past years, simultaneous high *P/T* DAC experiments using the resistively heated DAC (RH-DAC) techniques have been developed for studying materials properties in a wide *P/T* range. However, the mechanical instability of metallic gaskets used for sample confinement at high *P/T* conditions remains a limiting factor for exploiting the accessible *P/T* range of the RH-DAC. In this study, we present a new gasket configuration that overcomes these limitations. It is based on an amorphous boron–epoxy mixture inserted in a rhenium gasket. We show how these gasket inserts stabilize the sample chamber over a wide *P/T* range, allowing monitoring sample properties using X-ray diffraction and absorption spectroscopy up to 50 GPa and 1620 K.

ARTICLE HISTORY
Received 2 August 2016
Accepted 3 October 2016

KEYWORDS
High pressure and temperature; diamond anvil cell; resistive heating; internal heater; assembled gaskets

1. Introduction

Science at extreme conditions of pressure and temperature is a vibrant domain of research that addresses fundamental questions in a variety of scientific disciplines ranging from Earth and planetary sciences to fundamental physics and chemistry and materials research. Static high *P/T* studies are classically performed using internally or externally resistively heated diamond anvil cells (RH-DACs), laser-heated DACs or in large volume presses (*e.g.* multi-anvil or Paris–Edinburgh Presses).

High *P/T* studies using internally RH-DACs have become more important for studying materials behavior at simultaneous high *P/T* conditions (*i.e.* [1,2] for review). The RH-DAC reaches routinely temperatures up to 1400 K [3–5], while temperatures of up to 2000 K have been reported in a few experiments based on miniature heater techniques [6]. The RH-DAC is complementary to externally resistively and laser-heated DACs because it covers a temperature range from ambient to 1400 K that is difficult to fully access with these techniques. A key advantage over the laser-heated DAC consist in the precise control and regulation of the *P/T* conditions, the homogenous heating of the sample and the possibility to generate stable *P/T* conditions over a long period of time

CONTACT A. D. Rosa ✉ arosa@esrf.fr

(days). This latter aspect is of particular importance for measurements that require long acquisition times. In addition, the RH-DAC is compact and can be easily combined with different *in situ* methods, including X-ray diffraction (XRD), X-ray absorption (XAS), Raman, or Brillouin spectroscopy. These methods give access to various high *P/T* processes, including phase transformations, dissolution reactions, texture evolutions and speciation of elements in minerals and fluids [7–12].

Different designs of internally heated DACs have been reported, including geometries where the heating element fully surrounds the diamonds and gasket [3–5,13–16], or miniature heaters that are contained between the diamond culets [6,17–23]. Temperatures in excess of 2000 K at pressures up to 50 GPa have been reported for miniature heaters [6]. However, for these designs, the maximum temperature beyond 50 GPa was limited to 1600 K. It is worth noting that experiments beyond 50 GPa are very challenging due to the small size of the heater, insulating materials and electrodes. In this case, only solid materials can be introduced in the high pressure cavity. In the configuration, where the heater surrounds the diamonds, a rhenium gasket can be used allowing the loading of solids (single crystals and powders) and liquids. At ambient temperature, rhenium gaskets allow reaching pressures well beyond 100 GPa. Pure Re gaskets have been already employed up to 92 GPa and 1200 K in externally heated DACs [24]. However, we observed that at temperatures in excess of ~1170 K, especially thin rhenium gaskets (*i.e.* 35 µm) exhibit a reduced strength. At these high temperatures, Re can significantly deform, which is most likely related to the reduction of the shear modulus at elevated temperature. This deformation at high *T* presents a limiting factor in exploiting the full capabilities of the RH-DAC to reach temperatures in excess of 1170 K at simultaneous high pressures.

Previous ambient temperature high-pressure DAC studies have shown that gaskets containing an insert consisting of amorphous Boron Epoxy (aBE), c-BN epoxy (cBNE) or diamond powder epoxy are mechanically more stable. This was for instance demonstrated when these inserts are used to reinforce beryllium gaskets in order to maximize the sample thickness and reach higher pressures [25–29]. Pure aBE and cBNE gaskets have been successfully used in combination with a kapton foil for radial DAC XRD experiments up to 80 GPa [30,31]. Amorphous boron exhibits a high shear strength combined with a low X-ray absorption. It is therefore ideal for X-ray emission spectroscopy (XES), XAS or XRD experiments in radial DAC geometry. Because of its low thermal conductivity, it is also a good choice for large volume press experiments [32]. Recently, pure aBE disks have been employed for resistive heating experiments in combination with a mica foil and have shown good mechanical stability up to 20 GPa and 1100 K [33]. Similarly, composite Re/c-BN gaskets have been successfully employed up to 1100 K and 93 GPa in externally heated DACs [34].

Here, we show how a small insert of aBE introduced into the hole of a Re gaskets allows us to reach high *P/T* conditions of 1620 K and 50 GPa, *P/T* conditions that are difficult to reach with pure Re gaskets.

2. Experimental setup

2.1. aBE synthesis

We used, as starting materials, amorphous boron (Sigma-Aldrich; 99% pure; part No. B3135) and an epoxy resin and hardener (Struers EPOfix) in the ratio of 1:0.22:0.08 by

Table 1. Summary of performed experiments.

Exp#	Technique	aBE insert geometry	Culet size (μm) BA[a]	Thickness (μm)	Hole diameter Re/aBE (μm)	Max. P/T conditions
1	XRD	No insert	300/350	35	100	6 GPa, 1170 K
2	XRD	1	300/350	85	280/55	50 GPa, 1620 K
3	XAS	2	600	80	360/130	2 GPa, 1020 K

[a] In all experiments, Boehler Almax cut diamonds were employed [35].

weight. A homogenous product was obtained by mixing these substances in a mortar together with acetone. A small amount of this mixture was then distributed into individual plastic bags and placed in a vacuum desiccator for 2 h. The dried mixture was cold pressed at 0.3 GPa using a cylindrical mold. The cold-pressed aBE cylinders were wrapped with Teflon for further polymerization at 0.5 GPa and 600 K in order to increase the stiffness of the material.

2.2. Gasket insert geometries and preparation

For the present study, we tested two different aBE insert geometries (Table 1). In the first geometry, the Re gasket hole was lined with an aBE insert and additional material of aBE was used to cover the entire pre-indentation surface on one side of the Re gasket (Figure 1(a)). This composite gasket geometry significantly increases the total gasket thickness. To prepare this composite gasket, a hole was drilled in a pre-indented Re gasket and filled with aBE. Additional material of aBE was placed on top of the pre-indentation surface. This filled gasket was then compressed between two diamonds to produce a compact assembly, which was further laser drilled at its center to form the final sample container (Figure 1(a)). In the second geometry, we tested a simplified aBE insert configuration, consisting of a ring of aBE contained in a Re gasket hole (Figures 1(b) and 2). The sample cavity was again produced by laser drilling. Dimensions of the gaskets and employed diamond anvils are listed in Table 1.

3. High *P/T* experiments

Two XRD experiments were performed to compare the stability of a Re gasket and a Re gasket equipped with an aBE insert at high *P/T* conditions, Exp#1 and #2, respectively.

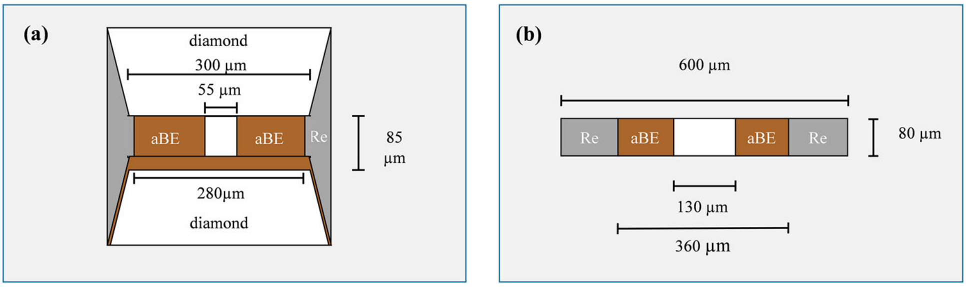

Figure 1. Illustration of the two aBE gasket insert geometries: (a) geometry 1 used in Exp#2 and (b) geometry 2 used in Exp#3 (see also Figure 2).

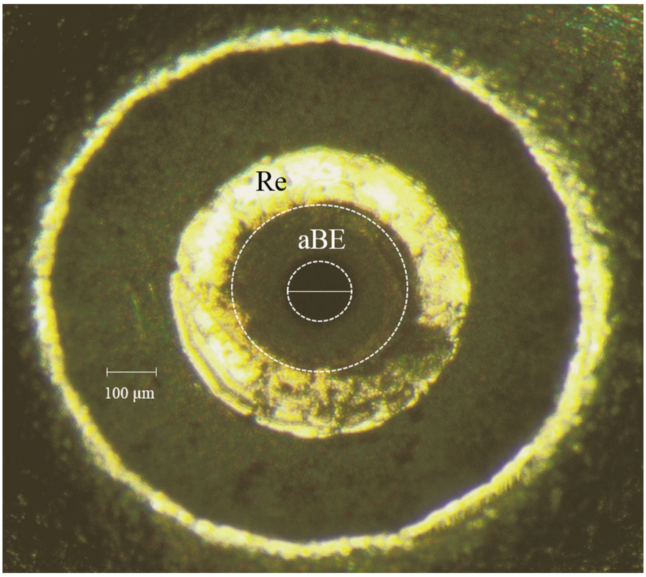

Figure 2. Photograph of an aBE insert of geometry 2 contained in a pre-indented Re gasket employed in Exp#3.

(Table 1). For the high *P/T* experiments, modified Letoulec-type membrane DACs were used; culet sizes are outlined in Table 1. The heating elements of the internally heated RH-DAC and its vacuum chamber will be detailed in a separate article. During the experiments, sample *P/T* conditions were determined *in situ* from internal *P/T* standards, including, a chip of gold and a pellet of NaCl of 5*7*5 μm^3 volume loaded together with the sample [36]. *P/T* conditions were obtained using the thermal equations of state of gold [37] and of NaCl [38]. Pressure and temperature were remotely controlled and care was taken that the vacuum remained below $1*10^{-6}$ bars during the entire experiment.

In Exp#1, a conventional Re gasket was employed and the sample comprised a powder of hydrous Mg_2SiO_4. The sample in Exp#2 was loaded in a Re gasket equipped with an aBE insert of geometry 1. In Exp#2, the sample consisted of a powder of antigorite containing 1.5 wt% iron ($Mg_{2.76}Fe^{2+}_{0.007}Fe^{3+}_{0.044}Si_{1.96}$ $Al_{0.037}O_5(OH)_4$), which was mixed with 1.5 wt% of pyrite (FeS_2). Both minerals employed in Exp.#1 and #2 are relevant for geosciences and exhibit close mechanical properties.

The two diffraction experiments (Exp#1, 2) were carried out at the ESRF beamline ID27. A monochromatic X-ray beam was used, tuned to an energy of 33.17 keV (0.3738 Å) and focused to $5 \times 2.8\ \mu m^2$ (horizontal × vertical size). Diffraction images were acquired using a flat panel PerkinElmer detector placed 450 or 550 mm from the sample. The detector to sample distance, detector tilt and rotation parameters were calibrated using a CeO_2 powder standard using the program DIOPTAS [39]. During Exp#1 and #2, the size of the sample chamber was determined from horizontal and vertical scans of the X-ray beam through the sample chamber and/or by finely meshed two-dimensional diffraction maps acquired with a step size of 5–10 μm and an exposure time of 5–10 s.

In experiments Exp.#1 and #2, we followed a *P/T* path corresponding to the geothermal gradient of subducted slabs with *T* increasing to ~1150 K between 1–6 GPa. At 6 GPa and

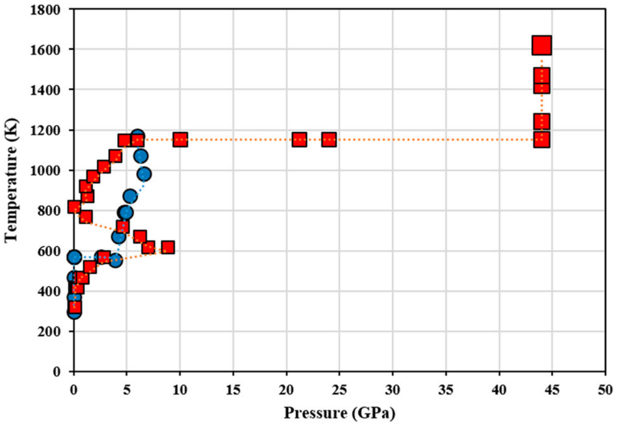

Figure 3. *P/T* pathways of the two XRD experiments Exp#1(blue circles) and Exp#2 (red squares). Presented temperatures are averaged thermocouple temperatures measured at each diamond, while sample pressures were calculated using the lattice parameter of Au. Uncertainties of *P/T* points are within the symbol size.

1170 K, the sample chamber in Exp#1 drifted towards the culet edge leading to a diamond anvil failure. In Exp#2, the pressure was further increased first to 50 GPa at a constant temperature of 1150 K. Finally, temperature was raised to 1620 K at a constant pressure of 50 GPa (Figure 3). At each *P/T* point, temperature was held constant for about 30–45 min and XRD data were taken after *T* stabilization. At the highest *P/T* point, the DAC zirconia seat broke few minutes after temperature increase and Exp#2 had to be stopped (Table 1).

4. Value added for gasket stability at high *T*

The aBE insert employed in Exp#2 allowed reaching far higher *P/T* conditions of 50 GPa and 1620 K, compared to Exp#1 in which a conventional Re gasket was used, which failed at 6 GPa and 1170 K. In Exp#2 boron started to recrystallize forming β-boron at 1240 K and 50 GPa, which did not affect the stability of the gasket. Based on the comparison between Exp#1 and #2, we suggest that employing an aBE insert avoids the opening of the Re gasket mainly because of the higher shear resistance of aBE at high *T* compared to pure Re. Moreover, the smaller sample chamber and the greater thickness of the aBE composite gasket compared to the conventional Re gasket (see Table 1), might have additionally stabilized it at high *P/T* conditions.

The observed maximal *T* stability of pure Re in the present study in Exp#1 (1170 K at 6 GPa) is slightly below the maximal *T* conditions reached in previous studies employing pre-indented Re gaskets (1200 K at 93 GPa) [24]. We note however, that the difference of 30 K is within the precision on *P/T* determination at the extreme conditions probed by Dubrovinskaia and Dubrovinsky [24]. Moreover, the stability of conventional Re gaskets might also depend on the chosen P/T pathway. Therefore, the maximal T stability of Re observed in the present study of ~1170 K presents only an indication rather than a strict temperature limit.

We observed that the sample chamber remained stable and centered on the culet during Exp#2 (Figure 4). In this experiment, the sample chamber decreased from an

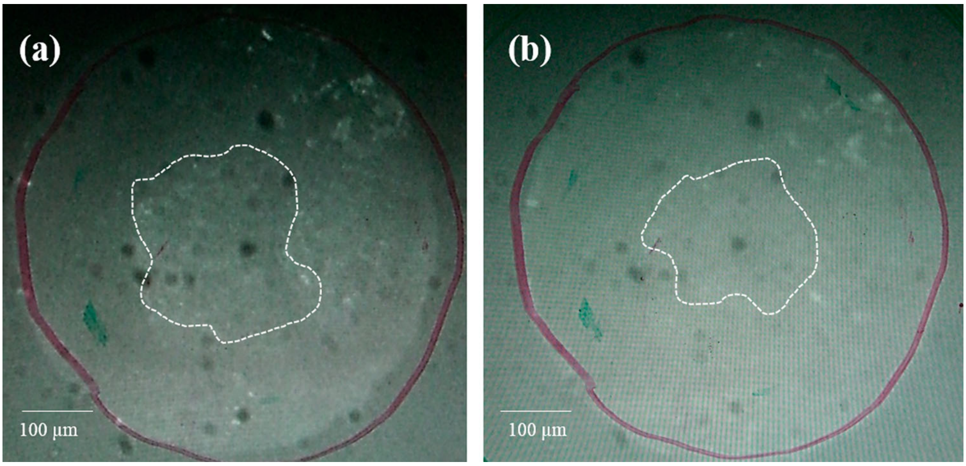

Figure 4. (a–b) Sample shape during Exp#2 in which the aBE insert geometry 1 was employed (a) 6.2 GPa, 670 K, (b) 6 GPa, 1150 K. The red and white line outline the diamond culet and the sample contained in the aBE insert, respectively. Both lines were drawn based on contrasts in gray scale between aBE and Re as well as aBE and sample. These contrasts further reduced significantly with increasing temperature. Note also, for this aBE insert geometry (1), the border between aBE and Re at high *P/T* is optically not distinguishable due the small layer of aBE on top of the Re. Dark points are particles on the objective lens of the microscope.

original $55 \times 55\ \mu m^2$ size to about $40 \times 40\ \mu m^2$ during the first pressurizing ramp up to 3 GPa. It then remained constant until pressure was increased to 50 GPa. At this pressure, the hole size further decreased to $20 \times 30\ \mu m^2$ and then remained stable while increasing temperature up to 1620 K.

The sample chamber hole in the aBE material, however, did not remain circular in Exp#2 because particles of the polymerized aBE easily mix with the sample. Figure 5 shows selected diffraction patterns of Exp#2, presenting the data quality obtained during the experiment at relatively low and high *T*. All diffraction peaks could be indexed. Contributions to the overall background arise mainly from the RH-DAC components, including the Mylar window and the diamonds as well as only ancillary from aBE, suggesting that the employment of aBE does not hinder the XRD data quality for crystalline samples. For amorphous and liquid samples, the signal quality could be influenced by the small diffused scattering background due to aBE, which can be reduced significantly by employing a small X-ray beam of $2 \times 2\ \mu m^2$ size and/or Soller-slits coupled with the RH-DAC.

5. Reactivity of aBE at high *T*

XAS experiments were carried out at the ESRF beamline BM23 using the μXAS station described in [40], in order to test the reactivity of the aBE material at high *P/T* conditions (Exp#3, Table 1). The sample employed in Exp#3 consisted of the same starting material as in Exp#2, which was loaded into an aBE insert of geometry 2. A *P/T* path similar to that of Exp#2 was followed at low pressure of 2 GPa up to 1020 K.

For the experiment, the X-ray beam was tuned to the energy of the iron K-edge (7.112 keV) using a double-crystal fixed exit monochromator equipped with two Si(111) crystals.

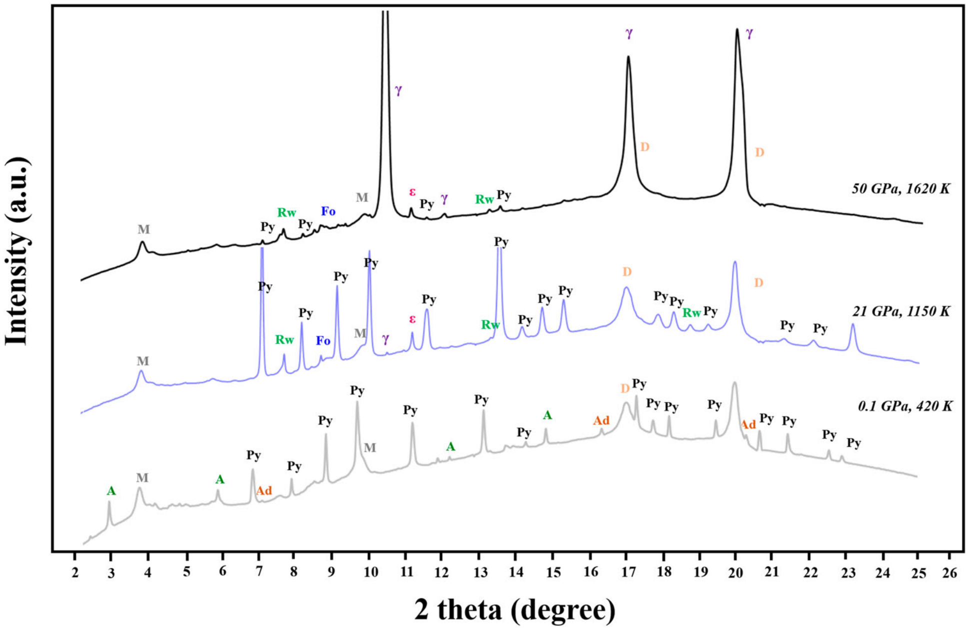

Figure 5. Diffraction patterns of selected *P/T* points acquired during Exp#2. Diffraction peaks are labeled as: A: antigorite; M, Mylar window of the RH-DAC; D: Diamond; Py: pyrite; Ad: andradite; Fo: forsterite; Rw: ringwoodite; γ: fcc-iron; ε: hcp-iron. At 21 GPa and 1150 K, diffraction peaks of pure hcp-iron (ε-Fe) as well as less intense peaks of fcc-iron (γ-Fe) appeared, while those of pyrite decreased gradually. With increasing *P/T* conditions and up to 50 GPa and 1620 K diffraction peaks of pure γ-Fe became very intense, while those of pyrite almost completely disappeared. The coexistence of Fo and Rw at 50 GPa and 1620 K might be related to the sluggish phase transformation kinetics in Mg_2SiO_4.

Beam focusing to 6 × 6 μm^2 and harmonic rejection was achieved through a Kirkpatrick Baez mirror system with Pt coating. XAS measurements were conducted in transmission mode using ionization chambers filled with appropriate gas mixtures. The fixed exit monochromator-crystal angles were calibrated to the iron K-edge energy of 7.112 keV using a standard iron foil of 3 μm thickness. Several times during the experiment the foil spectrum was acquired in order to correct potential drifts of the monochromator angle. Diffraction images were collected using a MarCCD detector placed 190 mm from the sample at a wavelength of 0.6199 Å corresponding to an energy of 20 keV. The sample-to-detector distance, beam center position, detector tilt angles were determined using a CeO_2 standard and the program DIOPTAS [39].

X-ray absorption near-edge structure (XANES) spectra were collected in temperature steps of 50 or 100 K between ambient temperature and 1020 K at constant high pressure. For each *P/T* point three XANES spectra were acquired during continuous scanning of the monochromator, with a scan time for each spectrum of ca. 10 min. XRD patterns of the sample and the gold pressure standard were obtained before and after each XANES scan with an exposure time of 5 min.

Figure 6 shows the averaged normalized iron *K*-edge XANES spectra collected during Exp#3 at a constant pressure of 2 GPa and selected *T*. At *T* exceeding 620 K, we observed a significant change of the spectral shape. In particular, the absorption edge continuously

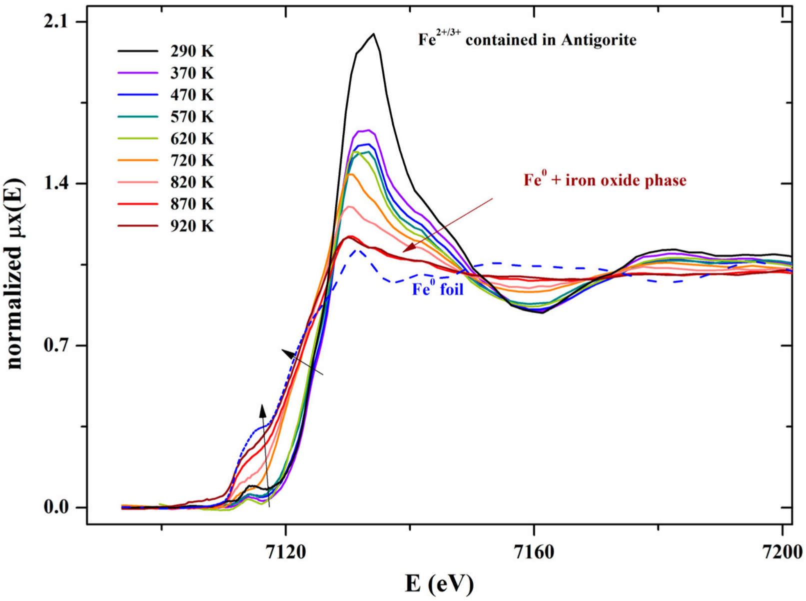

Figure 6. Normalized averaged iron XANES spectra acquired during Exp#3 at constant pressure (2 GPa) and selected temperatures. Black arrows indicate the shift of oxidized iron (Fe^{2+}/Fe^{3+}) contained in Antigorite XANES spectra features towards reduced iron (Fe^0) spectral features. For comparison the XANES spectra of the reference iron foil is plotted as a blue dashed line.

shifted towards lower energies. These changes coincided with the beginning of the breakdown reaction of antigorite to forsterite, enstatite and water, which was confirmed from the simultaneously collected XRD patterns. At 920 K the presence of a mixture of metallic iron and iron oxide phases in the sample was deduced from the XANES spectrum. This indicates that the Fe^{3+}/Fe^{2+} mixture previously contained in antigorite was reduced to metallic Fe^0. Such a drastic reduction of iron can only be ascribed to the formation of boron-oxides (B_2O_3) in the aBE insert which creates highly reducing conditions in the sample chamber. The reaction occurred during the experiments may be described as follows:

$$10Mg_{2.8}Fe_{0.2}Si_2O_5(OH)_4 + 44B \rightarrow 22B_2O_3 + 20H_2 + 2Fe\ + 6SiO_2 + 14Mg_2SiO_4.$$

Indeed, the formation of boron-oxides at high temperatures has been previously observed in hexagonal BN [41]. The presence of pure iron and/or boron-oxide could not be deduced from the diffraction patterns taken during serpentine breakdown in Exp#3, most likely due to the rather small abundances of these phases.

6. Conclusions

We have tested a new assembled gasket geometry based on inserts of aBE introduced into a rhenium gasket hole. These inserts allow reaching far higher *P/T* conditions up to 50 GPa and 1620 K than conventional Re gaskets, which failed at 1170 K and 6 GPa due to the plastic flow of Re at high temperature. Comparison of our experiments indicates that the composite gasket retains a higher stiffness at high temperatures exceeding 1170 K compared to pure rhenium.

The sample shape does not remain circular at high *P/T* condition, due to the porous nature of aBE. The mix of aBE and sample at the gasket hole rim does not alter the powder and single-crystal XRD or XAS data quality. The aBE insert can however not be employed in direct contact to oxidized samples due to the high redox potential of boron at elevated temperatures. Samples should therefore be isolated from the aBE insert by introducing, for example, an additional ring of Au or Pt sealed under pressure to avoid the diffusion of oxygen. The sample shape may also be stabilized by the introduction of this sealing ring, which might further allow employing a fluid or gas phase as pressure-transmitting medium.

In summary, the assemble gaskets tested in this study expand the accessible *P/T* range for resistively heated DAC experiments to thermodynamical conditions that are challenging to reach with this device and are close to the intrinsic limit of the RH-DAC. However, care must be taken to avoid reaction of the insert with the sample, which is a general problem in high *P/T* studies.

Acknowledgement

The authors thank the European Synchrotron Radiation Facility for providing beam time, Herve Cardon for advices on the perforated diamond geometry, Stany Bauchau for providing technical equipment during the experiment and Fabrice Brunet for fruitful discussions. The authors want to thank the two anonymous reviewers for their comments, which improved the presentation of this manuscript, and S. Klotz for fast editorial handling.

Disclosure statement

No potential conflict of interest was reported by the authors.

References

[1] Liermann H-P. X-Ray diffraction; modern experimental techniques. Boca Raton (FL): Pan Standford; 2015. Chapter 10, X-ray diffraction at extreme conditions: today and tomorrow; p. 255–314.

[2] Dubrovinskaia N, Dubrovinsky L. Advances in high-pressure technology for geophysical applications. Amsterdam: Elsevier; 2005. Chapter 25, Internal and external electrical heating in diamond anvil cells; p. 487–501.

[3] Liermann H-P, Merkel S, Miyagi L, et al. Experimental method for in situ determination of material textures at simultaneous high pressure and high temperature by means of radial diffraction in the diamond anvil cell. Rev Sci Instrum. 2009;80:104501:1–8.

[4] Pasternak S, Aquilanti G, Pascarelli S, et al. A diamond anvil cell with resistive heating for high pressure and high temperature X-ray diffraction and absorption studies. Rev Sci Instrum. 2008;79(8):085103:1–5.

[5] Du Z, Miyagi L, Amulele G, et al. Efficient graphite ring heater suitable for diamond-anvil cells to 1300 K. Rev Sci Instrum. 2013;84:024502:1–5.

[6] Zha CS, Bassett WA. Internal resistive heating in diamond anvil cell for in situ x-ray diffraction and Raman scattering. Rev Sci Instrum. 2003;74:1255–1262.

[7] Pippinger T, Miletich R, Burchard M. Multipurpose high-pressure high-temperature diamond-anvil cell with a novel high-precision guiding system and a dual-mode pressurization device. Rev Sci Instrum. 2011;82:1:29–43.

[8] Rosa AD, Hilairet N, Ghosh S, et al. *In situ* monitoring of phase transformation microstructures at Earth's mantle pressure and temperature using multi-grain XRD. J Appl Cryst. 2015;48:1346–1354.

[9] Speziale S, Marquardt H, Duffy TS. Reviews in Mineralogy and Geochemistry: spectroscopic methods in mineralogy and materials science. Budapest: Eötvös University Press. Volume 78, Chapter 14, Brillouin scattering and its application in geosciences, 2014; p. 543–603.

[10] Louvel M, Sanchez-Valle C, Malfait WJ, et al. Zr complexation in high pressure fluids and silicate melts and implications for the mobilization of HFSE in subduction zones. Geochim Cosmochim Acta. 2013;104:281–299.

[11] Komabayashi T, Fei Y, Meng Y, et al. In-situ X-ray diffraction measurements of the γ-ε transition boundary of iron in an internally-heated diamond anvil cell. Earth Plant Sci Lett. 2009;282:252–257.

[12] Sanchez-Valle C, Martinez I, Daniel I, et al. Dissolution of strontianite at high PT conditions: an in-situ synchrotron X-ray fluorescence study. Am Mineral. 2003;88(7):978–985.

[13] Bureau H, Burchard M, Kubsky S, et al. In situ characterization of geological materials at high pressure and temperature: techniques and observations. High Pressure Res. 2006;26(3):251–265.

[14] Muñoz M, Bureau H, Malavergne V, et al. In situ speciation of nickel in hydrous melts exposed to extreme conditions. Phys Scr. 2005;T115:921–922.

[15] M. Muñoz, S. Pascarelli, G. Aquilanti, et al. Hyperspectral μ-XANES mapping in the diamond-anvil cell: analytical procedure applied to the decomposition of (Mg, Fe)-ringwoodite at the upper/lower mantle boundary. High Pressure Res. 2008;28:665–673.

[16] Andrault D, Muñoz M, Bolfan-Casanova N, et al. Experimental evidence for perovskite and post-perovskite coexistence throughout the whole D ″region. Earth Plant Sci Lett. 2010;293:90–96.

[17] Burchard M, Kubsky S, Bureau H, et al. X-ray transmission properties of intelligent anvils in diamond anvil cells. High Pressure Res. 2006;26:235–241.

[18] Miletich R, Cinato D, Johaenntgen S. An internally heated composite gasket for diamond-anvil cells using the pressure-chamber wall as the heating element. High Pressure Res. 2009;29:290–305.

[19] Dubrovinsky LS, Dubrovinskaia N, Langenhorst F, et al. Iron–silica interaction at extreme conditions and the electrically conducting layer at the base of Earth's mantle. Nature. 2003;422:58–61.

[20] Dubrovinsky LS, Saxena SK. Iron at extreme conditions: in situ X-ray study of P-V-T relations in internally heated diamond anvil cell and modeling of interatomic potential of iron. Petrology. 1998;6:535–545.

[21] LeToullec R, Datchi F, Loubeyre P, et al. High Pressure Science and Technology. A new device for high temperature and high pressure: a heating gasket in a ceramic DAC. Proc. Joint 15th AIRAPT and 33rd EHPRG International Conference; Warsaw: World Scientific Publishing; 1996; p. 54–56.

[22] Mao HK, Bell P, Hadidiacos C. Experimental phase relations of iron to 360 kbar, 1400 ∘C, determined in an internally heated diamond-anvil apparatus. San Francisco (CA): High-Pressure Research in Mineral Physics, TERRAPUB/AGU; 1997; p. 135–138.

[23] Boehler R, Nicol M, Zha CS, et al. Resistance heating of Fe and W in diamond-anvil cells. Phys B. 1986;139–140:916–918.

[24] Dubrovinskaia N, Dubrovinsky L. Whole-cell heater for the diamond anvil cell, Rev. Sci Instrum. 2003;74:3433–3438.

[25] Wang L, Yang W, Xiao Y, et al. Application of a new composite cubic-boron nitride gasket assembly for high pressure inelastic x-ray scattering studies of carbon related materials. Rev Sci Instrum. 2011;82:073902:1–5.

[26] Funamori N, Sato T. A cubic boron nitride gasket for diamond-anvil experiments. Rev Sci Instrum. 2008;79:053903.

[27] Lin JF, Shu J, Mao H-K, et al. Amorphous boron gasket in diamond anvil cell research. Rev Sci Instrum. 2003;74(11):4732–4736.

[28] Zou GT, Ma YZ, Mao K-K, et al. A diamond gasket for the laser-heated diamond anvil cell. Rev Sci Instrum. 2001;72:1298–1301.

[29] Boehler R, Ross M, Boercker DB. Melting of LiF and NaCl to 1 Mbar: systematics of ionic solids at extreme conditions. Phys Rev Lett. 1997;78:4589–4592.

[30] Marquardt H, Miyagi L. Slab stagnation in the shallow lower mantle linked to an increase in mantle viscosity. Nat Geosci. 2015;8:311–314.

[31] Rosa AD, Sanchez-Valle C, Nisr C, et al. Shear wave anisotropy in textured phase D and constraints on deep water recycling in subduction zones. Earth Planet Sci Lett. 2013;377–378:13–22.

[32] Morard G, Mezouar M, Rey N, et al. Optimization of Paris–Edinburgh press cell assemblies for in situ monochromatic X-ray diffraction and X-ray absorption. High Pressure Res. 2007;27(2):223–233.

[33] Miyagi L, Kanitpanyacharoen W, Raju S, et al. Combined resistive and laser heating technique for in situ radial X-ray diffraction in the diamond anvil cell at high pressure and temperature. Rev Sci Instrum. 2013;84:025118:1–9.

[34] Antonangeli D, Komabayashi T, Occelli F, et al. Simultaneous sound velocity and density measurements of hcp iron up to 93 GPa and 1100 K: an experimental test of the Birch's law at high temperature. Earth Planet Sci Lett. 2012;331–332:210–214.

[35] Boehler R, De Hantsetters K. New anvil designs in diamond-cells. High Pressure Res. 2004;24(3): 391–396.

[36] Crichton WA, Mezouar M. Noninvasive pressure and temperature estimation in large-volume apparatus by equation-of-state cross-calibration. High Temp – High Press. 2002;34(2):235–242.

[37] Shim S-H, Duffy TS, Takemura K. Equation of state of gold and its application to the phase boundaries near 660 km depth in Earth's mantle. Earth Planet Sci Lett. 2002;203:729–739.

[38] Matsui M, Higo Y, Okamoto Y, et al. Simultaneous sound velocity and density measurements of NaCl at high temperatures and pressures: application as a primary pressure standard. Am Mineral. 2012;97:1670–1675.

[39] Prescher C, Prakapenka VB. *DIOPTAS*: a program for reduction of two-dimensional X-ray diffraction data and data exploration. High Pressure Res. 2015;35:223–230.

[40] Mathon O, Beteva A, Borrel J, et al. The time-resolved and extreme conditions XAS (TEXAS) facility at the European Synchrotron Radiation Facility: the general-purpose EXAFS bending-magnet beamline BM23. J Synchrotron Rad. 2015;22:1548–1554.

[41] Wendlandt R, Huebner S. The redox potential of boron nitride and implications for its use as a crucible material in experimental petrology. Am Mineral. 1962;67:170–174.

Supplementary figure for Chapter 4.5

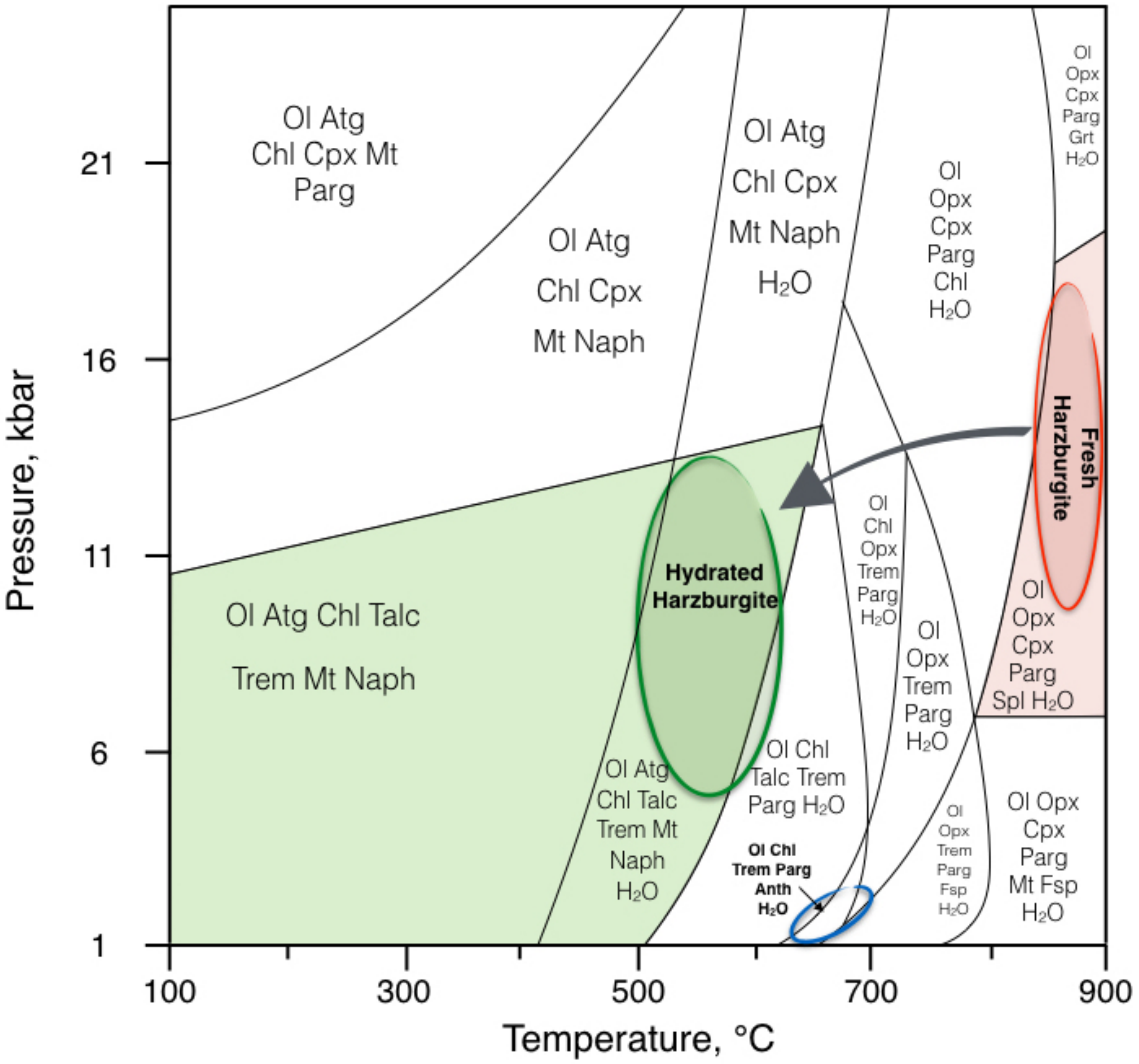

Fig. 4.5-S1. P-T pseudosection for the bulk composition of fresh harzburgite with additional H_2O (6 wt.%) computed with Theriak-Domino program. Green field indicates stability of hydrated lithologies with antigorite, pink field represents stability of pargasite-bearing harzburgites. Blue circle indicates stability field of anthophyllite-bearing hydrated assemblages. Abbreviations are: Ol – olivine, Atg – antigorite, Chl – chlorite, Trem – tremolite, Mt – magnetite, Naph – Na-phlogopite, Cpx – clinopyroxene, Parg – pargasite, Anth – antophyllite, Opx – orthopyroxene, Fsp – feldspar, Grt – garnet.